Master Thesis: Modelling flow and contaminant transport in Sardas site affected by lindane from Inquinosa in Sabiñánigo (Huesca)

Author: Brais Sobral Areán

Tutors: Javier Samper and Acacia Naves

Date: 7 July 2020

h²
Hochschule
Magdeburg • Stendal
Fachbereich Wasser und Kreislaufwirtschaft

INTERNATIONAL MASTER IN WATER ENGINEERING

Universidad de A Coruña
ETS de Ingenieros de Caminos, Canales y Puertos
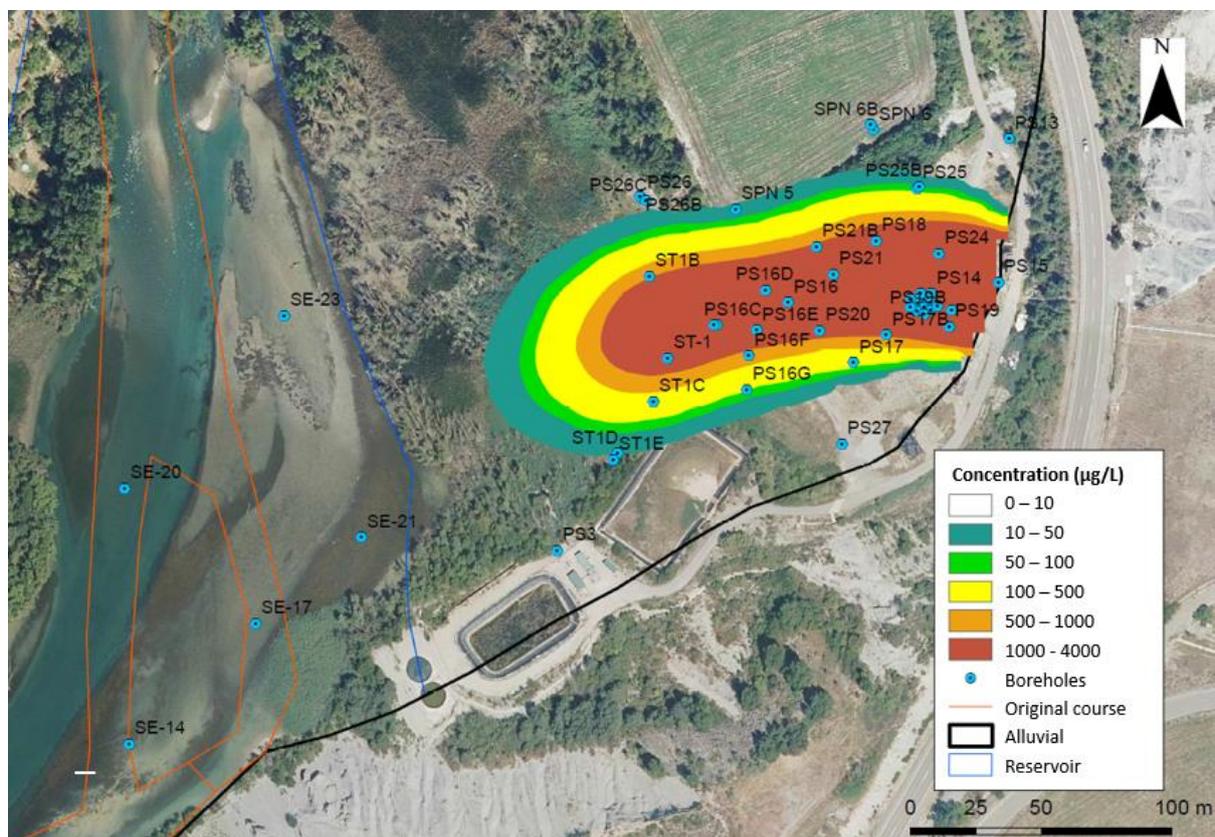
SUMMARY

The INQUINOSA lindane factory in Sabiñánigo (Spain) operated since 1975 until 1992. Dust and liquid wastes from the lindane production were disposed at the Sardas landfill. The Sardas landfill lies over the Larrés marls without waterproofing. It occupies an area of 4 ha and is located less than 1 km to the East of the downtown. The conceptual model of the site was tested by EMGRISA (2014) with a groundwater flow model performed with MODFLOW (Harbaugh *et al.*, 2005). This master's thesis presents 2D steady-state and transient numerical models of groundwater flow and contaminant transport of the Sardas site, which have been performed with the finite-element computer code CORE^{2D} V5. First, a 2D model along a vertical profile in E-W direction, which runs along the thalveg of the original gully, has been constructed to test the conceptual hydrogeological model of the site. The numerical model confirms the conceptual model. The average water inflow to the Sardas landfill ranges from 20 m^3/d to 30 m^3/d. Most of the inflow comes from the infiltration of the surface runoff of the ravine located in the header of the landfill and the infiltration of surface and subsurface runoff along the perimeter ditches. The landfill outflows take place by pumping wells, underneath and around the front slurry-wall. The subsurface discharge of the landfill percolates into the Gállego alluvial aquifer. The 2D horizontal numerical models of groundwater flow through the gravels of alluvial aquifer confirm the strong influence of the daily periodic fluctuations of the water level of the Sabiñánigo reservoir and the Gállego river on groundwater hydraulic heads. The numerical models of the pumping and tracer tests showed the spatial heterogeneities and anisotropy of the hydraulic conductivity of the gravels and allowed the estimation of the porosity and dispersivity the gravels. The leachates from the landfill discharge into the reservoir through the silting sediments, which deposited at the bottom of the Sabiñánigo reservoir. The vertical hydraulic conductivity and the distribution coefficient of HCH of these sediments play a major role on the discharge of HCH to the reservoir.

Keywords: Landfill, lindane (HCH), groundwater flow, contaminant transport, numerical models.

INDEX

TABLES INDEX

FIGURES INDEX

1. INTRODUCTION

The accumulation of persistent organic pollutants from the former lindane factory of INQUINOSA in Sabiñánigo (Huesca) is of great concern for the water quality of the Ebro river basin and represents a serious risk to human health and ecosystems. Lindane is the commercial isomer of hexachlorocyclohexane (HCH) that was widely used as a pesticide until it was banned. The INQUINOSA factory operated from 1975 until 1992. Residues from lindane production, in powder and liquid form, were disposed first at the Sardas landfill and later in the Bailín landfill site in an almost uncontrolled manner. The pollution caused by INQUINOSA's activities in Sardas and Bailín constitute one of the greatest environmental challenges in the Ebro river basin. At the beginning of the 1990s, the diversion of the N-330 was built and its path cut across the Sardas landfill. Due to this work, approximately 50 000 m^3 of waste from the landfill was moved to the lower part of the site (Figure 1.1).
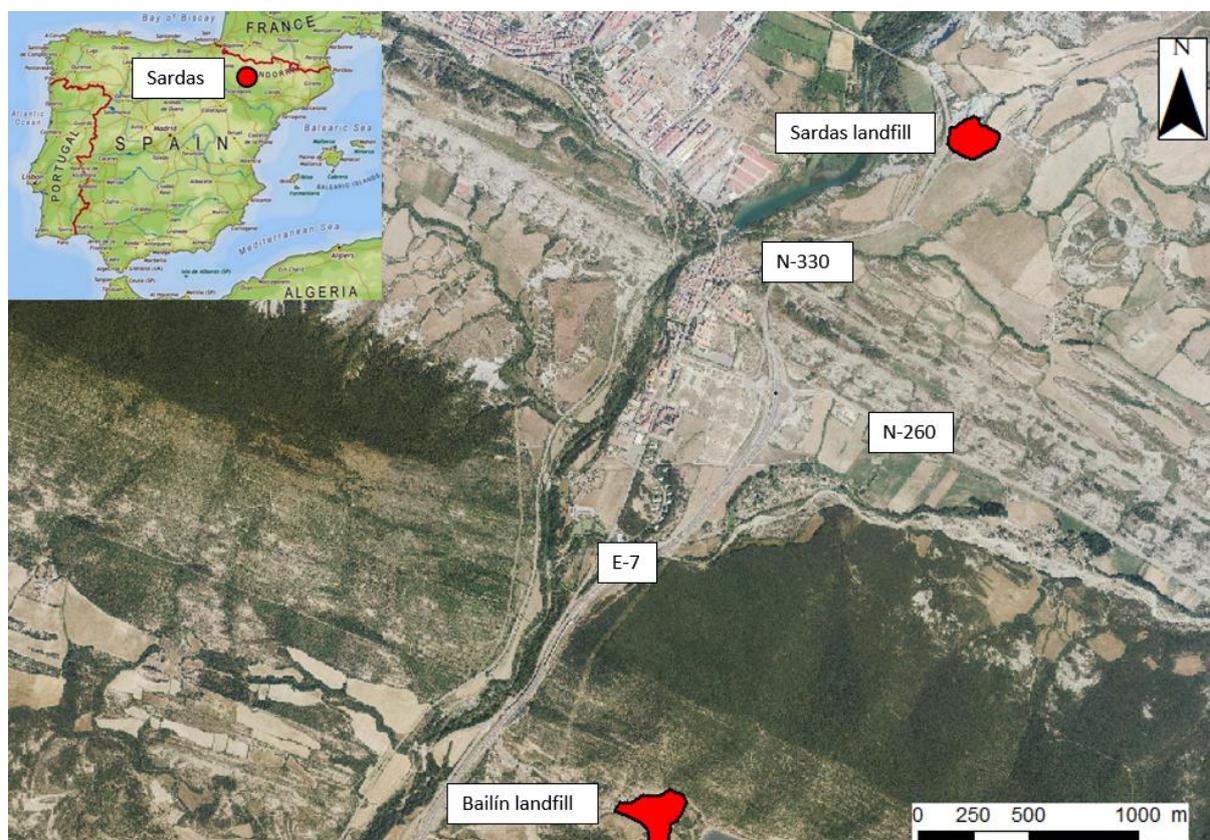
Figure 1.1. Location of the Sardas and Bailín landfills.

The landfill was sealed at the surface and laterally in 1992 and 1993 with a multilayer cover which included a clay layer and a HDPE sheet. The multilayer cover was designed to prevent the inflow of precipitation into the landfill. Perimeter waterproofing of the landfill was also carried out. Bentonite/cement slurry walls of 2 to 3 m depth and 0.5 m thick were constructed along the perimeter of the landfill. A deeper front slurry – wall was constructed facing the N - 330 road.

The Spanish National Company for the Management of Industrial Waste S.A. (EMGRISA) was appointed by Environmental Department of the Aragon Regional Government (DGA) to perform the hydrogeological monitoring of the Sardas site at Sabiñánigo (Huesca). EMGRISA is in charge of groundwater monitoring, water sampling, pumping of leachates in areas of HCH emergence, the control of the spills from the dump, as well as the periodic extraction of accumulated organochlorine free phase in piezometers equipped with pumping devices (EMGRISA, 2018).

The conceptual model of the site was defined from the field work carried out by EMGRISA since 2009. This conceptual model was tested with a groundwater flow model performed with MODFLOW (EMGRISA 2014).

1.1 Description of the study area

The Sardas landfill is located on the left bank of the Gállego river less than 1 km east of the Sabiñánigo downtown (Figure 1.2). The site occupies an area of almost 4 ha and includes the landfill and the area between the foot of the landfill and the Gállego river.

Part of the landfill materials were removed and spread on the alluvial of the Gállego river in the 1990s during the construction of the N-330 national road. The N-330 road divides the site into two parts. The Sardas site includes the following elements: 1) The Sardas landfill, 2) The area at the foot of the landfill, 3) The two leachate ponds and 4) The active carbon treatment plant. Sardas landfill is located on the Larrés marls, which is a fractured formation with low to very low hydraulic conductivity. It presents more permeable zones associated with densely-fractured areas. Downstream from the landfill, the marls are covered by the landfill deposits removed during the construction of the N-330 road, and the alluvial formation of the Gállego river, which is formed

by an upper layer of sandy silts of low permeability and a lower layer of highly-permeable gravels and sands with an average thickness of 5 m.
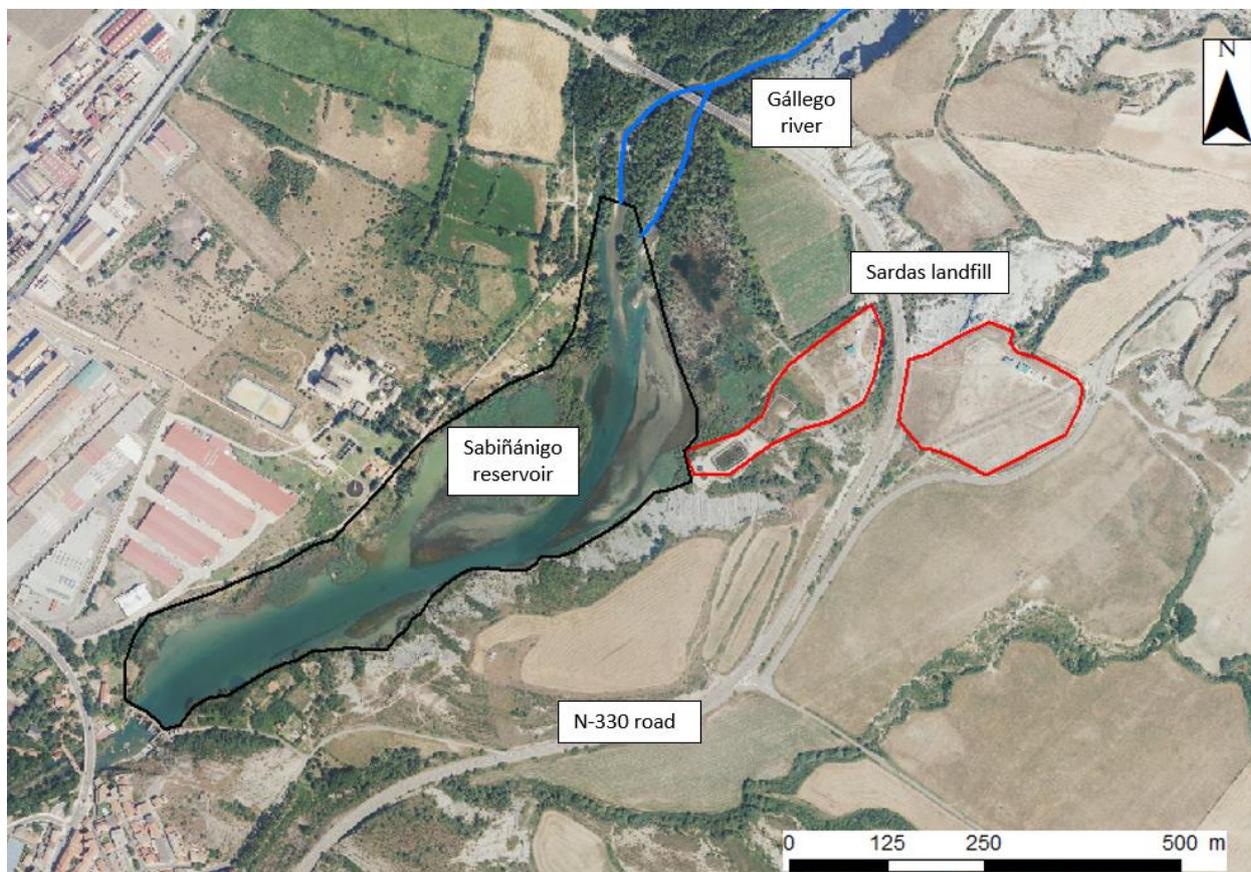
Figure 1.2.   Location of the Sardas landfill by the Sabiñánigo reservoir. The location of the Gállego river and the N-330 road are also indicated.

The river system of the study area is of the dendritic type (CHE 2010). The Gállego River is the largest river in the area, together with its main tributary, the Aurín River. The Gállego river flows into the Sabiñánigo reservoir with two different branches. The Aurín river flows into the Gállego river 1 km upstream the reservoir. Several hydropower units were built at the beginning of the 20th century along Gállego river, which favoured the installation of numerous industrial factories in the Sabiñánigo area such as that of INQUINOSA. The Sabiñánigo reservoir was built in 1965 and occupies the old riverbed, a large part of the alluvial plain and the lower Gállego terraces. On the left bank there are cliffs about 35 m high formed in the grey marls of the area. The right bank is formed by a terrace of low height and wide extension (CHE 2010).

The Sabiñánigo reservoir was built to supply nearby towns and villages and to generate hydroelectric power. Due to the high regulation of the Gállego river with the upstream reservoirs of Búbal with a surface of 234 ha and a total volume of 66 hm^3 and Lanuza with a surface of 114 ha and a total volume of 65 hm^3, the oscillations of the Sabiñánigo reservoir depend mainly on its hydroelectric use. These oscillations affect the groundwater flow in the area. The measured piezometric heads in the boreholes drilled on the left bank (downstream of the Sardas landfill) show oscillations, which are damped and delayed with respect to those of the Sabiñánigo reservoir.

The Sabiñánigo reservoir, with a height of 763.9 m, occupied, at the time of its construction, an area of 21.97 ha and had a storage capacity of about 0.873 hm^3 (CHE 2010). It has undergone an intense process of siltation, and it is estimated that between 1965 and 2009 some 780 000 m^3 of sediments have been deposited at the bottom of the reservoir. Its storage capacity has decreased 86.1%, occupying an area of 11.71 ha and having a storage capacity of 0.093 hm^3 at the same height. The depth of the reservoir has fallen from an average of 4 m to 0.8 m at an altitude of 763.9 m. The maximum depth has decreased from 9.4 m to 4.3 m (CHE 2010).

1.2 Previous conceptual and numerical models

A conceptual model of the groundwater flow was developed by EMGRISA for the Department of the Environment of the Regional Government of Aragon (DGA) focused on the alluvial area downstream of the Sardas landfill (EMGRISA, 2014). The model is based on the geological and hydrogeological data obtained from the field work during the drilling campaigns and the monitoring of the Sardas site.

The model occupies an area of approximately 1.40 ha. The model domain is bordered to (Figure 1.3):

1) The north by a stream

2) The east by the N-330 road, the Sardas landfill itself and a small gully

3) The south by the leachate ponds and a marl slope

4) The west by the Sabiñánigo reservoir

The topography is smooth with a slight slope towards the west.
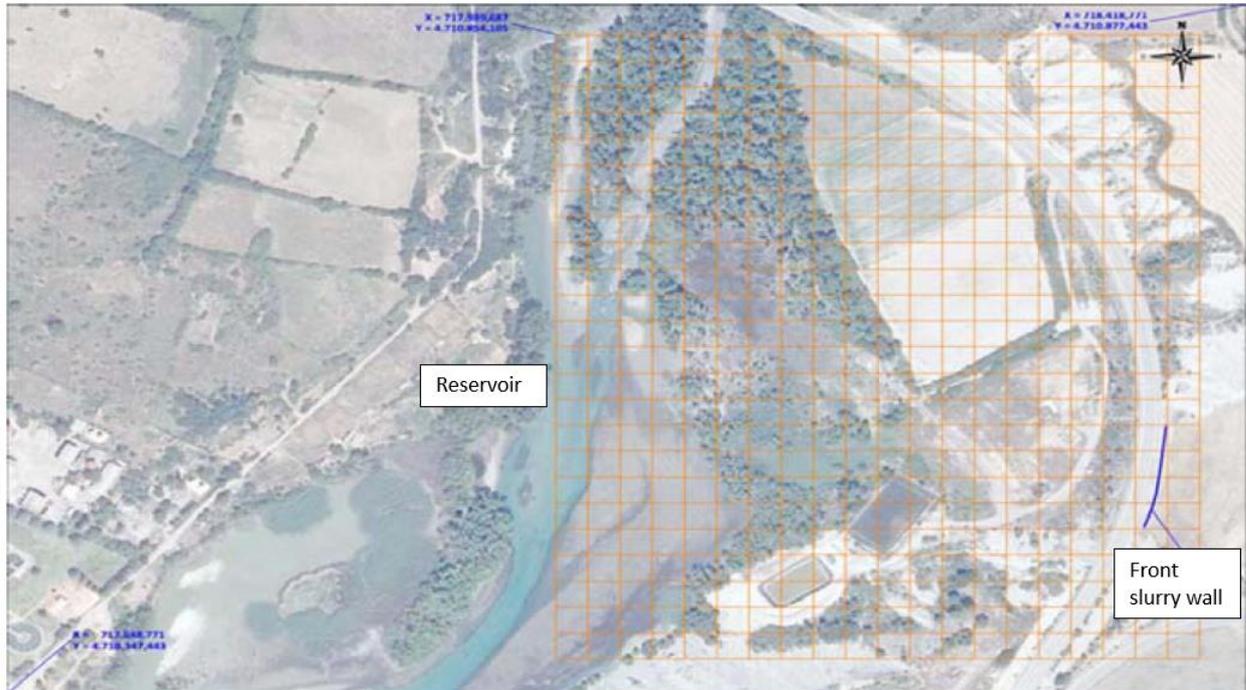
Figure 1.3. Aerial photograph with the EMGRISA model domain (EMGRISA, 2014).

The study area presents a stratigraphy consisting mainly of a substrate made up of deposits of grey marls (Larrés marls formation). These are deposits of grey marls with abundant micro fauna of several hundreds of metres thickness. The Quaternary deposits are mainly made up of clayey silts, as well as gravel and sand, forming an approximate thickness of around 15 m. On top of these materials, there are some waste filling materials from the Sardas landfill, about 4 m thick.

The waste filling materials, alluvial silts and gravels have different permeabilities, the latter being the most permeable. Groundwater in the gravels is confined by the alluvial silts and waste filling materials. The underlying tertiary substrate is composed of grey marls. These materials behave as a double porosity medium. The shallowest layer of marls is fractured, altered and decompressed and, therefore, presents a larger porosity and permeability. The deepest parts of the marls are less fractured and have very low permeability.

The conceptual model proposed by EMGRISA (EMGRISA, 2014) includes the following three layers:

- Filler layer 1.

- Silt layer 2.

- Gravel and sand layer 3.

The south and east borders of the model are considered impermeable. The northern edge of the model coincides with a flow line and is treated as a non-flow boundary. The western boundary coincides with the Sabiñánigo reservoir.

The use of this reservoir for hydropower causes daily oscillations in the reservoir water level from 0.8 to 1 m. The oscillations of the reservoir level have a direct influence on the hydraulic heads in the alluvial aquifer. The average hydraulic head of the reservoir is equal to 765.294 m.a.s.l.

Recharge from precipitation is assumed equal to 140 mm/year. The total leachate from the landfill is estimated equal to 20 m^3/day-

EMGRISA (2014) used MODFLOW (Harbaugh, A.W. *et al.*, 2005) for the groundwater flow model. The mesh consists of 29 columns and 31 rows, resulting in a length in the E-W direction of 400 m and the N-S of 480 m. The cells range in size from 20x20 m, 20x10 m and 10x10 m. The highest mesh density is found in the central area of the grid, where a higher data density is available. There is a gradual increase in the size of the cells towards the boundaries of the model.

Table 1.1 summarizes the hydraulic conductivities of the EMGRISA model (2014).

Table 1.1.   Hydraulic conductivities of the EMGRISA model (2014).

Geological formation	Horizontal hydraulic conductivity K_h (m/d)	Vertical hydraulic conductivity K_v (m/d)
Layer 1. Backfill	$1.00 \cdot 10^{+0}$	$1.00 \cdot 10^{-1}$
Cells under the reservoir	$1.00 \cdot 10^{-2}$	$1.00 \cdot 10^{-3}$
Layer 2. Silt	$1.00 \cdot 10^{-1}$	$1.00 \cdot 10^{-2}$
Cells under the reservoir	$1.00 \cdot 10^{-2}$	$1.00 \cdot 10^{-3}$
Gravel and sand	$1.00 \cdot 10^{+2}$	$1.00 \cdot 10^{+2}$

The main conclusions of the EMGRISA model include:

- The calibrated groundwater recharge is 112 mm/year except near the foot of the slope of the N-330 road where the recharge is 136 mm/year.

- There are strong vertical hydraulic gradients in the filling and the silt layers at the eastern edge. In this area the flow is vertically downwards towards the gravels.

- Most of the groundwater flow takes place in the gravel layer.

Table 1.2 shows the calibrated water inflows and outflows and the steady-state water balance of the numerical model.

Table 1.2.   Steady-state water balance in the EMGRISA model (EMGRISA, 2014).

	Inflows (m^3/d)	Outflows (m^3/d)
Inflow from the Sardas landfill	20	-
Recharge	45.6	-
Reservoir	-	65.8
Total	65.6	65.8

Once calibrated, the model was used to simulate the transient groundwater flow in a simulation period of 36 hours. The oscillations in the reservoir level produce a fluctuation in the water flows from the alluvial formation into the reservoir and vice versa from the reservoir into the alluvial. The average groundwater flow from the alluvial aquifer into the reservoir ranges from 142 to 147 m^3/d while the average water inflow from the reservoir into the alluvial aquifer ranges from 48.3 m^3/d to 50.8 m^3/d.

1.3 Scope

Chapter 2 presents a summary of the state of the art in lindane pollution and groundwater flow and solute transport modelling in lindane sites. Chapter 3 presents the main objectives of the thesis. Chapter 4 describes the steady state flow model along the A – A' profile and Chapter 5

describes the transient flow model along the profile. Chapter 6 describes the steady state 2D horizontal groundwater flow model in the gravels of the Gállego alluvial from the Sabiñánigo dam to the confluence of the Gállego and Aurín rivers. Chapter 7 shows the transient state 2D horizontal model. The flow and solute transport model of dissolved HCH is presented in Chapter 8. Chapter 9 presents numerical model of the pumping test model carried out in 2018 in the PS14B borehole. Chapter 10 shows the numerical model of the tracer test carried out in 2018 also in the PS14B borehole. The main conclusions of the Master thesis are presented in Chapter 11.

2. STATE OF THE ART

The technical hexachlorocyclohexane (HCH) was used in the 1950s as pesticide in Europe (Vijgen 2019). The application of the HCH mixture was soon discovered to be harmful to humans. In the late 1950s, companies started working on the isolation of the ɣ isomer, known as lindane, which in the right concentration would be tasteless and harmless (Vijgen 2019).

Synthesised raw HCH contains a total of eight stereoisomers which are termed α- to θ-HCH depending on the spatial arrangements of the chlorine atoms. Among these, only the α, β, γ, δ and ε isomers are stable. They are formed in reaction mixtures in the following percentages: 55–80% α isomer; 5–14% β isomer; 8–15% γ isomer; 2–16% δ isomer, and, 3–5% ε isomer (Vijgen 2011).

The use of lindane is banned in the EU since 2008 (Schonard 2016) because of its suspected carcinogenic, persistent, bioaccumulative and endocrine disrupting properties. In 2009, lindane (γ – HCH), α – HCH and β – HCH were included in the Stockholm Convention on Persistent Organic Pollutants in order to achieve the global elimination of these substances (Schonard 2016).The use of lindane has been banned in at least 52 countries. Furthermore, various bilateral and multilateral international agreements and treaties have addressed lindane prohibition such as the Rotterdam Convention and the Protocol on Persistent Organic Pollutants of the Convention on Long Range Transboundary Air Pollution (Vijgen 2011).

The estimated amount of HCH/Persistent Organic Pollutants (POPs) wastes ranges from 4.2 and 7.2 million tonnes. Most of the regulations have focused on lindane because of its previous use as a pesticide in agriculture (Vijgen 2011). However, the accumulation and storage of wastes from lindane production has resulted in the pollution of natural water bodies such as lakes, rivers or aquifers in several countries. Lindane and other HCH-isomers are persistent in the environment, they bioaccumulate in living organisms and are toxic to human health and the environment. Furthermore, there is evidence of their long-range transport (Schonard 2016). High concentrations of lindane in air were found in several countries. These elevated air concentrations were probably explained by atmospheric transport from the former high-density emission European countries (Schonard 2016).

Compared to other organochlorine pesticides, lindane and other HCH isomers are generally more water-soluble and volatile (Schonard 2016). Lindane also shows a strong tendency to be adsorbed into organic matter with a water/organic carbon partitioning coefficient (K_{oc}) ranging from 871 to 1671 L/kg. Therefore, the mobility of HCH is expected to be very low in formations with a high content of organic matter (Schonard 2016).

The production of lindane in the EU has resulted in the extensive contamination of soils, surface water and groundwater with toxic HCH isomers, chlorobenzenes, and dioxins (Schonard 2016). Hot-spots, with thousands, and often hundred thousands of tonnes of lindane and HCH waste, are pending remediation activities in at least the following countries (Schonard 2016): The Czech Republic, France, Germany, Hungary, Italy, Poland, Romania, Slovakia and Spain.

Lindane was produced in Spain in 4 factories. Two of them are located in the Basque Country (Asua-Erandio and Ansio-Barakaldo sites in Bizkaia). A third one is located in O Porriño (Galicia) and the fourth one is the Inquinosa factory in Sabiñánigo (Huesca). The old Inquinosa factory is only a few tens of meters from the Gállego River and still remains in a state of ruin and without being dismantled (EMGRISA 2018).

Chemical production plants are often located near rivers and, consequently, river floods have contributed to the mobilization of pollutants (Schonard 2016). Inquinosa produced lindane from 1975 to 1988 and ceased its activity in 1992. It has been estimated that Inquinosa produced more than 150 000 tonnes of waste with high content of lindane, HCH and other organochlorine compounds (EMGRISA 2018). The HCH waste was initially sent to another lindane production plant in France where it was recycled by thermal cracking (Fernández *et al.*, 2013). Later, in the absence of a market for the products of the cracking process (trichlorobenzene/ tetrachlorobenzene), the HCH wastes were packed in drums and dumped at different locations in the vicinity of the INQUINOSA plant (Fernández *et al.*, 2013).

It is estimated that the Sardas landfill currently contains 60 000 m^3 of HCH solid waste, about 30 m^3 of dense non-aqueous phase liquid (DNAPL) and 350 000 m^3 of hazardous municipal and industrial wastes (Fernández *et al.*, 2013). HCH wastes were transported from 1984 to 1989 to the Bailín landfill. A surface waterproofing of the Bailín landfill was carried out in 1992 (Schonard 2016). The wastes of the Bailín landfill were transported to a safety cell in 2014 at the same site to prevent the leaching of contaminants and the pollution of the Gállego River. The new safety cell included a lower and upper coating and leachate treatment.

DNAPL was detected in 2009 at the foot of the Sardas landfill. This unexpected leakage triggered field works and hydrogeological studies of the Sardas site (Fernández *et al.*, 2013). Several investigation techniques were applied: geological drilling and characterization of the drilling cores, geophysical, seismic and electrical tomography, piezometric head monitoring, hydraulic characterization by heat–pulse flowmeter measurements as well as pumping tests, and hydrochemical analyses (Fernández *et al.*, 2013). The monitoring network of the landfill includes 51 piezometers. Seven of them are connected to a pumping station for DNAPL extraction. The pumped dense phase is sent to an incinerator after decanting. The aqueous phase is stored in two ponds for in situ treatment in a wastewater treatment plant (Fernández *et al.*, 2013).

CHE (2010) presented a characterization of the Sabiñánigo reservoir located right next to the INQUINOSA factory and Sardas landfill. The thickness of the silting sediments at the bottom of the reservoir in 2009 ranged from 0.5 m to 8.1 m. The estimated volume of these silting sediments is about 780,000 m^3, and they have reduced the capacity of the reservoir by 86% to 89% (CHE 2010).

According to CHE (2010), the landfill leachate circulates through the quaternary terraces located at the foot of the landfill until it reaches the gravels located underneath the reservoir. The conceptual model of the site suggests that groundwater flows mainly through the Quaternary gravels as well as in the altered shallowest marl horizon (Fernández *et al.*, 2013). A general leachate accumulation is present in the anthropogenic fillings and alluvial silt sediments in the downstream area of the landfill. Mobilisation of the leachate towards the reservoir must have started almost as soon as the landfill came into operation in the 1960s because no actions were taken to prevent water pollution. The Sardas landfill was sealed in 1997. A seepage of HCH and DNAPL was detected in 2009 at the foot of the foot of the landfill downstream the front slurry – wall (CHE 2010). Leakage is suspected to flow below the front slurry – wall of the landfill into the alluvial of the Gállego river. DNAPL has been detected at several depths within the landfill, at the bottom of the gravels and in the marls (Fernández *et al.*, 2013).

3. OBJETIVES

The main objective of this Master Thesis is the numerical modelling of groundwater flow and contaminant transport from the Sardas landfill into the Sabiñánigo reservoir (Huesca, Spain) through the alluvial plan of the Gállego alluvial aquifer. The site is polluted with lindane disposed at the landfill by the Inquinosa factory. The subsurface discharge of the landfill percolates into the Gállego alluvial aquifer where groundwater flow is strongly affected by the daily fluctuations of the Sabiñánigo reservoir.

This objective was achieved by performing the following numerical models:

1) 2D steady and transient groundwater flow models along a vertical profile in E-W direction, which runs along the thalveg of the original gully. These models are performed to test the conceptual hydrogeological model of the Sardas site and evaluate the pros and cons of several remediation measures.

2) 2D steady and transient horizontal groundwater flow models through the gravels of the alluvial aquifer to: 1) Quantify the tidal effect of the daily fluctuations of the Sabiñánigo reservoir level on the aquifer hydraulic heads; 2) Estimate the hydraulic conductivity of the sediments at the bottom of the reservoir; and 3) Estimate the hydraulic conductivity of the gravels.

3) 2D steady and transient horizontal groundwater flow and solute transport models through the gravels of the alluvial aquifer to: 1) Estimate solute transport parameters from a tracer test; 2) Simulate HCH migration through the gravels and the clogging sediments; and 4) Quantify the HCH mass flux into the reservoir

The numerical models have been performed with CORE^{2D}, a finite element code for solving the flow, heat transfer and solute transport equations in porous and fractured media with irregular boundaries and non-uniform physical and geochemical properties (Samper *et al.*, 2003; 2009; 2011). CORE^{2D} solves the flow in both confined and free aquifers, as well as in partially saturated porous media. The code considers the following flow boundary conditions: fixed head, fixed water flow and mixed type condition. The groundwater flow equation is solved in terms of

piezometric heads for flow in confined and unconfined aquifers. The equations of groundwater flow, solutes and heat transport are solved with the Galerkin's finite element method. CORE^{2D} has been widely verified using analytical solutions of flow, heat and conservative solute transport equations and by comparing obtained results with those of other codes (Samper *et al.*, 2003; 2009; 2011).

4. TWO-DIMENSIONAL STEADY-STATE GROUNDWATER FLOW MODEL ALONG A VERTICAL PROFILE IN THE EAST-WEST DIRECTION

4.1 Introduction

This chapter presents the 2D steady-state groundwater flow model along a vertical cross-section in the East-West direction of the Sardas landfill and the Gállego alluvial aquifer. The model domain extends from the headwaters of the landfill until the Sabiñánigo reservoir. The chapter starts with a description of the available data. Then, the hydrogeological conceptual model is presented. Afterwards, the numerical model is described. Model calibration and results are presented next. The chapter ends with the main conclusions.

4.2 Available data

Most of the data for the numerical model was provided by EMGRISA. The meteorological data were used to estimate groundwater recharge with a hydrological water balance model (Samper *et al* 2018 a). The material zones of the model are taken from the borehole columns, where the lithology and the depth of the borehole, as well as the location of the grid, etc. are presented.

Hydraulic heads in boreholes were measured manually and with divers. The measured hydraulic heads in 19 boreholes have been used for model calibration. Table 4.1 lists the boreholes, the screen intervals, the elevation of the ground surface, the midpoint of the screened section, the bottom of the borehole, the geological formation in front of the screened section and the average measured head. Data from boreholes located near the profile have been used to fill data gaps. Average hydraulic heads were calculated from the available piezometric data measured automatically with a diver or manually with a probe.

Table 4.1. Boreholes used for model calibration, indicating the elevation of the ground surface, the midpoint of the screened section and the bottom of the borehole, the geological formation in which the screened section is located and the average measured head.

Borehole	Ground elevation (m)	Midpoint of the screened section (m)	Elevation of the bottom of the borehole (m)	Geological formation	Average measured hydraulic head (m)
PS26	767.34	760.47	757.74	Alluvial	765.05
PS26B	767.42	732.62	724.02	Marls	765.01
PS21	773.01	749.01	742.21	Marls	765.08
PS21B	771.80	761.40	758.60	Alluvial	765.03
PS14	774.81	762.81	756.81	Alluvial	765.12
PS19B	774.63	760.18	758.73	Alluvial	765.06
PS19C	775.24	766.24	764.24	Silts	767.69
PS5	775.41	761.31	757.41	Silts	766.93
PS7	776.28	764.88	756.18	Silts	767.87
PS29	776.65	759.65	757.65	Deep marls	774.20
PS29B	777.20	767.30	765.40	Shallow marls	774.19
PS29C	776.82	773.92	771.82	Wastes	774.16
PS22	788.19	774.19	765.49	Wastes	779.62
S37	789.50	779.50	764.50	Wastes	788.42
S39B	815.36	784.71	774.36	Wastes	788.91
S39G	815.58	785.33	776.08	Wastes	791.70
S39	815.64	788.89	782.44	Wastes	792.62
S39F	815.91	784.31	775.61	Wastes	791.80
S35E	811.15	795.90	793.65	Deep marls	802.15

The reservoir water level data were provided every 30 minutes. The calibration of the model was based on the estimates of hydraulic conductivity, K, of EMGRISA model (see Chapter 1). The flow rate of the discharge in the vicinity of the PS29C borehole (Ditch 1) was measured monthly (Figure 4.1).
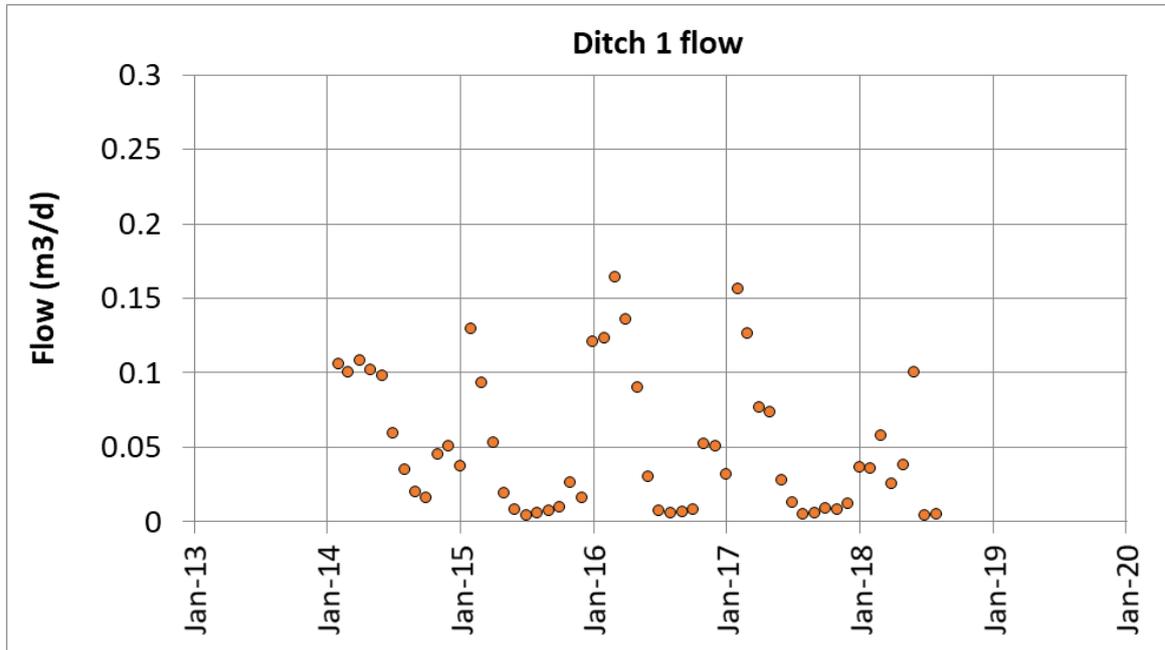
Figure 4.1. Monthly flow rate data in Ditch 1 used to calibrate the discharge in the Dirichlet boundary near borehole PS29C.

4.3 Hydrogeological conceptual model

4.3.1 Geology

The geological formations considered in the numerical groundwater flow model include (from West to East):

1) The alluvial of the Gállego river: It includes a shallow layer of silts and a deep layer of gravels. The thickness of the alluvial sediments decreases towards the East.

2) The Larrés marls which underlie the alluvial aquifer. The shallow layer of the marls, known as FAD, is more fractured, altered and decompressed.

3) The landfill fillings downstream the front slurry-wall

4) The landfill fillings upstream the front slurry-wall. The landfill fillings overlie the FAD marls and locally the silt layers resulting from the erosion of the marls

5) The geological formations upstream the landfill including a narrow layer of glacis.

4.3.2 <u>Vertical profile model</u>

Although groundwater flow in the Sardas site is three-dimensional, as a first approximation it was assumed that the flow is two-dimensional along a vertical profile. The geological and hydrogeological profile has an E-W direction and its layout coincides with the location of the following boreholes: PS26B, PS21, PS14, PS19B, PS5, PS29, S37, S39B, S39F and S35E. This profile has been used in previous studies to define the conceptual geological, hydrogeological and contaminant model of the site (Figure 4.1).

The available data for model calibration has been enlarged by projecting the data from boreholes located near the profile. The projected boreholes include: PS26, PS21B, PS19C, PS7, PS29B, PS29C, PS23, S39G, S39 and S35F1. Figure 4.2 shows the boreholes used for model calibration.
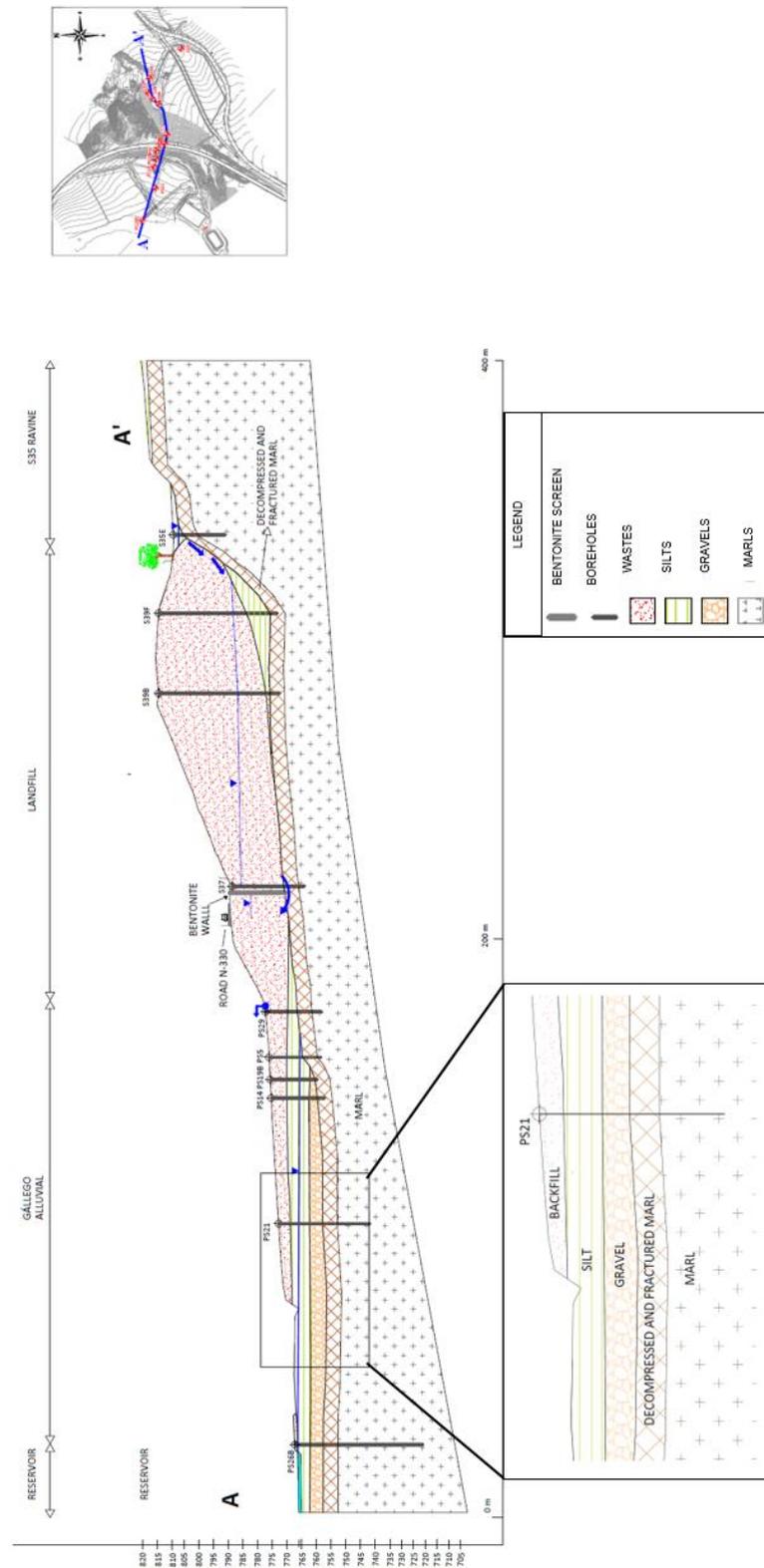
Figure 4.1. Scheme of the vertical cross-section of the Sardas site landfill which has been used in previous studies by EMGRISA and the Government of Aragon to define the conceptual model of the site (EMGRISA 2014).

Figure 4.2. Map of the site with the outline of the E-W hydrogeological profile and the location of the boreholes along the profile.

4.3.3   Conceptual model of flow in the vertical profile

The conceptual flow model used to model groundwater flow in the E-W profile is based on the following assumptions:

1) The flow is plain and contained in the vertical plane of the profile. The trace of the profile is shown in Figure 4.2.

2) The flow model has a thickness of 1 m. The equivalent inflows and outflows for the landfill have been calculated by assuming an equivalent thickness of 50 m.

3) The equivalent porous medium assumption is adopted for the fractured marls.

4.4 Numerical model

4.4.1   Spatial discretization

The vertical profile has a total length of 590 m and a thickness normal to the plane equal to 1 m. The upper limit of the model domain coincides with the average estimated water table. The lower limit of the model domain is located at an elevation of approximately 710 m. The maximum elevation of the model domain is 816.43 m.

The model domain is discretized with a 2D triangular finite element mesh (Figure 4.3). The mesh is composed of 2732 nodes and 5168 elements. It is refined in the Gállego alluvial and downstream and upstream the front slurry-wall. The size of the elements increases with depth in the marls.

The model domain has been divided into 3 zones to facilitate the visualization of the grid, the discretization, the material zones and the model results. These zones are shown from Figure 4.3 to Figure 4.6.
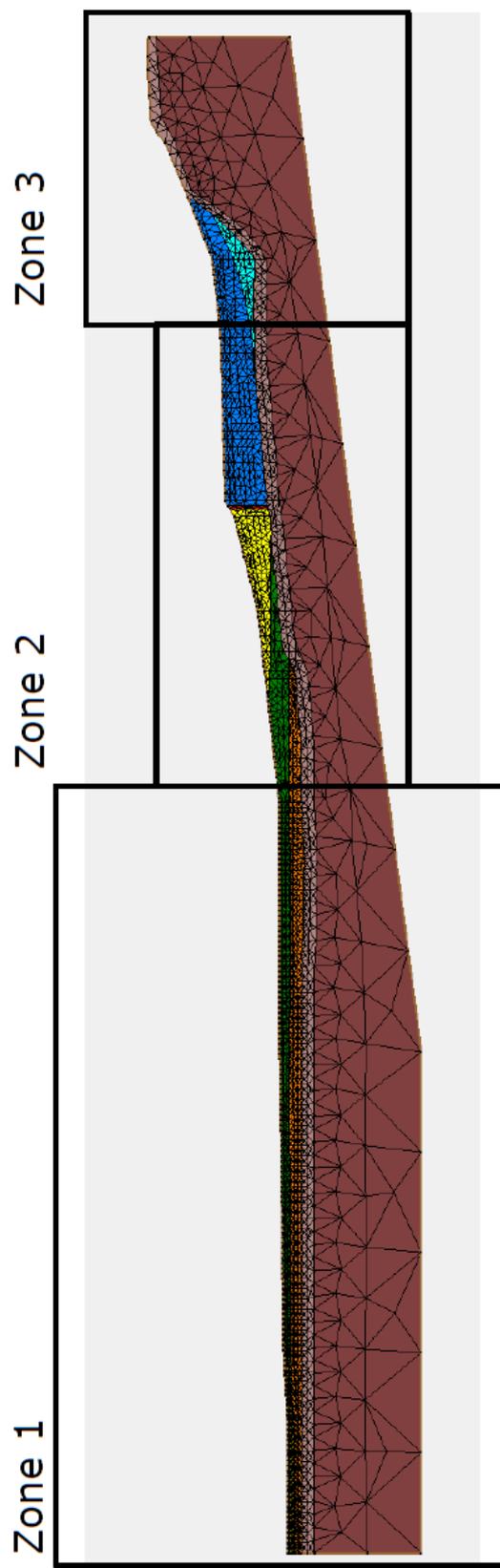
Figure 4.3.   East – West profile finite element mesh and division into three zones to show detail enlargements.

4.4.2 Model structure

The model domain has been divided into several material zones based on the hydrogeological conceptual model of EMGRISA (2014), the geology and the piezometric data. The material zones include (Table 4.2):

1) The alluvial silts which occupy the alluvial area and are limited in the east by the reservoir and in the west by the embankment of the N-330 road, although they are pushed (in the form of a wedge) under the waste filling almost to the front slurry-wall. They have an average vertical thickness of 4 m.

2) The gravels. They underlie the alluvial silts and are limited to the east by the reservoir and to the west by the embankment of the N-330 road. Their thickness is approximately constant and equal to 4 m.

3) The filling wastes downstream the front slurry-wall. They are located between the alluvial and the front slurry-wall. Their thickness ranges from 1 to 15.50 m.

4) The front slurry-wall. It is 18 m deep and has an extremely low hydraulic conductivity.

5) The wastes upstream the front slurry-wall. Their thickness ranges from 8 m to 18 m near the front slurry-wall. Their characteristics are different from those of the wastes downstream the front slurry-wall.

6) The marls erosion silts: They are silts originated from the erosion of the marls which have a variable thickness ranging from 0.20 m to 6 m.

7) The shallow marls of the Larrés formation are fractured, decompressed and altered (FAD marls) and therefore have a moderate hydraulic conductivity. There are no data for the vertical thickness of the FAD marls. A thickness of 5 m was adopted in the model.

8) The deep Larrés marls which are less fractured and have extremely low hydraulic conductivity. Their vertical thickness in the model ranges from 40 m under the alluvial plain to 25 m in the landfill.

Table 4.2.   Material zones used in the model.

Geological formation	Identification colour
Alluvial silts	
Gravels	
Waste downstream the front slurry-wall	
Waste upstream the front slurry-wall	
Silts from marl erosion	
Shallow marls	
Deep marls	
Front slurry-wall	
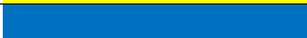
A material zone is a set of elements that share the same hydrodynamic properties: the hydraulic conductivity, K, and the specific storage, S_S. Fifteen material zones are defined in the numerical model. Their geometry is shown in Figure 4.4 to Figure 4.6. The material zones and their K and S_S values are listed in Table 4.3. Some of the geological formations such as the alluvial silts and the shallow marls are divided into several material zones to account for the spatial heterogeneity of the hydrodynamic properties.

The hydraulic conductivities have been derived from model calibration by using the measured piezometric data in boreholes. The reported values of K of the numerical model of EMGRISA (2014) have been used as initial estimates. Slight changes were made during model calibration. On the other hand, the initial estimates of K for the rest of the material zones (the shallow FAD marls, the deep unfractured marls, the wastes upstream the front slurry-wall and the marl erosion silts) were estimated from the literature.

Anisotropy has been considered only in the alluvial silts (zone B). Anisotropy was also considered also in the EMGRISA model (EMGRISA 2014). Available head data show vertical gradients in boreholes PS19B, PS19C, PS5 and PS7. This anisotropy can be explained by assuming a vertical hydraulic conductivity lower than the horizontal conductivity.

Table 4.3.   Calibrated values of the hydraulic conductivity and specific storage in material zones of the 2D model along the vertical profile.

Material zone	Geological formation	Colour	Horizontal hydraulic conductivity K_h (m/d)	Vertical hydraulic conductivity K_v (m/d)	Specific storage, S_S (m⁻¹)
1	Silting sediments		1	1	$2 \cdot 10^{-4}$
2	Alluvial silts A		$1 \cdot 10^{-2}$	$1 \cdot 10^{-2}$	$2 \cdot 10^{-4}$
3	Alluvial silts B		$1 \cdot 10^{-1}$	$1 \cdot 10^{-2}$	$2 \cdot 10^{-4}$
4	Alluvial silts C		$1 \cdot 10^{-2}$	$1 \cdot 10^{-2}$	$2 \cdot 10^{-4}$
5	Gravels		$4 \cdot 10^{+2}$	$4 \cdot 10^{+2}$	$2 \cdot 10^{-4}$
6	Wastes downstream		$4 \cdot 10^{-1}$	$4 \cdot 10^{-1}$	$6 \cdot 10^{-3}$
7	Wastes upstream A		2	2	$1 \cdot 10^{-2}$
8	Wastes upstream B		$1 \cdot 10^{-1}$	$1 \cdot 10^{-1}$	$5 \cdot 10^{-3}$
9	Marl erosion silts		$1.5 \cdot 10^{-1}$	$1.5 \cdot 10^{-1}$	$2 \cdot 10^{-3}$
10	Shallow marls A		$4 \cdot 10^{-2}$	$4 \cdot 10^{-2}$	$1 \cdot 10^{-4}$
11	Shallow marls B		$3.5 \cdot 10^{-2}$	$3.5 \cdot 10^{-2}$	$4 \cdot 10^{-3}$
12	Shallow marls C		$4.5 \cdot 10^{-2}$	$4.5 \cdot 10^{-2}$	$4 \cdot 10^{-2}$
13	Glacis		$1.5 \cdot 10^{-1}$	$1.5 \cdot 10^{-1}$	$1 \cdot 10^{-4}$
14	Deep marls		$1 \cdot 10^{-6}$	$1 \cdot 10^{-6}$	$1 \cdot 10^{-5}$
15	Front slurry-wall		$1 \cdot 10^{-6}$	$1 \cdot 10^{-6}$	$1 \cdot 10^{-5}$
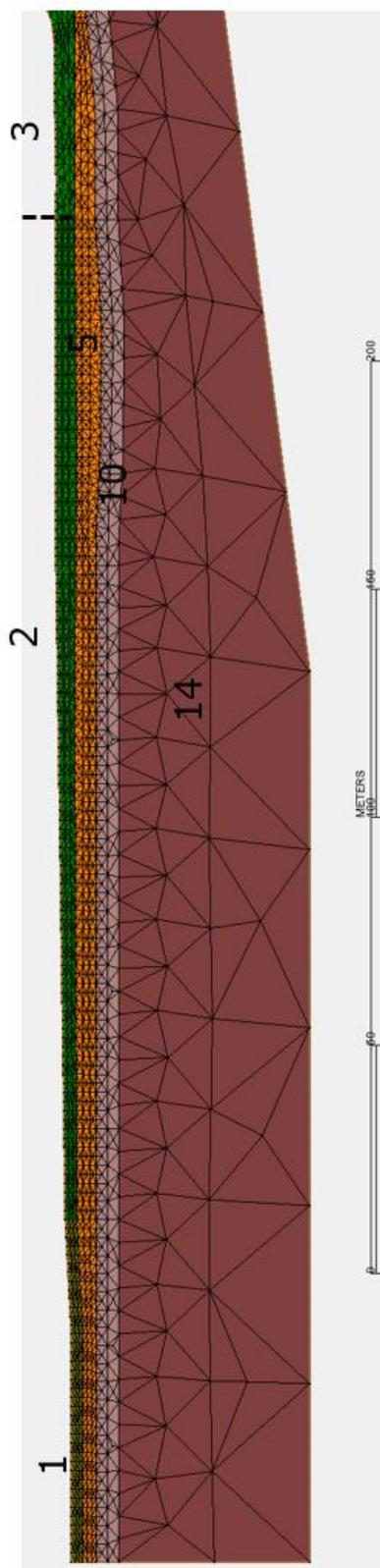
Figure 4.4. Zoom of zone 1 of the finite element mesh of the E-W profile numerical model from x = 0 to x = 325 m (see the location in Figure 4.3). Material zones are shown in different colours and labelled as indicated in Table 4.3.
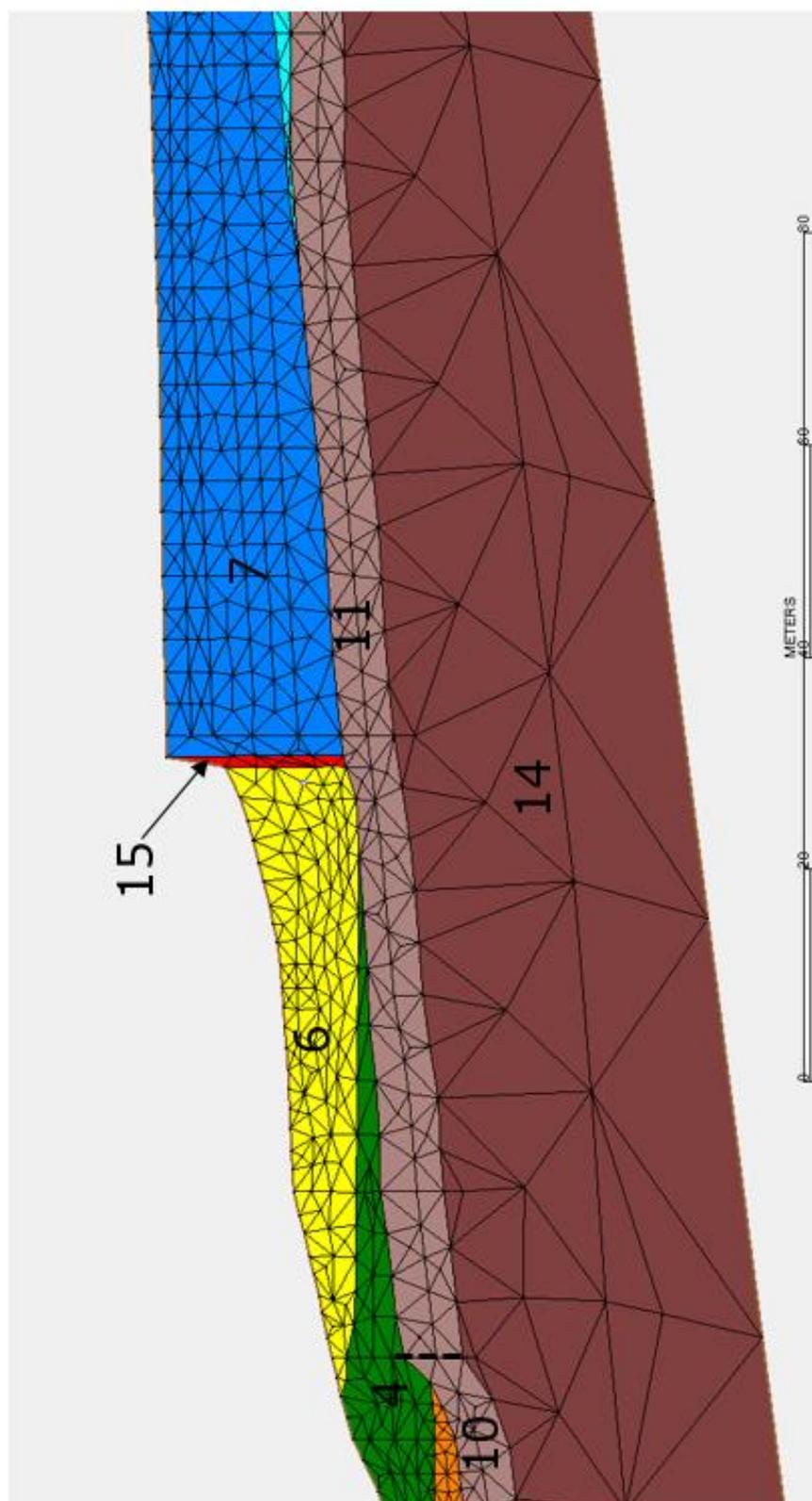
Figure 4.5. Zoom of zone 2 of the finite element mesh of the E-W profile numerical model from x = 325 to x = 470 m (see the location in Figure 4.3). Material zones are shown in different colours and labelled as indicated in Table 4.3.
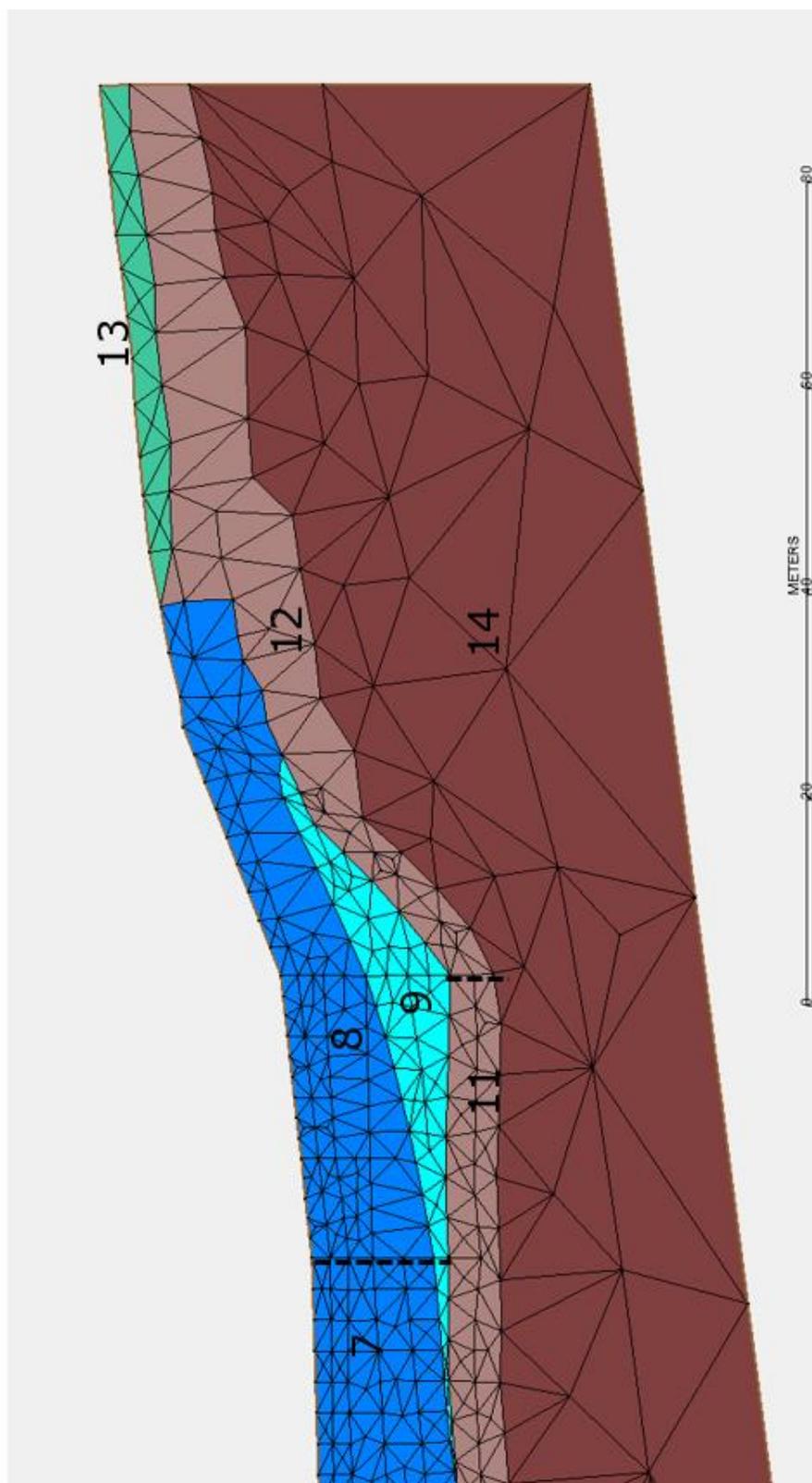
Figure 4.6. Zoom of zone 3 of the finite element mesh of the E-W profile numerical model from x = 470 to x = 590 m (see the location in Figure 4.3). Material zones are shown in different colours and labelled as indicated in Table 4.3.

4.4.3 Recharge and boundary conditions

Groundwater recharge was estimated by Samper *et al*. (2018 a) with a hydrological water model. Four recharge zones were considered (see Figure 4.7 and Table 4.4).
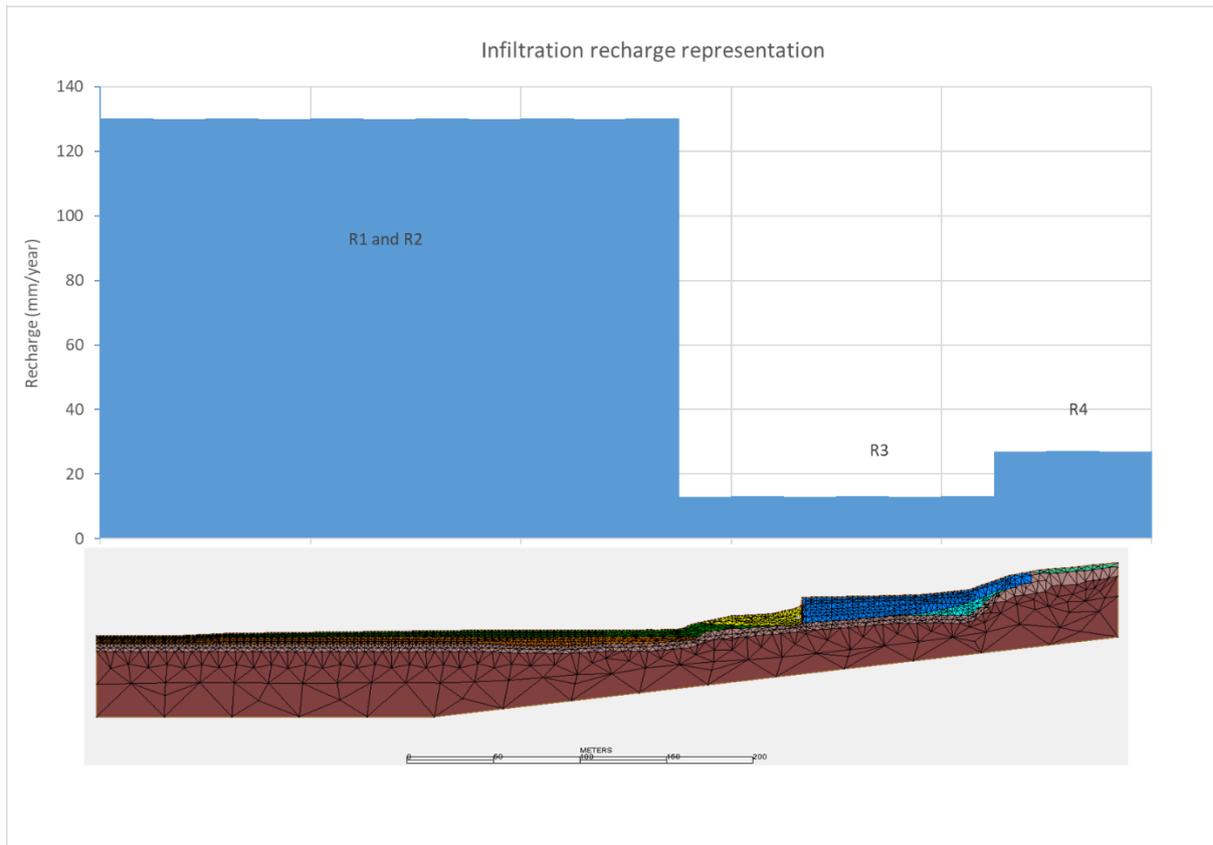
Figure 4.7. Groundwater recharge from rainfall along the E-W profile (mm/year).

Table 4.4. Groundwater recharge from rainfall along the E-W profile (mm/year).

Recharge zone	Distance interval from the origin (m)	Geological formation	Recharge (mm/year)
R1	0 – 331.93.	Gállego river alluvial	130
R2	331.93 – 407	Waste downstream	130
R3	407 – 523.73	Waste upstream	13
R4	523.73 – 590.18	Glacis	27

Figure 4.8 shows the finite element mesh and the model boundary conditions. The upper boundary of the model domain is a recharge boundary except for a node located in the vicinity of borehole PS29, where a seepage area is considered. The different recharge zones are simulated with a Neuman condition using a given flow rate from the average recharge in mm/year (as this is a steady model). The discharge in the PS29C borehole is simulated with a Dirichlet boundary condition. The head at this node is fixed equal to the measured head unaffected by pumping (774.45 m).

In addition, two other groundwater flow inputs with fixed flow have been estimated using the hydrometeorological model performed by Samper *et al.* (2018 a). The inflow from the runoff of the ravine upstream the landfill (near the borehole S35E) is simulated with a prescribed flow boundary condition. The flowrate has been estimated equal to 8.84 m^3/d. This inflow takes place over a width of approximately 50 m. Since the thickness of the model is 1 m, the unit inflow to the model is calculated by dividing the total inflow by the 50 m width. To avoid hydraulic head peaks in the vicinity of a single inlet node, this inflow has distributed in several nodes over a distance of 25 m. The position of the nodes is shown in Figure 4.9.

The inflow from the perimeter ditches of the landfill, due to the infiltration of surface runoff and interflow into the landfill and ditches, is also simulated with a prescribed flow condition. It is divided into two inflows: one inflow located immediately upstream the front slurry-wall, which has been calibrated from piezometric data at the S38C borehole, and the other inflow takes place near the S39 boreholes. Both inflows are implemented in a set of nodes, from the front slurry-wall to approximately the edge of the landfill, as shown in Figure 4.10. The inflow rate upstream the front slurry-wall equal to 7.47 m^3/day and the inflow near the S39 boreholes is equal to 4.37 m^3/day. The total flow is divided by the landfill width (which was estimated to be 50 m) to obtain the inflow rate per unit thickness. This inflow is distributed along several nodes.

The reservoir has been simulated with a Dirichlet type boundary condition. The head at the node located on the top of the silts and the silting sediments along the flood plain of the Gállego river is set equal to 765 m, the average water level in the Sabiñánigo reservoir.
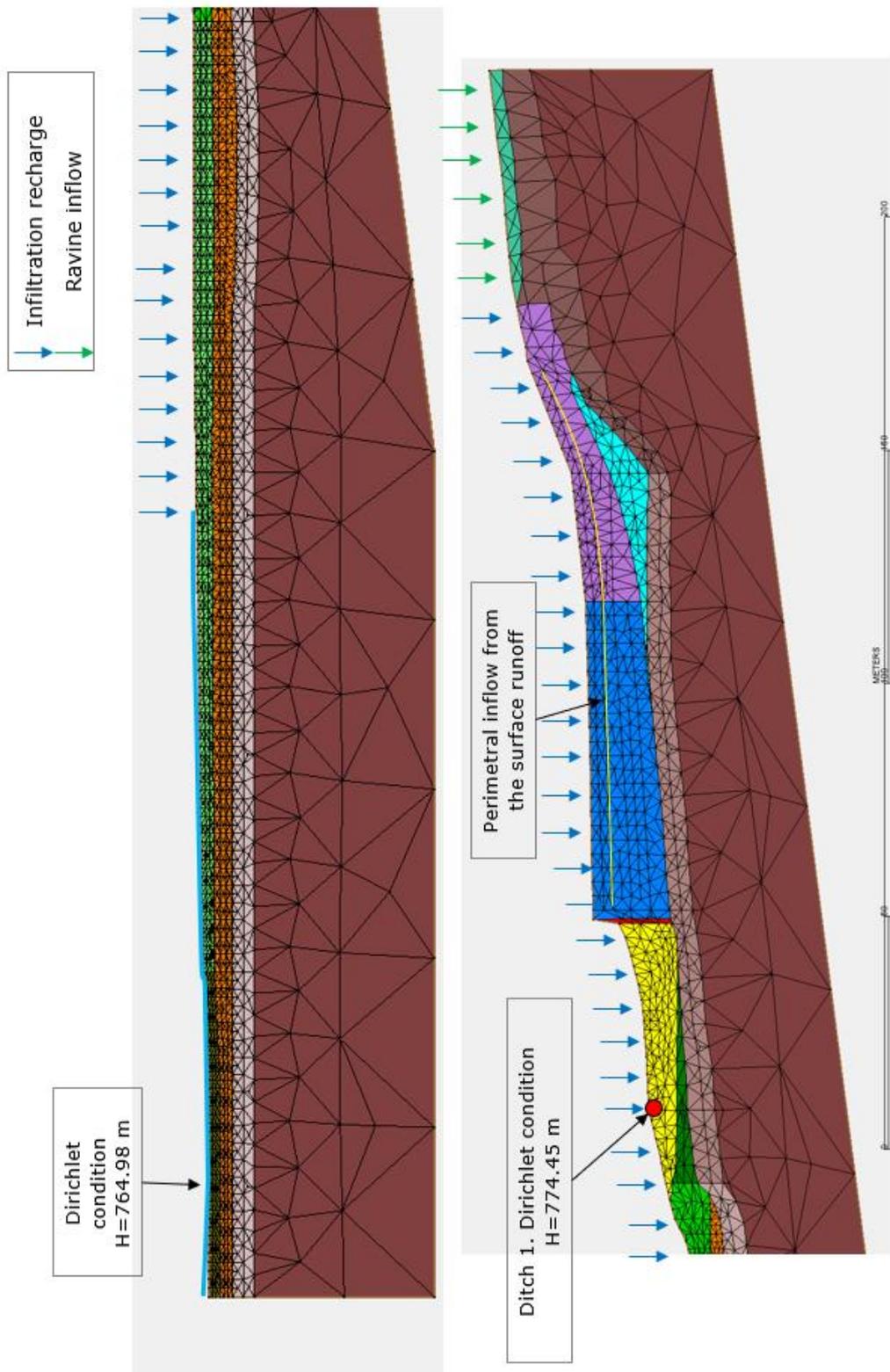
Figure 4.8.   Finite element mesh and boundary conditions of the model along the vertical profile.
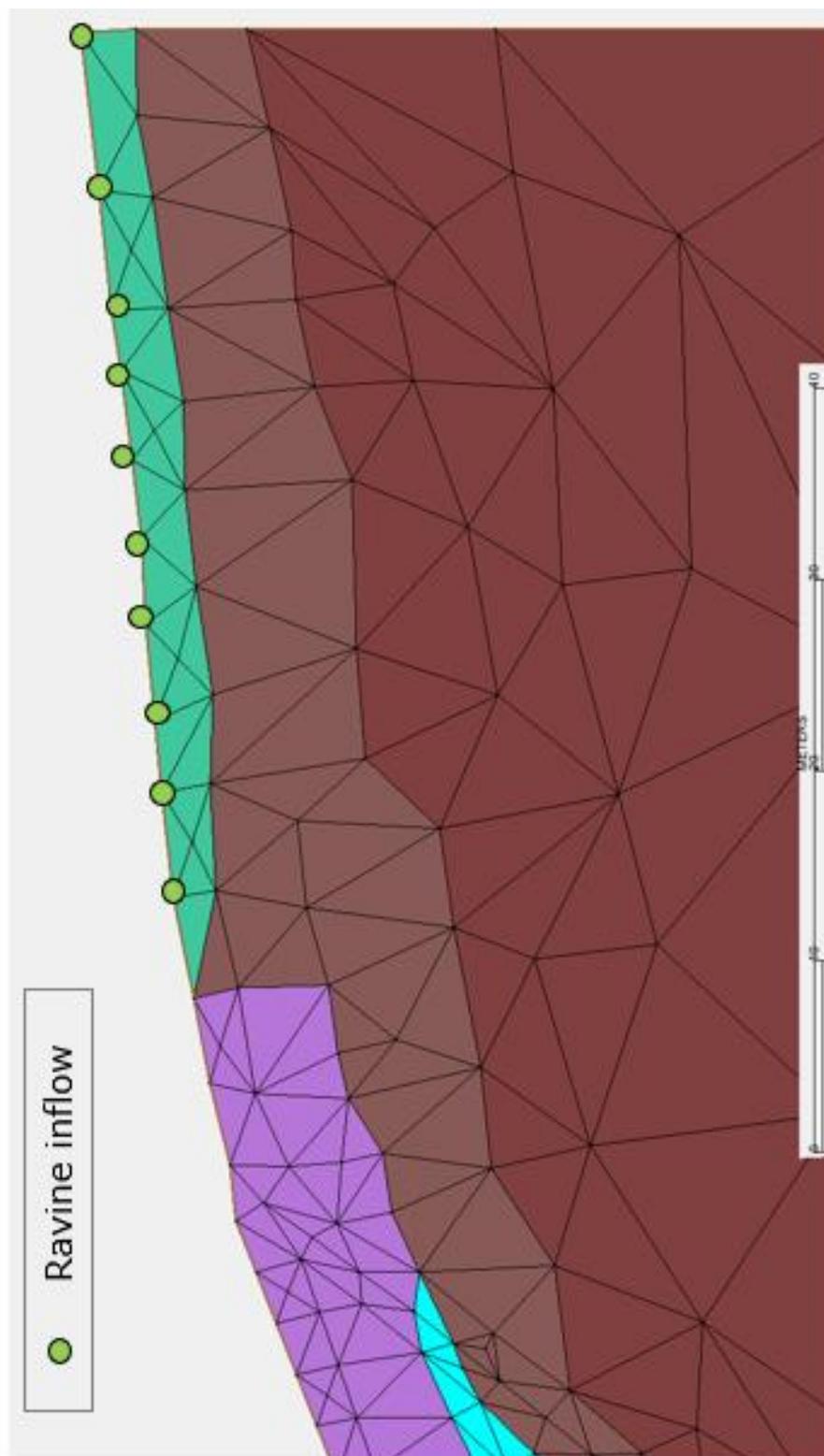
Figure 4.9. Location of the nodes in which a fixed flow boundary condition is used to simulate the inflow from the runoff of the ravine upstream the landfill.
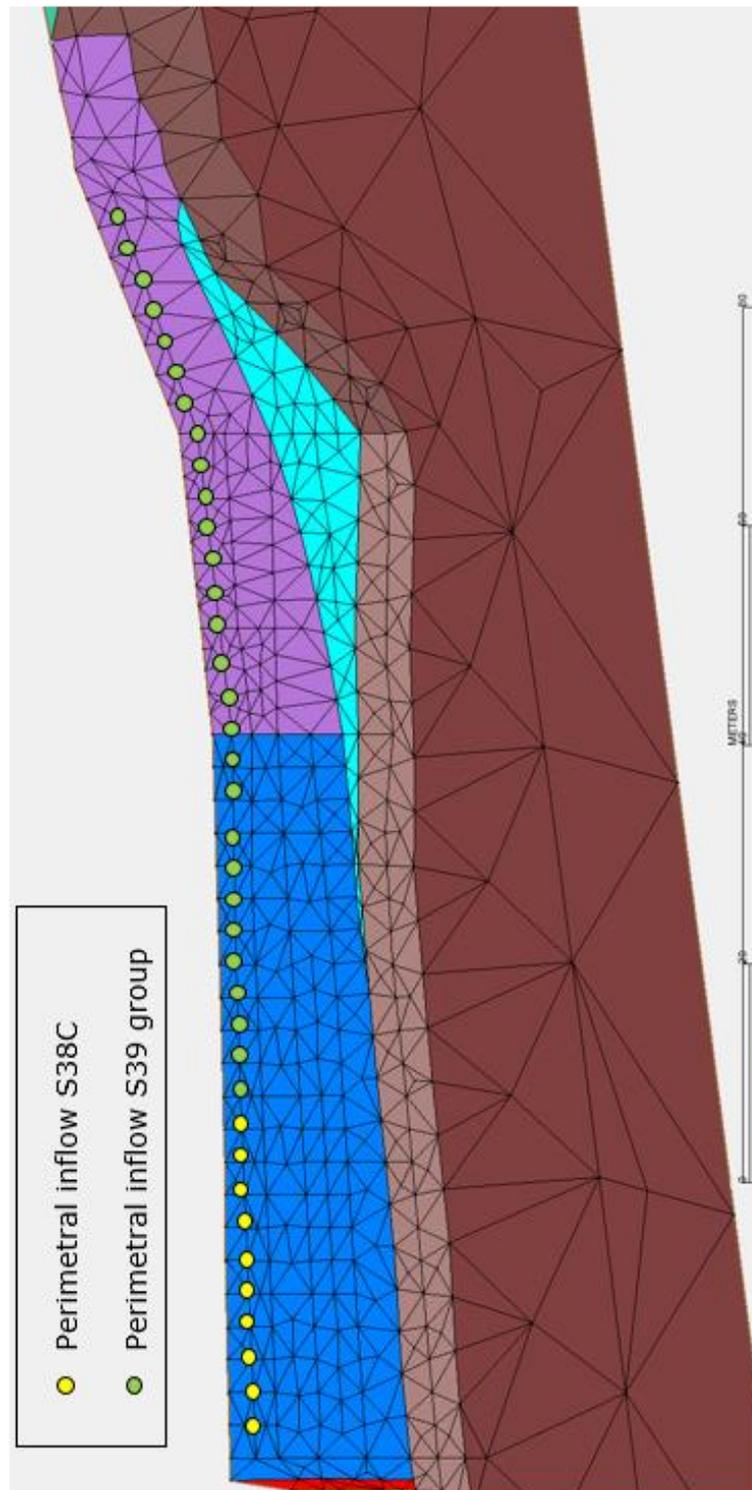
Figure 4.10. Location of the nodes in which a fixed flow boundary condition is used to simulate the inflow from the surface runoff and interflow. The inflow due to flow into the landfill through the ditches located immediately upstream the front slurry-wall near the S38C borehole are marked with yellow symbols, while the inflows near the S39 boreholes are marked with green symbols.

The upper limit of the model is the water table which has been estimated from available piezometric data. The following aspects have been considered:

1) The water table in the alluvial near the Sabiñánigo reservoir is, in general, near the ground surface.

2) The hydraulic gradient is very small in the lower part of the filling located upstream the front slurry-wall because the landfill materials have a high hydraulic conductivity.

Figure 4.11 shows the topography and the estimated water table surface along the profile. Figure 4.12 shows the estimated water table and the material zones of the numerical model along the profile defined by EMGRISA (2014).
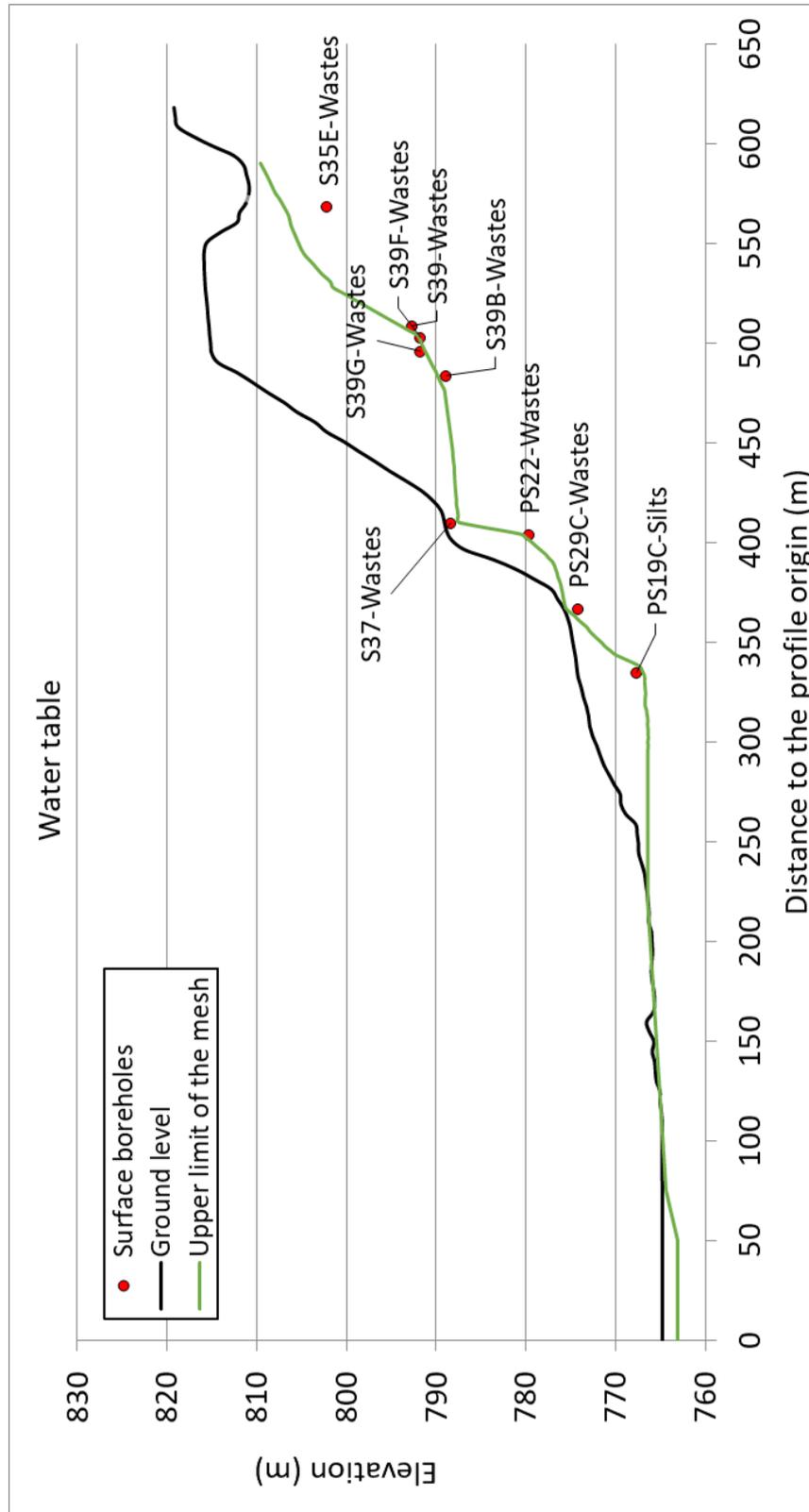
Figure 4.11. Topography and estimated water table along the E-W direction vertical profile of Sardas site. The red dots represent the average measured heads at the boreholes located along the profile and the yellow dots represent the average measured heads at boreholes projected onto the profile.
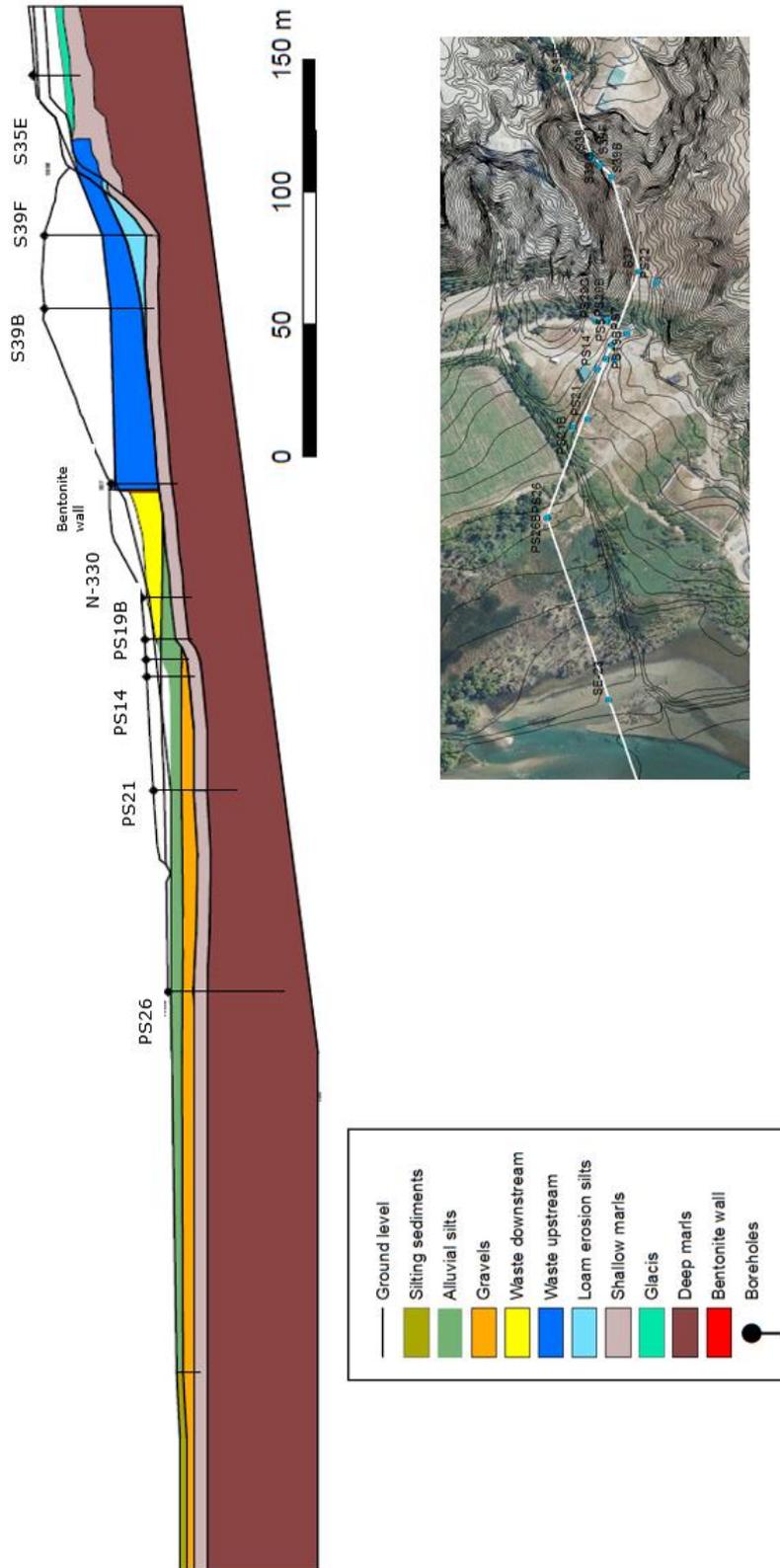
Figure 4.12. Estimated water table along the topographic profile of the Sardas landfill site which includes the material zones.

4.5 Model calibration and results

4.5.1   Calibration methodology

The steady state numerical model has been calibrated by trial and error using average measured piezometric heads and considering that the water table is similar to the estimated water table, making sure the water table is always below the ground surface. Average measured hydraulic head in a borehole has been compared with the computed head at the node of the mesh closest to it. The hydraulic conductivities of the material zones and the leakage flow rate in the vicinity of the PS29C borehole (Ditch 1) have been calibrated while being consistent with the ranges defined by EMGRISA (2014).

The flow rates collected in Ditch 1 have been measured in the last few years. Pumping in boreholes located in the landfill have been performed in order to reduce the leakage flow rates during those years. In the steady state numerical model, in which pumping is not considered, the leakage flow rate is assumed greater than the average flow rate measured in Ditch 1.

The Nash-Sutcliffe criteria has been used to quantify the goodness of fit of the computed hydraulic heads (Krause *et al*, 2005). The Nash index, E, is defined as:

$$E = 1 - \frac{\sum_{i=1}^{N}(h_m - h_c)^2}{\sum_{i=1}^{N}(h_m - h_p)^2}$$

where h_m and h_c are the average measured hydraulic head (h_m) and the computed hydraulic head (h_c) in borehole i, and N is the number of boreholes where data are available. The value of E ranges from -∞ to 1. A value of E equal to 1 corresponds to a perfect fit, while a negative E value corresponds to a very poor fit.

4.5.2   Calibration results

Table 4.5 presents the calibrated hydraulic conductivities. The calibrated outflow near PS29C borehole is 0.19 m^3/d. This value is higher than the measured data. However, the vicinity of Ditch 1 has been pumped to extract pollutants found in nearby boreholes which might cause a reduction in the measured discharge. Table 4.5 presents the comparison of the computed hydraulic heads, the calculated residuals, the Nash index and the determination coefficient.

Figure 4.13 and Figure 4.14 illustrate the excellent fit of computed heads to the measured heads. The absolute values of the residuals are smaller than 1 m.

Table 4.5. Average measured hydraulic heads and computed hydraulic heads in the boreholes after calibration. The residuals in each borehole have been calculated as the difference between the measured and the computed heads. The Nash index and the determination coefficient have also been calculated.

Borehole	Average measured head (m)	Computed head (m)	Residue
PS26	765.05	765.03	0.02
PS26B	765.01	765.03	-0.02
PS21	765.08	765.06	0.02
PS21B	765.03	765.04	-0.01
PS14	765.12	765.05	0.07
PS19B	765.06	765.05	0.01
PS19C	767.69	767.66	0.03
PS5	766.93	767.09	-0.16
PS7	767.87	767.84	0.03
PS29	774.20	773.53	0.67
PS29B	774.19	774.15	0.04
PS29C	774.16	774.65	-0.49
PS22	779.62	779.71	-0.09
S37	788.42	788.30	0.12
S39B	788.91	788.95	-0.04
S39G	791.70	791.80	-0.10
S39	792.62	792.53	0.09
S39F	791.80	792.31	-0.51
S35E	802.15	802.38	-0.23
Mean residual		-0.0285	
Nash index		0.9996	
R^2 (Determination coefficient)		0.9996	
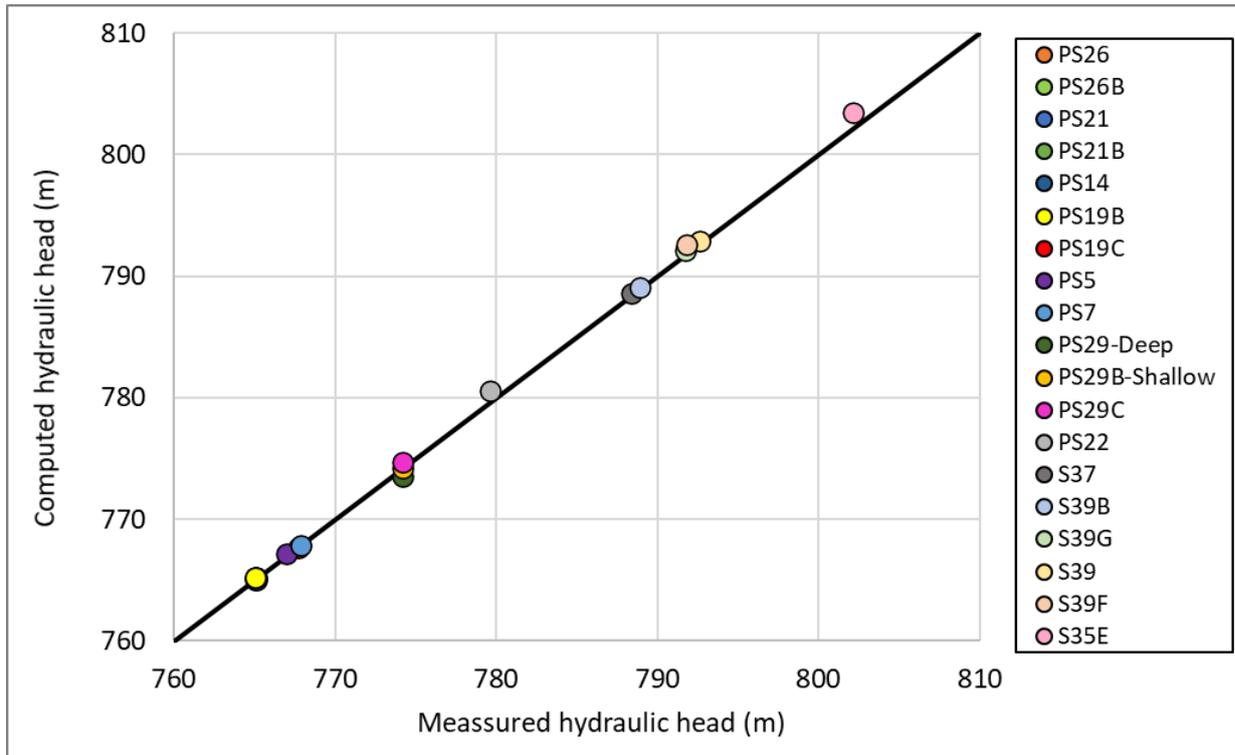
Figure 4.13. Scattergram of the average and computed heads.
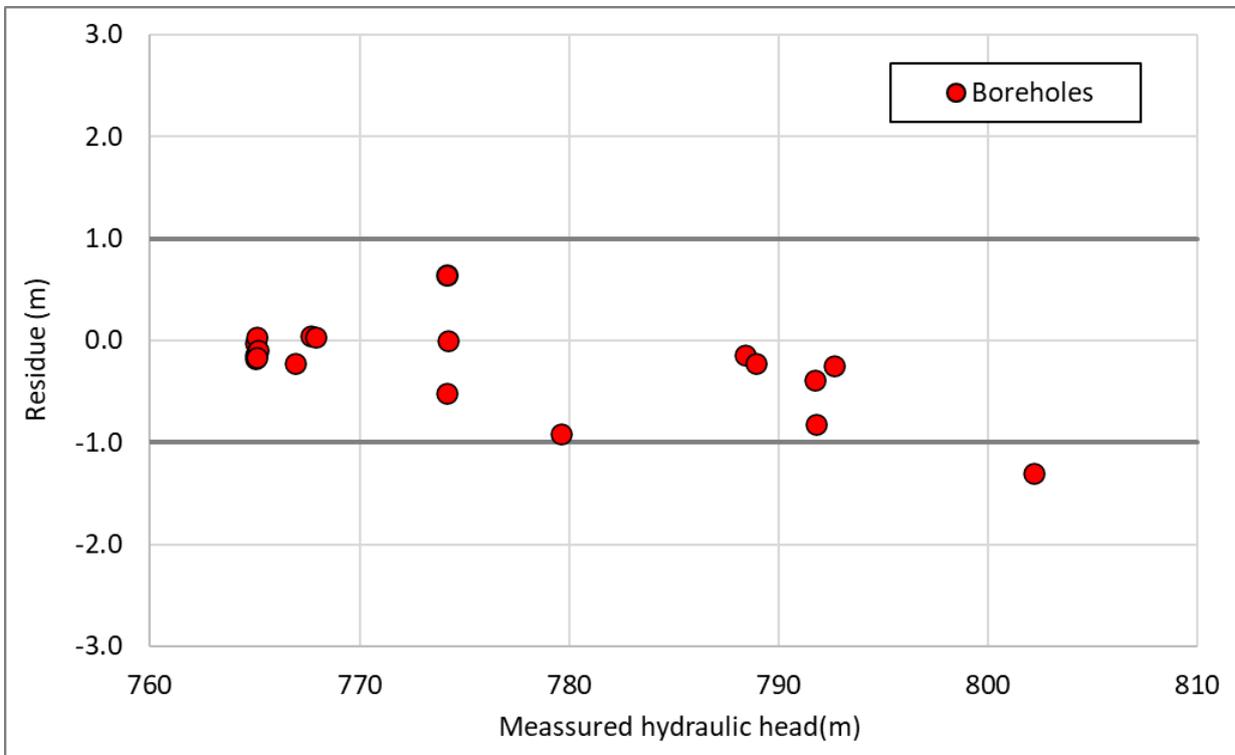
Figure 4.14. Scattergram of the residuals (differences between the measured and the computed hydraulic heads) and the average measured hydraulic heads.

The computed water table is very similar to the one initially used as upper limit of the model domain and it is below the ground surface along the profile (Figure 4.15). The hydraulic head computed near PS29 borehole is shallow. The computed outflow is consistent with the groundwater discharge to Ditch 1.

On the other hand, the model reproduces the vertical gradient measured in the PS19B and PS19C boreholes, which have their screen sections in gravels and silts, respectively. The computed hydraulic heads in the silts are higher than those in the gravels downstream the front slurry-wall.

The numerical model also reproduces the difference in hydraulic heads between boreholes S37 and PS22 located upstream and downstream the front slurry-wall, respectively.

Figure 4.16 shows the computed hydraulic head contour plot along the vertical profile. The upper boundary of the model domain coincides with the water table. There is a significant inflow from the runoff of the ravine upstream the landfill, as well as another inflow along the perimeter ditches of the landfill. The western limit in the silts and gravels is the outflow boundary to the reservoir and to the alluvial gravels. The piezometric gradient in the gravels is very small. Figure 4.17 shows a zoom of the hydraulic head contour plot of Figure 4.16 in the wastes located downstream the front slurry-wall. The hydraulic head gradient in the silts confining the gravels has both horizontal and vertical components. The gradient in the gravels is much lower because the gravels have a very large hydraulic conductivity.

Figure 4.18 shows a zoom of the hydraulic head contour plot of Figure 4.16 in the area of the landfill upstream the front slurry-wall. A very low gradient is observed in the lowest part of the landfill upstream the front slurry-wall, due to the high hydraulic conductivity of the landfill. In the upper part of the landfill, however, there is a significant difference between the hydraulic heads in boreholes S35E and S39B. Upstream the landfill, the flow is from the marls to the landfill wastes.
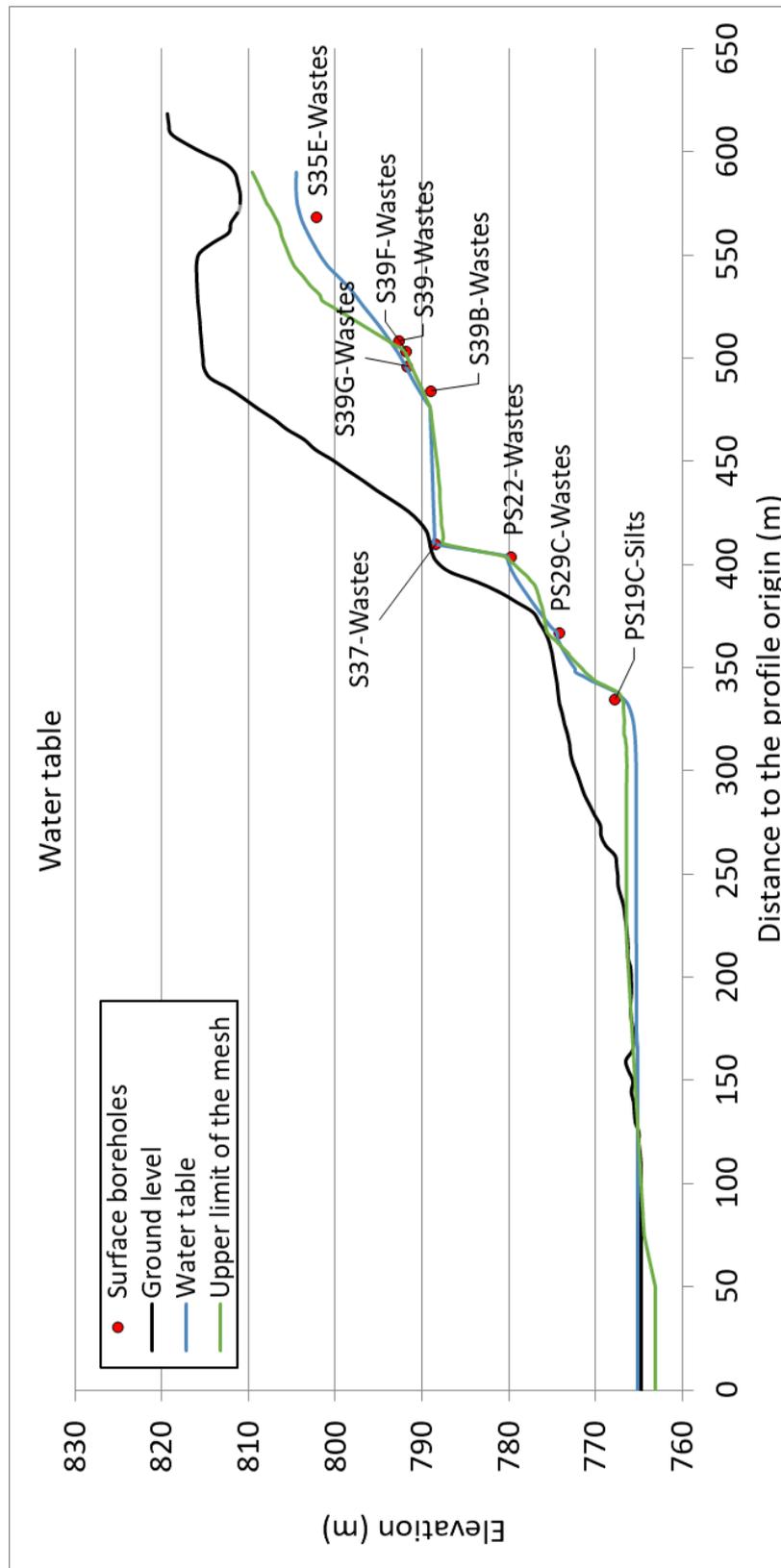
Figure 4.15.   Computed water table. Only piezometric data from shallow boreholes have been included.
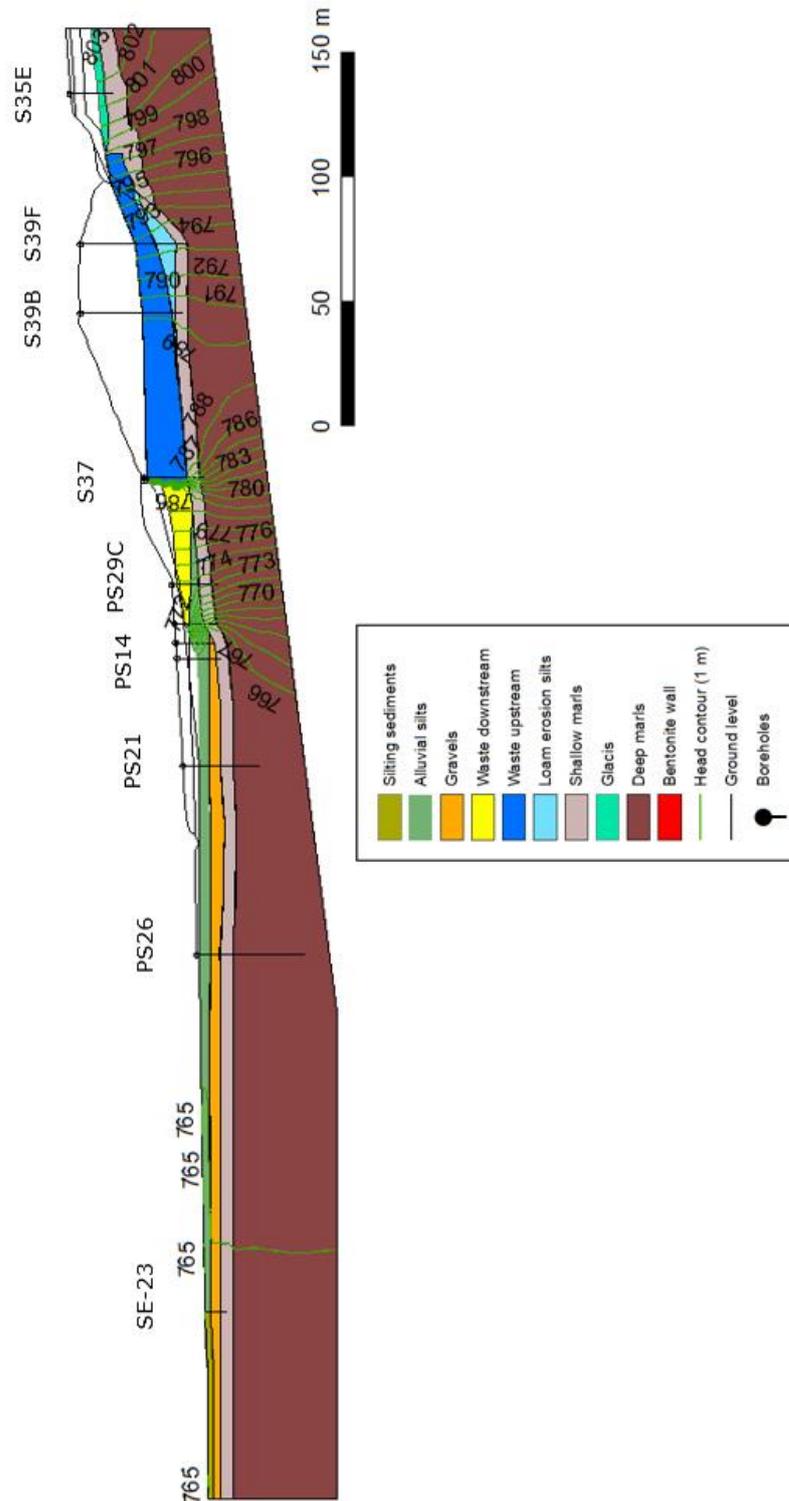
Figure 4.16. Computed hydraulic head contour plot (each 1 m) along the vertical profile. The model domain, shadowed with different colours for each material, and the topographic profile are also shown. The water table indicated by the shadowed materials coincides with the upper boundary of the model domain. Observation boreholes are shown as vertical lines.
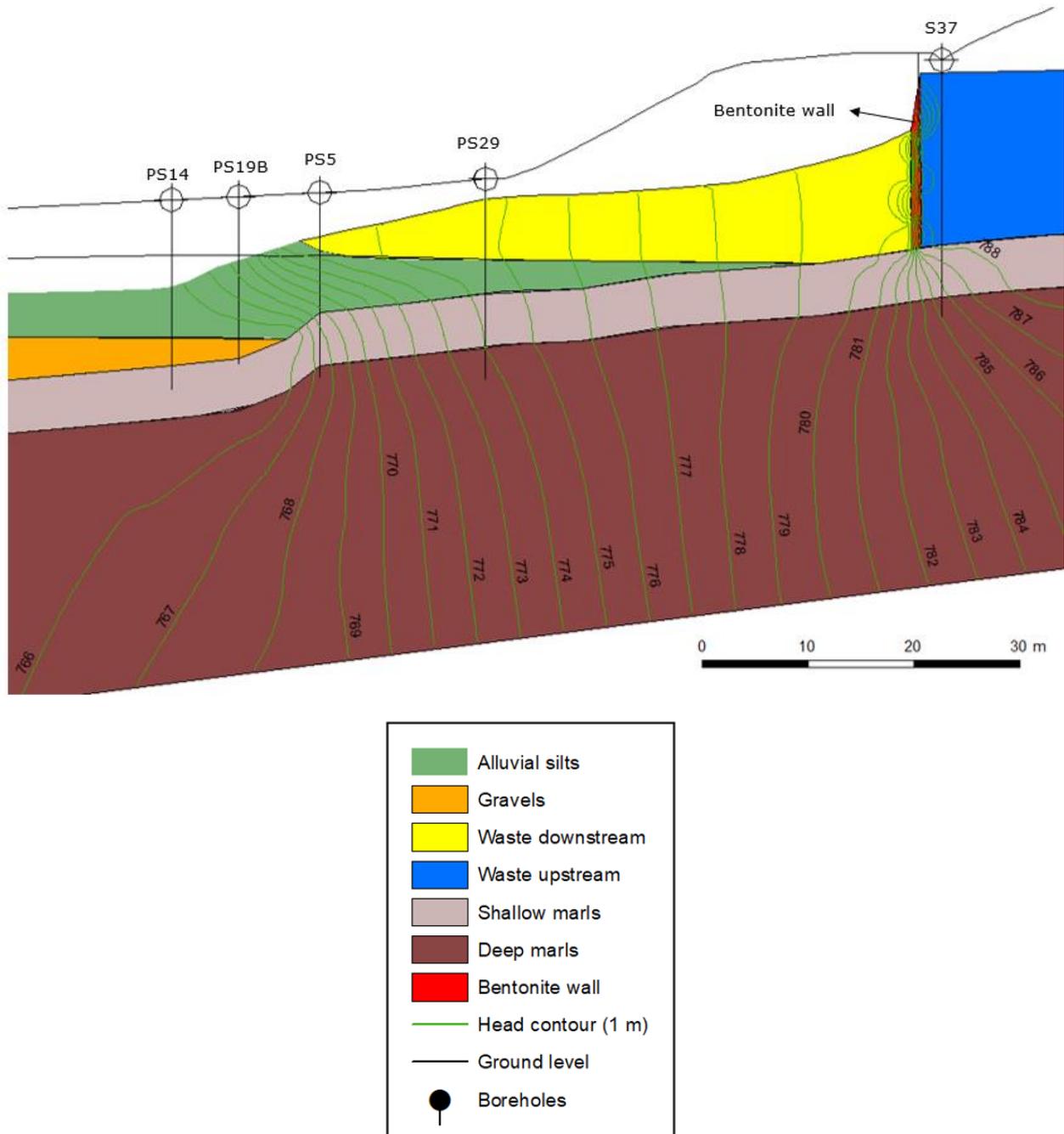
Figure 4.17. Zoom of the computed hydraulic head contour plot of Figure 4.16 into the downstream the front slurry-wall on the slope of the N-330 road. The water table is indicated by the shadowed material zones.
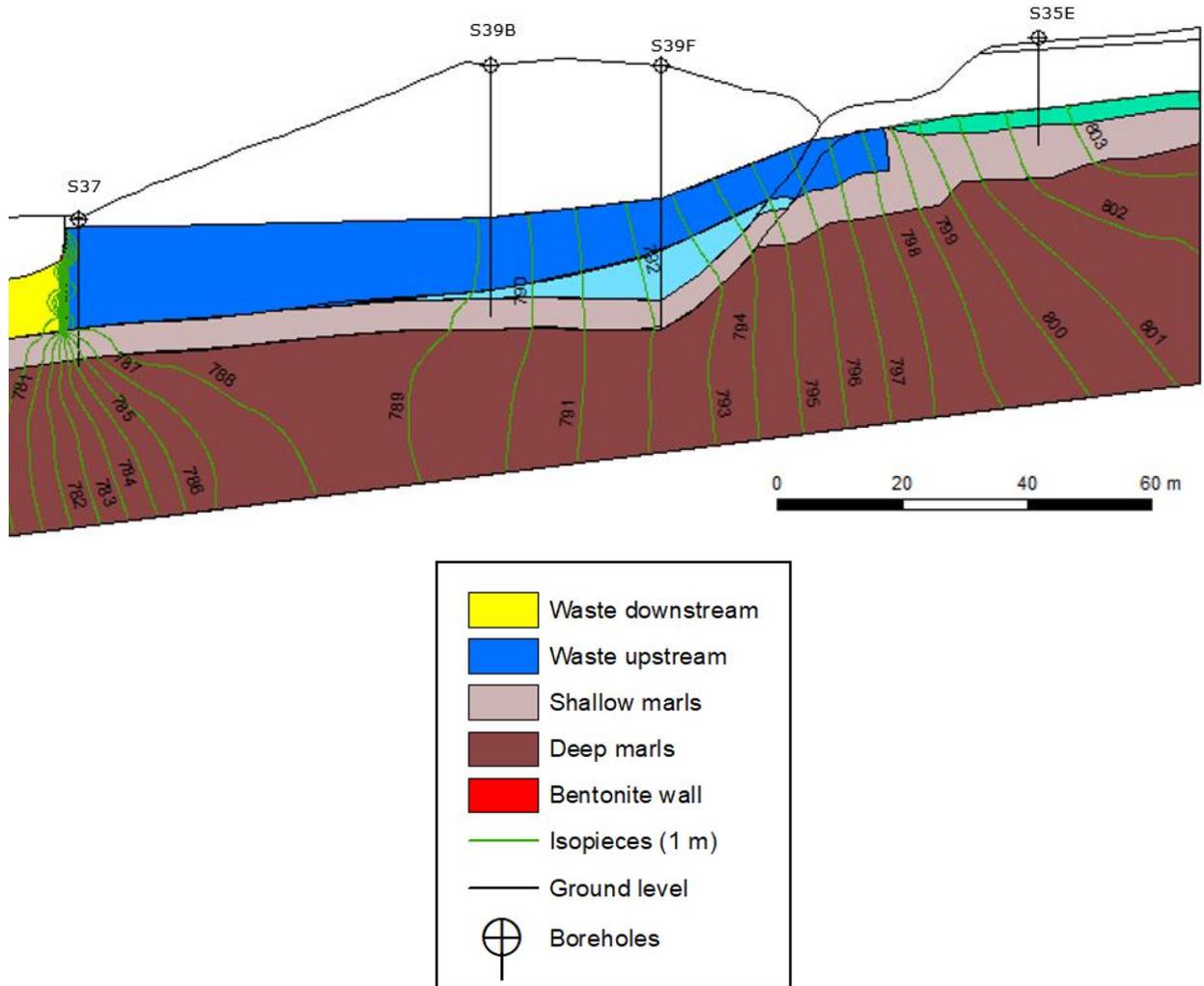
Figure 4.18. Zoom of the computed hydraulic head contour plot of Figure 4.16 between the front slurry-wall and the landfill east limit. The water table is indicated by the shadowed material zones.

4.5.3   Groundwater balance in the model domain

Groundwater inflows in the model domain include (Table 4.6):

1) Recharge by infiltration of rainwater through the water table which is equal to 4.46 m^3/day and is equivalent to 18% of the total inflow.

2) Recharge from the perimeter ditches which is equal to 11.84 m^3/day and is equivalent to 47 % of the total inflow.

3) Recharge from the ravine near the S35E borehole which is equal to 8.84 m^3/day and is equivalent to 35 % of the total inflow.

The inflows per unit thickness are listed in Table 4.6.

Table 4.6.   Water inflows per unit thickness (unit inflow), total inflow for an average thickness of 50 m and percentage of the total water inflows of each water inflow.

Inflows	Unitary flow (m^3/day)	Total flow (m^3/day)	% Inflow
Infiltration recharge	$8.92 \cdot 10^{-2}$	4.46	17.74
Perimeter inlets	$2.37 \cdot 10^{-2}$	11.84	47.09
Ravine inflow	$1.77 \cdot 10^{-2}$	8.84	35.17
Total	$5.03 \cdot 10^{-1}$	25.14	100.00

Table 4.7.   Water inflow rates per unit thickness of recharge due to rainwater infiltration (Table 4.4).

Zone	Description	Inflow (m^3/day)
1	Gállego river alluvial	$6.45 \cdot 10^{-2}$
2	Waste downstream	$2.06 \cdot 10^{-2}$
3	Waste upstream	$4.16 \cdot 10^{-3}$
4	Glacis	$4.4 \cdot 10^{-3}$
	Total	$8.92 \cdot 10^{-2}$

Water outflows from the numerical model take place towards the Sabiñánigo reservoir and the seepage area near PS29C borehole. Table 4.8 present the water outflows. Most of the groundwater discharge occurs from the aquifer to the reservoir (62%). The remaining discharge (38%) takes place into the Ditch 1. The error in the water balance in the calibrated numerical model is equal to $3 \cdot 10^{-3}$ m^3/day.

Table 4.8.   Water outflow rates per unit thickness (unit flow) and total outflows for a thickness of 50 m.

Outflows	Unitary flow (m^3/day)	Total flow (m^3/day)	% Inflow
Reservoir	0.31	15.57	62.10
Ditch 1	0.19	9.50	37.90
Total	0.50	25.08	100.00

4.6 Conclusions

A 2D steady-state groundwater flow along a vertical cross-section in the East-West direction, which runs along the thalveg of the original gully, has been presented. The model has been used to test the conceptual hydrogeological model of the site. The model domain extends from the headwaters of the landfill until the Sabiñánigo reservoir.

The steady-state groundwater flow model has been calibrated with average hydraulic heads measured in boreholes located along the profile. The hydraulic conductivities have been calibrated based on available prior estimates from field tests and previous models. Gradual variations in the hydraulic conductivities have been considered for the shallow altered marls and the alluvial silts.

The model reproduces the average hydraulic heads measured in 19 boreholes. The fit of the numerical model to the measured data is excellent because the average residual is equal to -2.85 cm, the Nash index is equal to 0.9996 and the absolute values of the hydraulic head residuals are smaller than 1 m.

The average water inflow to the Sardas landfill ranges from 20 m^3/d to 30 m^3/d. Most of the inflow comes from the infiltration of the surface runoff of the ravine located in the header of the landfill and the infiltration of surface and subsurface runoff along the perimeter ditches. The

landfill outflows take place by pumping wells, underneath and around the front slurry-wall. The subsurface discharge of the landfill percolates into the Gállego alluvial aquifer. The water inflows into the model domain come from: 1) The runoff of the ravine upstream the landfill near borehole S35E (35%), 2) The recharge along the perimeter ditches (47%) and 3) The recharge from rainfall (18%). Most of the groundwater discharges into the Sabiñánigo reservoir through the layer of silting sediments.

The main conclusions of the 2D steady-state groundwater flow along the vertical cross-section in the East-West direction include:

1) The numerical model confirms the conceptual model proposed by EMGRISA (2014) for the Sardas site.

2) The front slurry-wall acts as a barrier to groundwater flow from the landfill to the floodplain. The numerical model reproduces the piezometric drop measured at both sides of the wall.

3) The hydraulic conductivity of the underlying Larrés marls is very low and hinders groundwater flow except for its shallowest layer, which is more fractured, altered and decompressed (FAD marls).

4) Most of the groundwater flow takes place through the gravels and discharges into the Sabiñánigo reservoir through the layer of silting sediments.

5. TWO-DIMENSIONAL TRANSIENT STATE GROUNDWATER FLOW MODEL ALONG A VERTICAL PROFILE IN THE EAST-WEST DIRECTION

5.1 Introduction

This chapter presents the 2D transient-state groundwater flow model along a vertical cross-section in the East-West direction of the Sardas landfill and the Gállego alluvial aquifer. The model domain, the finite element mesh, the model structure, parameter values and boundary conditions are similar to those of the steady-state model presented in Chapter 4. The chapter starts with the numerical model of the transient flow and continues with model results. The chapter ends with the main conclusions.

5.2 Numerical model

Numerical simulations have been performed for two-time horizons. A multiannual time horizon was performed for the period 2013 to 2019. A bimonthly simulation has been performed to simulate more accurately the daily fluctuations of the reservoir level and groundwater hydraulic heads.

5.2.1 Time discretization

The time domain of the multiannual simulation extends from January 1st, 2013 to September 29th, 2019. This simulation was performed with daily time increments.

The bimonthly transient model was prepared to analyse the effect of the changes in the water level of the reservoir on the groundwater hydraulic heads. A dry period has been chosen in order to isolate the effects of the reservoir oscillation. The simulation period of the bimonthly model extends from 00:00 of July 28th, 2016 to 15:30 of September 7th 2016. This simulation was performed with time increments of 30 minutes.

5.2.2 Initial conditions

The computed steady state hydraulic heads have been used to define the initial conditions of the multiannual transient-state simulation which started on 00:00 July 28th 2016.

5.2.3 Recharge and boundary conditions

Rainfall recharge was estimated by Samper *et al*. (2018a) using a hydrological model. The recharge zones of the transient model are similar to those of the steady-state numerical model (Figure 4.7 and Table 4.4). The recharge time functions for each recharge zone in the multiannual model are shown in Figure 5.1 and Figure 5.2.

Recharge is simulated by a fixed inflow in the nodes of the boundary at the top of the model domain.
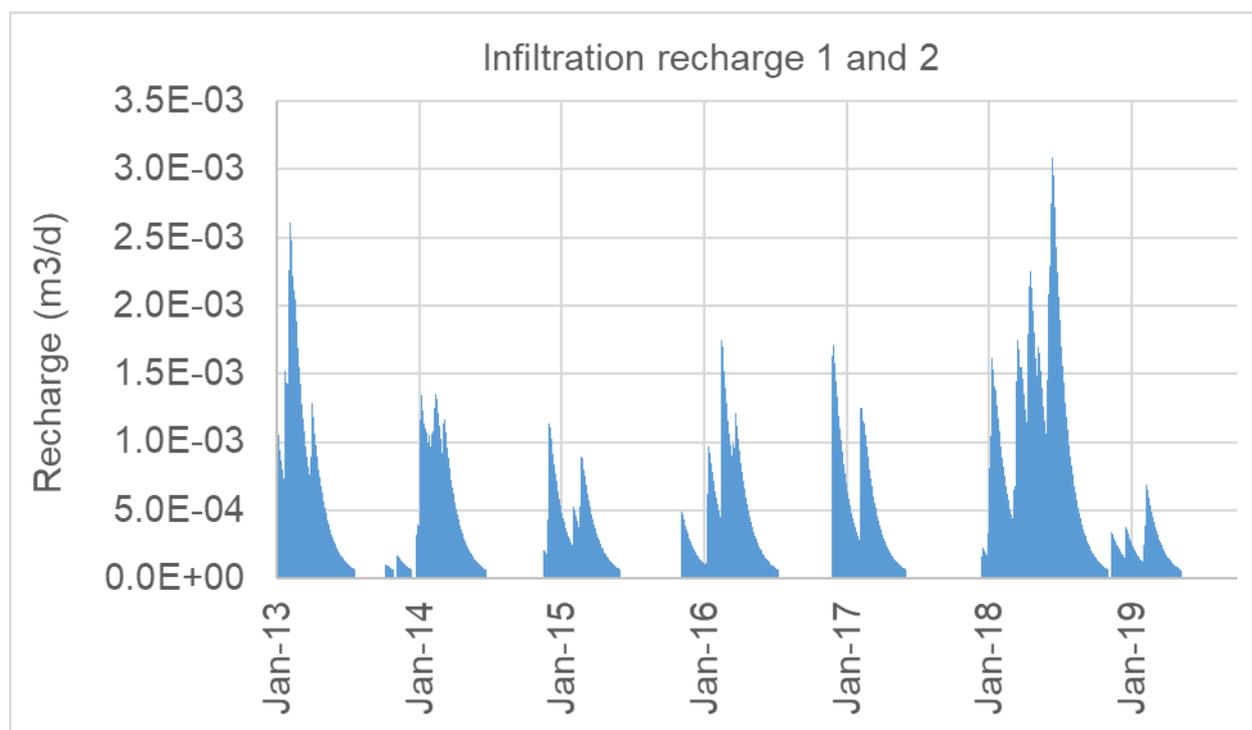
Figure 5.1.   Infiltration recharge function of the multiannual model in zones 1 (silt in the alluvial) and 2 (wastes downstream the front slurry-wall).
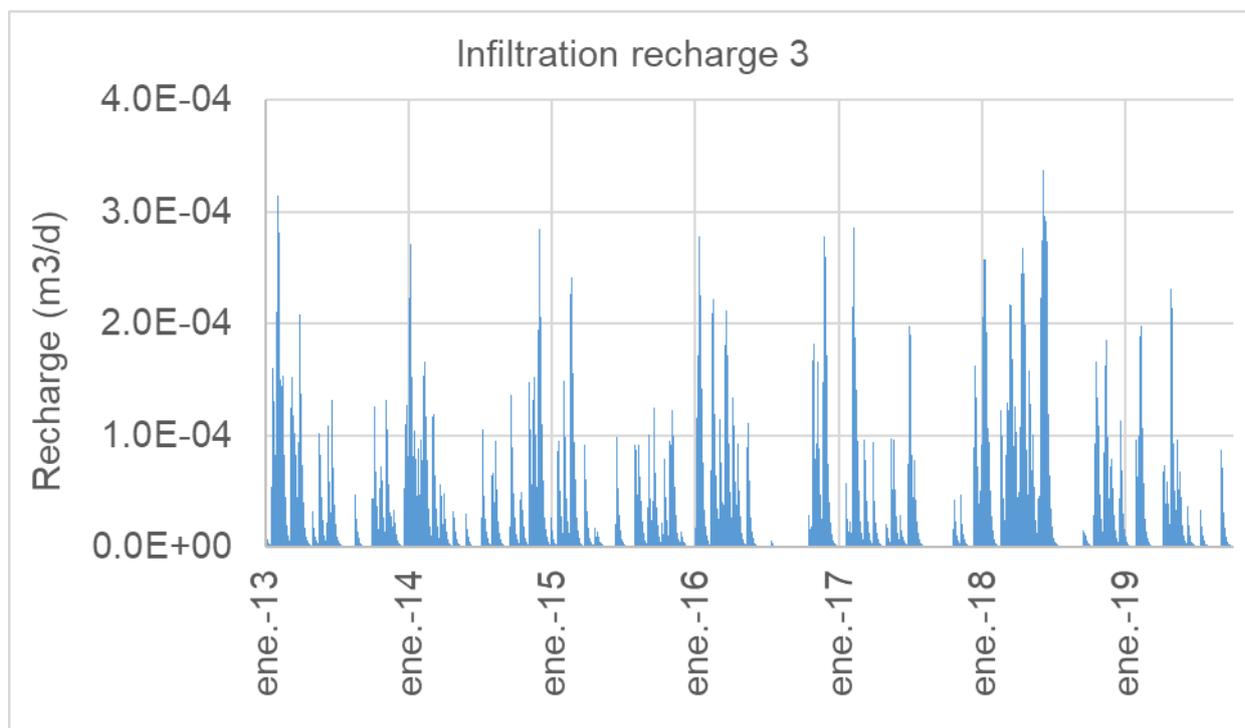
Figure 5.2.   Infiltration recharge function of the multiannual model in zone 3 (wastes upstream the front slurry-wall).

A dry time period was chosen for the bimonthly transient model. There is no recharge in this period in recharge zones R1, R2 and R4. Figure 5.3 shows the recharge time function in recharge zone R3 in the bimonthly transient model zone. One can see that there is recharge only in the first two days.
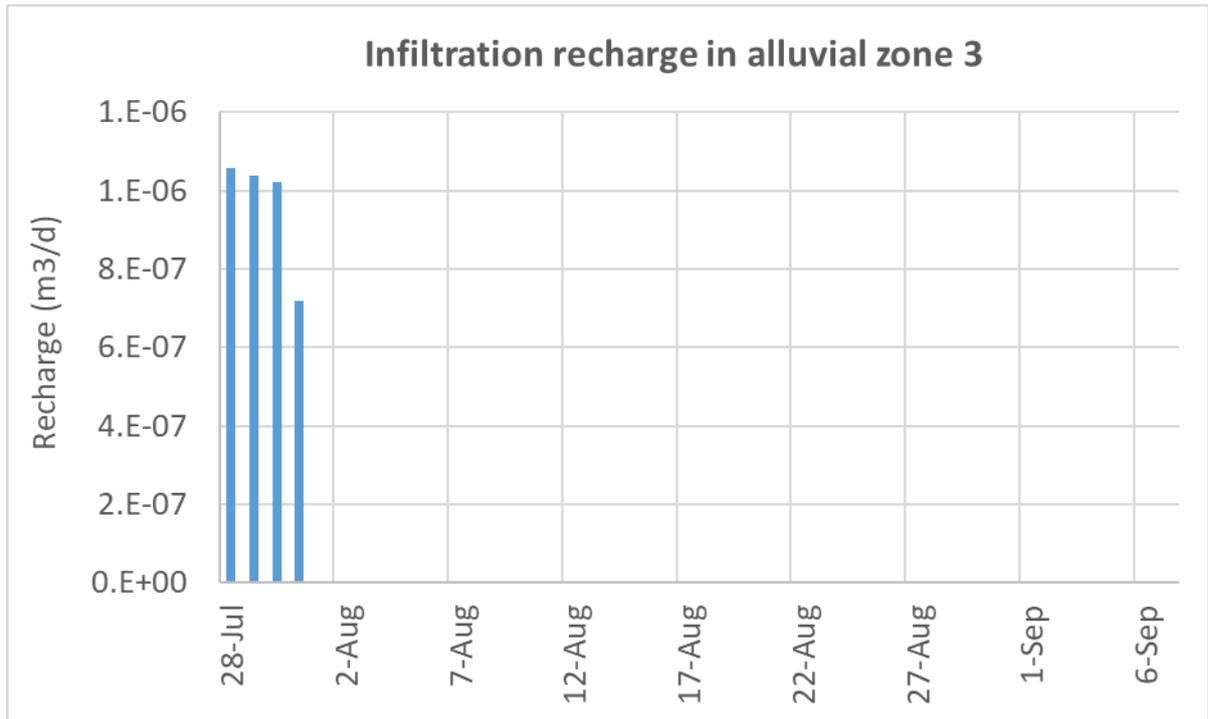
Figure 5.3. Recharge time function for the bimonthly transient model in zone 3 (wastes upstream the front slurry-wall).

The inflow from the runoff of the ravine upstream the landfill near borehole S35E is simulated with a Neumann boundary condition. Figure 5.4 shows the inflow rates from the runoff of the ravine upstream the landfill in the multiannual model. During the bimonthly transient model period there is no inflow in this boundary.
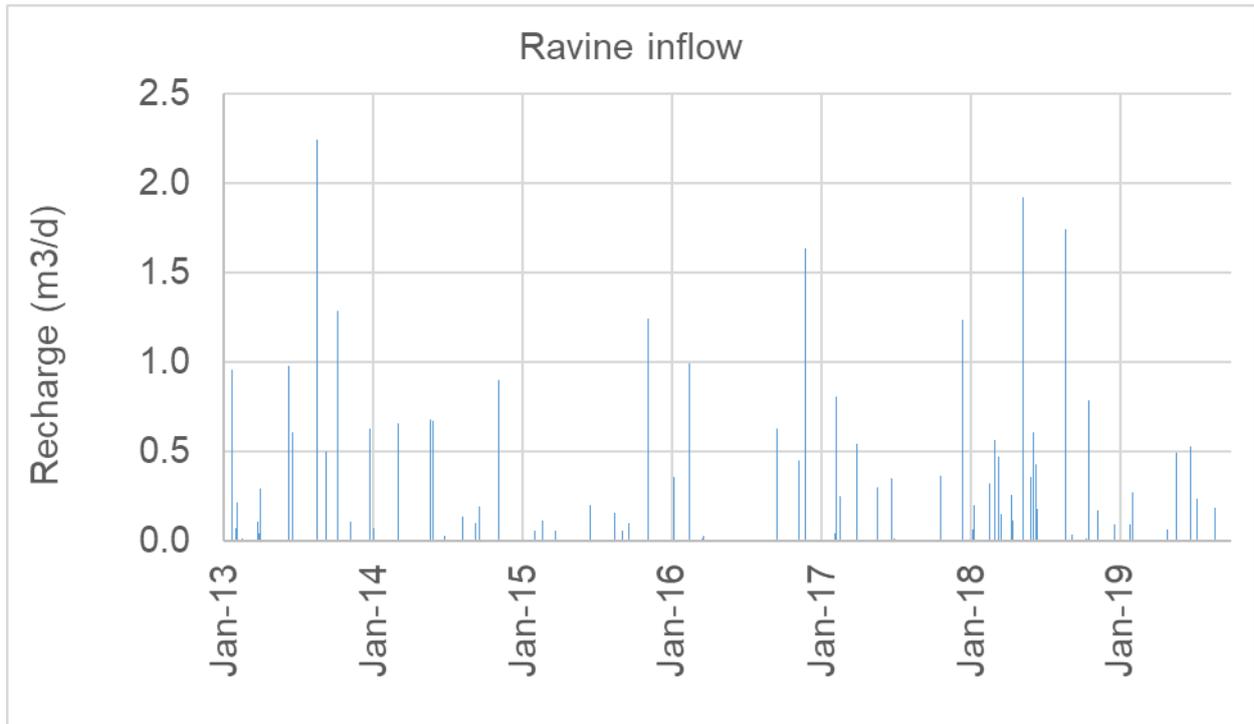
Figure 5.4.   Inflow from the ravine runoff upstream the landfill considered in the multiannual transient model.

There are inflows into the landfill along the perimeter ditches (Figure 5.5). One of them is in the surroundings of the S38C borehole. The second one is located near the S39 boreholes. The inflow rates were derived by Samper *et al.* (2018a) with a hydrological water balance model. Figure 5.6 and Figure 5.7 show the time evolution of the inflows along the perimeter ditches in the multiannual transient state model. Figure 5.8 and Figure 5.9 show the inflows for the bimonthly model.
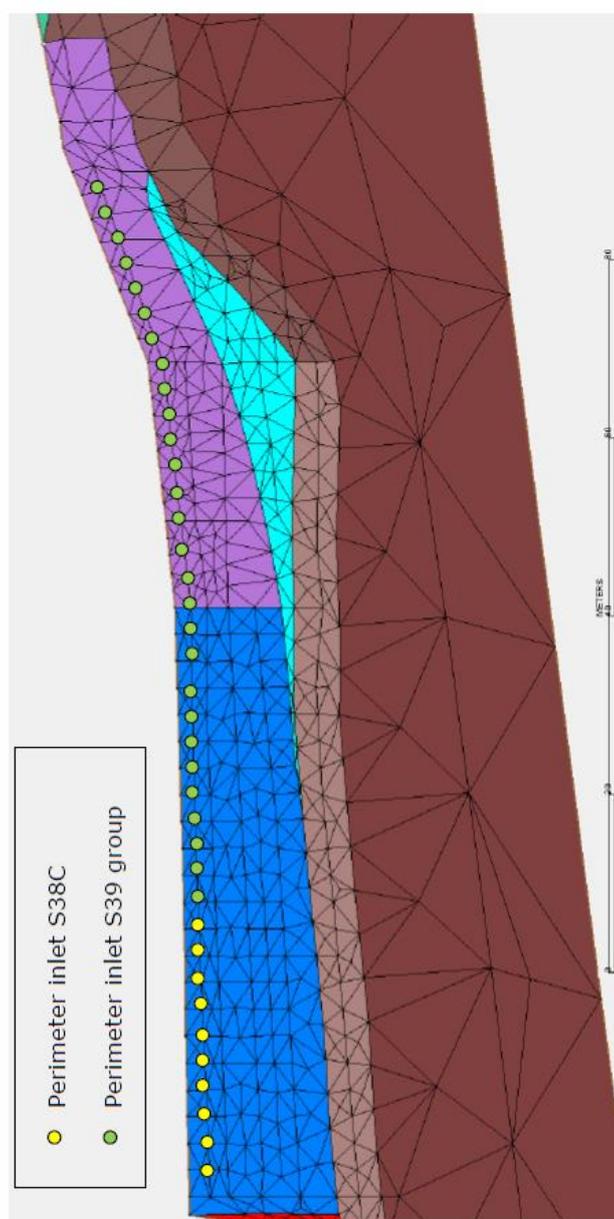
Figure 5.5. Location of the nodes in which a fixed flow boundary condition is defined in order to simulate the inflow due to the infiltration of the run-off through the ditches. The inflow into the landfill through the ditches located immediately upstream the front slurry-wall near the S38C borehole are distinguished with yellow dots, while the two inflow through the ditches near the S39 boreholes are distinguished with green dots.
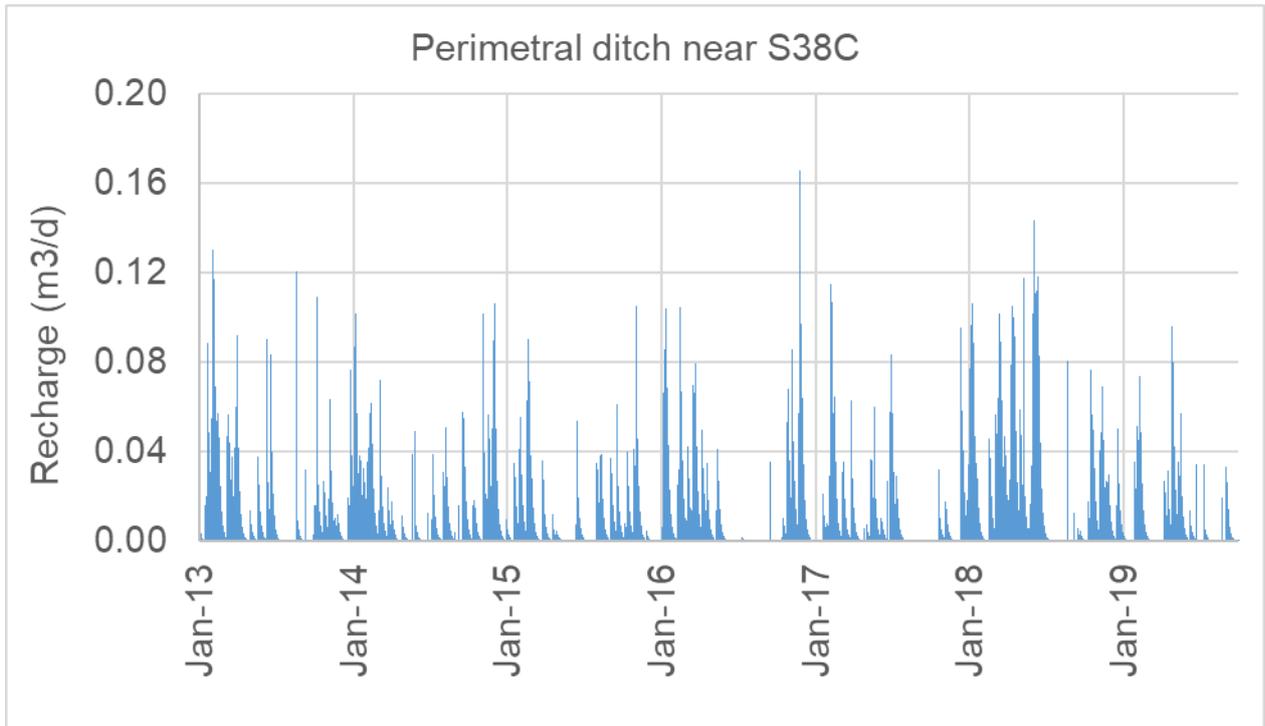
Figure 5.6. Time evolution of the inflow rate from the perimeter ditches in the surroundings of the S38C borehole considered in the multiannual transient state model.
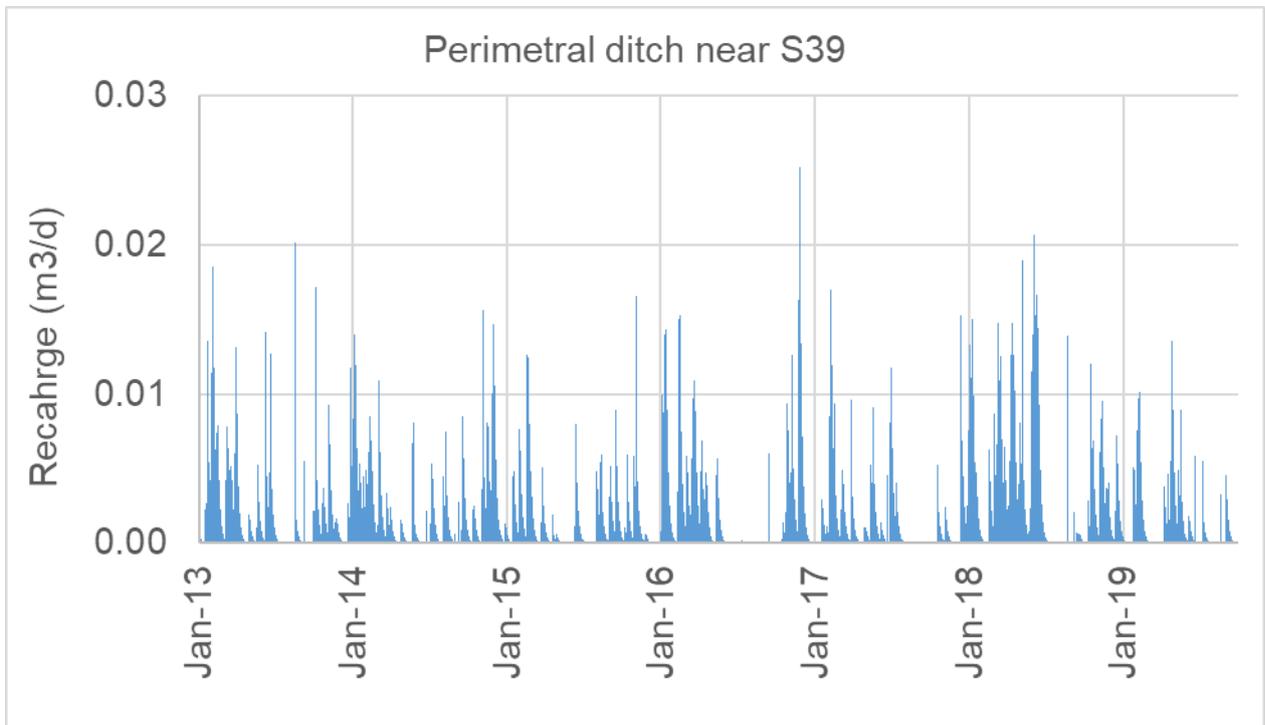
Figure 5.7. Time evolution of the inflow rate from the perimeter ditches in the surroundings of the S39 group of boreholes considered in the multiannual transient model.

Perimetral ditch near S38C
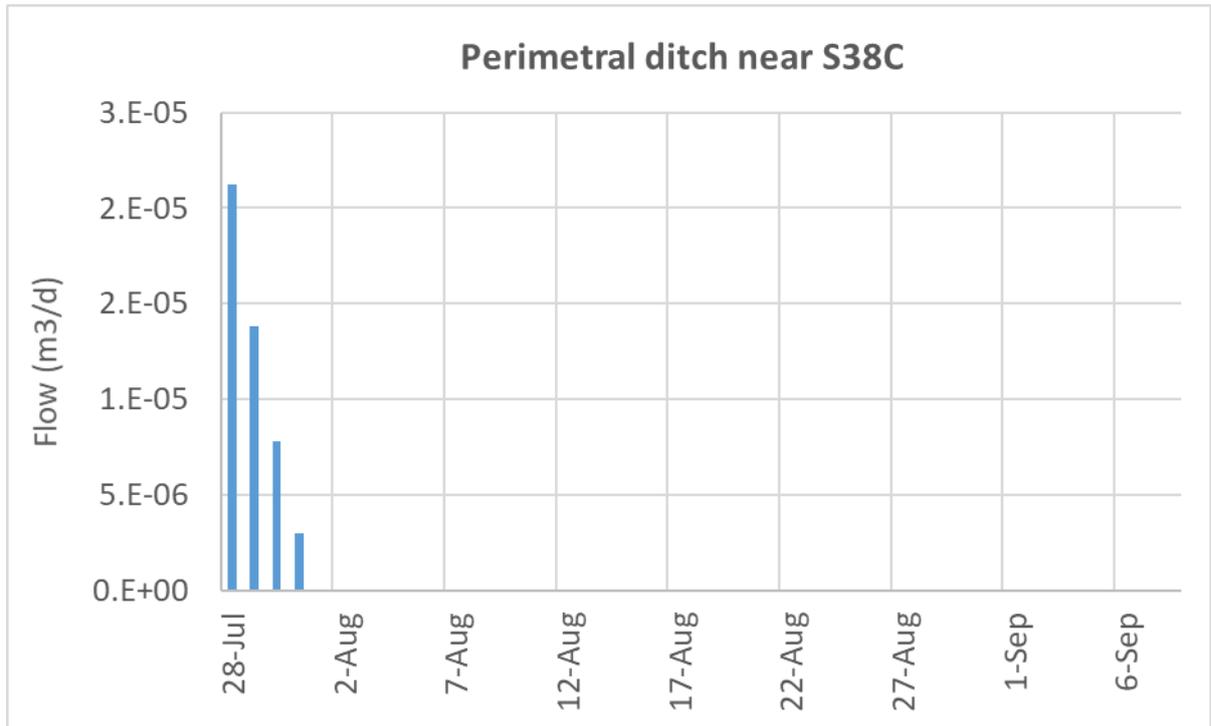
Figure 5.8. Time evolution of the recharge from the perimeter ditches in the surroundings of the S38C borehole considered in the bimonthly transient model.

Perimetral ditch near S39
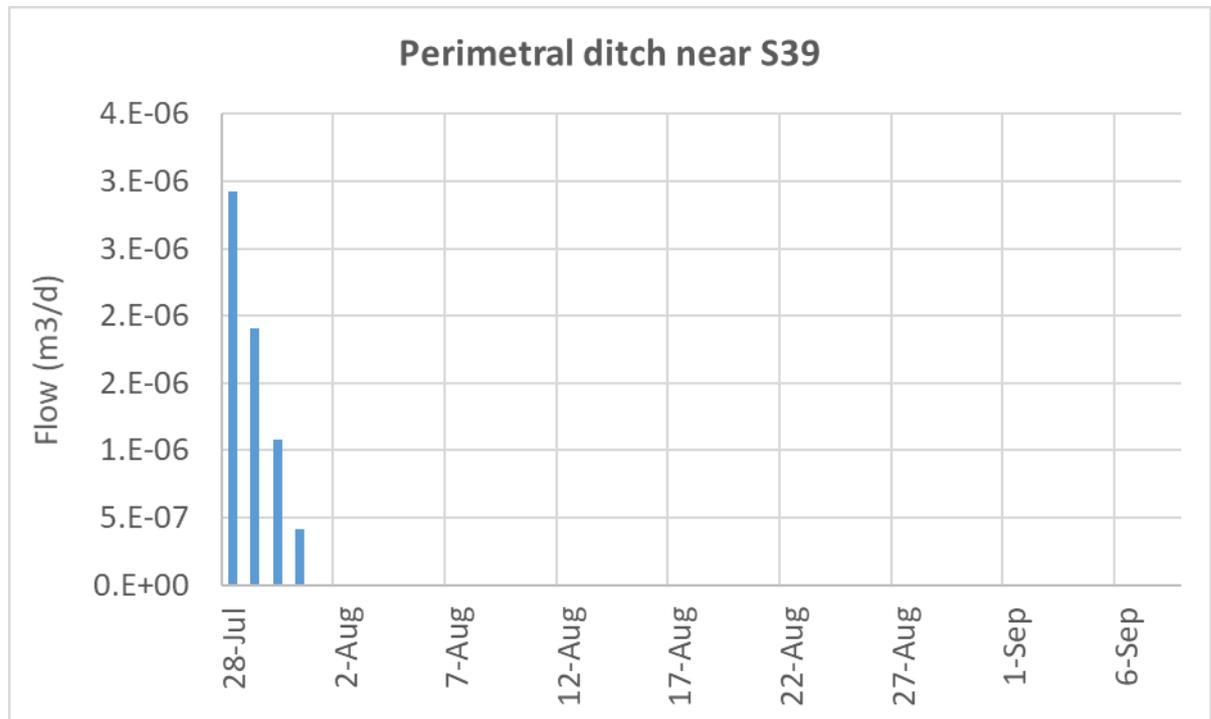
Figure 5.9. Time evolution of the recharge from the perimeter ditches in the surroundings of the S39 borehole group considered in the bimonthly transient model.

INTERNATIONAL MASTER IN
WATER ENGINEERING

EMGRISA has pumped water in borehole S37 located in the backfill upstream the front slurry-wall. Monthly pumped water volumes were provided by EMGRISA (Figure 5.10). Pumping started in June 2014 and continues nowadays. The pumped volume is transformed into pumping rate per unit width of landfill by dividing the pumped volume by 50 m.

Pumping in borehole S37 has been simulated in the transient-state model by using a Neuman boundary condition. The pumped volume per unit width has been distributing along the nodes of the finite element mesh located in the vertical line of the S37 borehole. Monthly constant pumping rates have been considered in the S37 borehole. Figure 5.11 and Figure 5.12 shows the monthly pumping rates per unit width of landfill considered in the multiannual and bimonthly models, respectively.
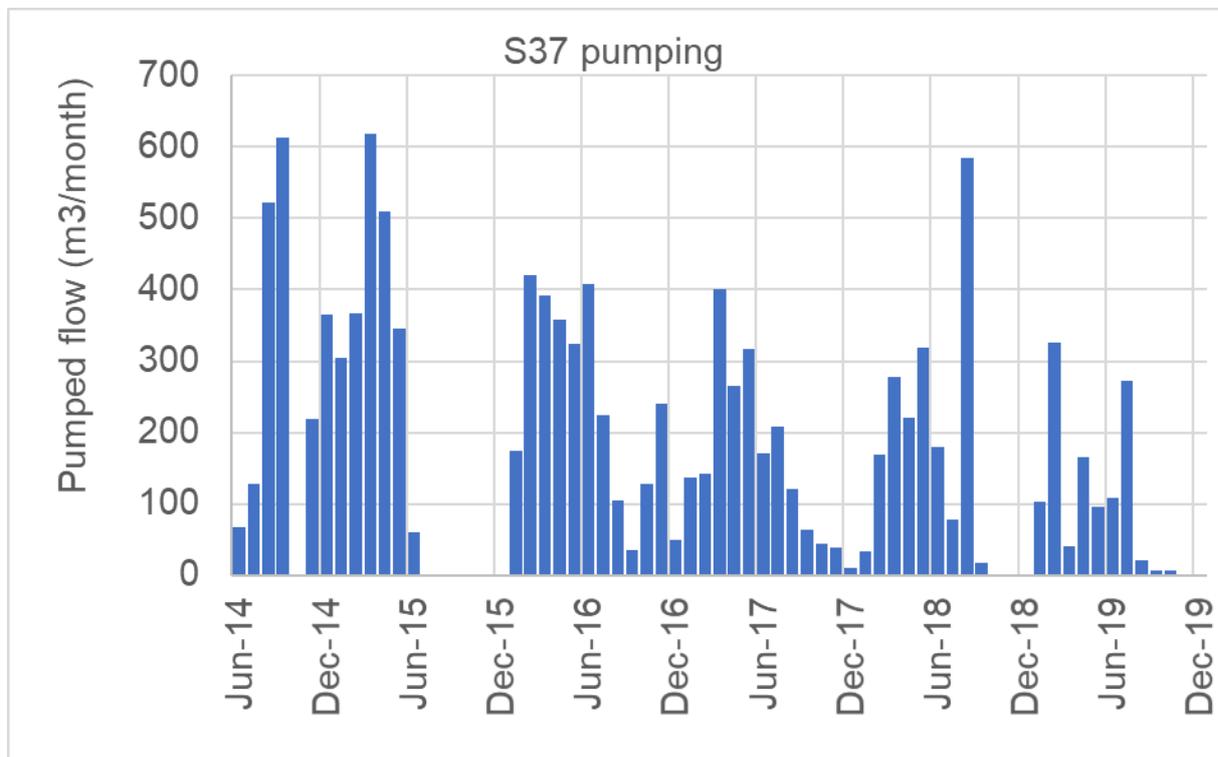
Figure 5.10.   Time evolution of the monthly pumped water volumes in S37 borehole provided by EMGRISA.
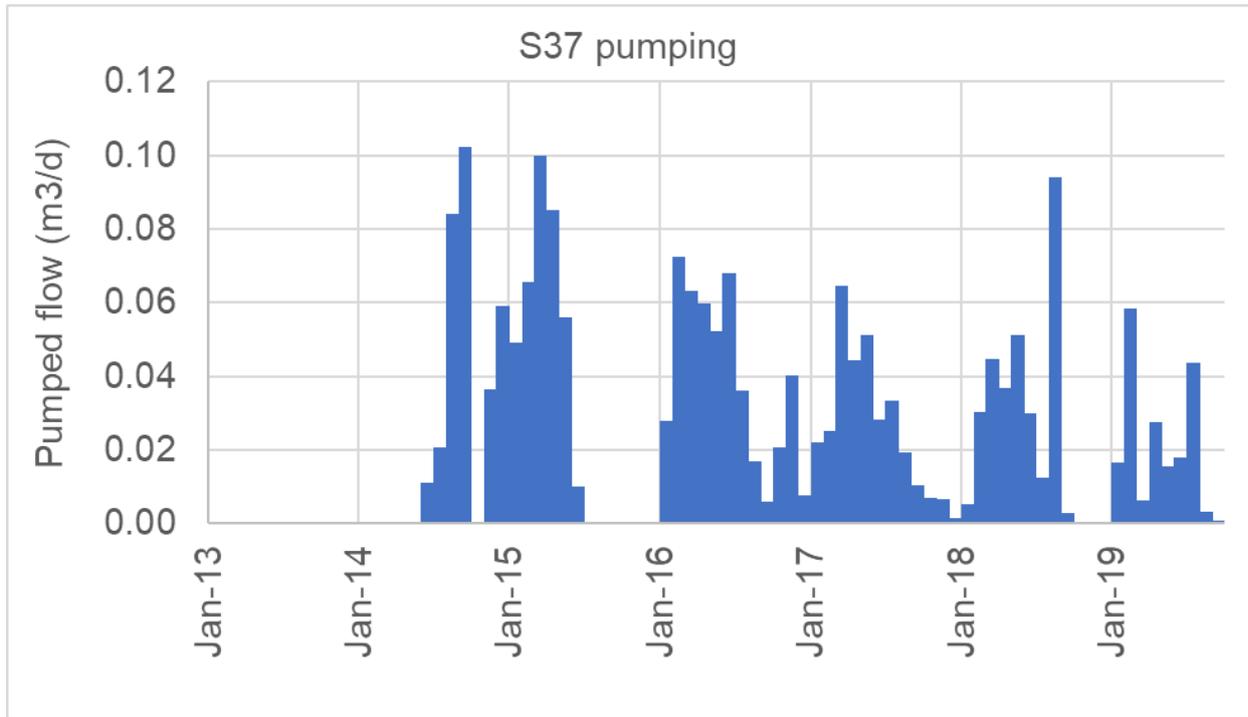
Figure 5.11. Time evolution of unitary outflow by pumping in the S37 borehole considered in the multiannual transient state model.
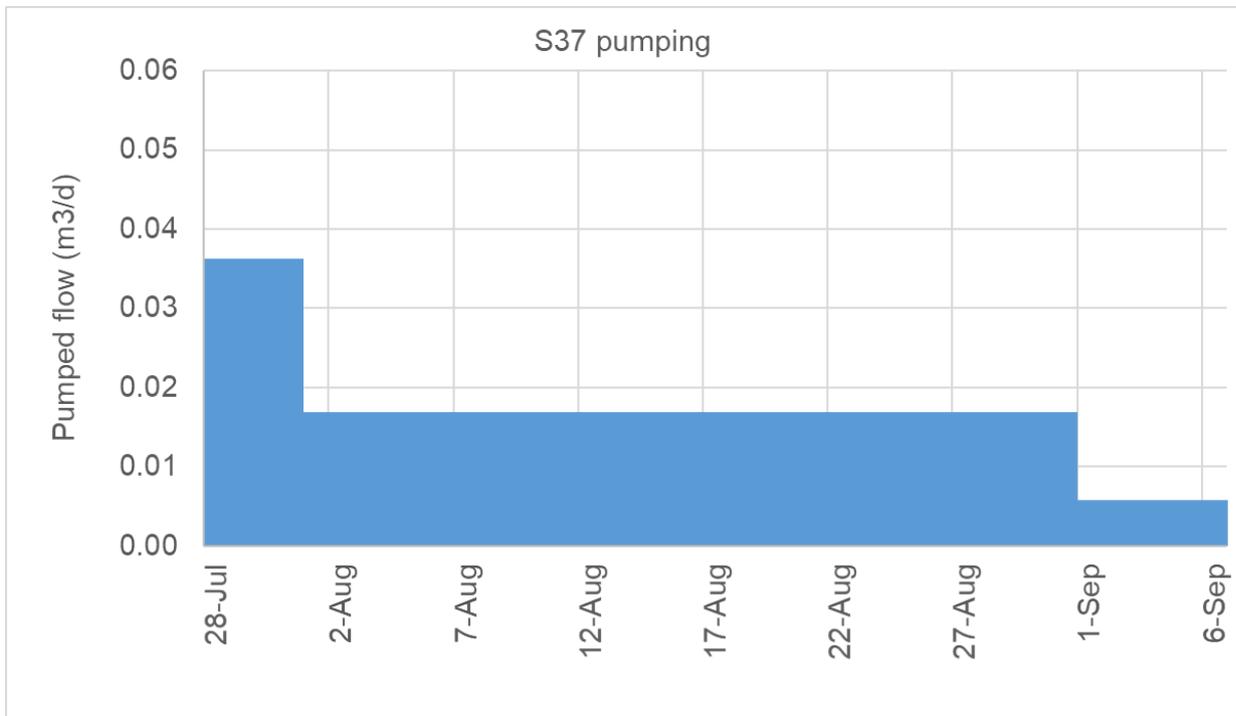
Figure 5.12. Time evolution of the monthly pumping rates per unit width of landfill in the S37 borehole in the bimonthly model.

The errors in simulating the pumping in a profile model have been minimized by introducing an additional boundary condition to account for the cone of depression of hydraulic heads. A Cauchy type boundary condition has been considered in 3 "re-injection" nodes near the pumping borehole S37. The reference hydraulic head has been assumed constant and equal to the computed steady-state hydraulic head. The leakage coefficient has been calibrated. Figure 5.13 shows the location of the nodes where boundary conditions have been defined to simulate the pumping in the S37 borehole.
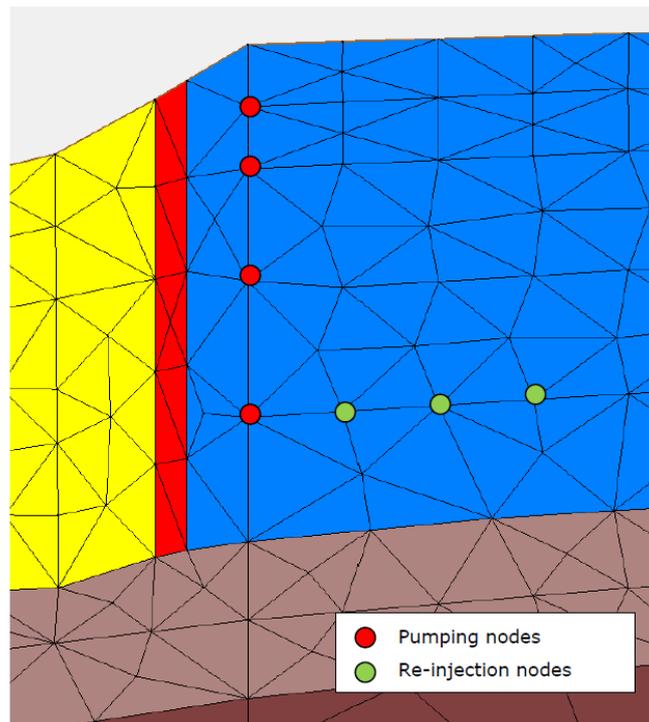
Figure 5.13. Location of the nodes in which boundary condition have been imposed to simulate the pumping in S37 borehole. The pumping flow has been fixed in four nodes (red dots) and a Cauchy condition has been defined in three nodes (green nodes).

The boundaries considered impervious are the same than those in the steady state numerical model. In the upwelling in the area of the PS29C a Cauchy condition has been adopted with the PS29C interpolated hydraulic head as fixed head (Figure 5.14) and a calibrated leakage coefficient equal to 10 m^2/d.
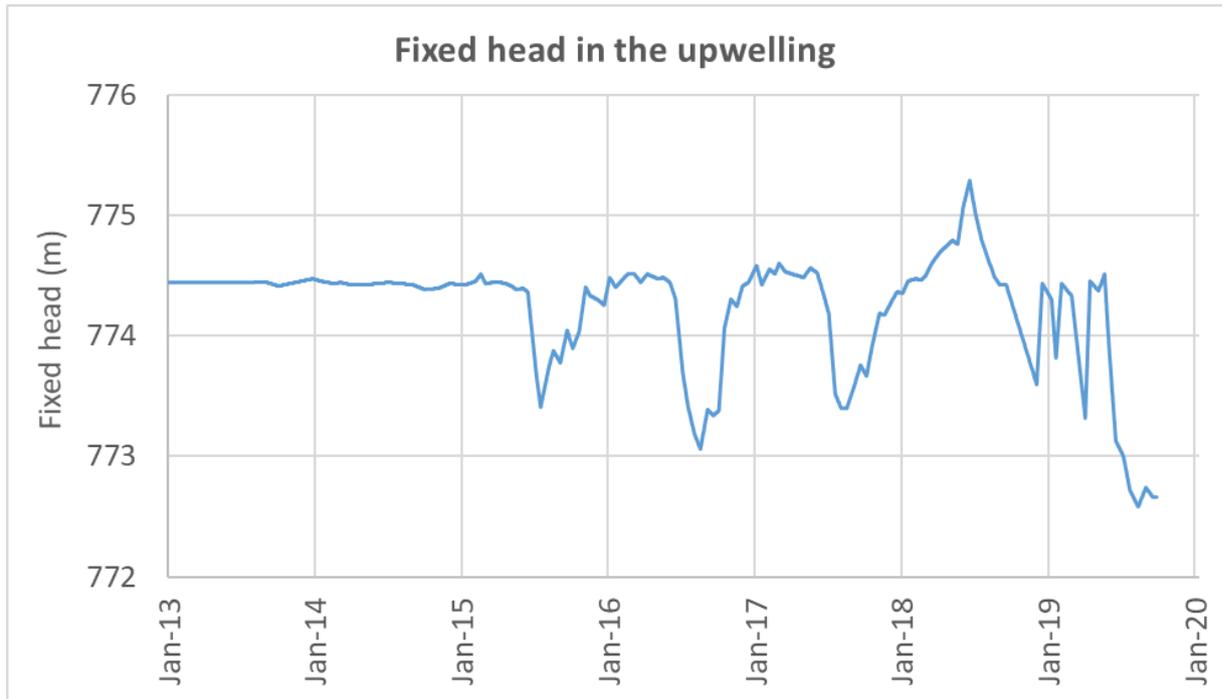
Figure 5.14. Time evolution of the fixed head considered in the seepage area of PS29C borehole in the multiannual numerical model.

The water level of the Sabiñánigo reservoir has been used as a prescribed time-varying head boundary condition. The reservoir water level is continuously monitored with a diver. The gaps in the data have been filled with measured water levels in previous weeks. Figure 5.15 presents the time evolution of the reservoir water levels considered in the multiannual transient model. A synthetic series of reservoir water level has been generate from 1st January 2013 to 26th February 2014 based on water level data measured from 2014 and 2015.Figure 5.16 present the time evolution of the reservoir water levels considered in the bimonthly transient state model.
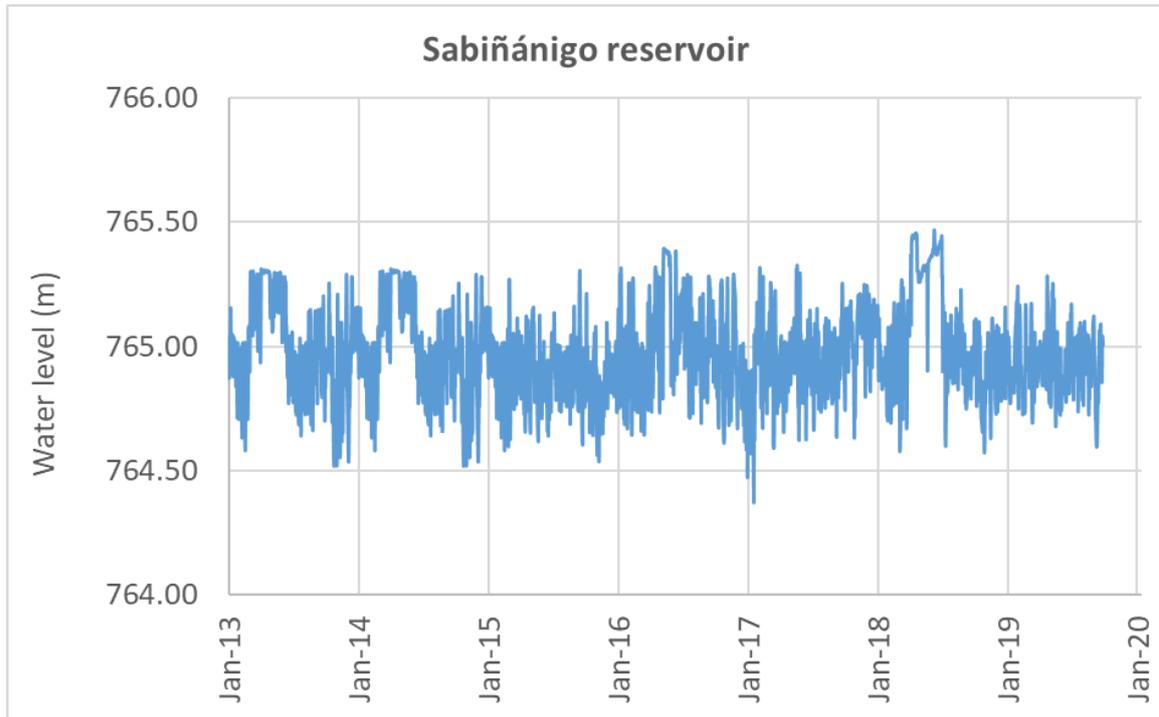
Figure 5.15. Time evolution of the water level of the Sabiñánigo reservoir considered in the multiannual numerical model. Measured water levels are considered for all the simulation period except from 1st January 2013 to 26th February 2014 for which a synthetic series has been generated.
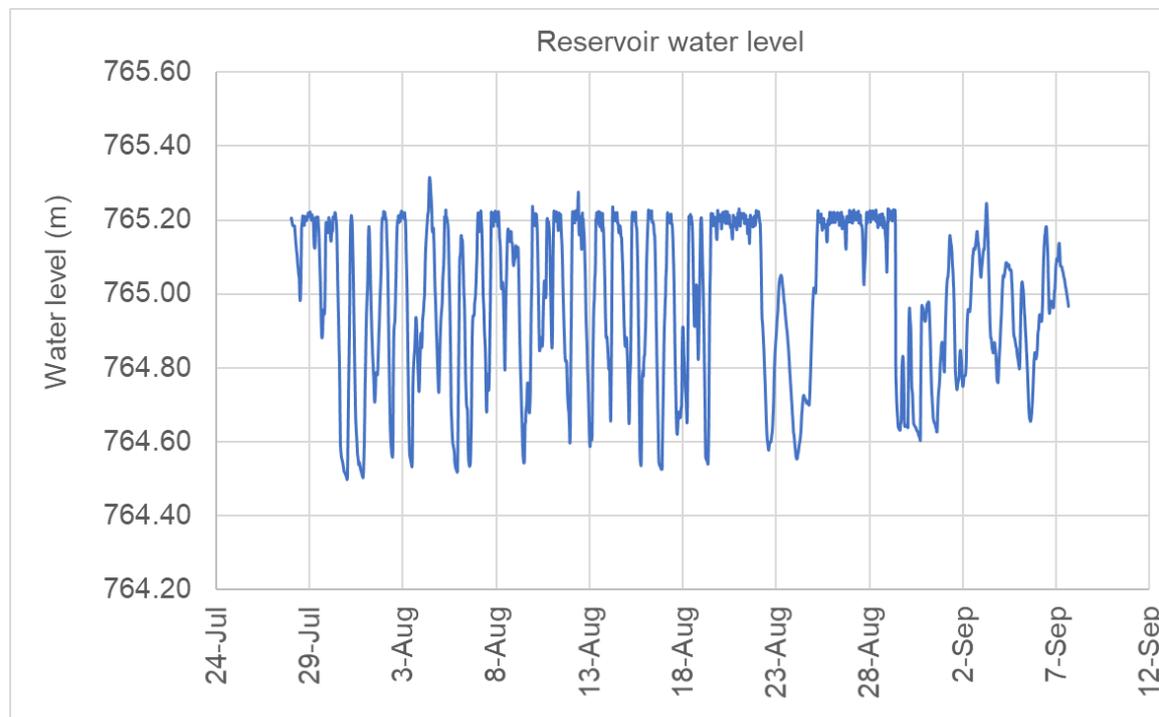
Figure 5.16. Time evolution of measured water level of the Sabiñánigo reservoir from July 28th to September 7th 2016 in the bimonthly numerical model.

5.3 Model Results

5.3.1 Hydrographs

Figure 5.17 to Figure 5.33 show the computed hydrographs with the multiannual transient model and the measured heads in the following boreholes: PS26, PS26B, PS21, PS21B, PS14, PS19B, PS19C, PS5, PS7, PS29B, PS29C, PS22, PS37, PS39B, PS39, PS39F, PS39F and PS35E.
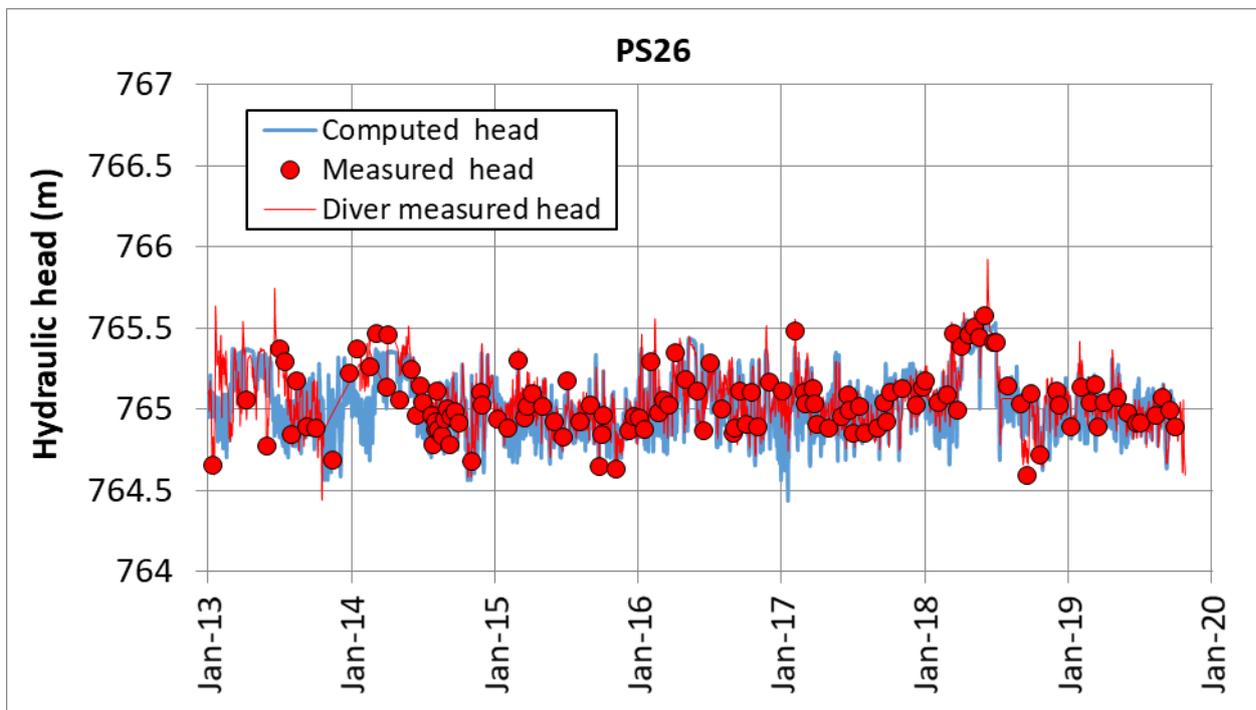
Figure 5.17. Measured hydraulic heads with hydro-level probe (symbols), measured heads with diver (red line) and computed hydraulic heads (blue line) in PS26 borehole.
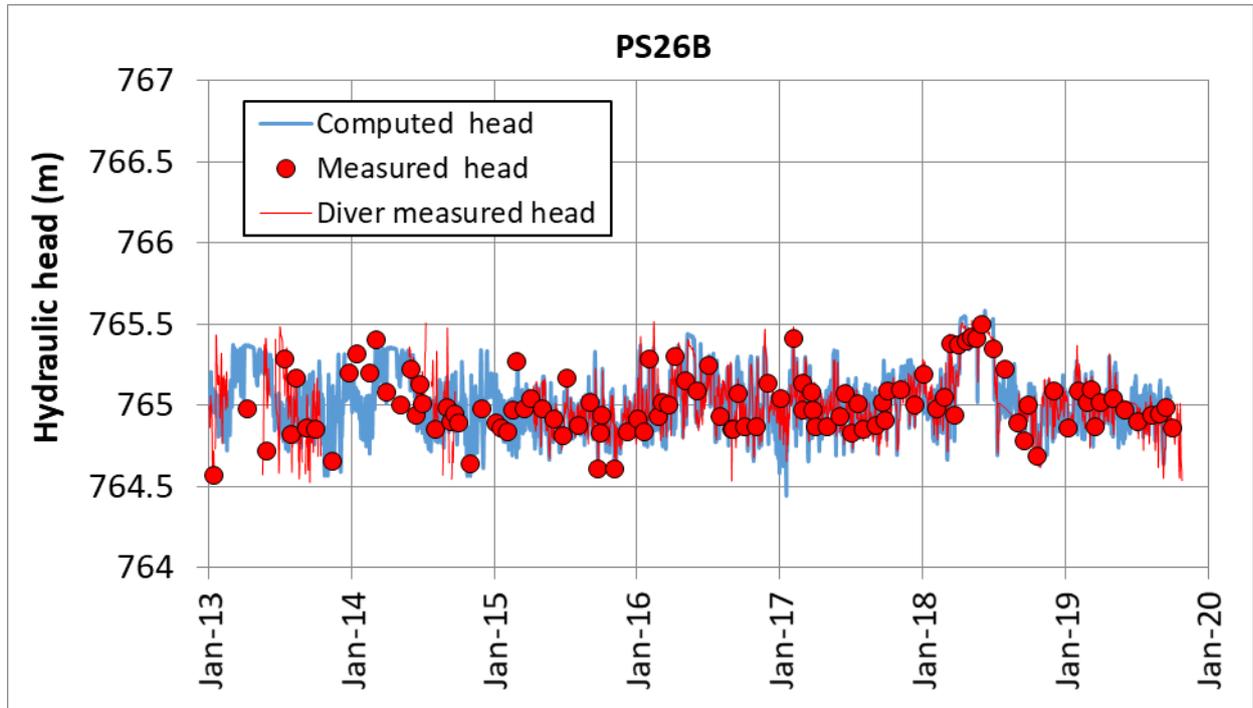
Figure 5.18. Measured hydraulic heads with hydro-level probe (symbols), measured heads with diver (red line) and computed hydraulic heads (blue line) in the PS26B borehole.
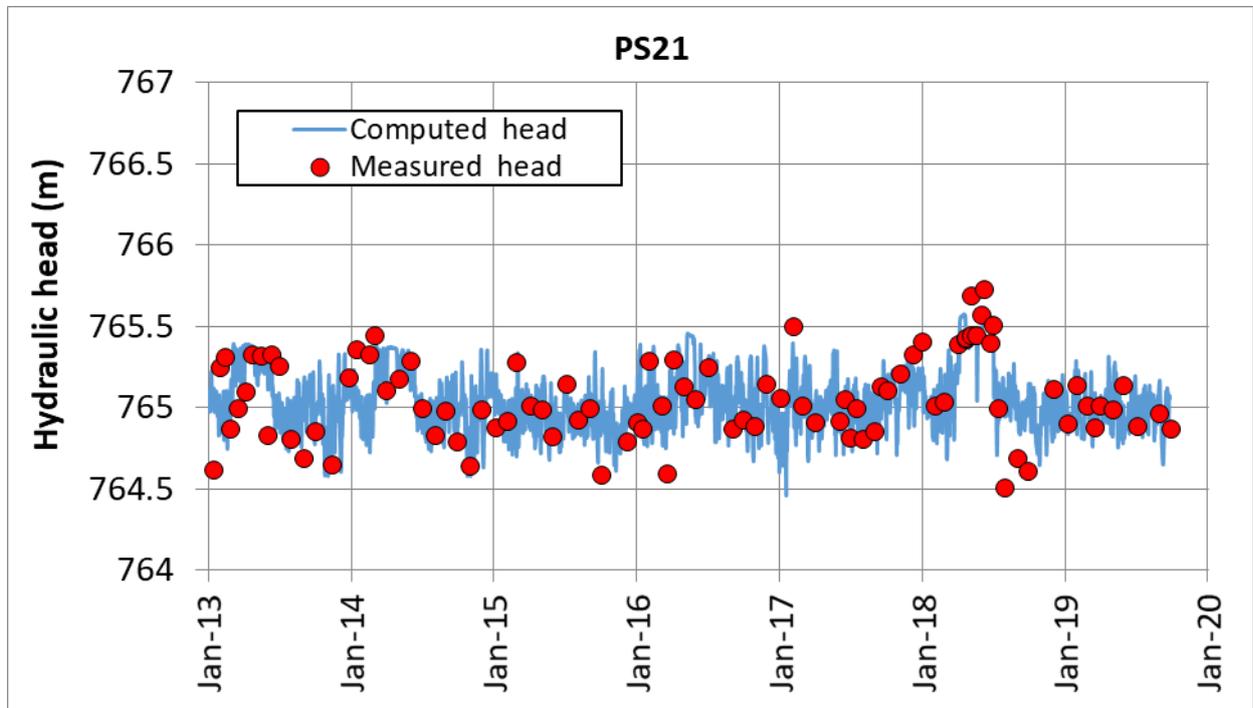
Figure 5.19. Measured hydraulic heads with hydro-level probe (symbols), measured heads with diver (red line) and computed hydraulic heads (blue line) in the PS21 borehole.
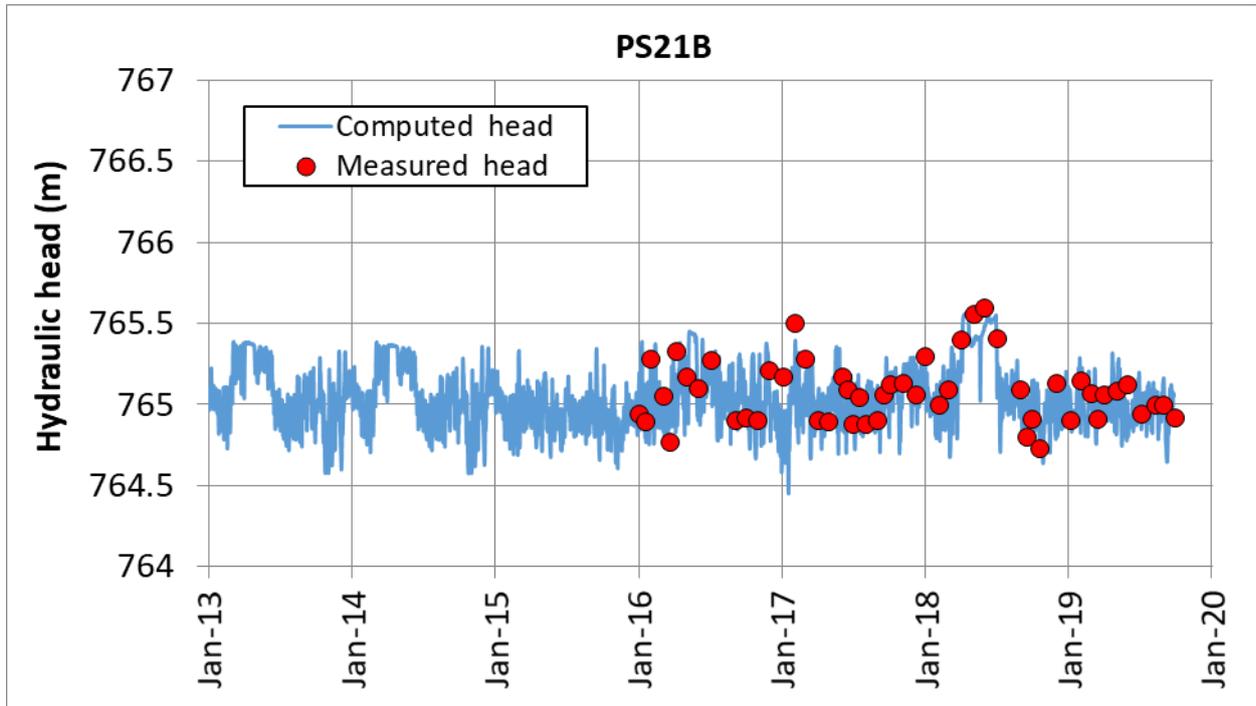
Figure 5.20. Measured hydraulic heads with hydro-level probe (symbols) and computed hydraulic heads (blue line) in the PS21B borehole.
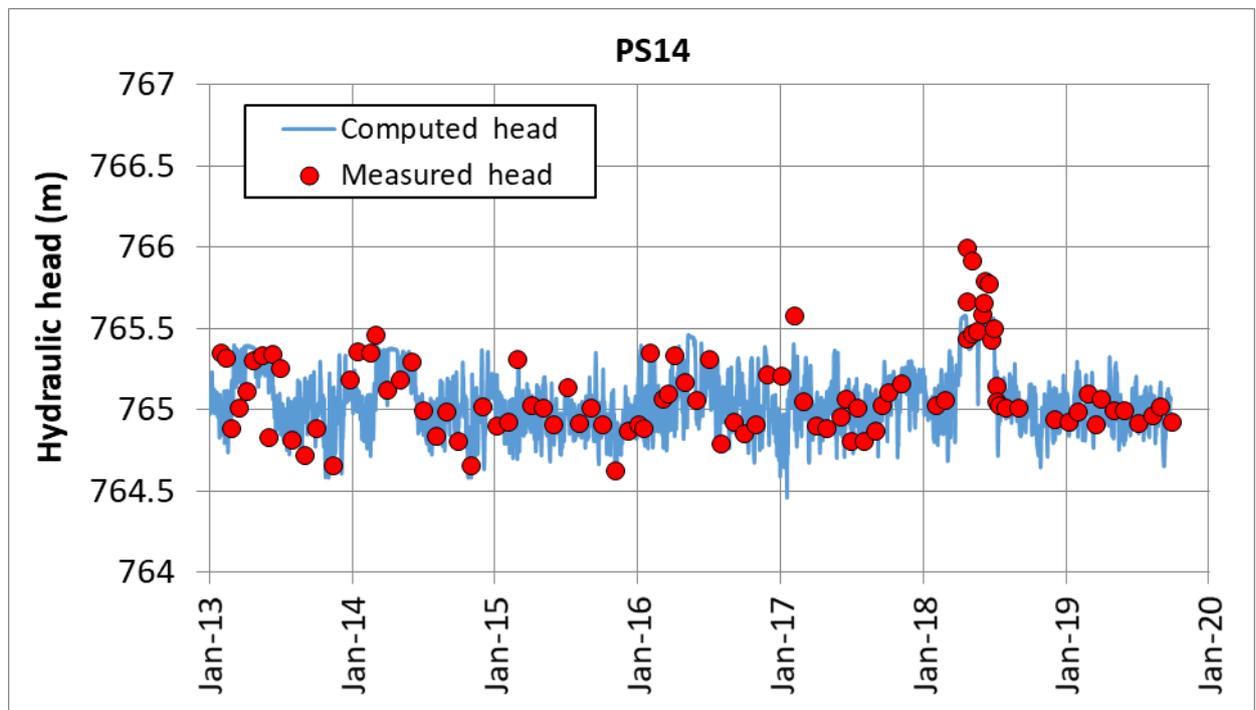
Figure 5.21. Measured hydraulic heads with hydro-level probe (symbols) and computed hydraulic heads (blue line) in the PS14 borehole.
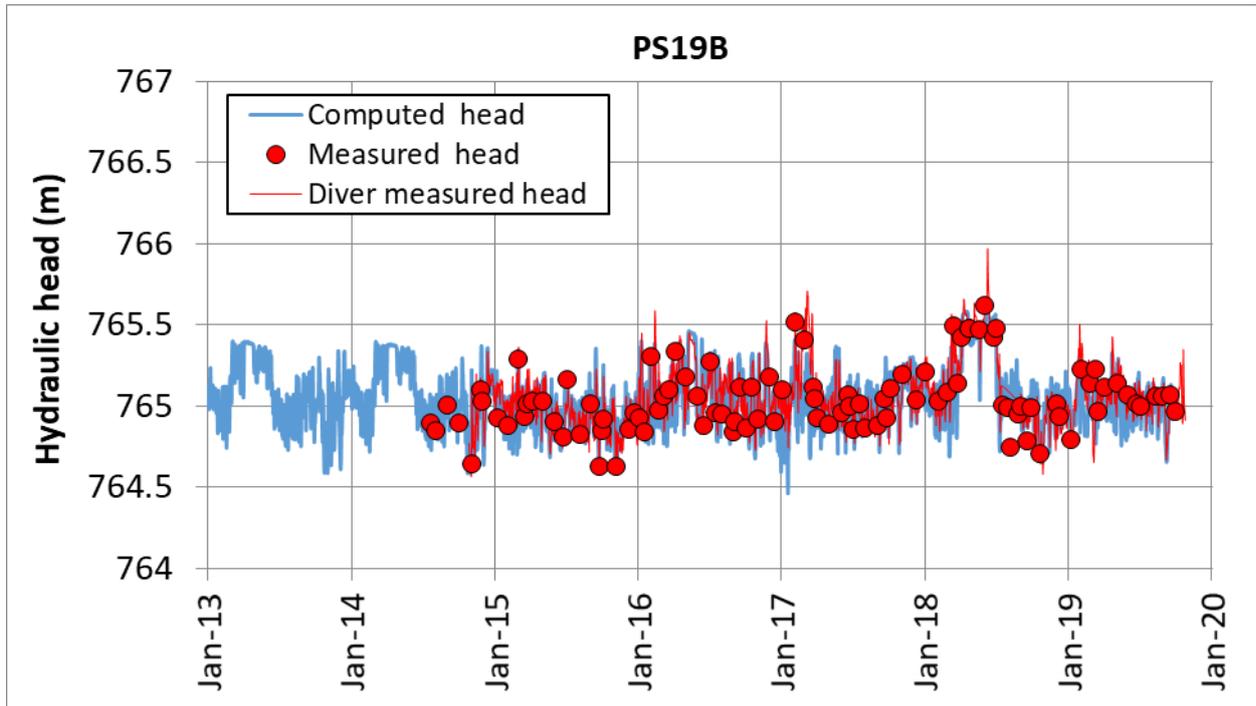
Figure 5.22. Measured hydraulic heads with hydro-level probe (symbols), measured heads with diver (red line) and computed hydraulic heads (blue line) in the PS19B borehole.
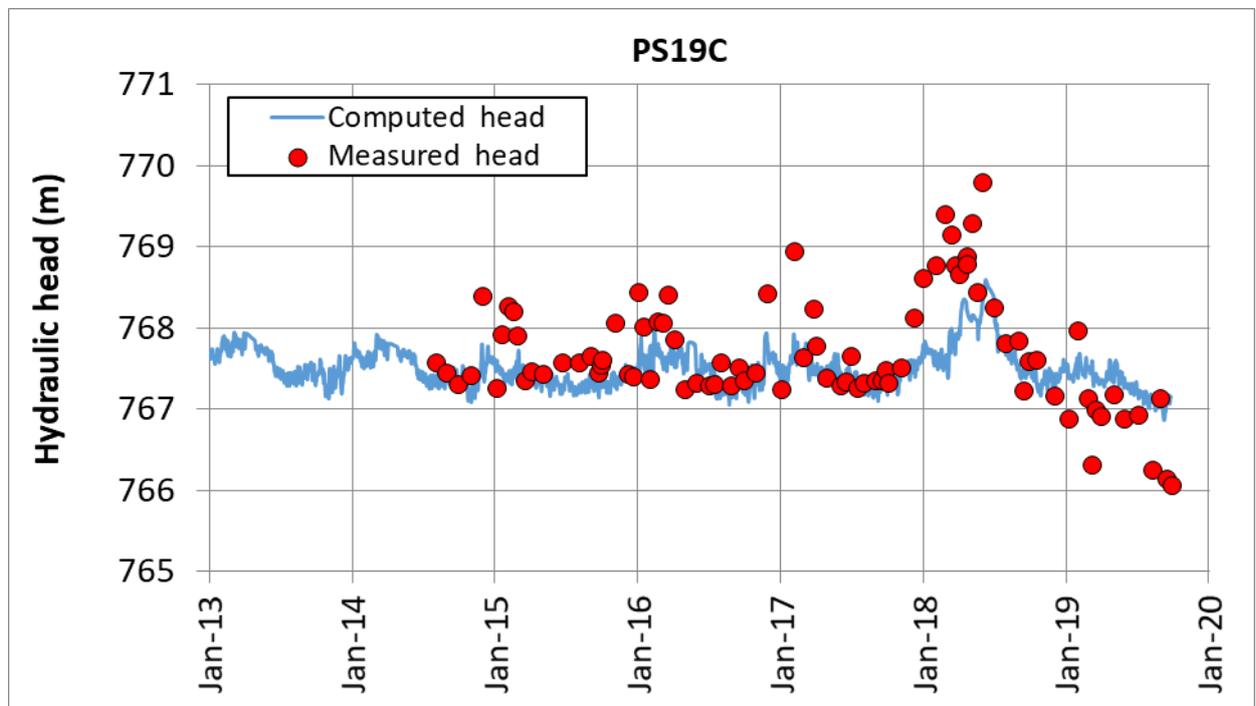
Figure 5.23. Measured hydraulic heads with hydro-level probe (symbols), measured heads with diver (red line) and computed hydraulic heads (blue line) in the PS19C borehole.
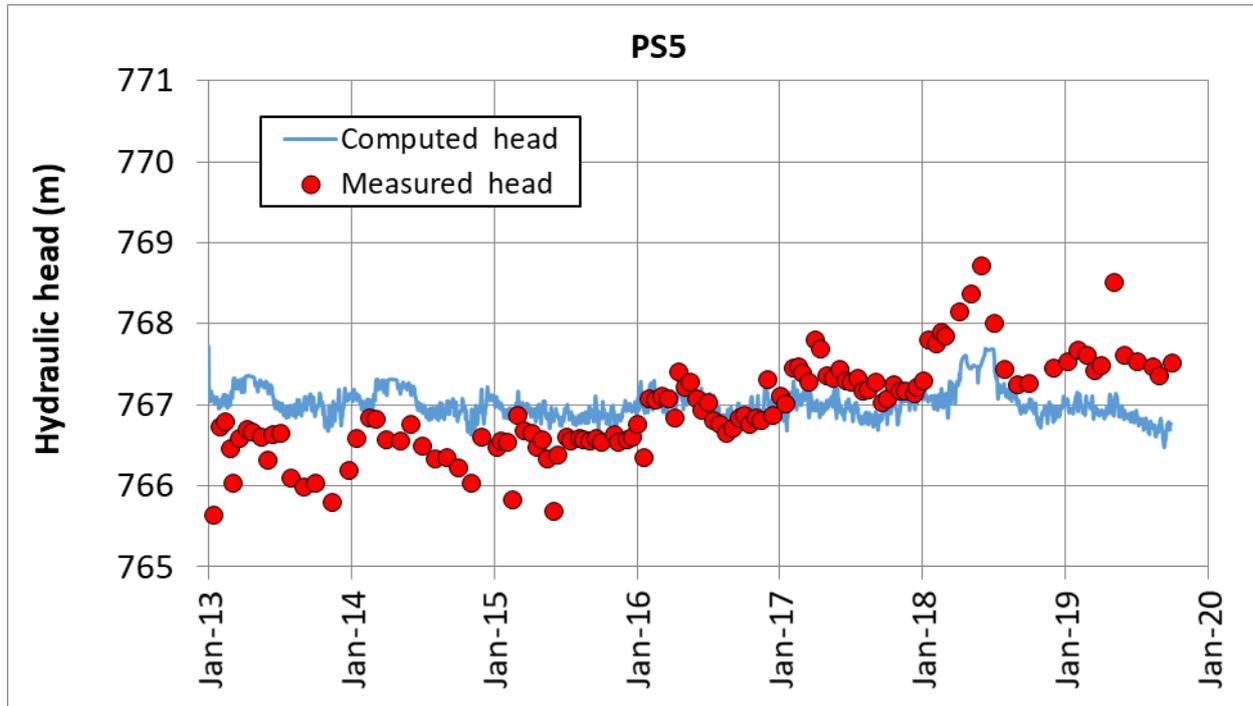
Figure 5.24. Measured hydraulic heads with hydro-level probe (symbols), measured heads with diver (red line) and computed hydraulic heads (blue line) in the PS5 borehole.
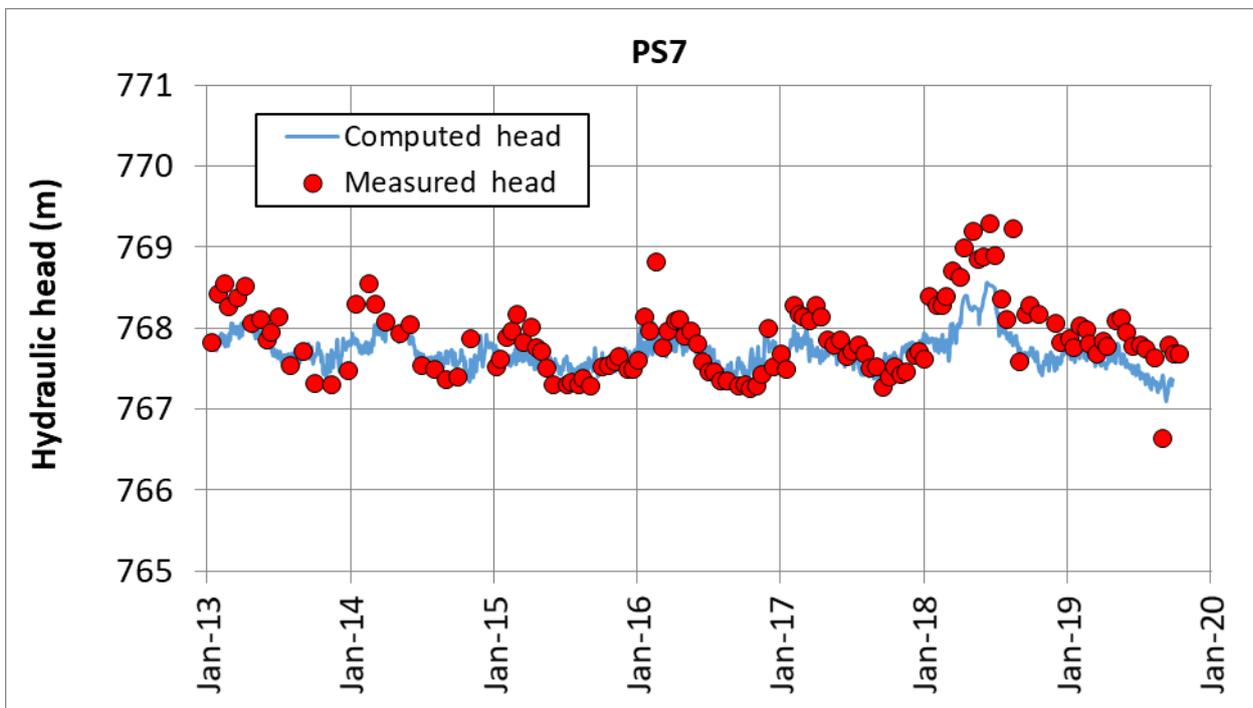
Figure 5.25. Measured hydraulic heads with hydro-level probe (symbols), measured heads with diver (red line) and computed hydraulic heads (blue line) in the PS7 borehole.
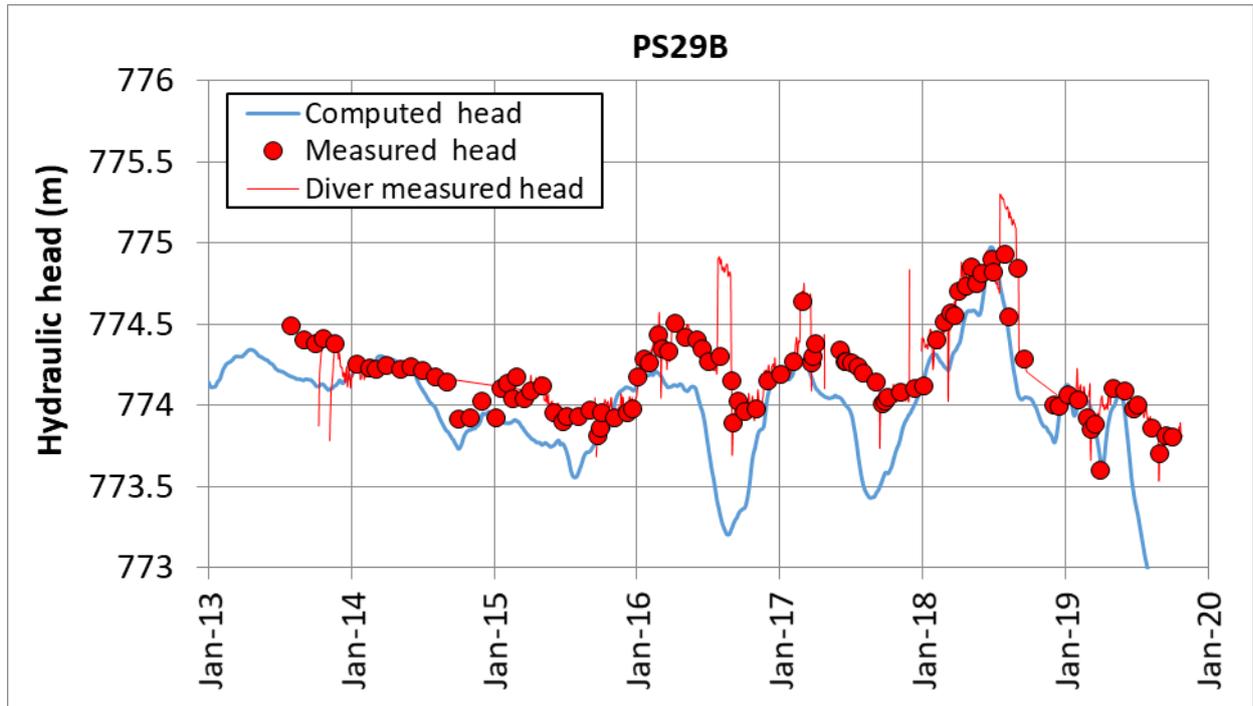
Figure 5.26. Measured hydraulic heads with hydro-level probe (symbols), measured heads with diver (red line) and computed hydraulic heads (blue line) in the P29B borehole.
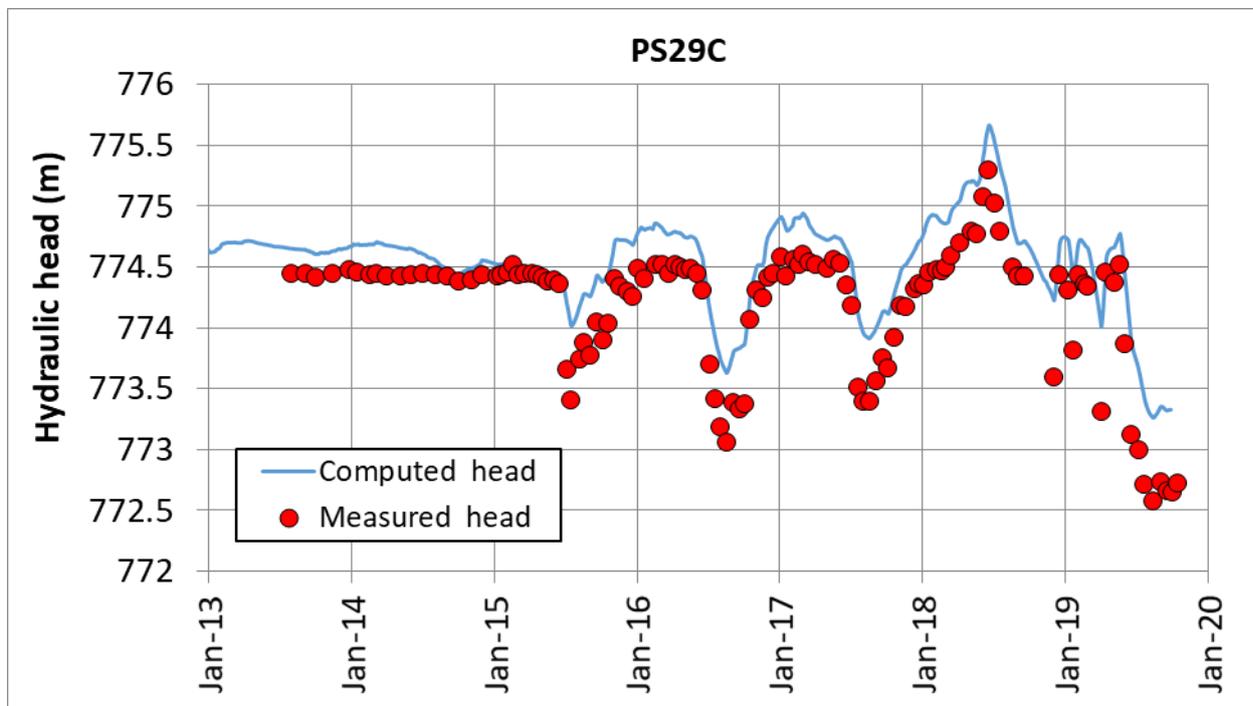
Figure 5.27. Measured hydraulic heads with hydro-level probe (symbols), measured heads with diver (red line) and computed hydraulic heads (blue line) in the PS29C borehole.
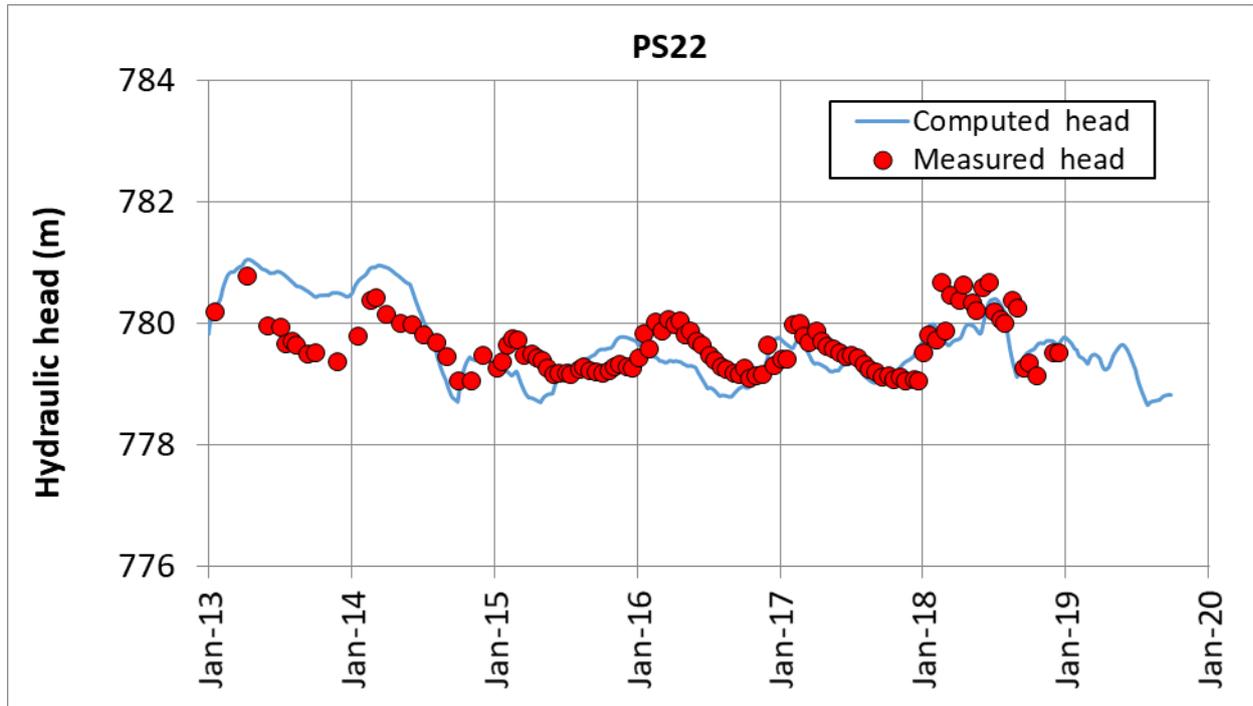
Figure 5.28. Measured hydraulic heads with hydro-level probe (symbols), measured heads with diver (red line) and computed hydraulic heads (blue line) in the PS22 borehole.
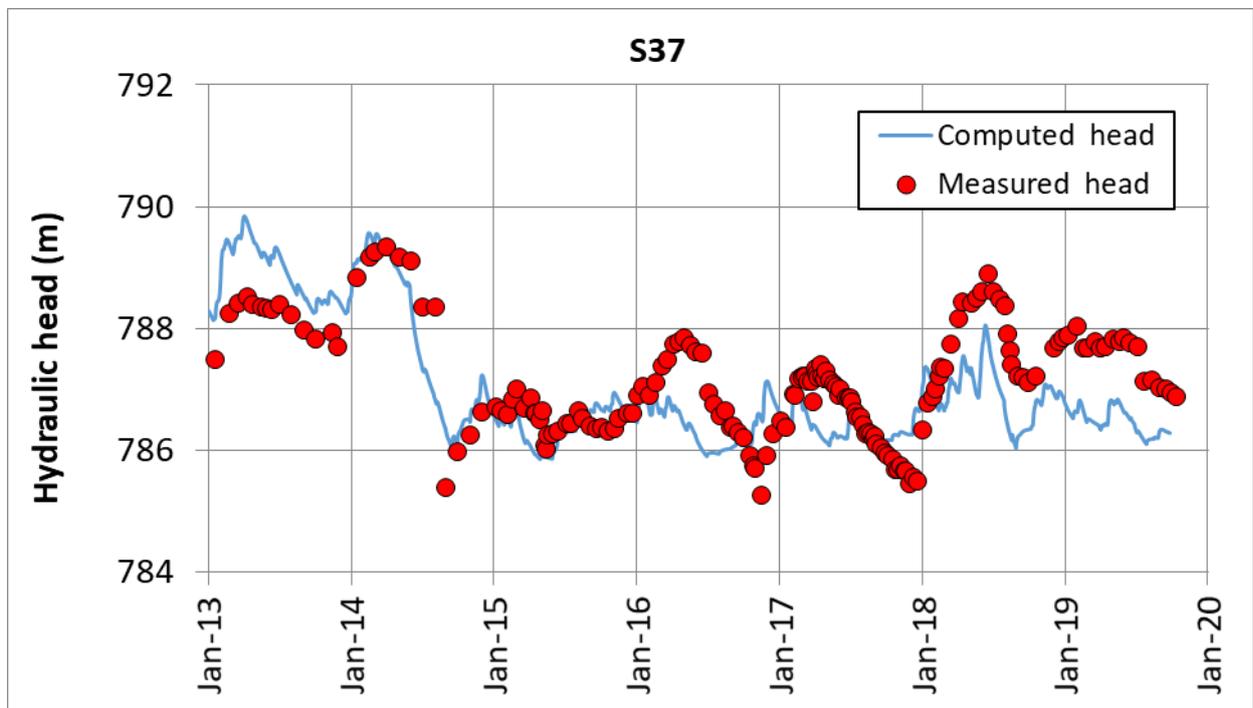
Figure 5.29. Measured hydraulic heads with hydro-level probe (symbols), measured heads with diver (red line) and computed hydraulic heads (blue line) in the S37 borehole.
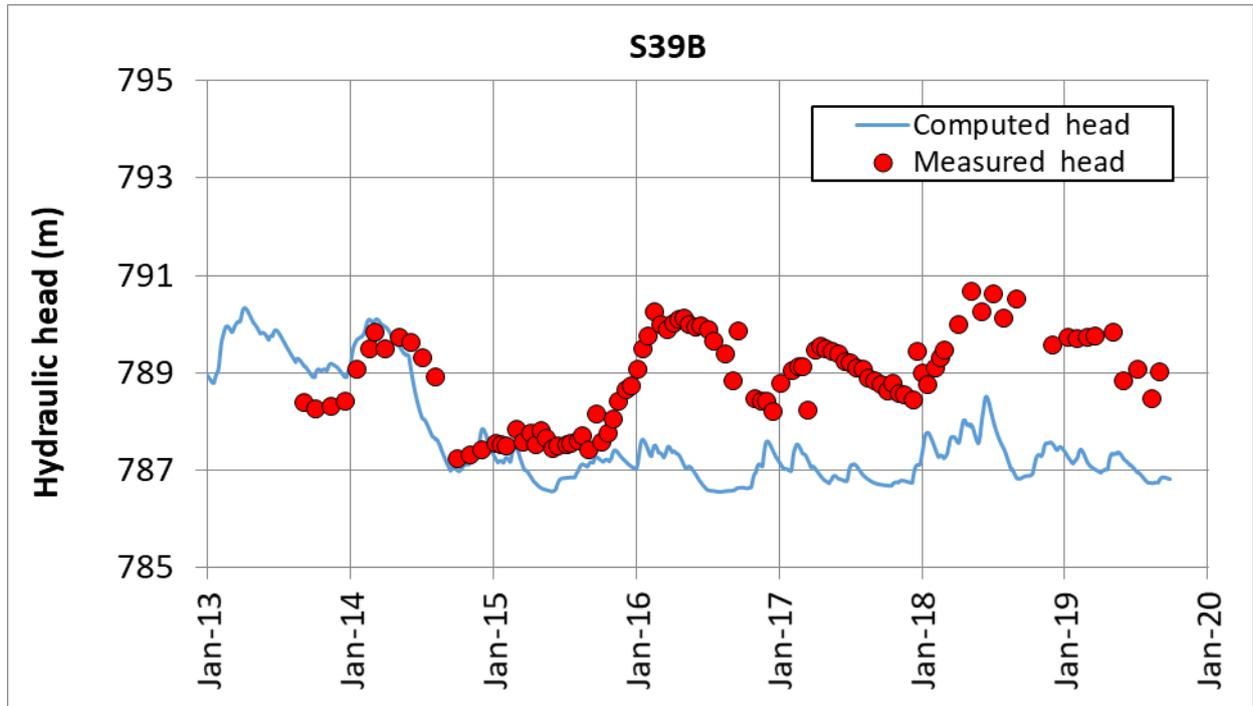
Figure 5.30.   Measured hydraulic heads with hydro-level probe (symbols), measured heads with diver (red line) and computed hydraulic heads (blue line) in the S39B borehole.
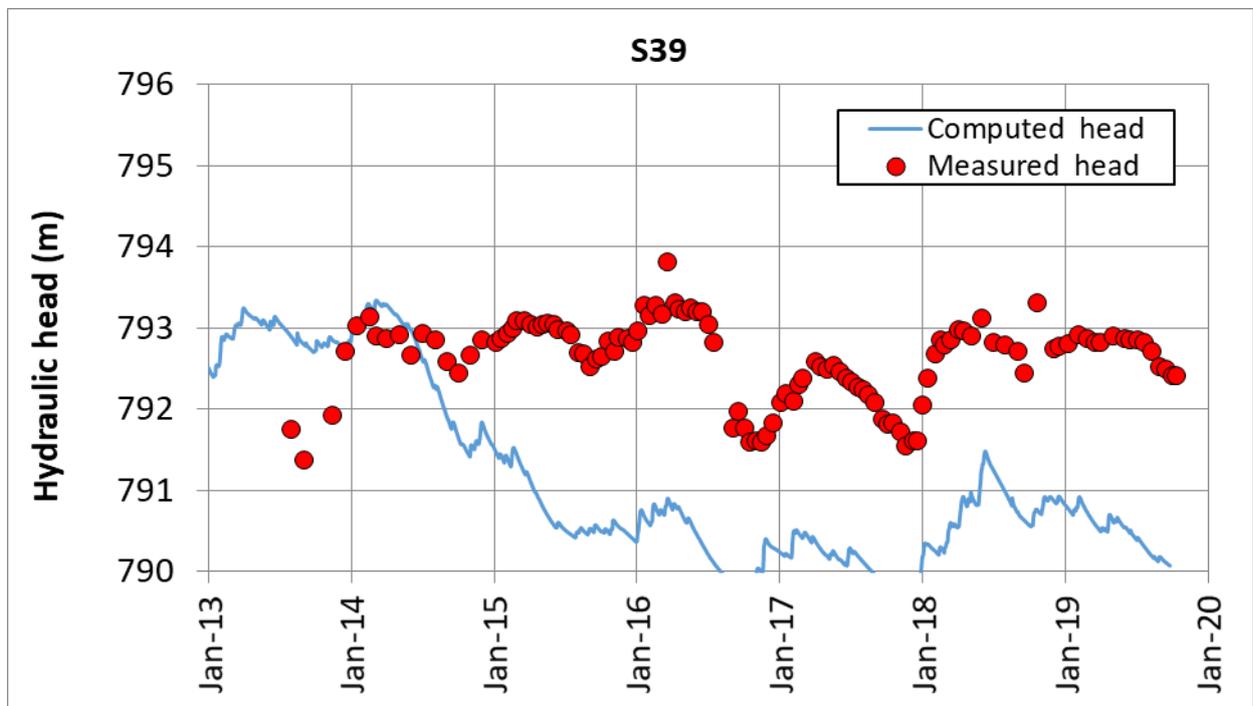
Figure 5.31.   Measured hydraulic heads with hydro-level probe (symbols), measured heads with diver (red line) and computed hydraulic heads (blue line) in the S39 borehole.
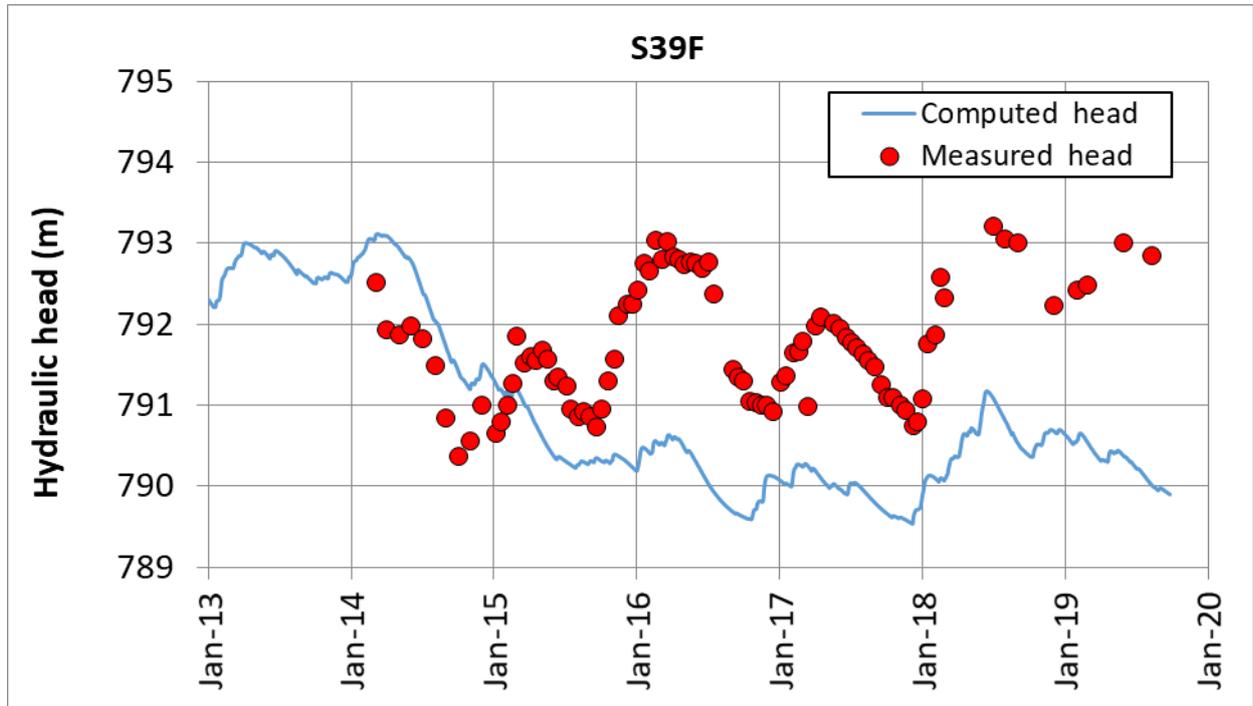
Figure 5.32. Measured hydraulic heads with hydro-level probe (symbols), measured heads with diver (red line) and computed hydraulic heads (blue line) in the S39F borehole.
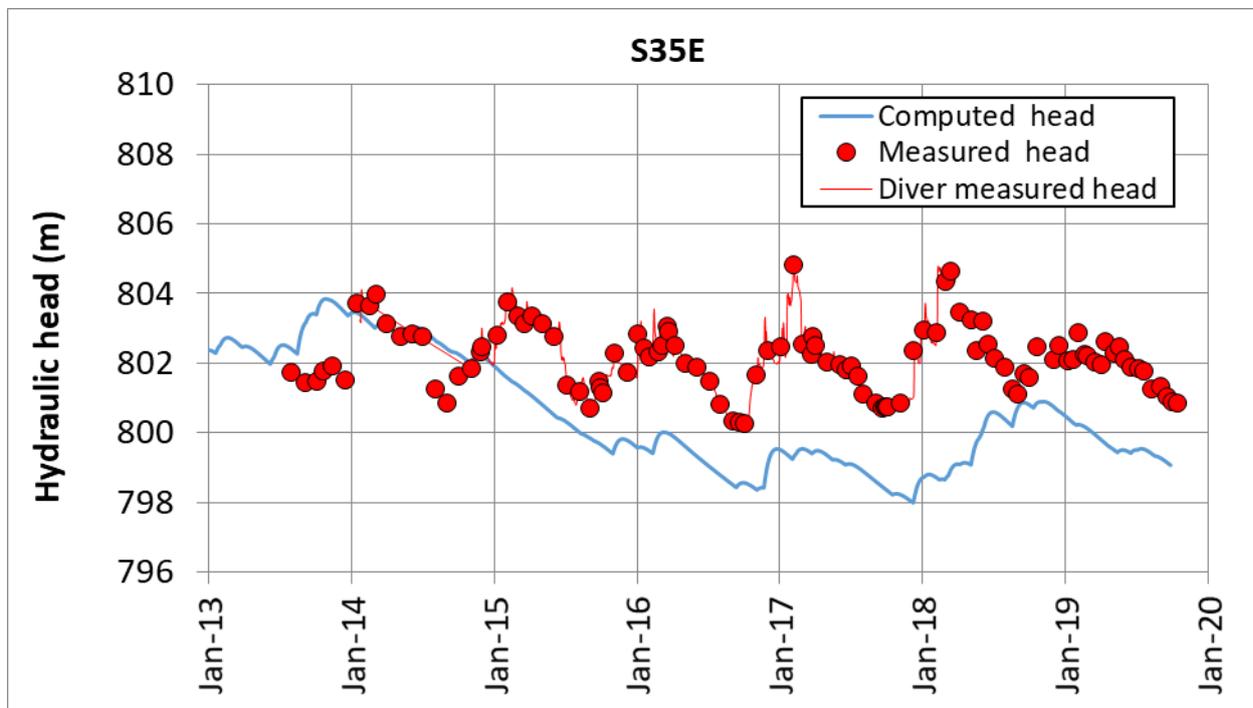
Figure 5.33. Measured hydraulic heads with hydro-level probe (symbols), measured heads with diver (red line) and computed hydraulic heads (blue line) in the S35E borehole.

The computed hydrographs in boreholes located in the alluvial gravels show fluctuations similar to those measured in the water level of the reservoir with a slight offset and damping. The boreholes showing this behaviour include (in order of increasing distances from the reservoir): PS26, PS26B, PS21, PS21B, PS14 and PS19B. In general, the model reproduces the magnitude of the hydraulic head fluctuations.

The measured hydraulic heads in the PS5 borehole follow an increasing trend with periodic drops, which could be due to the pumping carried out in the boreholes twice a year, in May and September, as part of the site remediation tasks. To analyse the evolution of the hydraulic heads area,

The computed hydraulic heads around PS29 borehole are influenced by the fixed hydraulic head in that area. The measured hydraulic heads show oscillations that are not reproduced by the computed heads.

The differences between measured heads downstream and upstream the bentonite wall is properly simulated.

The analysis of the computed hydraulic heads in the S39 boreholes shows that there are two different periods. The first period is from the start of the simulation on 1st January 2013 to November 2015. The second period is from November 2015 to the end of the simulation on 30th September 2019. The model reproduces the measured hydraulic heads from 2013 to 2014 in boreholes S39B and S39F. Measured head in S39 borehole presents a different time evolution until January 2016. The model underestimates hydraulic heads from January 2016 in all the three boreholes.

Figure 5.34 to Figure 5.41 show the measured and computed hydraulic heads with the bimonthly transient-state model in the selected boreholes.

Upstream the front slurry-wall, the computed hydraulic heads show significant deviations from the measured heads, with residuals larger than 2 m (the results are not shown). These errors are possibly since the initial conditions adopted may not be suitable.

The calculated hydrographs in the PS26, PS26B, PS21, PS21B, PS14 and PS19B boreholes located in the alluvial are influenced by the changes in the water level of the Sabiñánigo reservoir. The computed hydraulic heads reproduce the fluctuations of the measured hydraulic head using divers although in a smoother way.

The model does not reproduce entirely the oscillations measured in the PS19C borehole, which records the heads in the alluvial silts, possibly due to uncertainties in their specific storage coefficient.
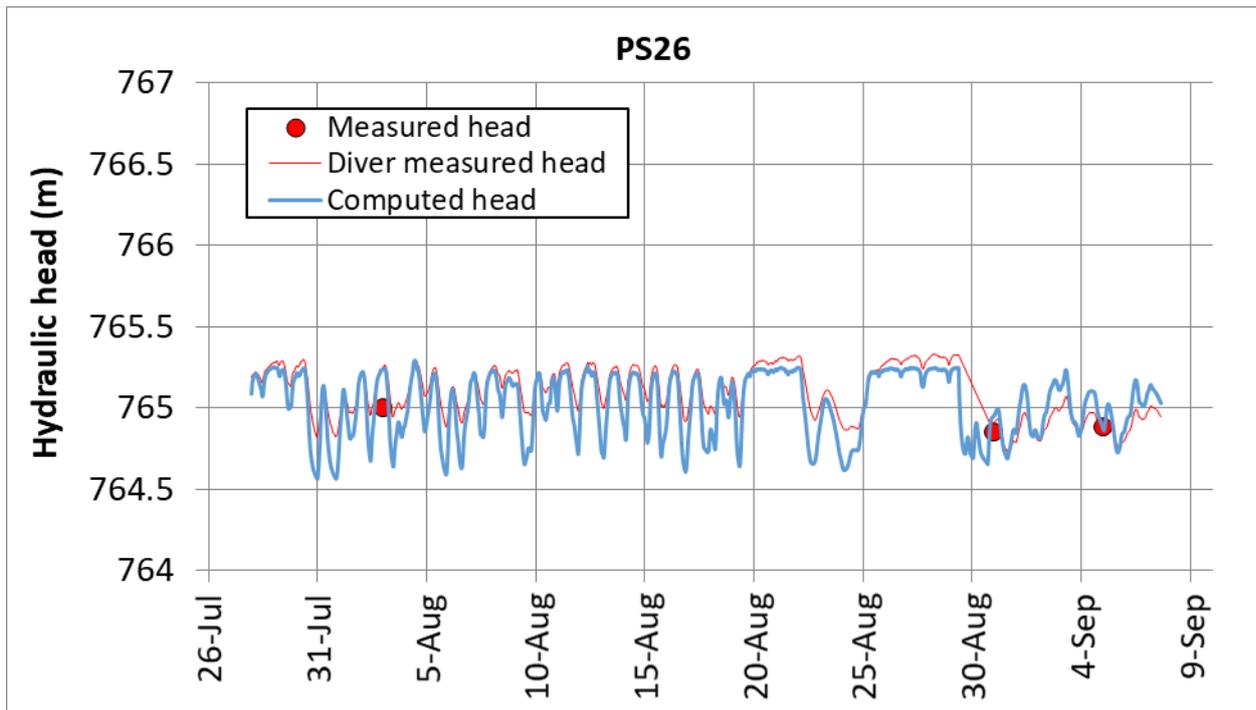
Figure 5.34.   Comparison of manually measured hydraulic heads (red dots) and measured head using a diver (red line) with computed hydraulic heads (blue line) in the PS26 borehole from July to September 2016.
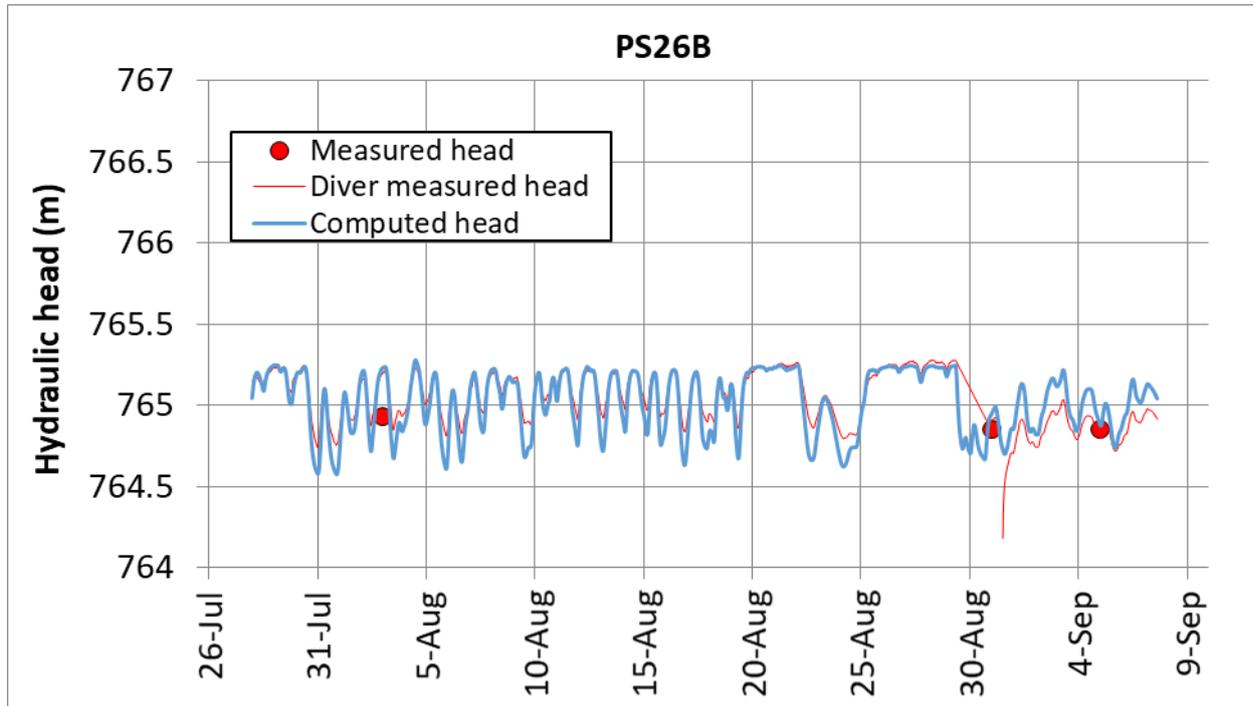
Figure 5.35. Comparison of manually measured hydraulic heads (red dots) and measured head using a diver (red line) with computed hydraulic heads (blue line) in the PS26B borehole from July to September 2016.
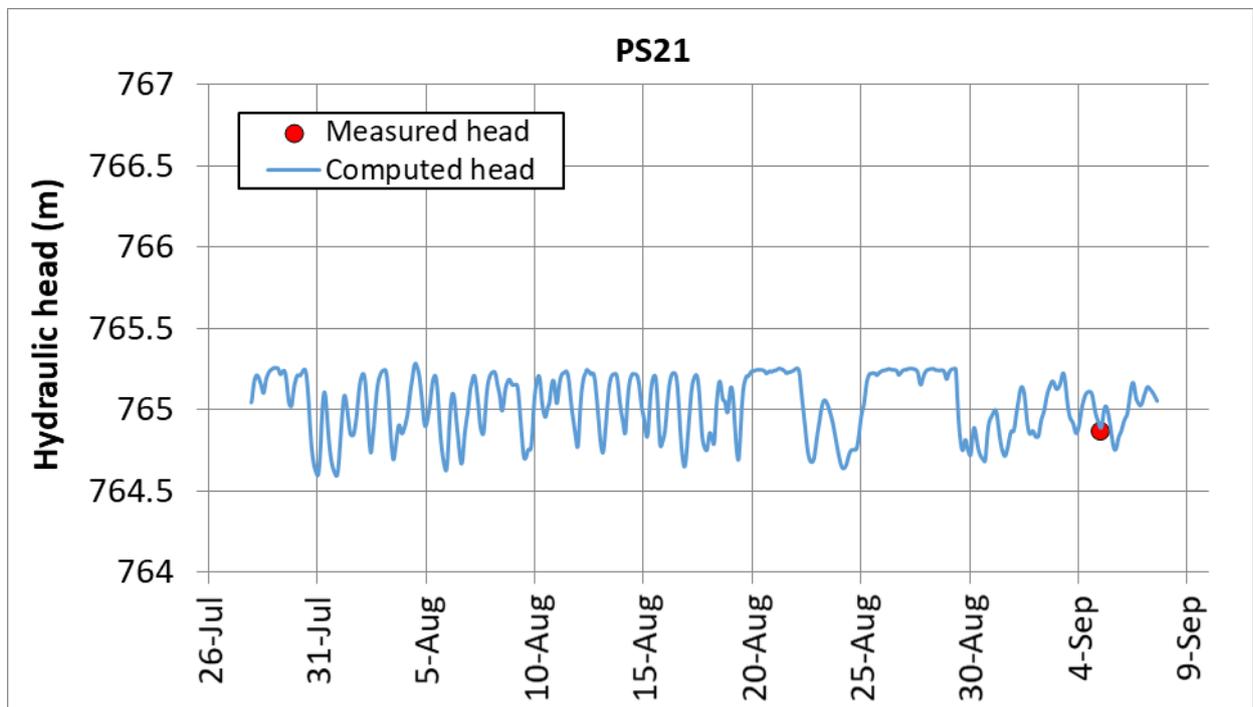
Figure 5.36. Comparison of manually measured hydraulic heads (red dots) and measured head using a diver (red line) with computed hydraulic heads (blue line) in the PS21 borehole from July to September 2016.
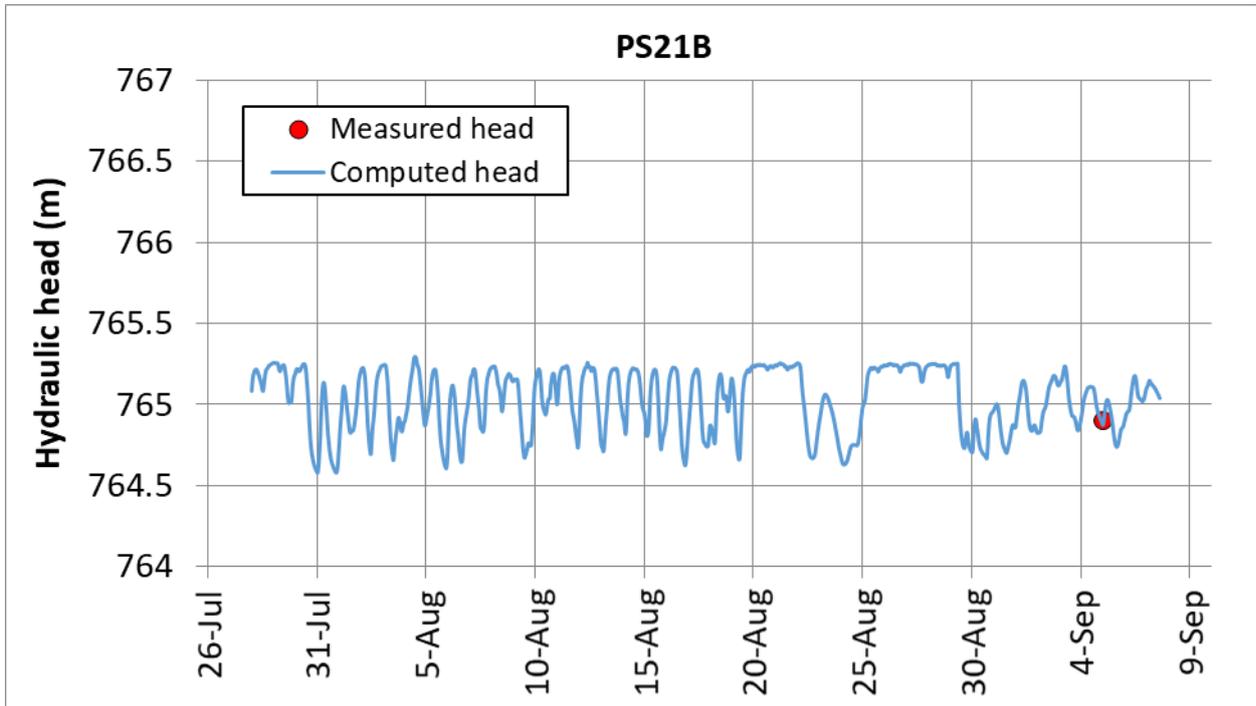
Figure 5.37. Comparison of manually measured hydraulic heads (red dots) and measured head using a diver (red line) with computed hydraulic heads (blue line) in the PS21B borehole from July to September 2016.
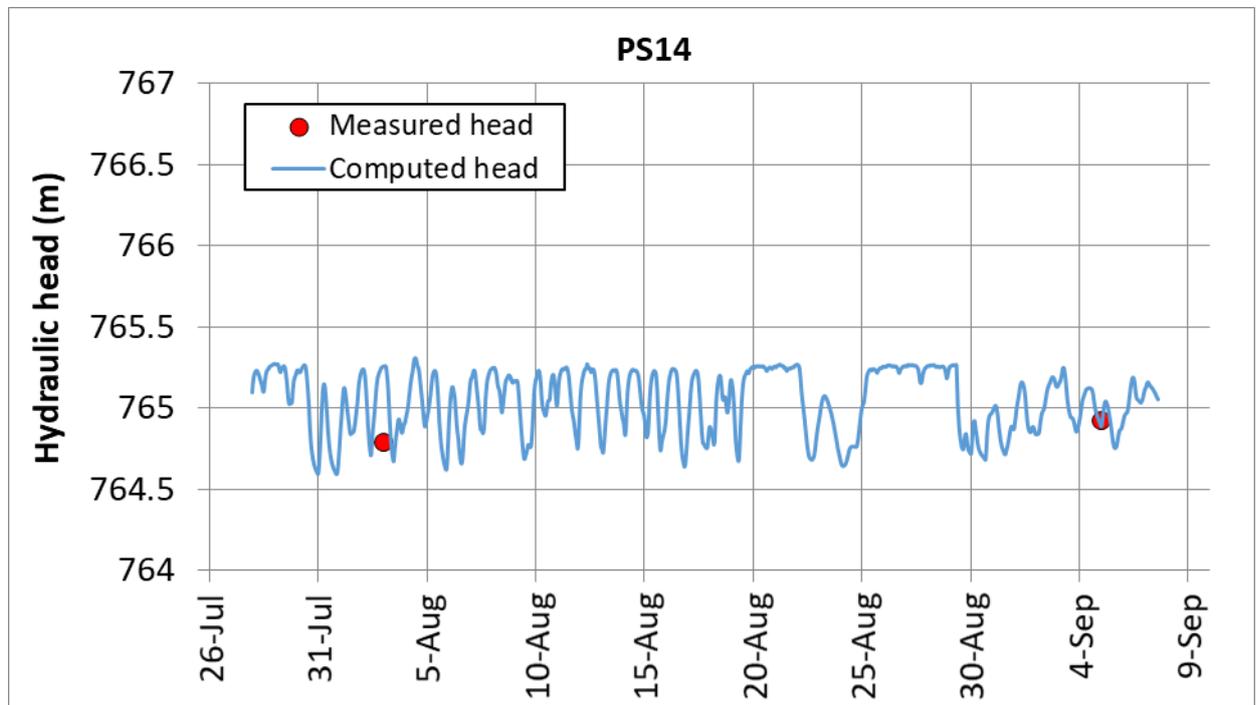
Figure 5.38. Comparison of manually measured hydraulic heads (red dots) and measured head using a diver (red line) with computed hydraulic heads (blue line) in the PS14 borehole from July to September 2016.
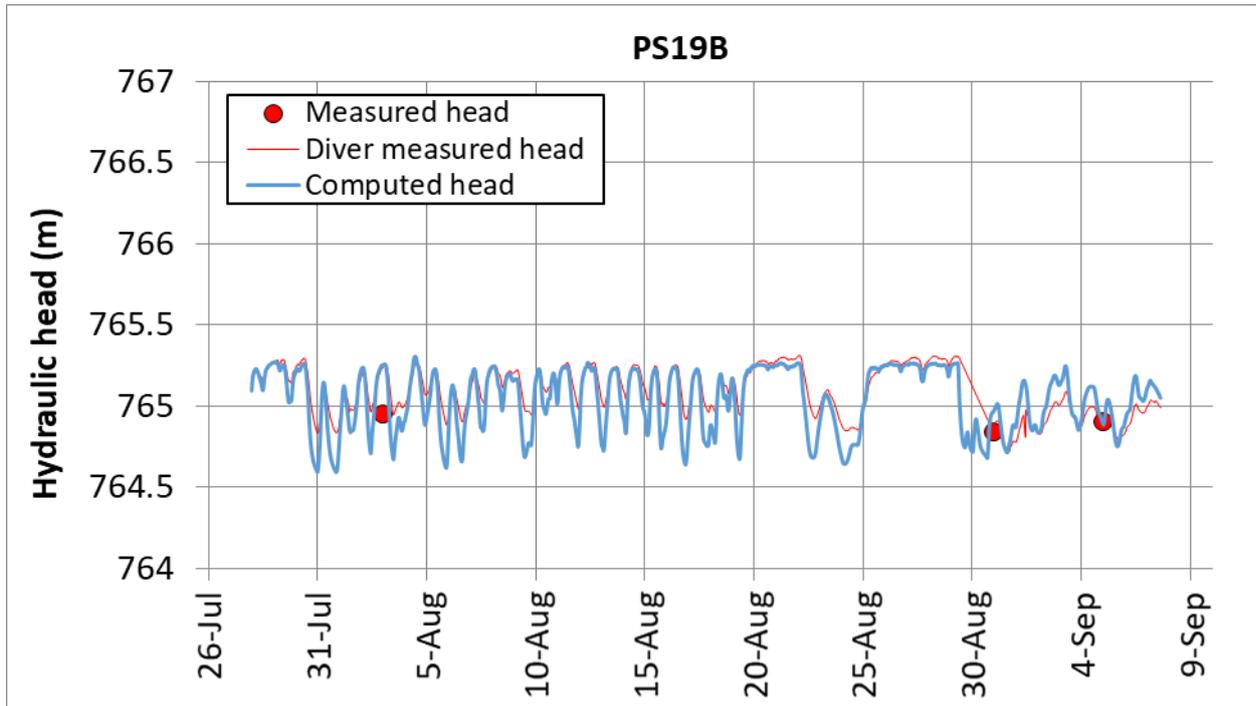
Figure 5.39. Comparison of manually measured hydraulic heads (red dots) and measured head using a diver (red line) with computed hydraulic heads (blue line) in the PS19B from July to September 2016.
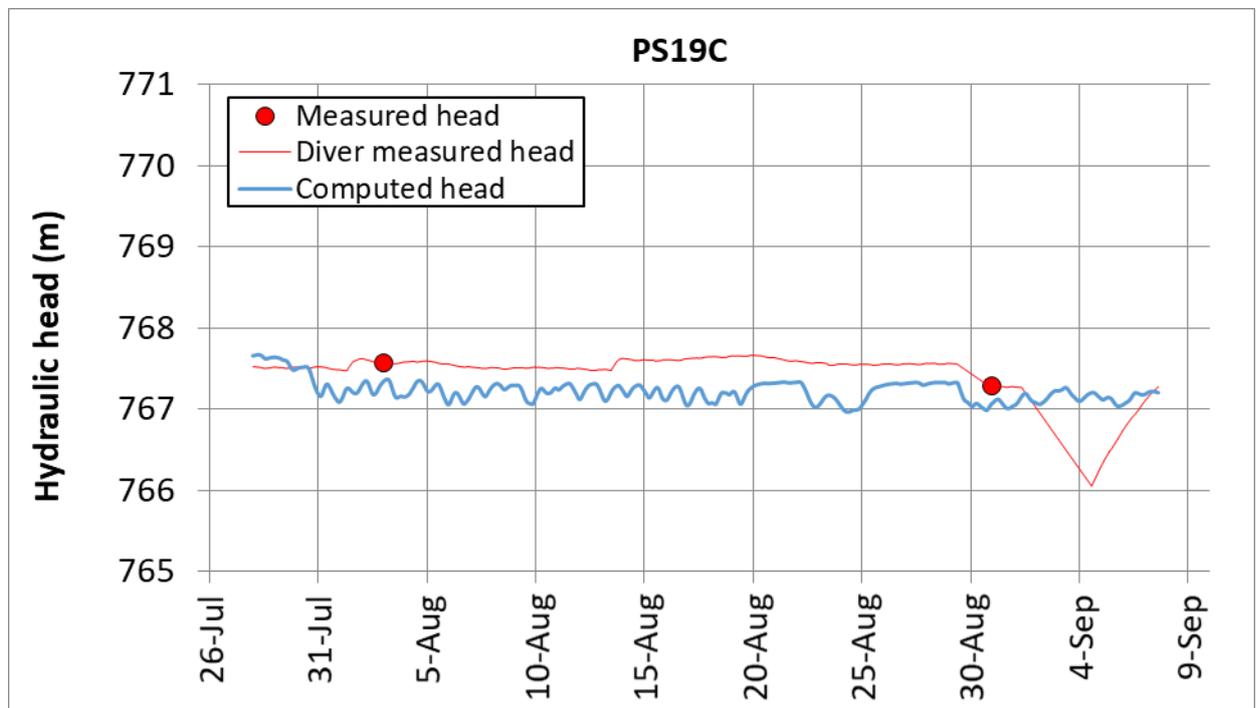
Figure 5.40. Comparison of manually measured hydraulic heads (red dots) and measured head using a diver (red line) with computed hydraulic heads (blue line) in the PS19C borehole from July to September 2016.
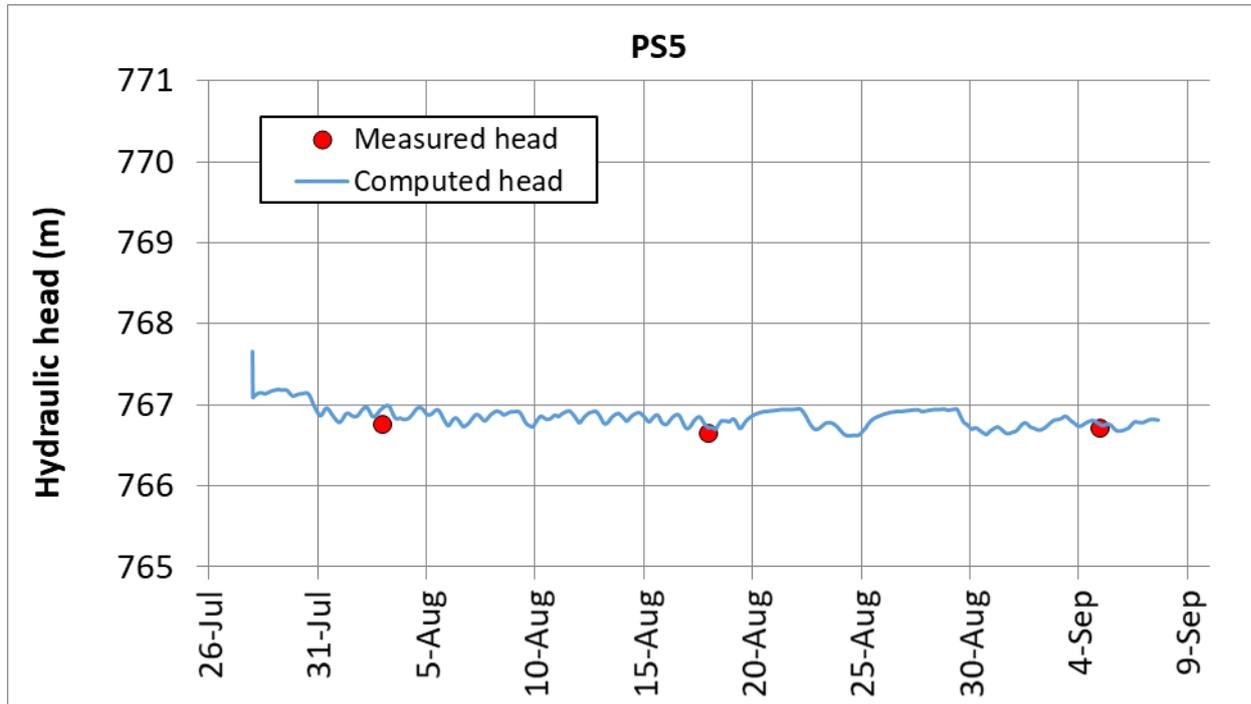
Figure 5.41.   Comparison of manually measured hydraulic heads (red dots) and measured head using a diver (red line) with computed hydraulic heads (blue line) in the PS5 borehole from July to September 2016.

5.3.2   Hydraulic head contours

Figure 5.42 to Figure 5.48 show the hydraulic head contour maps calculated in: July 2013, January 2014, September 2015, March 2016, July 2017, January 2018 and September 2019. These plots illustrate the hydraulic head patterns in different seasons.

The hydraulic head gradient in the alluvial gravels is extremely small because the gravels have a very large hydraulic conductivity and the groundwater flow is small. The measured hydraulic heads in this area are greatly influenced by the oscillations of the water level of the reservoir. The hydraulic gradient in the lower part of the landfill wastes, upstream the front slurry-wall, is also low. There is also a significant drop in the water table from PS22 to PS29 and PS5 boreholes.
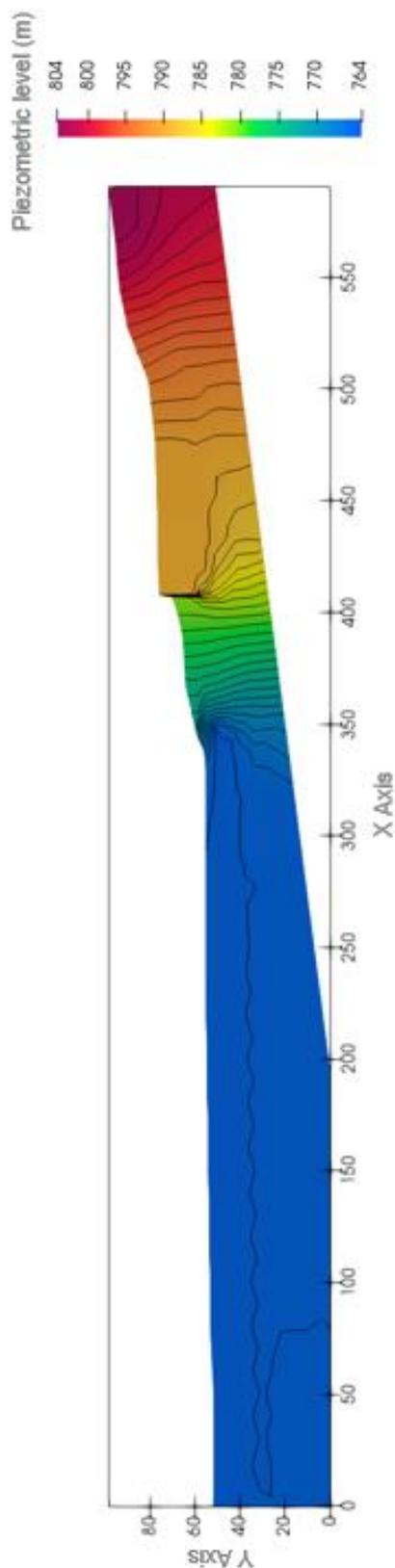
Figure 5.42.   Computed hydraulic head contour map along the vertical profile in July 1st 2013.
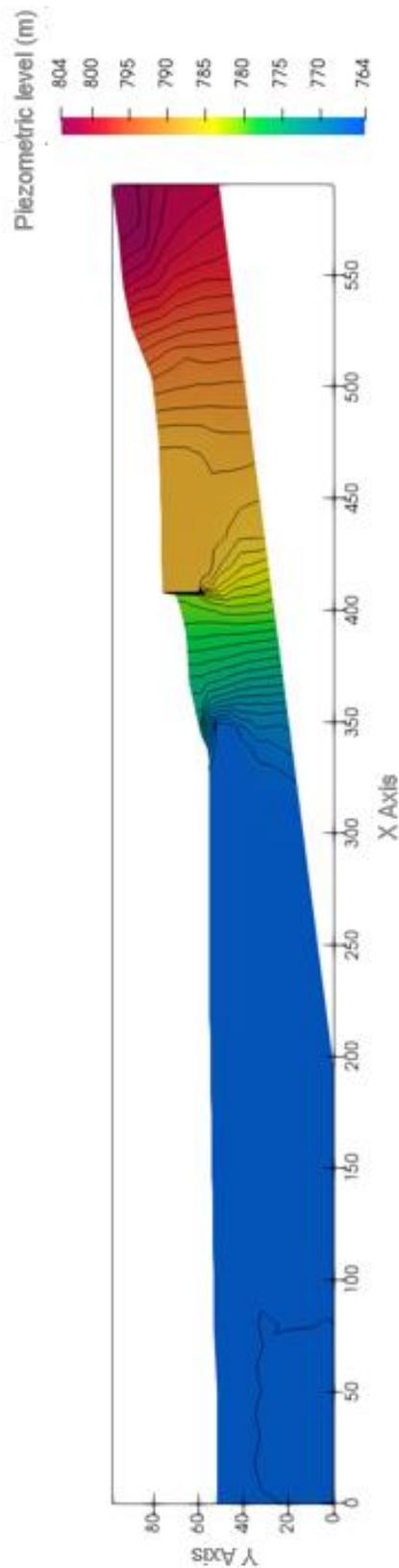
Figure 5.43. Computed hydraulic head contour map along the vertical profile in January 1st 2014.
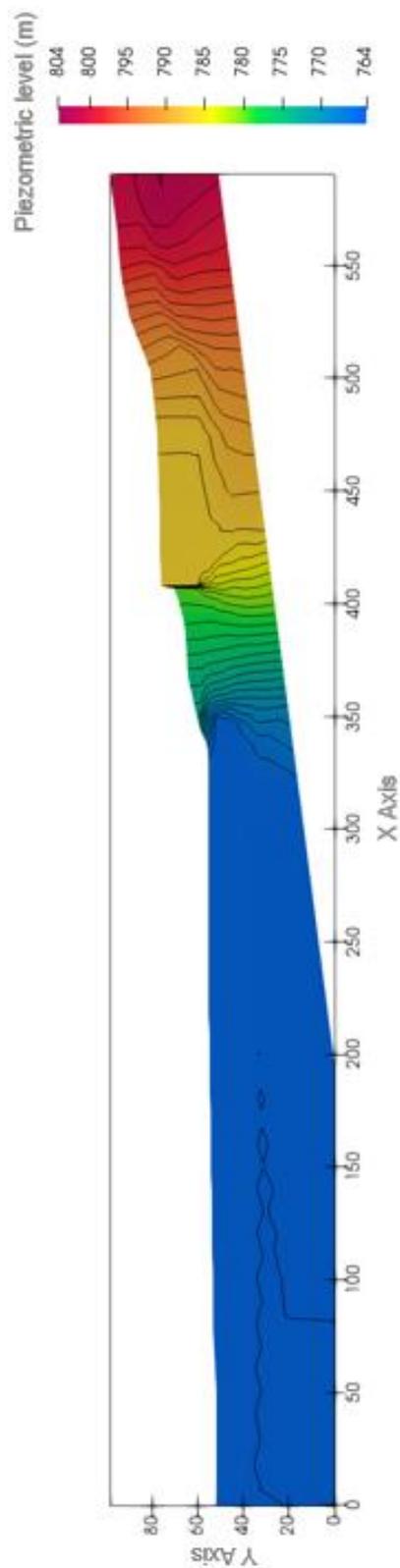
Figure 5.44.   Computed hydraulic head contour map along the vertical profile in September 1st 2015.
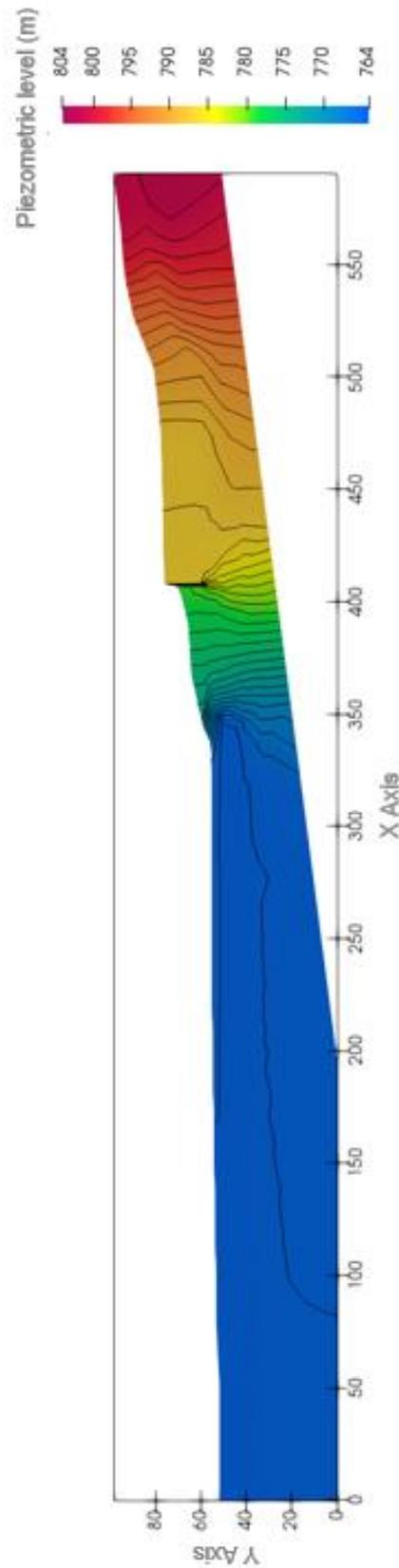
Figure 5.45. Computed hydraulic head contour map along the vertical profile in March 1ˢᵗ 2016.
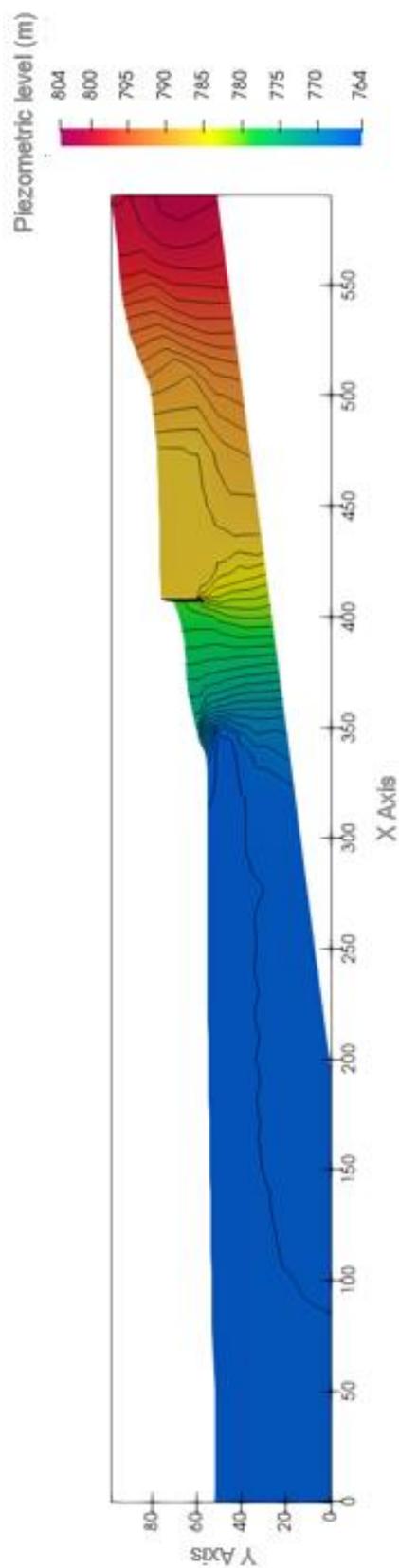
Figure 5.46. Computed hydraulic head contour map along the vertical profile in July 1st 2017.
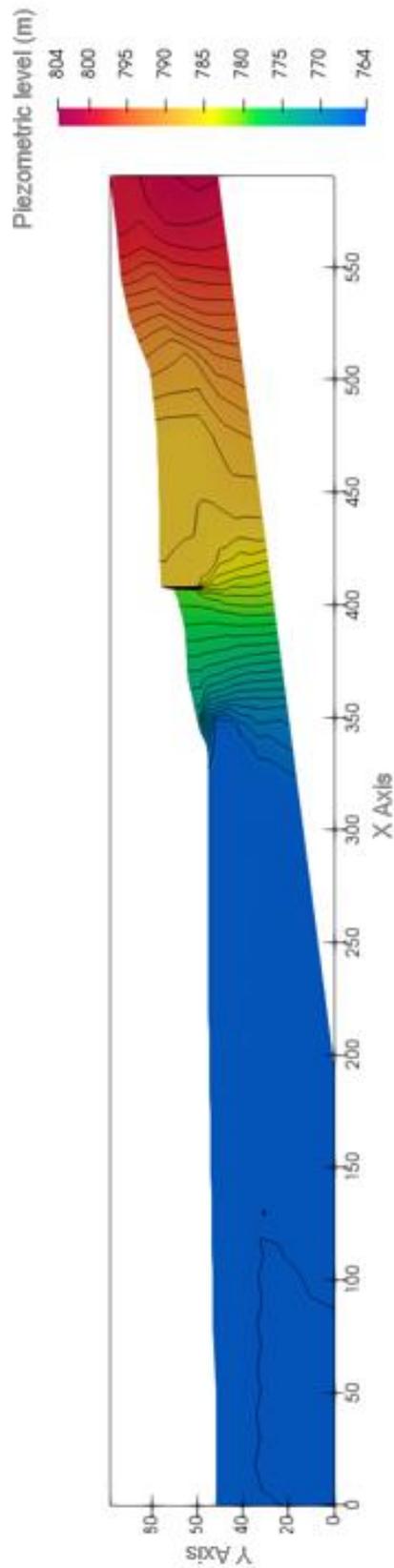
Figure 5.47. Computed hydraulic head contour map along the vertical profile in January 1st 2018.
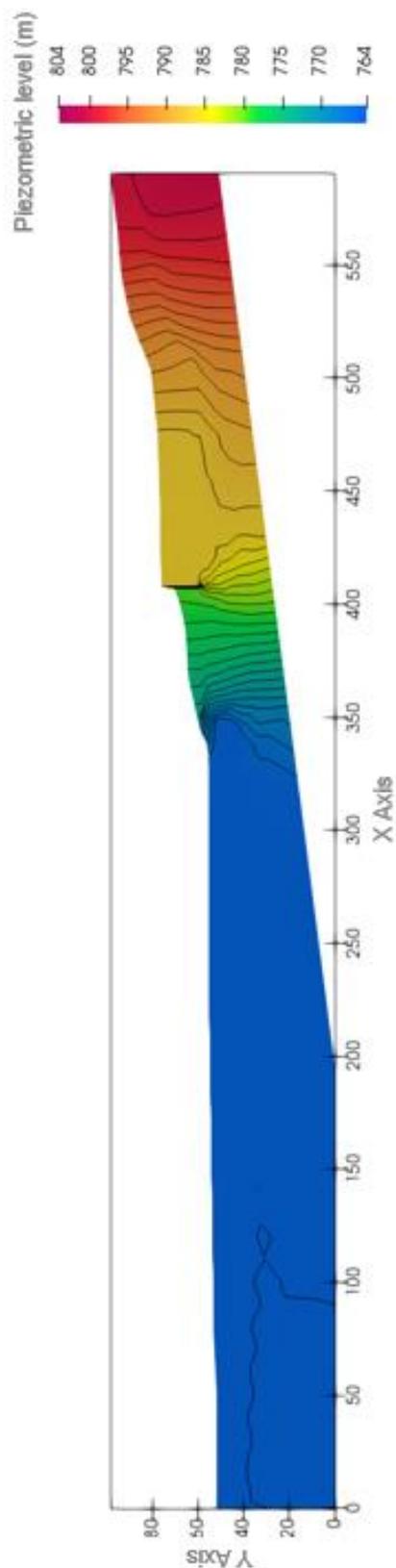
Figure 5.48. Computed hydraulic head contour map along the vertical profile in September 1ˢᵗ 2019.

5.3.3   <u>Computed water table</u>

Figure 5.49 to Figure 5.55 show the water table calculated in July 2013, January 2014, September 2015, March 2016, July 2017, January 2018 and September 2019. These plots are useful to illustrate the changes in the flow pattern in different seasons. After 6 months, in July 2013, the water table in the entire profile rises slightly with respect to the steady-state water table. This rise is due to the increase of the recharge. After 1 year, in January 2014, the water table rises in the area of the ravine. The water table in September 2015 is much lower than the steady state water table. It should be noted that pumping in the S37 borehole began in June 2014. In March and April 2015, a significant flowrate was pumped. The water table in 2016, 2017, 2018 and 2019 show similar trends.
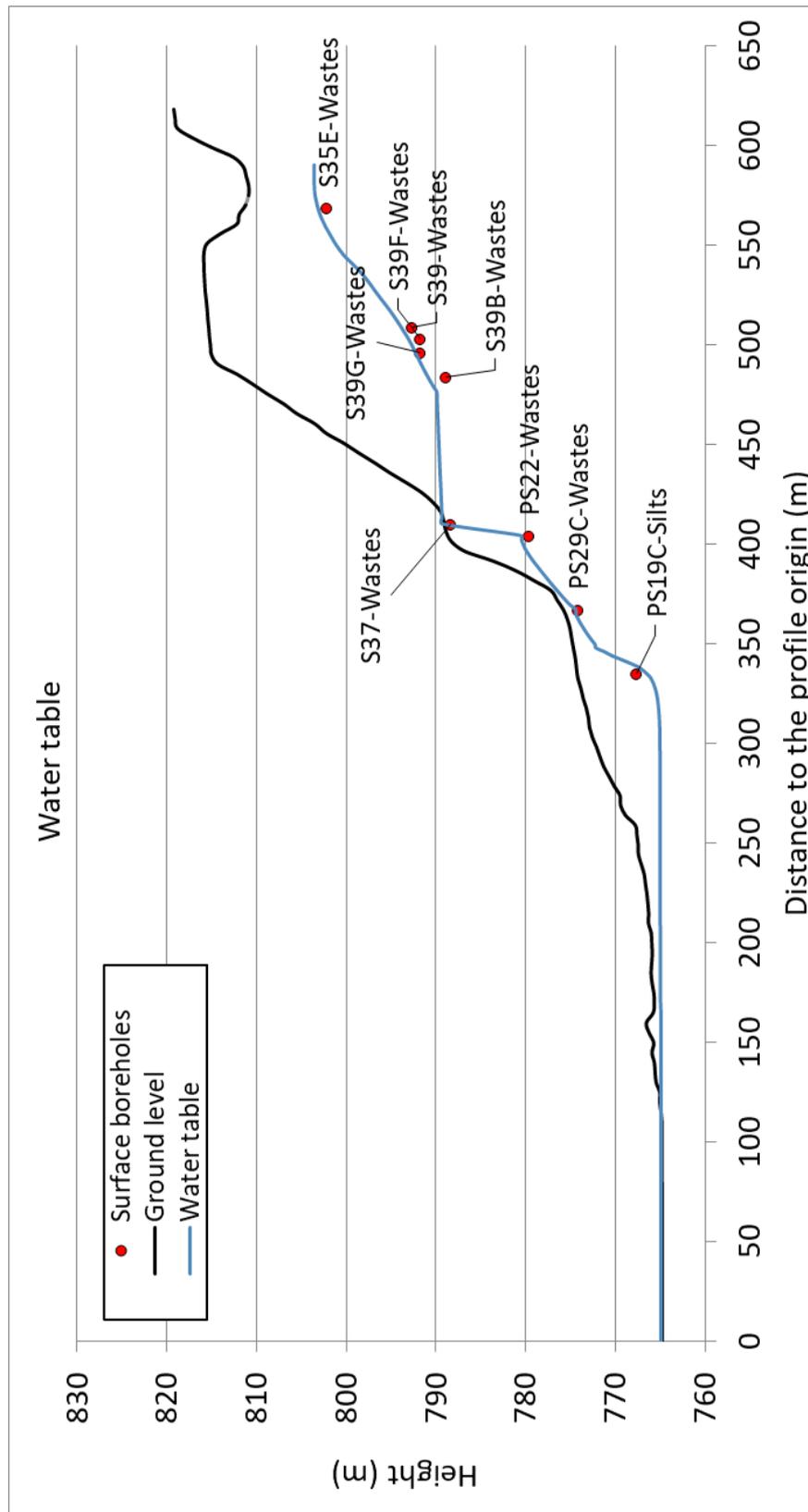
Figure 5.49. Computed water table in July 1st 2013.
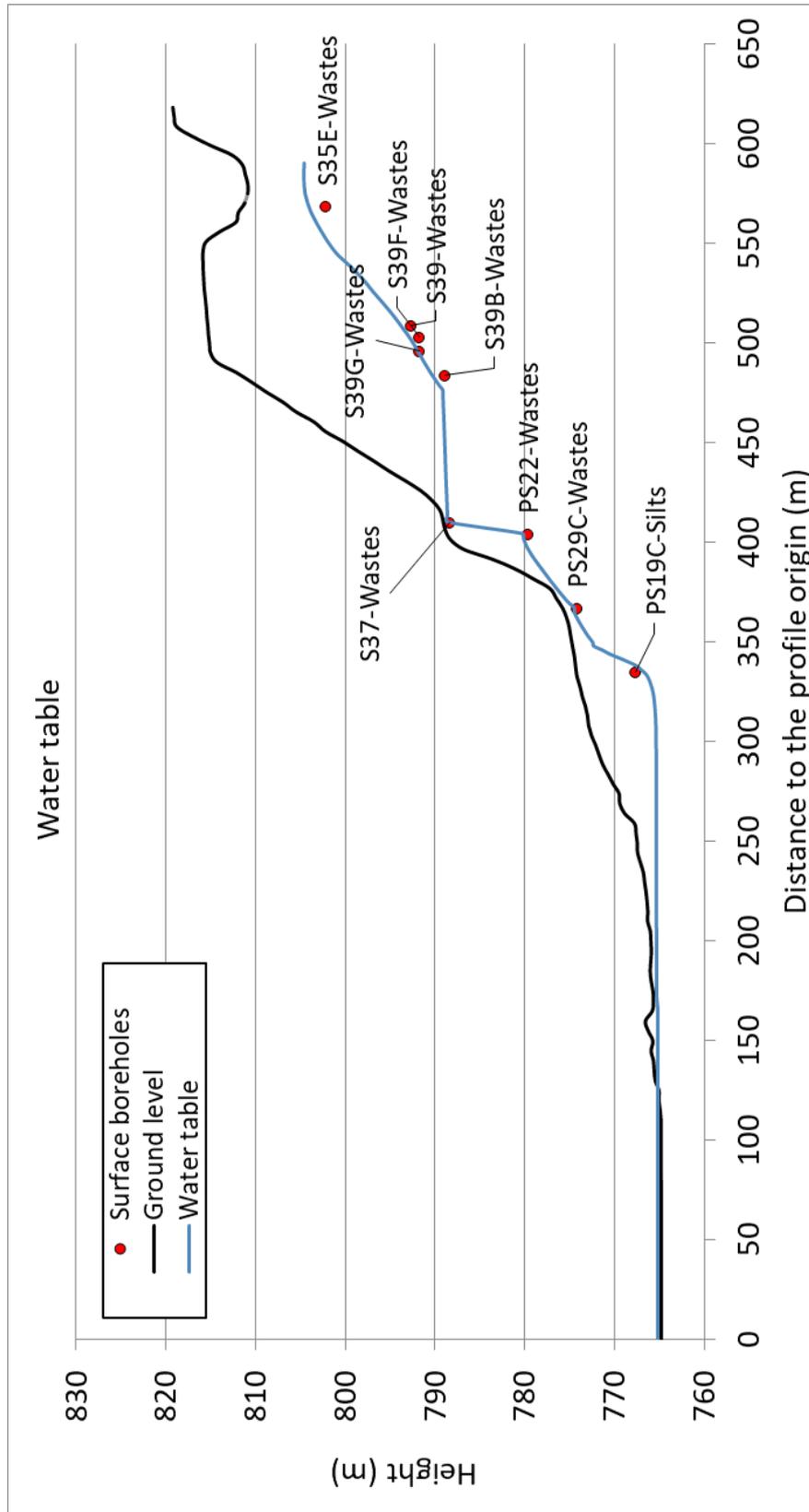
Figure 5.50. Computed water table in January 1ˢᵗ 2014.
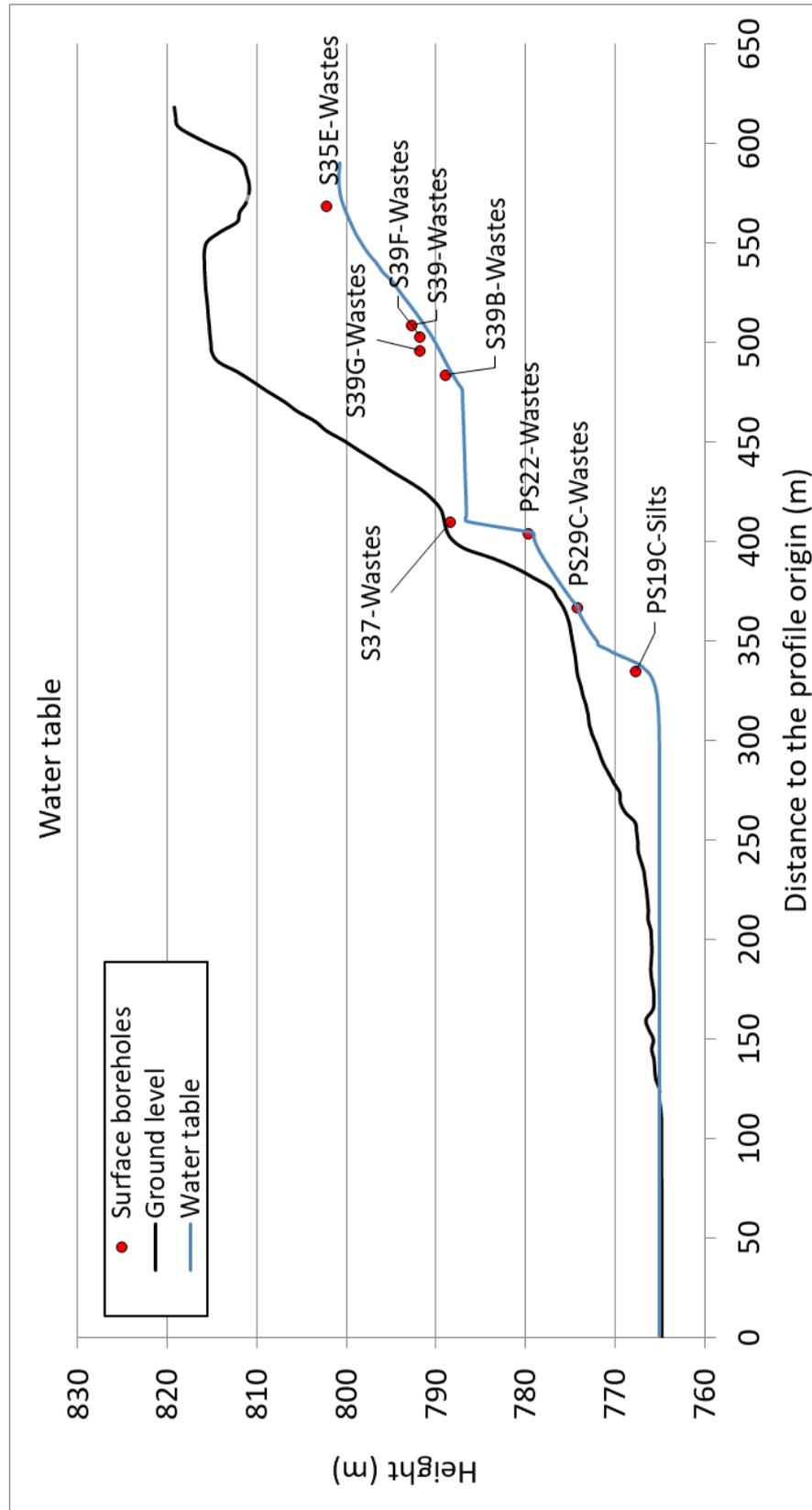
Figure 5.51. Computed water table in September 1st 2015.
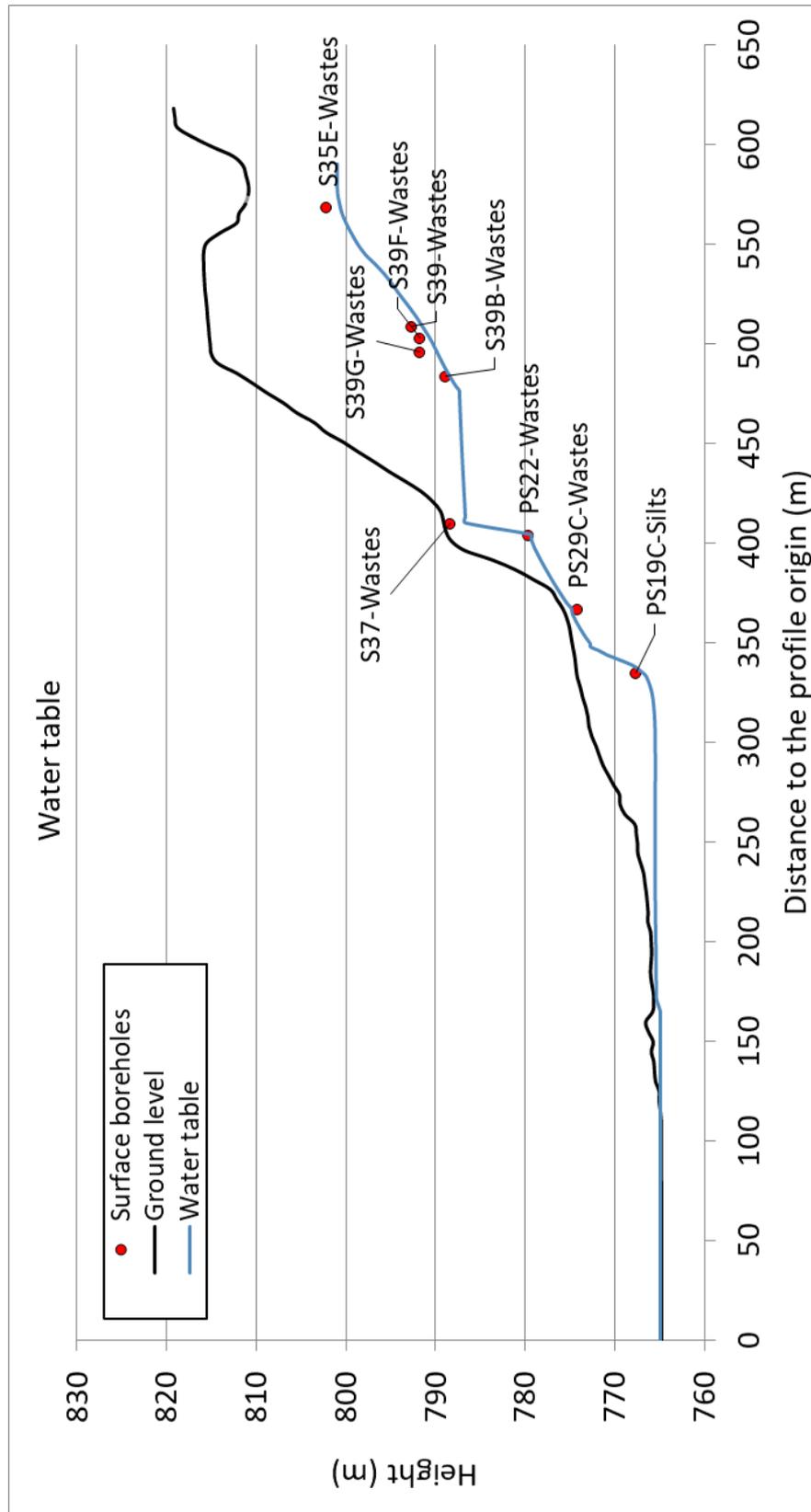
Figure 5.52.   Computed water table in March 1st 2016.
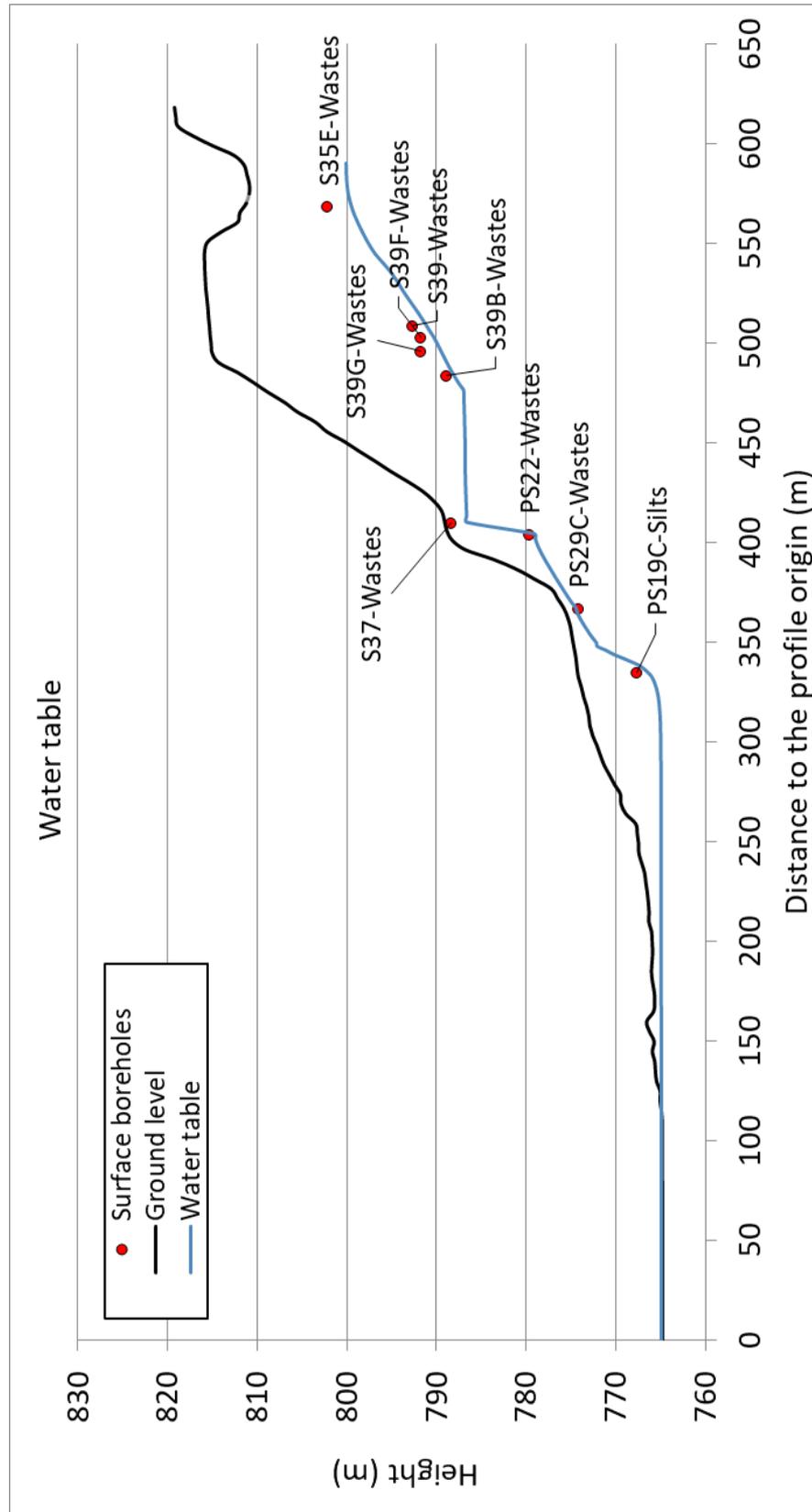
Figure 5.53. Computed water table in July 1st 2017.
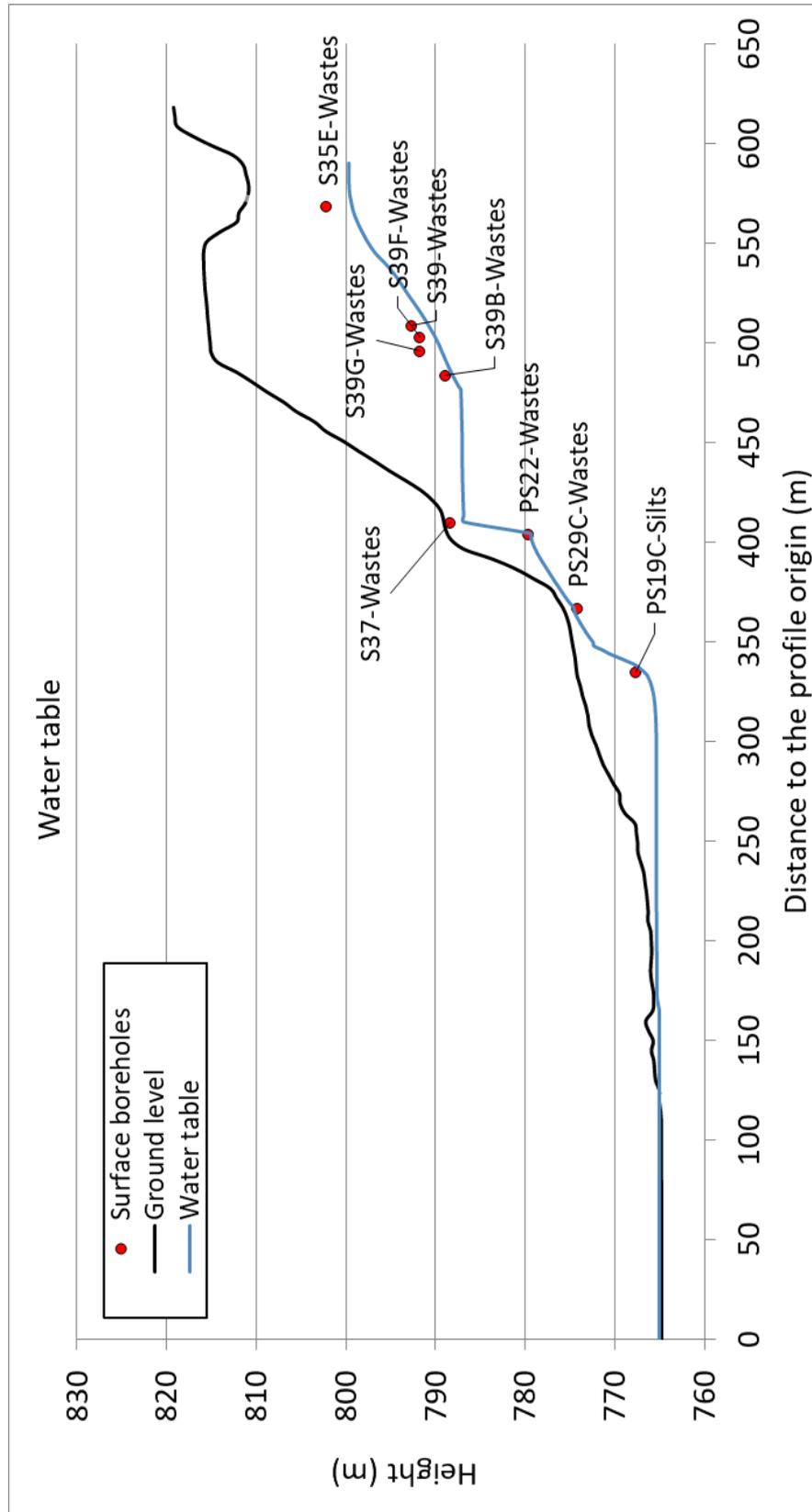
Figure 5.54. Computed water table in January 1st 2018.
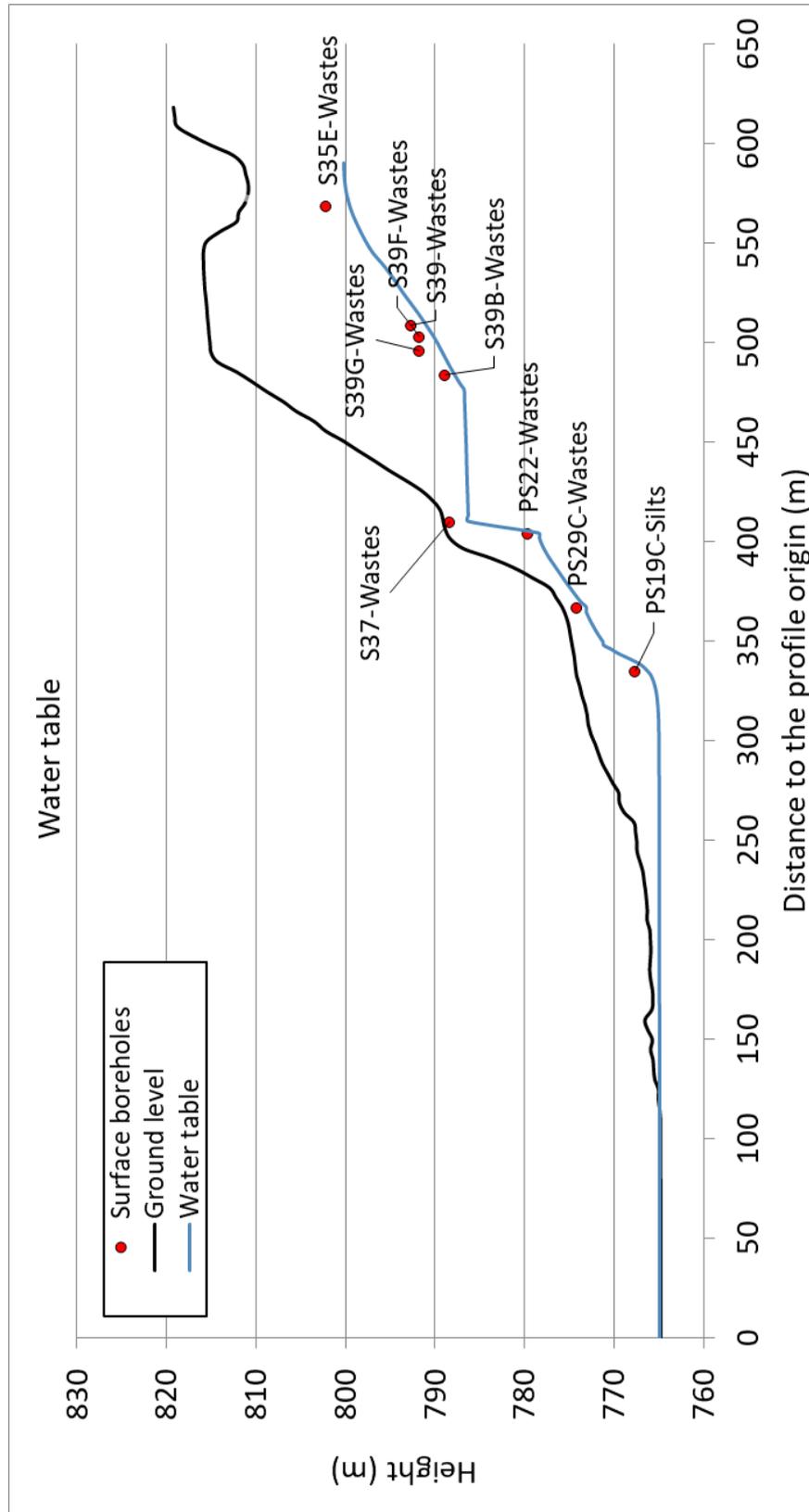
Figure 5.55. Computed water table in September 1st 2019.

5.3.4 Water balance

Total water inflows in the model domain are similar to those of the steady-state model (Table 5.1). They include:

1) Recharge by infiltration of rainwater, which is equal to 4.85 m^3/day and is equivalent to 21.36 % of the total inflow.

2) Recharge from the perimeter ditches, which is equal to 9.86 m^3/day and is equivalent to 43.40 % of the total inflow.

3) Recharge from the ravine near the S35E borehole, which is equal to 6.88 m^3/day which is equivalent to 30.29 % of the total inflow.

4) Re-injection nodes near the remediation pumping, which is equal to 1.12 m^3/day which is equivalent to 4.95 % of the total inflow.

Table 5.1.   Water inflows per unit width (unit inflows), total inflows for a width of 50 m and percentage of the total water inflows.

Inflows	Unitary flow (m^3/day)	Total flow (m^3/day)	% Inflow
Infiltration recharge	0.10	4.85	21.36
Perimeter inlets	0.20	9.86	43.40
Ravine inflow	0.14	6.88	30.29
Re-injection nodes flow	0.02	1.12	4.95
Total	0.45	22.71	100.00

Water outflows from the numerical model take place towards the Sabiñánigo reservoir, at leakage area near the PS29C borehole and pumping in borehole S37. Table 5.2 lists the water outflows. Most of the groundwater discharges into the reservoir (60%). The seepage discharge near the PS29C is 21 % and pumping is 19 %.

Table 5.2. Water outflows per unit width (unit outflows), total outflows for a width of 50 m and percentage of the total water outflows.

Outflows	Unitary flow (m³/day)	Total flow (m³/day)	% Inflow
Reservoir	0.31	15.34	59.80
Ditch 1	0.11	5.47	21.35
Pump	0.10	4.83	18.85
Total	0.51	25.65	100.00

Figure 5.56 shows the calculated outflow at the seepage area near borehole PS29C (Ditch 1) and the measured flow rates. The calculated discharge is of the same order of magnitude as the measured seepage. However, there are significant deviations in the time variability which could be due to model uncertainties around the seepage area, uncertainties and errors in the measured flow rates, which may include in some cases the contribution from rainfall runoff.
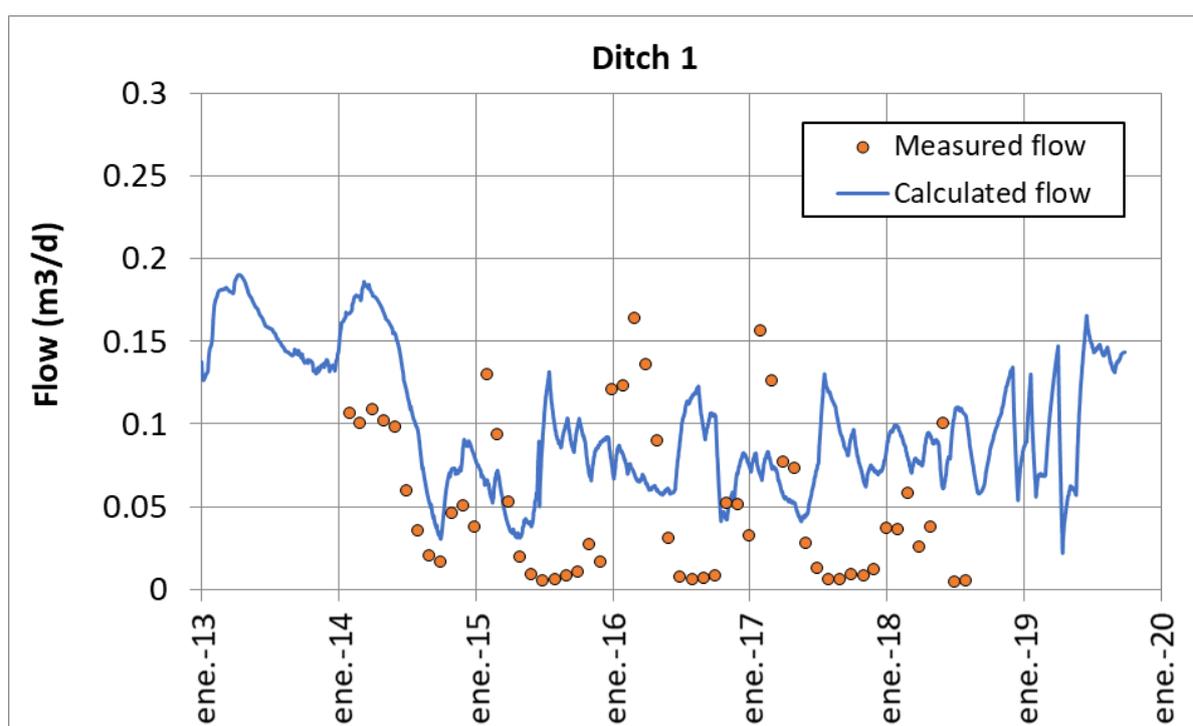
Figure 5.56. Measured (symbols) and computed (line) seepage flowrates in Ditch 1 near PS29C borehole.

5.4 Conclusions

A 2D transient groundwater flow model along a vertical cross-section in the East-West direction, which runs along the thalveg of the original gully, has been presented. The model has been used to test the conceptual hydrogeological model of the site. The model domain extends from the headwaters of the landfill until the Sabiñánigo reservoir. Multiannual and bimonthly numerical simulations have been performed.

The multiannual transient model of groundwater flow confirms the water inflows estimated with the hydrological water balance model. The average inflow ranges from 20 m^3/d to 30 m^3/d. Most of the inflows come from the runoff of the ravine located at the headwaters of the landfill and the perimeter ditches of the landfill. The outflows of landfill take place underneath the front slurry-wall and by pumping in well S37.

The calculated hydraulic heads reproduce for the most part the measured hydrographs in the alluvial and floodplain silts. Hydraulic head discrepancies are found in wells PS29B and PS29C located near the seepage area. The boundary condition at the seepage should be studied more in depth in future studies.

The model reproduces the hydraulic head hydrographs recorded in the inner landfill boreholes. Groundwater pumping in borehole S37 has been simulated with the simplifying assumption of planar flow. The computed hydraulic heads in the series of S39 boreholes reproduce the measured heads from January 2013 to November 2015. However, the model underestimates the measured hydraulic heads after January 2016.

The water level of the reservoir shows periodic oscillations with an amplitude of 1 m. These oscillations produce a tidal effect on the hydraulic heads in the alluvial aquifer. The bimonthly transient model reproduces the fluctuations of measured hydraulic heads with some smoothing. The discrepancies between measured and computed hydraulic heads may be due to uncertainties in the initial hydraulic heads.

6. 2D STEADY-STATE HORIZONTAL GROUNDWATER FLOW MODEL THROUGH THE GRAVELS OF THE ALLUVIAL OF THE GÁLLEGO RIVER

6.1 Introduction

This chapter presents a 2D steady-state horizontal groundwater flow model through the gravels of the Gállego river alluvial aquifer from the mouth of the Aurín river to the Sabiñánigo dam (Figure 6.1). This model aims at: 1) Quantifying the tidal effect of the daily fluctuations of the Sabiñánigo reservoir level on the aquifer hydraulic heads; 2) Estimating the hydraulic conductivity of the sediments at the bottom of the reservoir; and 3) Estimating the hydraulic conductivity of the gravels. The chapter starts with a description of the available data. Then, the numerical model is described. Model calibration and model results are presented next. The chapter ends with the main conclusions.
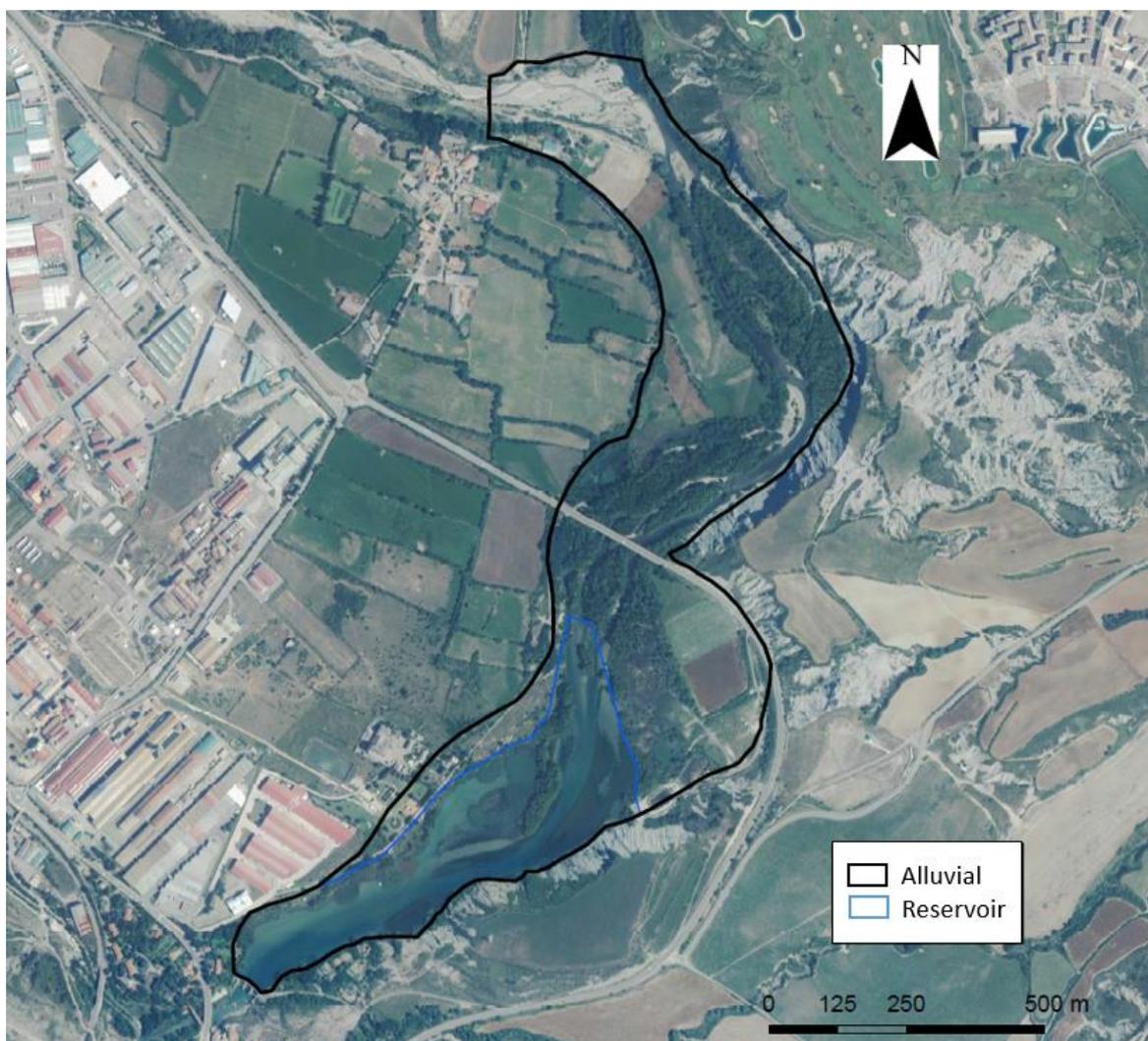
Figure 6.1. Location of the limit of the model domain and Sabiñánigo reservoir on an orthophoto of the study area.

6.2 Available data

The groundwater flow model has been defined based on the data derived from the following sources:

1) The digital terrain model (DTM) of the area

2) Hydrogeology report and hydrological balance models, and groundwater flow and contaminant transport models in the sites affected by INQUINOSA. Actividad nº 3: Modelos numéricos de flujo y transporte de solutos del emplazamiento de Sardas (Samper *et al.*, 2018 c).

3) Report on alluvial hydrogeology: *Estudio hidrogeológico del acuífero aluvial del río Gállego en Sabiñánigo (Huesca)* perfomed by Guadaño (2018).

4) Report carried out by the Association Notio: *Ensayos de bombeo dentro de las labores de investigación complementaria del emplazamiento de la antigua fábrica de Inquinosa afectada por contaminación por HCH – año 2017* (NOTIO, 2017).

5) Report carried out by the Ebro Basin Distric Administration: *Análisis ambiental de los sedimentos y del entorno del embalse de Sabiñánigo (Huesca) y evaluación de riesgos en septiembre de 2010* (CHE, 2010).

6) Boreholes carried out by EMGRISA in the study area (EMGRISA, 2011; 2013; 2014; 2015; 2016; 2017).

Measured hydraulic heads in the boreholes are available throughout the model domain as well as the water level of the reservoir. Hydraulic head data from 32 boreholes were used to calibrate the model. Head data are available from January 2013 to August 2019. All boreholes have hydro-level measurements of the hydraulic head and 7 of the 32 boreholes have continuous head measurements with diver. Table 6.1 presents the boreholes used for calibration with an indication of the lithology, the source of information and the average measured hydraulic head.

Daily precipitation, air temperature and evaporation data are available from 1941 to 2019. In addition, data from the Sabiñánigo and Yebra de Basa stations of the AEMET station network have been made available. From this information, the recharge was estimated using hydrological water balance models (Samper et al., 2018a).

Table 6.1. Boreholes used for the calibration of the numerical model, indicating the geological formation tapped by the screened section of the casing, the source of information and the average measured hydraulic head.

Borehole	Lithology	Source	Measured hydraulic head (m)
ST1	Gravels	EMGRISA	765.03
ST1B	Gravels	EMGRISA	765.03
ST1C	Gravels	EMGRISA	765.01
ST1D	Gravels	EMGRISA	765.01
ST1E	Gravels	EMGRISA	765.02
ST2	Gravels	EMGRISA	764.99
ST4	Gravels and silts	Guadaño (2018)	765.05
ST6	Gravels and silts	Guadaño (2018)	766.00
PS3	Gravels	EMGRISA	764.97
PS8	Gravels	EMGRISA	765.04
PS13	Gravels	EMGRISA	765.01
PS14	Gravels	EMGRISA	765.03
PS16	Gravels	EMGRISA	765.04
PS16C	Gravels	EMGRISA	765.04
PS16D	Gravels	EMGRISA	765.05
PS16E	Gravels	EMGRISA	765.15
PS16F	Gravels	EMGRISA	765.06
PS16G	Gravels	EMGRISA	765.01
PS17	Gravels	EMGRISA	765.00
PS18	Various lithologies	EMGRISA	765.01
PS19	Gravels	EMGRISA	765.03
PS19B	Gravels	EMGRISA	765.03
PS20	Gravels	EMGRISA	765.02
PS21B	Gravels	EMGRISA	765.06
PS24	Gravels	EMGRISA	765.02
PS25B	Gravels	EMGRISA	765.02
PS26	Gravels	EMGRISA	765.06
INQUI-S1	Various lithologies	(NOTIO, 2017)	764.76
INQUI-S2	Various lithologies	(NOTIO, 2017)	766.68
INQUI-S10	Gravels	(NOTIO, 2017)	765.54
INQUI-S11	Gravels and marls	(NOTIO, 2017)	765.82
CHE-1 (ST-3)	Gravels	(NOTIO, 2017)	765.04

6.3 Numerical Model

6.3.1 Model domain

The numerical model accounts for groundwater flow through the gravels of the alluvial of the Gállego river from the mouth of the Aurín river in the Gállego river to the Sabiñánigo dam (Figure 6.1).

The model domain borders to the north with the mouth of the River Aurín on the Gállego river. The southern boundary is the Sabiñánigo reservoir dam. The model boundary on the left bank coincides with the Gallego river and the reservoir border. On the right bank, in the area of INQUINOSA, the model boundary coincides with the contact of the alluvial plain and the fluvioglacial terrace. The jump from the fluvioglacial terrace to the fluvial terrace has been defined from the DTM, the shadow map calculated from the DTM (Figure 6.2) and the data derived from drilled boreholes in the alluvial (NOTIO 2017). The model domain occupies an area of 57.79 ha.
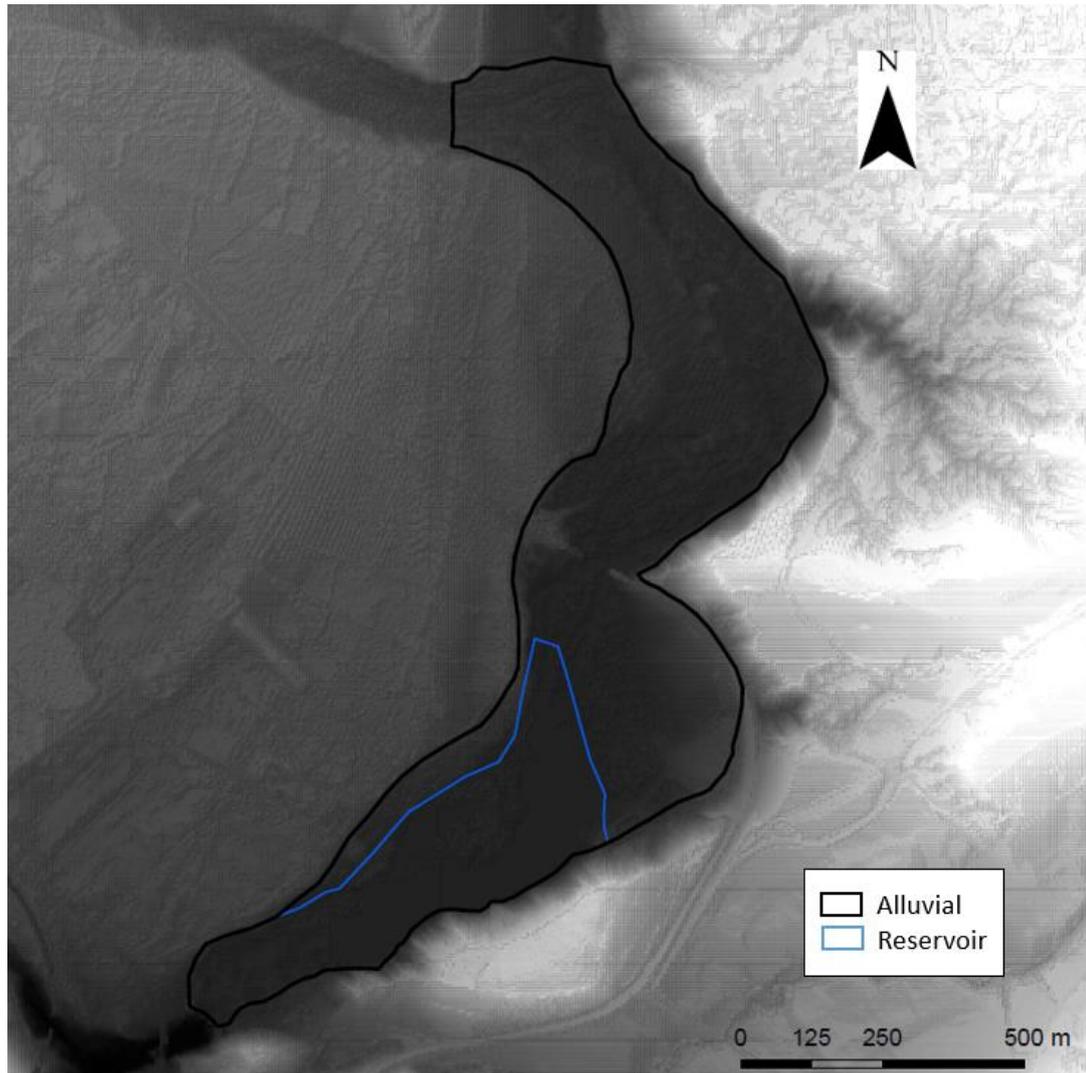
Figure 6.2.   Boundary of the model domain and reservoir domain on the shadow map calculated from the IGN (National Institute of Geography of Spain) digital terrain model (https://www.ign.es/web/ign/portal).

Data on the thickness of the gravel and sand layers from the cores of the boreholes drilled in the area of the reservoir (CHE, 2010), in the INQUINOSA site (NOTIO, 2017) and downstream the Sardas landfill (EMGRISA) were compiled. A map of gravel thickness has been drawn up by kriging the available data with the ArcGIS program. The thickness of sand layers interspersed in gravels is included in the gravel thickness. A constant thickness of 2.5 m has been assumed upstream the bridge of the N-330 national road given the lack of data in that area (Figure 6.3).
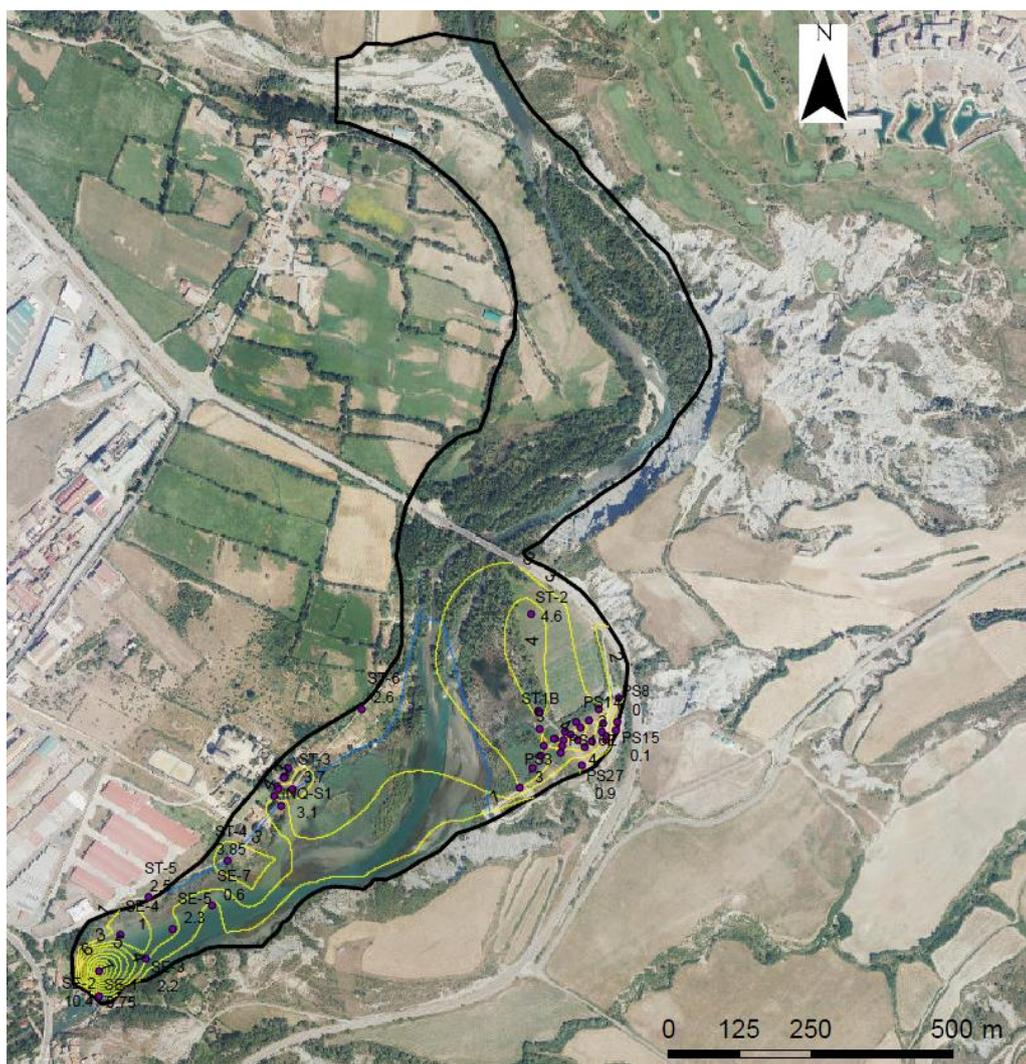
Figure 6.3. Gravel thickness contour plot considered in the groundwater flow model in the alluvial. The thickness of sand layers interspersed in gravels is included in the gravel thickness.

6.3.2 Spatial discretization

The numerical 2D horizontal model domain is discretized with a triangular finite element mesh (Figure 6.4). The mesh has 2348 nodes and 4475 elements. The elements are largest far from the landfill where the gravels outcrop and in the crop terraces upstream the bridge of the N-330 national road. An intermediate size has been adopted in the reservoir and in the course of the Gállego river. The mesh has been especially refined downstream the Sardas landfill where most of the boreholes with piezometric data are located.
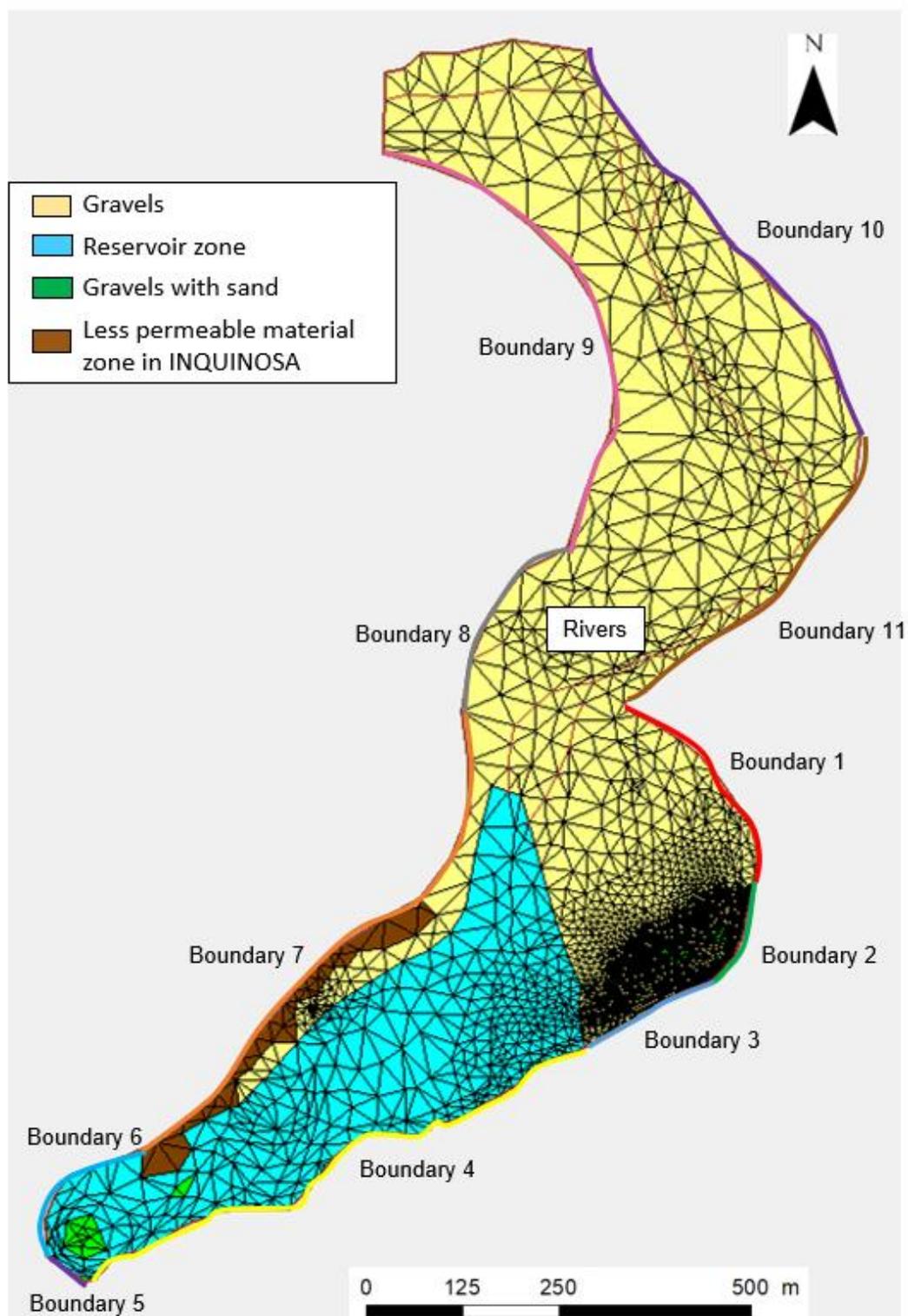
Figure 6.4.   Finite element mesh, material zones and boundary sections of the 2D horizontal model.

6.3.3   Materials

The spatial distribution of the material zones considered in the model is shown in Figure 6.4. Table 6.2 lists the material zones and the calibrated values of K and S_S for each material. The initial hydraulic conductivities considered in the calibration have been derived from the pumping tests carried out in the area. In general, the hydraulic head in the gravel layer varies very little throughout the model domain due to the high hydraulic conductivity of the gravels. The measured hydraulic heads on the right bank near INQUINOSA are higher than in the rest of the boreholes. Some of those boreholes could be drilled in the colluvial of the fluvioglacial terrace. A less permeable material zone has been defined in the model to simulate measured hydraulic head gradient.

Table 6.2.   Calibrated hydraulic conductivities and specific storage coefficents calibrated in the alluvial material zones.

Material zone	Geological formation	Colour	Area (hm^2)	Hydraulic conductivity K_h (m/d)	Specific Storage Coefficient (m^{-1})
1	Gravels		41.09	$2.00 \cdot 10^{+2}$	$2.00 \cdot 10^{-4}$
2	Gravels under the reservoir		15.20	$2.00 \cdot 10^{+2}$	$2.00 \cdot 10^{-4}$
3	Gravels with sand		0.42	$2.00 \cdot 10^{+2}$	$2.00 \cdot 10^{-4}$
4	Less permeable material zone in INQUINOSA		1.50	$1.70 \cdot 10^{+0}$	$2.00 \cdot 10^{-4}$
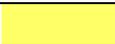
6.3.4   Recharge and boundary conditions

The recharge was estimated by Samper et al. (2018 a) by using a hydrological water balance model. The model domain is divided in two recharge zones (Figure 6.5). In the area where gravels outcrop, recharge is larger than in the area where the gravels are confined by the silts. The wooded areas are assumed to coincide with unconfined gravels, while crop fields coincide with outcrops of alluvial silts. Recharge values are listed in Table 6.3.
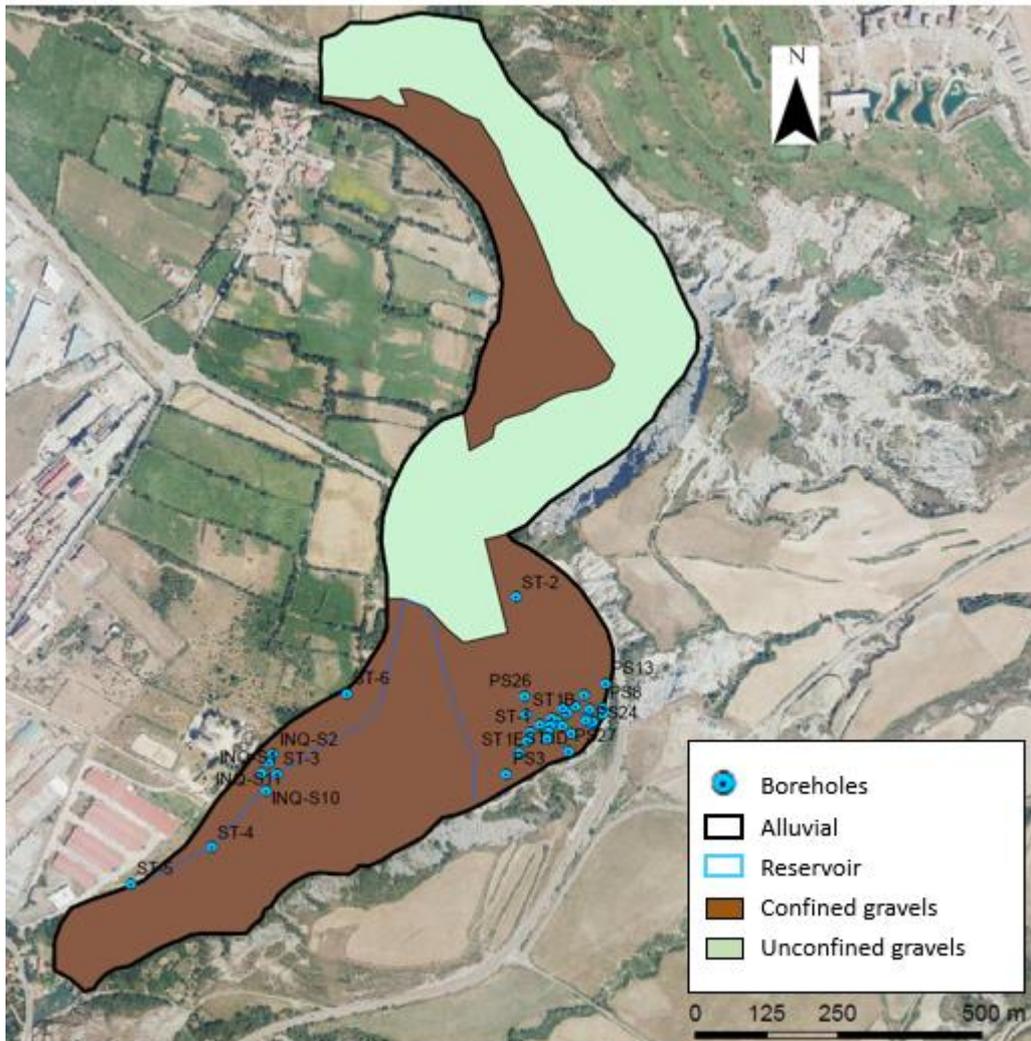
Figure 6.5. Map of the recharge areas used in the model. The areas in which the gravels are confined are shown in brown and the areas in which the gravels emerge are shown in green.

Table 6.3. Groundwater recharge in the two alluvial zones.

Material	Recharge (mm/year)
Alluvial where gravels are confined	130
Alluvial where gravels are unconfined	170

Figure 6.4 shows the model boundary conditions. Boundary conditions along the two banks of the alluvial are simulated with a Neuman condition (fixed flow) by assuming that the flow is uniform by sections. The total flow of boundary section 2 (Sardas landfill) has been assumed to be equal to 21.86 m³/d, similar to the flow passing underneath the front slurry-wall. The rest of

the flows have been calibrated by using measured hydraulic head data. Table 6.4 shows the boundary inflows per unit length of boundary section, the total inflows in each boundary section and the percentage of the total inflow.

Table 6.4. Boundary inflows per unit length, total inflow (m^3/d) in each boundary section and percentage of the total inflow. The boundary sections are shown in the Figure 6.4.

Boundary section	Unitary inflow (m^2/d)	Inflow (m^3/d)	% Flow
1	0.100	35.459	2.35
2	0.170	21.859	1.45
3	0.100	19.230	1.28
4	0.100	79.120	5.25
6	0.400	85.604	5.68
7	1.000	713.882	47.35
8	0.400	141.564	9.39
9	0.400	287.911	19.09
10	0.100	66.464	4.41
11	0.100	56.696	3.76
TOTAL	3.030	1507.788	100

The Gállego river in the model area consists of a main channel that is divided twice into two branches. The river has been simulated by using a Cauchy condition with an external head and a leakage coefficient. Channel hydraulic heads have been defined by considering a moderate slope of 0.003 for the Gállego river and a slope of 0.177 for the Aurín river. These slopes have been estimated from the DTM. Figure 6.6 and Figure 6.7 show the hydraulic heads prescribed along the Gállego and Aurín rivers. The leakage coefficient has been taken equal to 200 m^2/d.
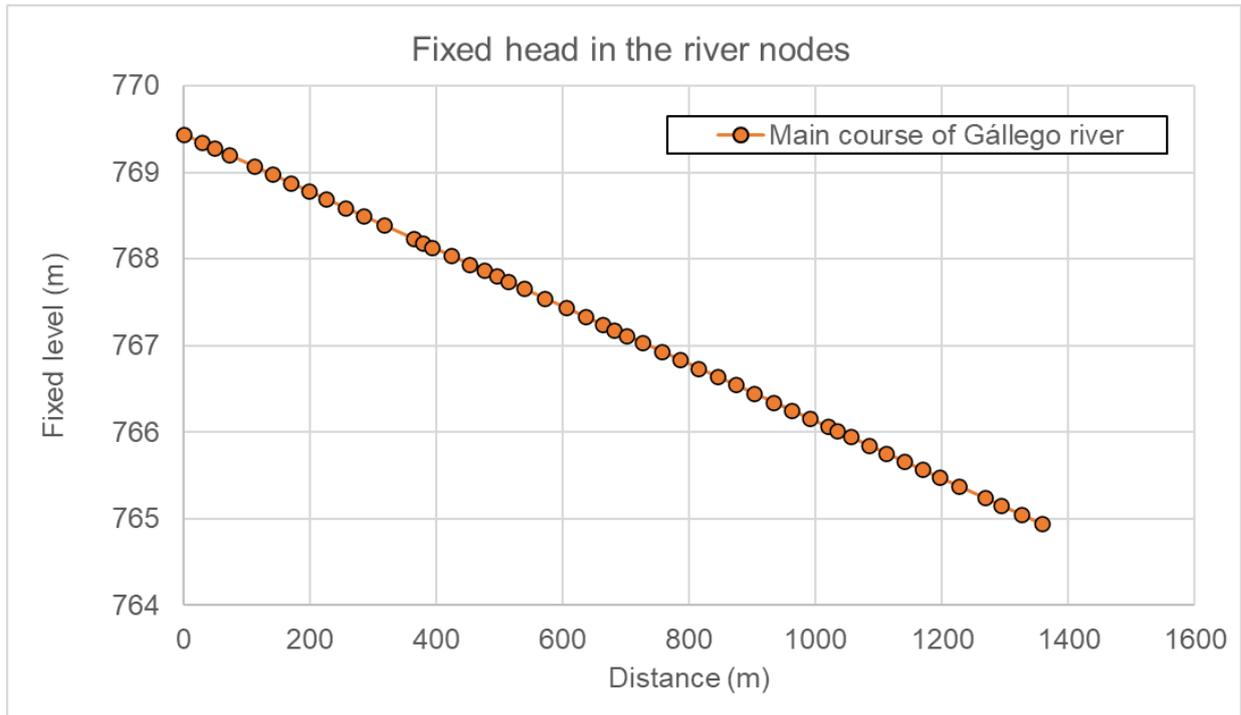
Figure 6.6.   Prescribed hydraulic heads at the nodes along the main course of the Gállego river.
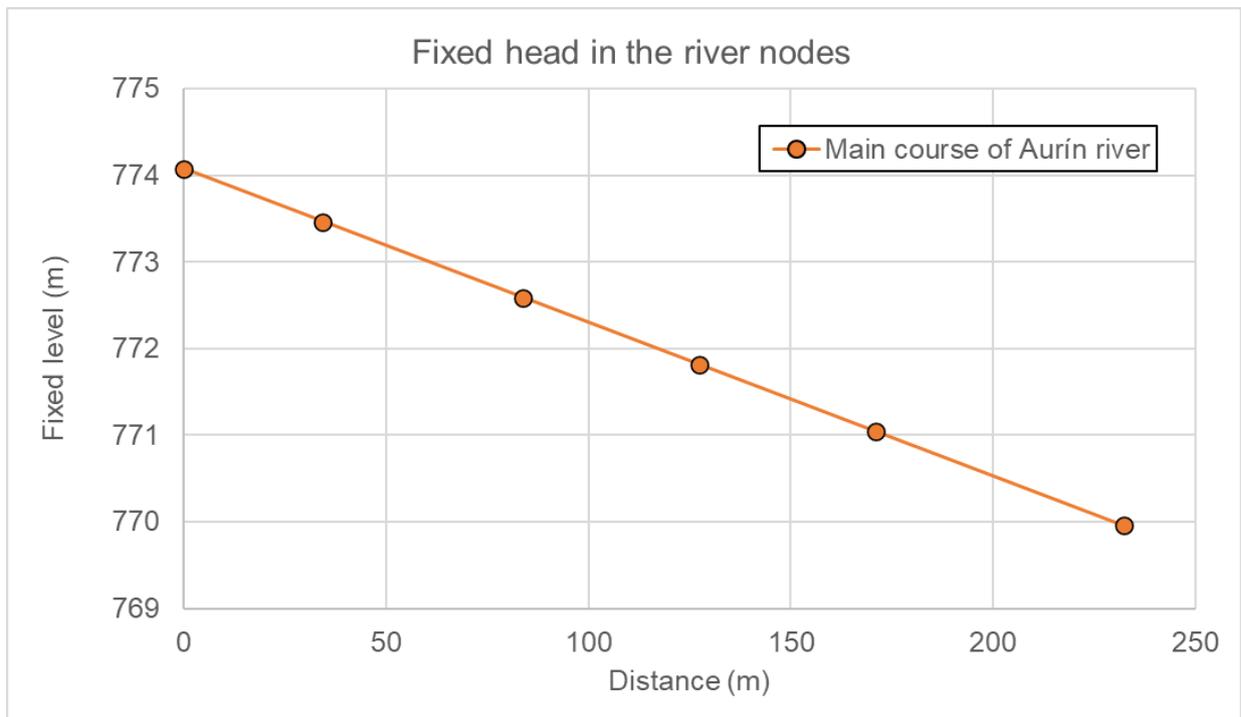
Figure 6.7.   Prescribed hydraulic heads at the nodes along the main channel of the Aurín River.

INTERNATIONAL MASTER IN
WATER ENGINEERING

The reservoir has also been simulated with a Cauchy type condition. The leakage coefficient has been calculated according to the following equation:

$$\alpha_{calibrated} = \frac{K_{silts} \cdot V_{node}}{e_{silts} \cdot b_{acuifer}} = \frac{0.04 \cdot V_{node}}{2 \cdot b_{acuifer}}$$

where V_{node} is the nodal volume, K_{silts} is the vertical hydraulic conductivity of the silt layer, e_{silts} is the thickness of the silt layer and $b_{aquifer}$ is the thickness of the gravel aquifer, which has been calculated as the average thickness of the elements surrounding the node.

It has been assumed that the original course of the Gállego river before the construction of the dam has been filled with sediments of a hydraulic conductivity larger than that of the alluvial silts. The location of the original course has been derived from historical maps, aerial views and orthophotos. Figure 6.8 shows the former riverbed area on a historical orthophoto taken in the American flight of 1956. The leakage coefficient in the former riverbed area has been calculated according to the following equation:

$$\alpha_{calibrated} = \frac{K_{sediments} \cdot V_{node}}{e_{silts} \cdot b_{acuifer}} = \frac{0.2 \cdot V_{node}}{2 \cdot b_{acuifer}}$$

which considers a vertical hydraulic conductivity of the sediments of 0.2 m/d which is larger than that of the silt layer.
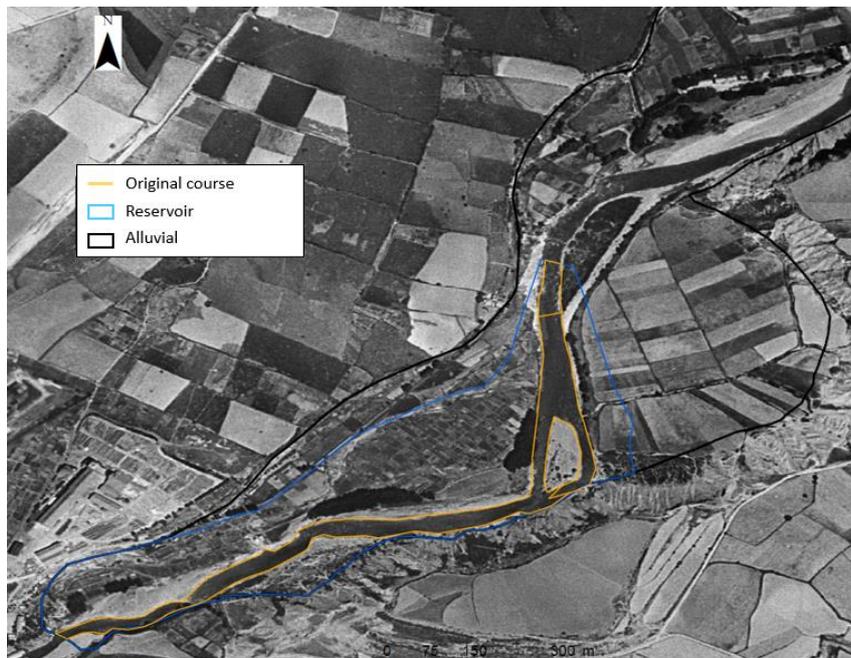
Figure 6.8.   Former Gállego riverbed before the dam construction on the orthophoto taken in the American flight of 1956.

The boundary condition in section 5 simulates the outflow underneath the Sabiñánigo dam (Figure 6.4). A Cauchy condition has been adopted with a constant fixed hydraulic head equal to 752 m and a total leakage coefficient equal to 90 m^2/d. The fixed head and leakage coefficient were estimated during the model calibration. The leakage coefficient has been distributed among the 4 nodes along this boundary. The 66 % of outflow has been allocated to the two intermediate nodes and 33 % to the end's nodes. The hydraulic heads and leakage coefficients considered in the model along the dam boundary are listed in Table 6.5.

Table 6.5. Fixed hydraulic heads and leakage coefficients considered in the nodes along the boundary section 5 simulating the outflow underneath the Sabiñánigo dam.

Node	Fixed hydraulic head (m)	Leakage coefficient (m^2/d)
1901	752	30
1902	752	15
1952	752	30
1953	752	15

6.4 Model calibration and model results

6.4.1 Preliminary calibration

Model calibration has been carried out by using the available hydraulic head data in boreholes of the INQUINOSA factory (NOTIO, 2017), the boreholes of the Sardas landfill area (EMGRISA) and the hydraulic heads measured by Guadaño (2018). Table 6.1 shows the boreholes in which data are available, the lithology in which the screen of the borehole is located, the source of the data and the average measured hydraulic heads.

Table 6.6 presents the comparison of the computed hydraulic heads using the calibrated model with the average measured hydraulic head in the boreholes. The calculated residuals, the Nash index and the determination coefficient are also included.

Table 6.6. Average measured hydraulic heads and computed hydraulic heads in the boreholes after calibration. The residuals in each borehole are calculated as the difference between the measured and computed heads. The Nash index and the determination coefficient are also included.

Borehole	Measured hydraulic head (m)	Computed hydraulic head (m)	Residual (m)
ST1	765.03	765.28	-0.25
ST1B	765.03	765.29	-0.27
ST1C	765.01	765.28	-0.26
ST1D	765.01	765.26	-0.25
ST1E	765.02	765.26	-0.24
ST2	764.99	765.41	-0.42
ST4	765.05	765.15	-0.10
ST6	766.00	765.54	0.46
PS3	764.97	765.23	-0.26
PS8	765.04	765.36	-0.32
PS13	765.01	765.36	-0.36
PS14	765.03	765.34	-0.31
PS16	765.04	765.32	-0.27
PS16C	765.04	765.30	-0.26
PS16D	765.05	765.31	-0.26
PS16E	765.15	765.31	-0.16
PS16F	765.06	765.30	-0.24
PS16G	765.01	765.30	-0.29
PS17	765.00	765.33	-0.32
PS18	765.01	765.34	-0.33
PS19	765.03	765.34	-0.32
PS19B	765.03	765.34	-0.31
PS20	765.02	765.32	-0.30
PS21B	765.06	765.33	-0.26
PS24	765.02	765.34	-0.32
PS25B	765.02	765.35	-0.33
PS26	765.06	765.30	-0.24
INQUI-S1	764.76	765.31	-0.55
INQUI-S2	766.68	765.81	0.87
INQUI-S10	765.54	765.24	0.30
INQUI-S11	765.82	765.53	0.28
CHE-1 (ST-3)	765.04	765.26	-0.22
Mean residual		-0.1911	
Nash index		-1.2907	
R2 (Determination coefficient)		0.7062	

The fit of the computed heads to the measured hydraulic heads is good (Figure 6.9). Only two boreholes have residuals with absolute values greater than 0.5 m. The residual is less than 1 m in all boreholes (Figure 6.10). However, the computed hydraulic heads in the boreholes downstream the landfill are consistently higher than the measured data. This discrepancy has been addressed in the final model calibration.
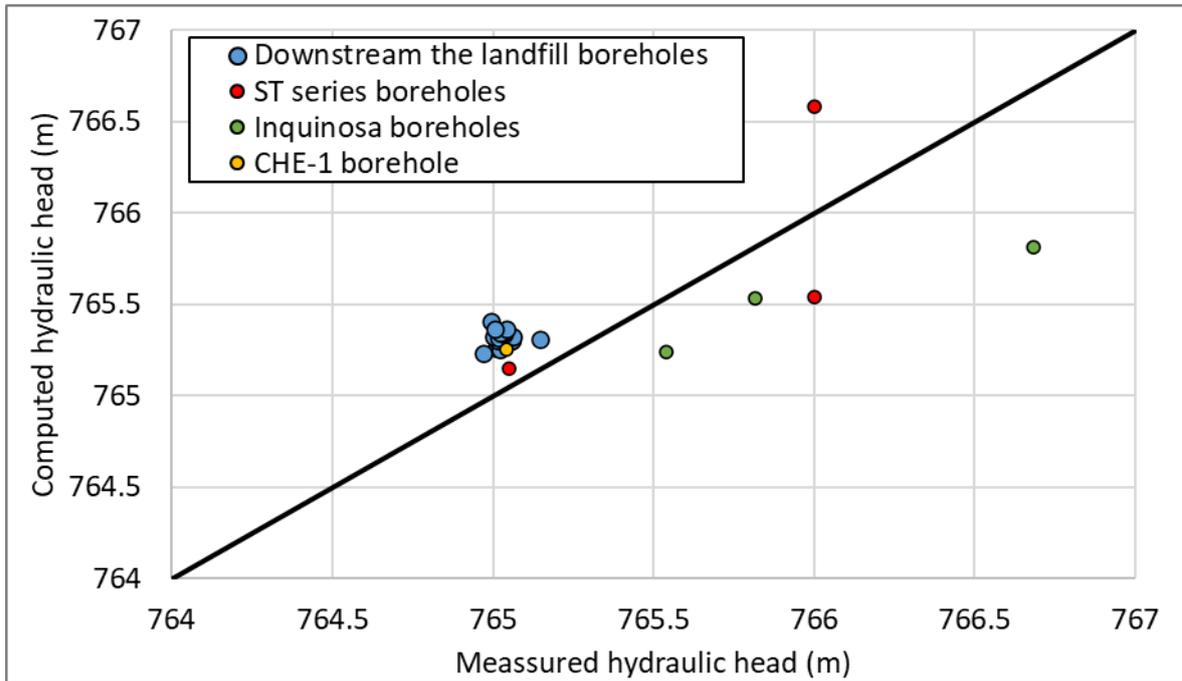
Figure 6.9. Scattergram of the measured and computed hydraulic heads (results of the preliminary calibration).
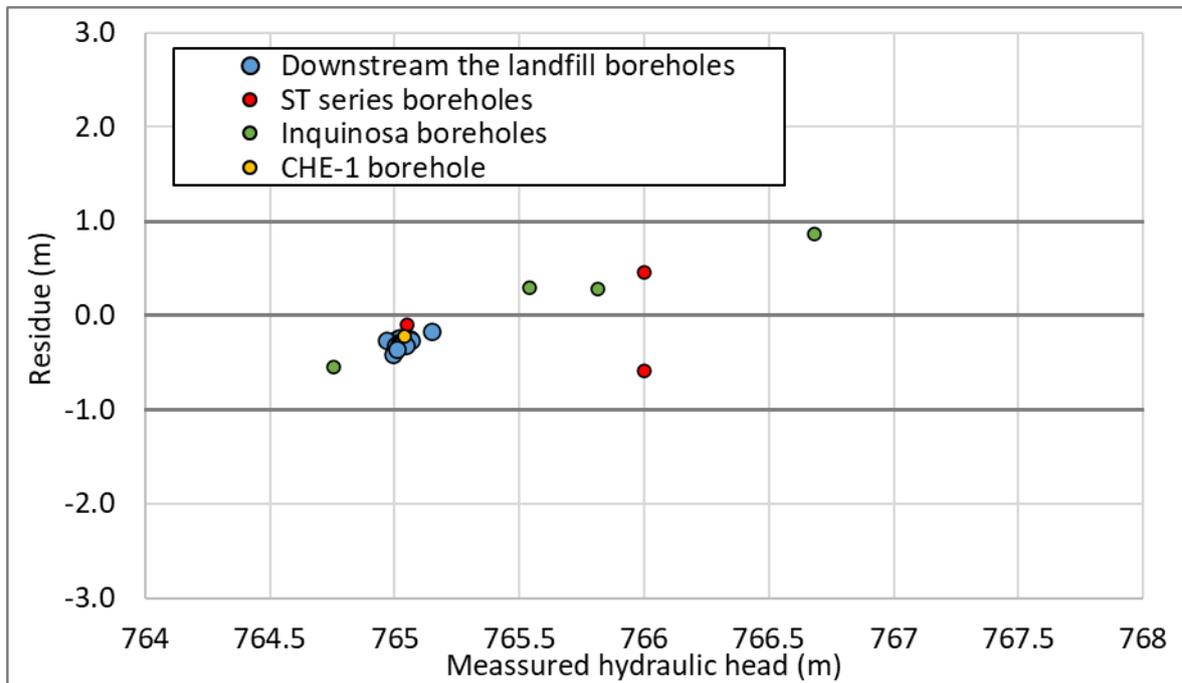
Figure 6.10. Scatter plot of the residuals, calculated as the difference between measured and computed hydraulic heads, and the average measured hydraulic heads (results of the preliminary calibration).

Figure 6.11 shows the map of calculated hydraulic heads model domain. The hydraulic head contours are represented every 0.5 m. There is a strong gradient on the right bank of the Gállego river upstream the reservoir due to the existence of a less permeable zone. Figure 6.12 presents a zoom of the piezometric map in the area downstream the Sardas landfill. A flow towards the former Gállego riverbed. Figure 6.13 shows a zoom to the map of hydraulic head contours on the Sabiñánigo dam area, where a strong gradient can be seen in the less permeable area and upstream the dam. This gradient upstream the dam illustrates the existence of a groundwater flow below the dam foundations.
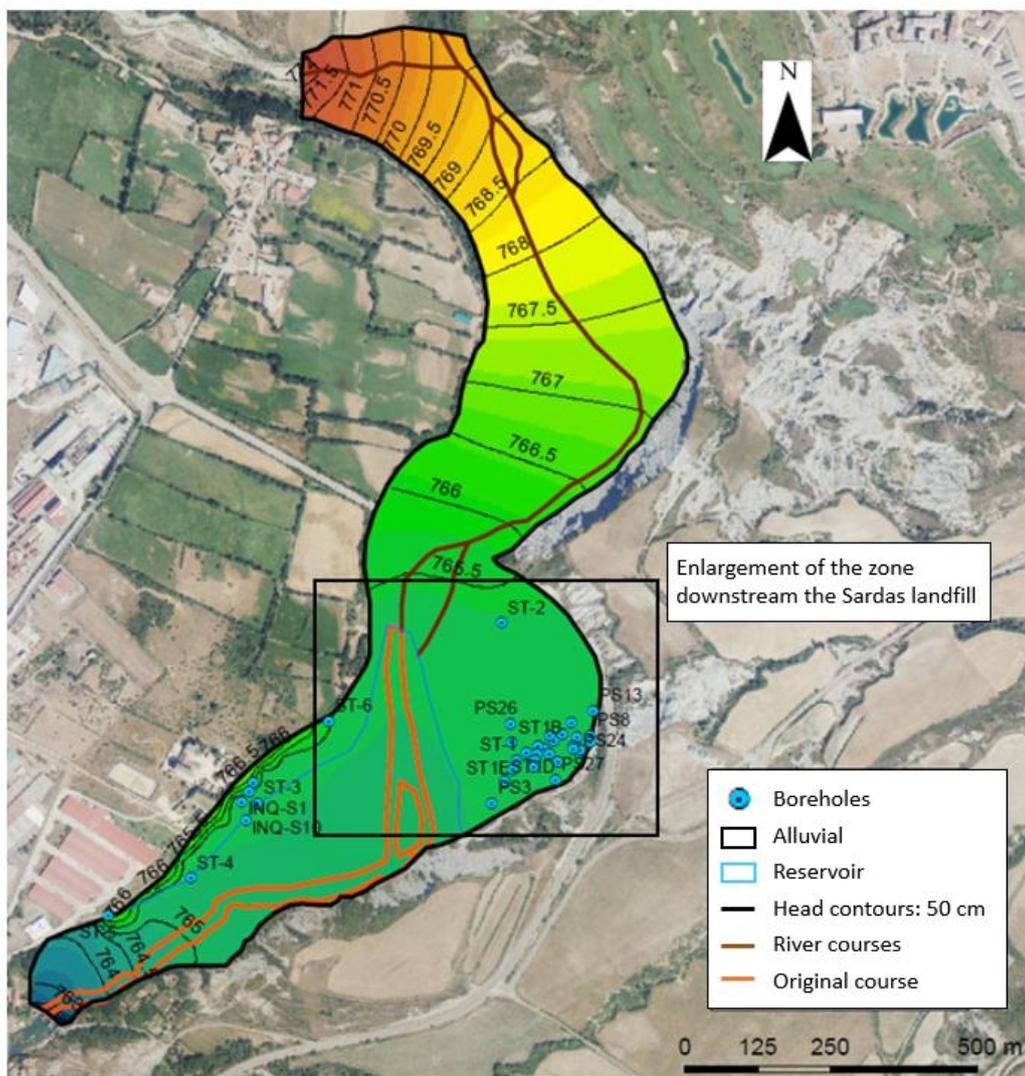
Figure 6.11. Map of calculated hydraulic head contours using the preliminary steady state groundwater flow 2D horizontal model. The hydraulic head contours interval is of 50 cm. The area inside the black rectangle is shown in the Figure 6.12.
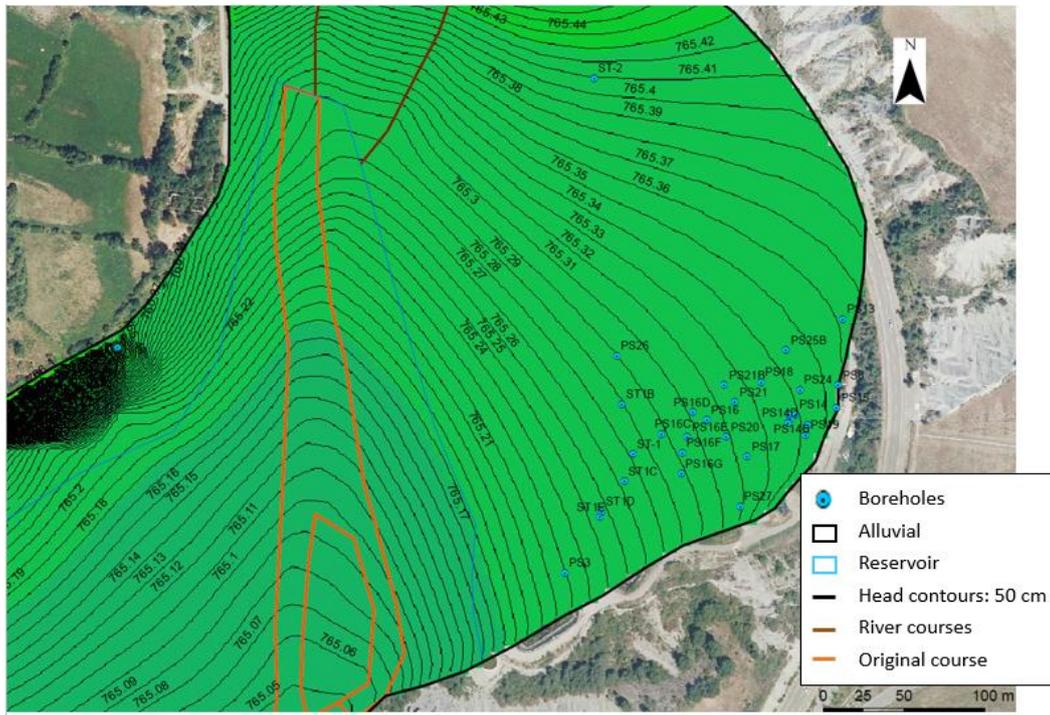
Figure 6.12. Zoom to the map of hydraulic head contours calculated using the preliminary steady state groundwater flow 2D horizontal model to the area located downstream the Sardas landfill (see location in Figure 6.11). Hydraulic head contours interval is 1 cm.
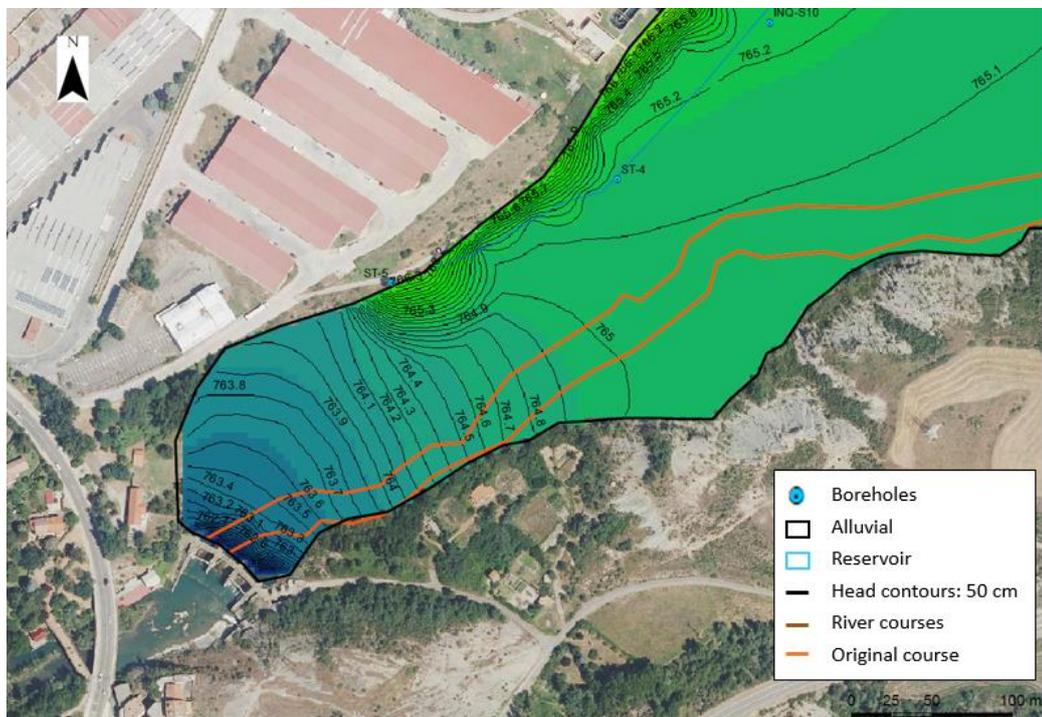
Figure 6.13. Zoom to the map of hydraulic head contours calculated using the preliminary steady state groundwater flow 2D horizontal model to the area located to the area around the Sabiñánigo dam. Hydraulic head contours interval is 10 cm.

6.4.2   Final model calibration

The calibration of the model was improved from the analysis of the residuals of the hydraulic heads in the boreholes and the sensitivity runs to changes in the main parameters. Sensitivity runs to changes in the vertical hydraulic conductivity of the alluvial silts and the silting sediments, which affect the leakage coefficient and, therefore, the outflow from the gravels to the reservoir, have been performed. The hydraulic conductivities of the alluvial silts and silting sediments have been increased to 0.1 and 0.4 m/d, respectively. Also, the hydraulic conductivity of the gravels has been increased from 200 m/d to 400 m/d and the leakage coefficient of the riverbed nodes from 200 m^2/d to 500 m^2/d. The computed hydraulic heads are extremely sensitive to the change in the slope of the Gállego river upstream the reservoir. Two sections with different slopes have been defined in the revised model. Figure 6.14 shows the diagram of the calibrated slopes in different sections of the Gállego river. Figure 6.15   shows the fixed hydraulic head assigned to the nodes located along the main channel of the Gállego River.
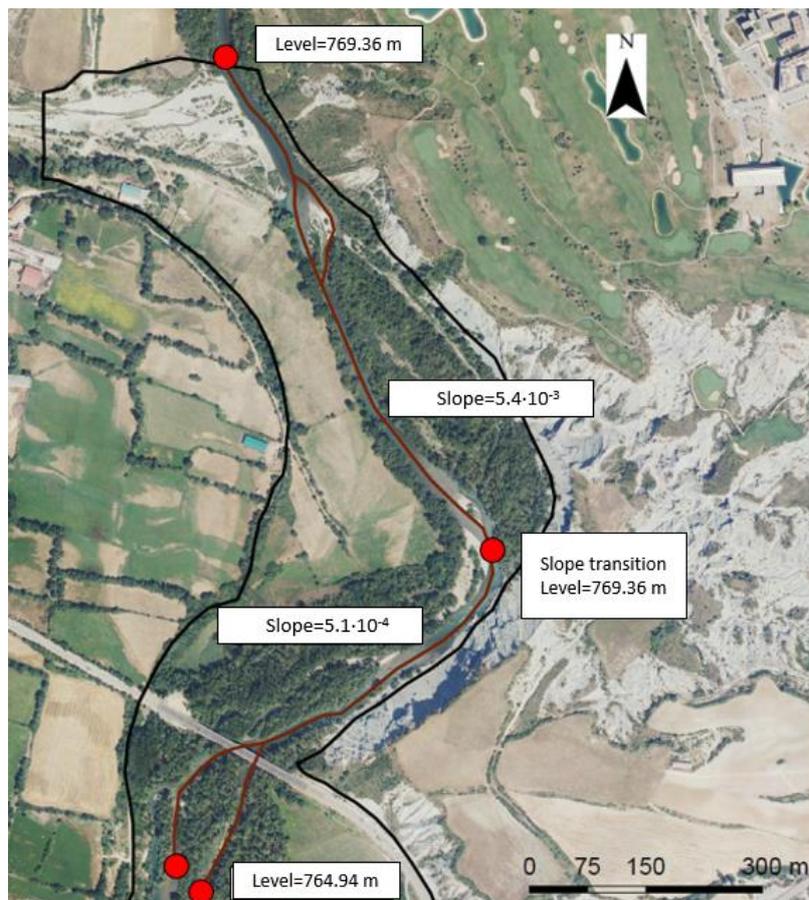
Figure 6.14.   Diagram of the calibrated slopes along the course of the Gállego river upstream the Sabiñánigo reservoir.
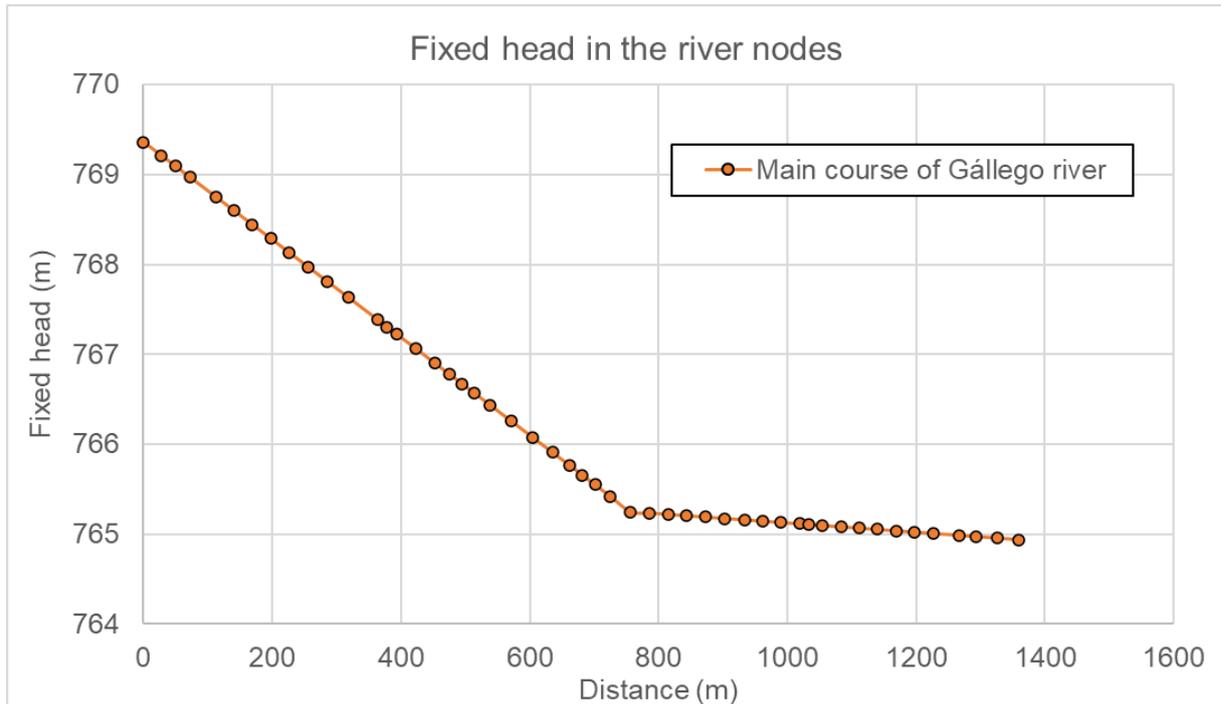
Figure 6.15. Fixed hydraulic heads in the nodes of the Gállego riverbed considered in the model.

Calculated hydraulic heads using the improved numerical and their comparison with average measured hydraulic heads in the boreholes are presented in Table 6.7. The hydraulic head fit is good (Figure 6.16). Only a borehole has an absolute value of the residual larger than 0.5 m and all of them are smaller than 1 m (Figure 6.17). The largest discrepancies are found in the boreholes in the INQUINOSA area because the gradients in that area are much larger than in the rest of the model domain. The Nash's index for the improved model is equal to 0.71 which means a much better fit than that of the preliminary calibration.

Table 6.7. Average measured hydraulic heads and computed hydraulic heads in the boreholes after calibration. The residuals in each borehole have been calculated as the difference between the measured and computed heads. The Nash index and the determination coefficient are also included.

Borehole	Measured hydraulic head (m)	Computed hydraulic head (m)	Residual (m)
ST1	765.03	765.06	-0.02
ST1B	765.03	765.06	-0.03
ST1C	765.01	765.05	-0.04
ST1D	765.01	765.05	-0.04
ST1E	765.02	765.05	-0.03
ST2	764.99	765.07	-0.07
ST4	765.05	765.03	0.02
ST6	766.00	765.27	0.73
PS3	764.97	765.04	-0.08
PS8	765.04	765.08	-0.04
PS13	765.01	765.08	-0.07
PS14	765.03	765.07	-0.04
PS16	765.04	765.06	-0.02
PS16C	765.04	765.06	-0.02
PS16D	765.05	765.06	-0.01
PS16E	765.15	765.06	0.08
PS16F	765.06	765.06	0.00
PS16G	765.01	765.06	-0.05
PS17	765.00	765.07	-0.07
PS18	765.01	765.07	-0.06
PS19	765.03	765.08	-0.05
PS19B	765.03	765.08	-0.05
PS20	765.02	765.07	-0.05
PS21B	765.06	765.07	0.00
PS24	765.02	765.07	-0.05
PS25B	765.02	765.07	-0.06
PS26	765.06	765.06	0.00
INQUI-S1	764.76	765.12	-0.36
INQUI-S2	766.68	766.77	-0.09
INQUI-S10	765.54	765.09	0.45
INQUI-S11	765.82	765.83	-0.02
CHE-1 (ST^{-3})	765.04	765.09	-0.05
Mean residual		-0.0052	
Nash index		0.7166	
R^2 (Determination coefficient)		0.7776	

INTERNATIONAL MASTER IN WATER ENGINEERING
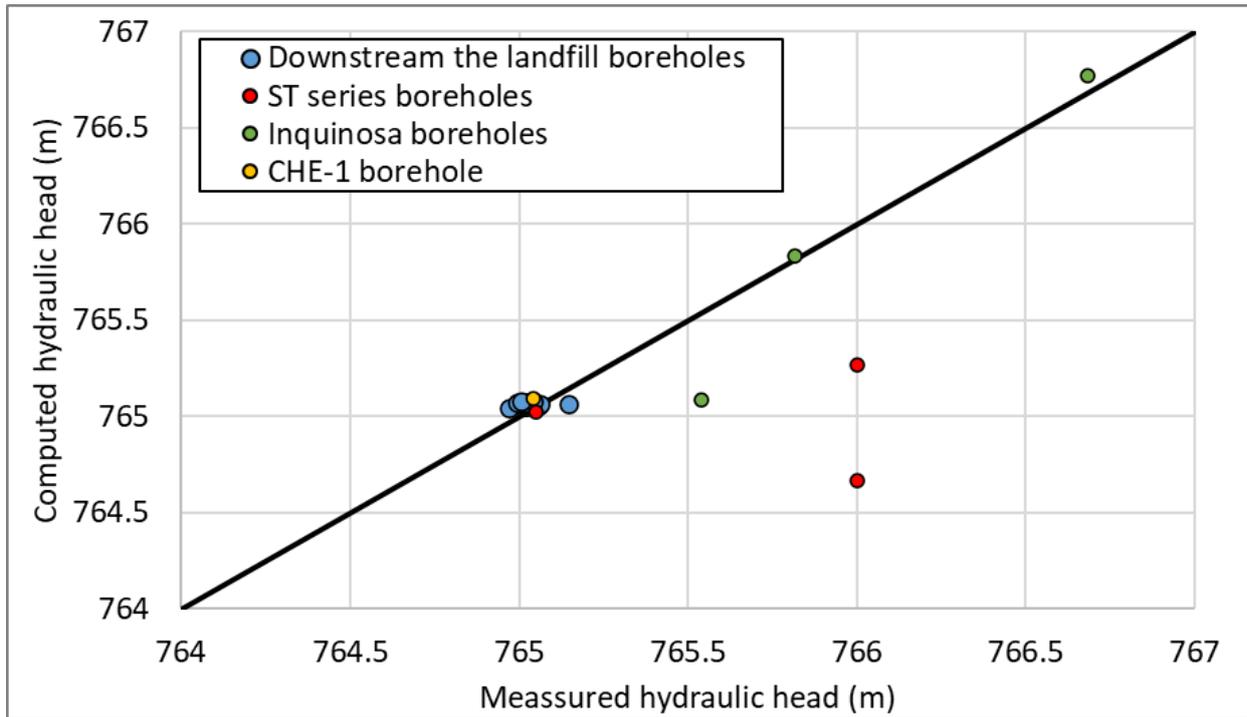
Figure 6.16. Scattergram of the computed and measured hydraulic heads (results with the final calibration).
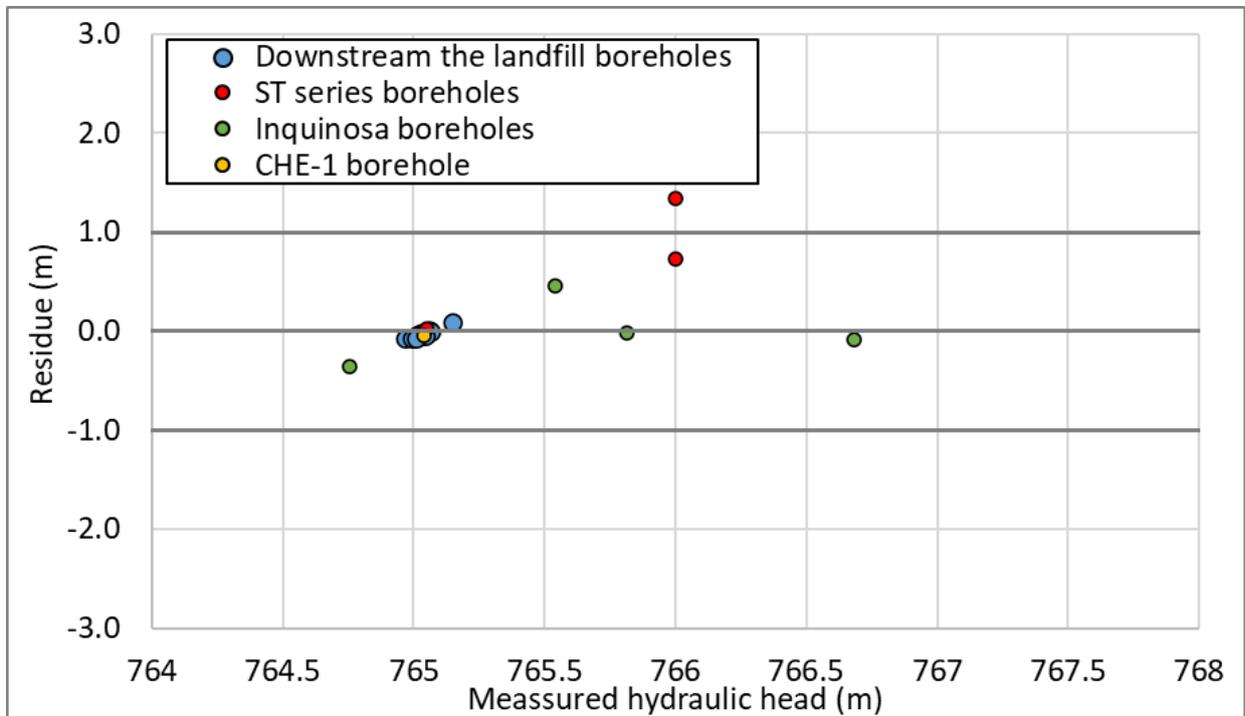
Figure 6.17. Scatter plot of the residuals, calculated as the difference between measured and computed hydraulic head, and the average measured hydraulic head (results with the final calibration).

Figure 6.18 shows the contour plot of computed hydraulic heads with the calibrated model with an equidistance of 0.5 m. There is a strong gradient on the right bank of the reservoir near INQUINOSA due to the lateral inflow and to the existence of a less permeable zone. Figure 6.19 presents a zoom of the map in the area located downstream the Sardas landfill. A flow towards the former course of Gállego river takes place. Figure 6.20 presents a zoom of the map of hydraulic head contours around the Sabiñánigo dam, where a strong hydraulic head gradient can be observed in the area of the less permeable material and upstream from the dam. The gradient of the hydraulic head in the area of the landfill is approximately equal to $2 \cdot 10^{-4}$.
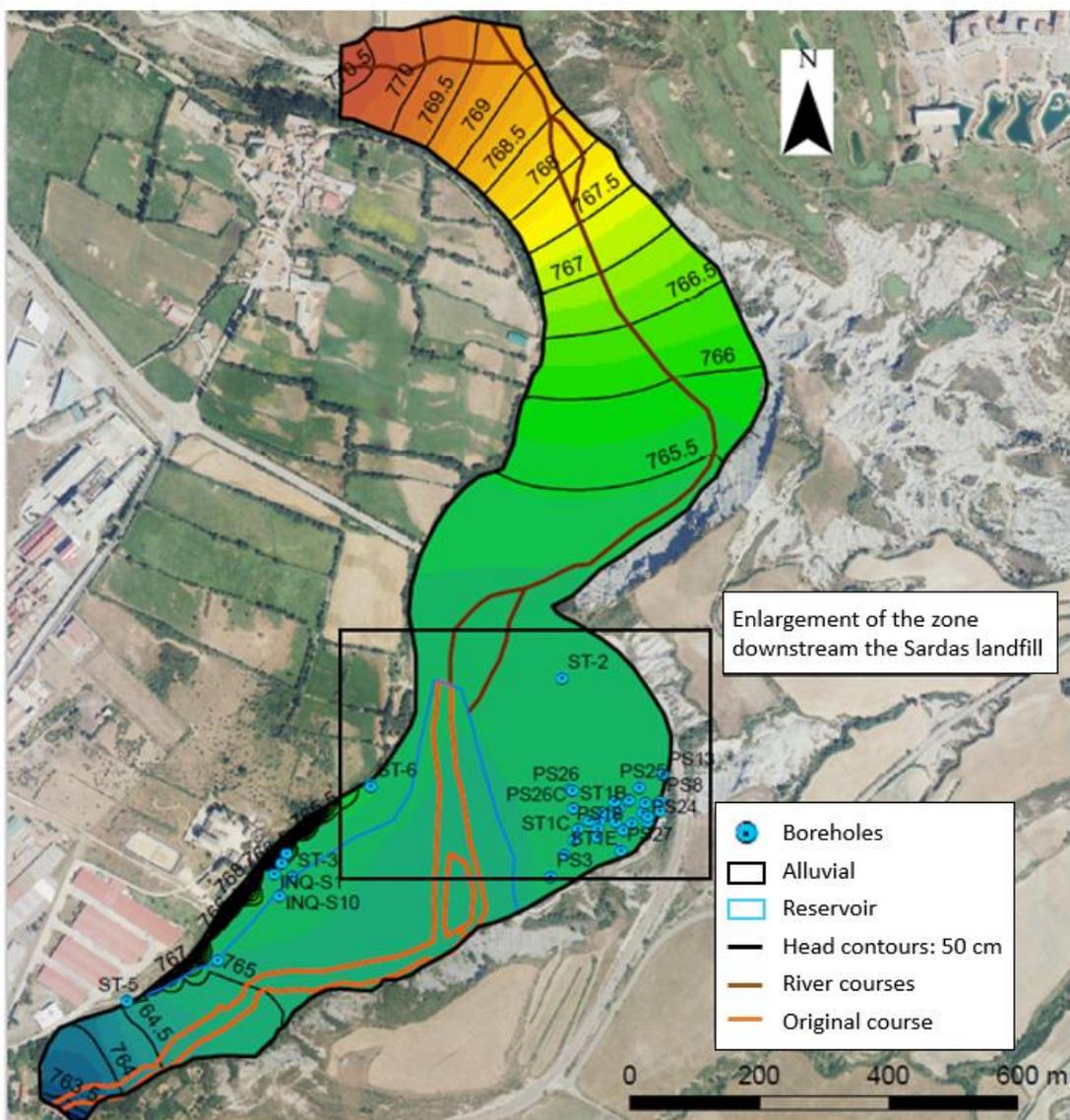
Figure 6.18. Map of hydraulic head contours calculated using the calibrated steady state groundwater flow 2D horizontal model. The hydraulic head contours interval is of 50 cm. The area inside the black rectangle is shown in the Figure 6.19.
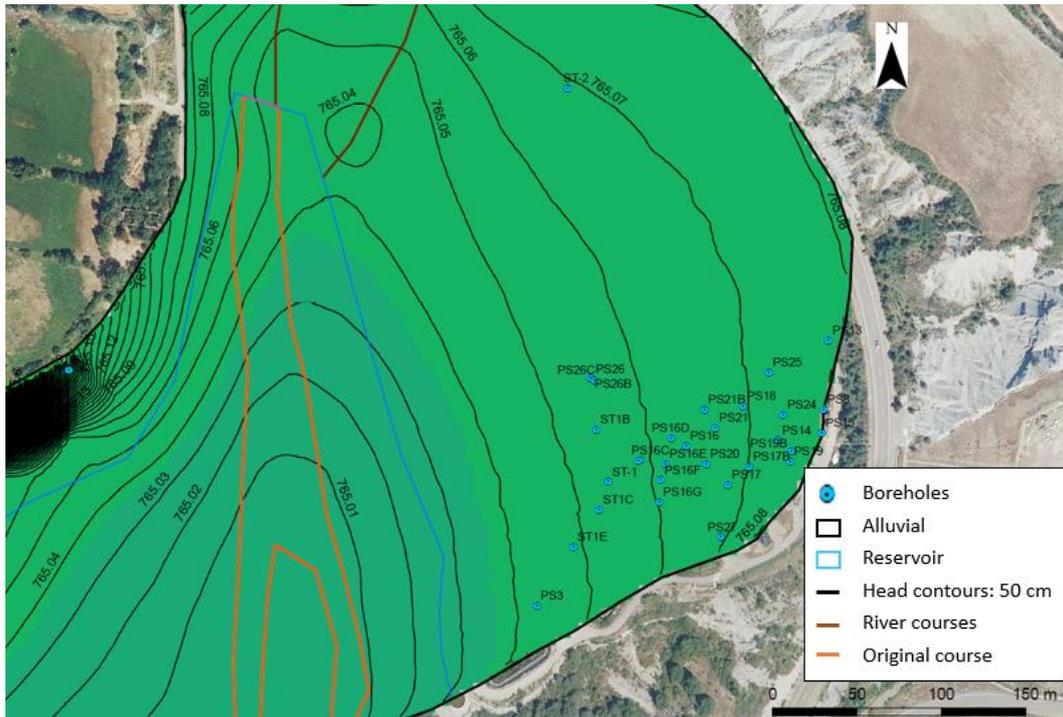
Figure 6.19.   Zoom the map of hydraulic head contours calculated using the calibrated steady state groundwater flow 2D horizontal model to the area located downstream the Sardas landfill (see location in Figure 6.18). Hydraulic head contours interval is 1 cm.
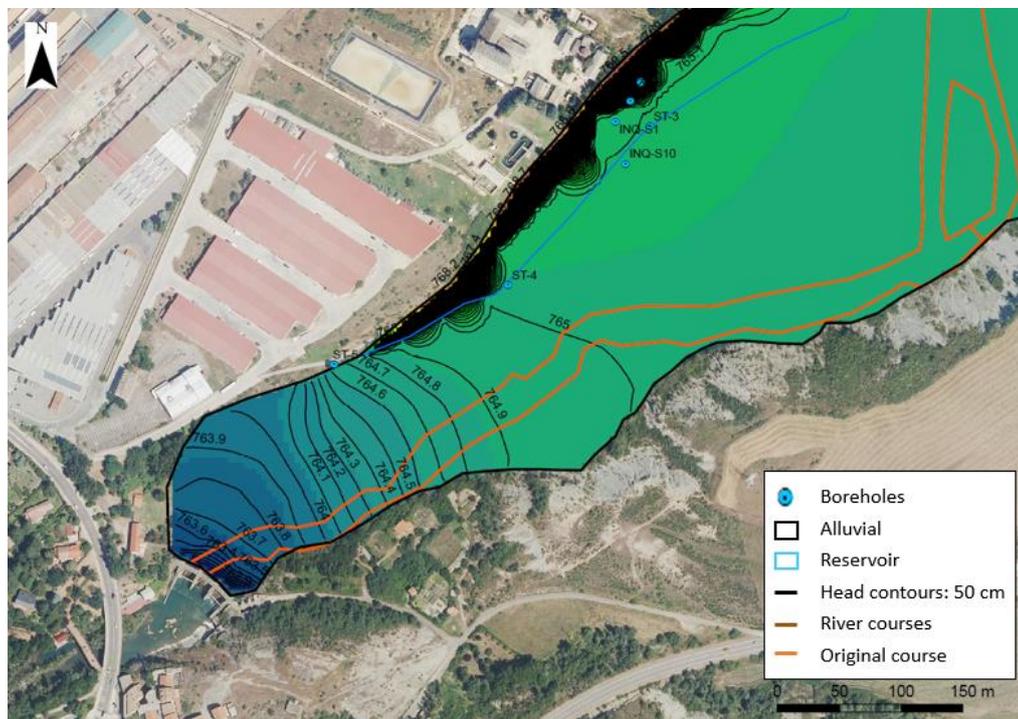
Figure 6.20.   Zoom to the map of hydraulic head contours calculated using the preliminary steady state groundwater flow 2D horizontal model to the area located to the area around the Sabiñánigo dam. Hydraulic head contours interval is 10 cm.

6.4.3 Groundwater balance in the model domain

Water inflows in the domain if the numerical model include (Table 6.8):

1) Left margin boundary inflows which are equal to 278.83 m^3/day and are equivalent to 9.12 % of the total inflow.

2) Right margin boundary inflows which are equal to 1228.96 m^3/day and are equivalent to 40.18 % of the total inflow.

3) Recharge by rainwater infiltration in the area where gravels are confined which is equal to 57.76 m^3/day and is equivalent to 1.89 % of the total inflow.

4) Recharge by rainwater infiltration in the area where the gravels are unconfined which is equal to 59.51 m^3/day and is equivalent to 1.95 % of the total inflow

5) Inflow from the Aurín riverbed to the aquifer which is equal to 1433.36 m^3/day and is equivalent to 46.87 % of the total.

Table 6.8.   Water inflows in the numerical model and percentage of each component with respect to the total water inflow.

Inflows	m^3/day	%
Left margin	278.83	9.12
Right margin	1228.96	40.18
Recharge in confined gravels	57.76	1.89
Recharge in unconfined gravels	59.51	1.95
Aurín riverbed	1433.36	46.87
Total	3058.41	100

Water outflows from the numerical model include the outflow to the Sabiñánigo reservoir, the outflow underneath the dam and the discharge into the Gállego river. Table 6.9 lists the groundwater outflows. The two branches of the Gállego river in this area of the model are denoted as north and south branches. Most of the groundwater discharge takes place into the Gállego main river course (53.40 %). An important part of that water comes from the Aurín river inflow.

Table 6.9.   Groundwater outflows (m³/d) in the steady-state model.

Outflows	m³/d	%
Reservoir	394.81	12.10
Dam	879.37	26.95
Gállego main river course	1742.69	53.40
Gállego river north branch	77.96	2.39
Gállego river south branch	168.45	5.16
Total	3263.28	100.00

The error in the water balance in the 2D steady-state horizontal numerical model is equal to 7 %.

In addition to the overall water balance in the model domain, the inflows, outflows and the flow across the section of the bridge of the N-330 road are listed in Table 6.10. The groundwater flow across the section of the N-330 bridge is equal to 536 m³/d.

Table 6.10.   Average daily flows (m³/d) upstream and downstream the N-330 bridge.

Split balance	Inflow (m³/d)	Outflow (m³/d)	Transferred flow (m³/d)
Upstream the N-330 bridge	2007.42	-1471.38	-536.04
Downstream the N-330 bridge	1088.14	-1782.22	

Figure 6.21 shows the map of the areas of the inflow from the reservoir into the gravels and the outflow from the gravels into the reservoir. The Aurín river flows into the aquifer at its mouth on the Gállego river. This can also be seen in the hydraulic head contour maps. On the other hand, the alluvial aquifer discharges into the Gállego river downstream the Aurín river. Near the dam, there is a flow from the reservoir into the aquifer, due to the reduction in hydraulic heads as consequence of the dam boundary condition, having a fixed hydraulic head of 752 m. Figure 6.22 shows the map of the inflows (+) and outflows (-) from the aquifer into the reservoir.
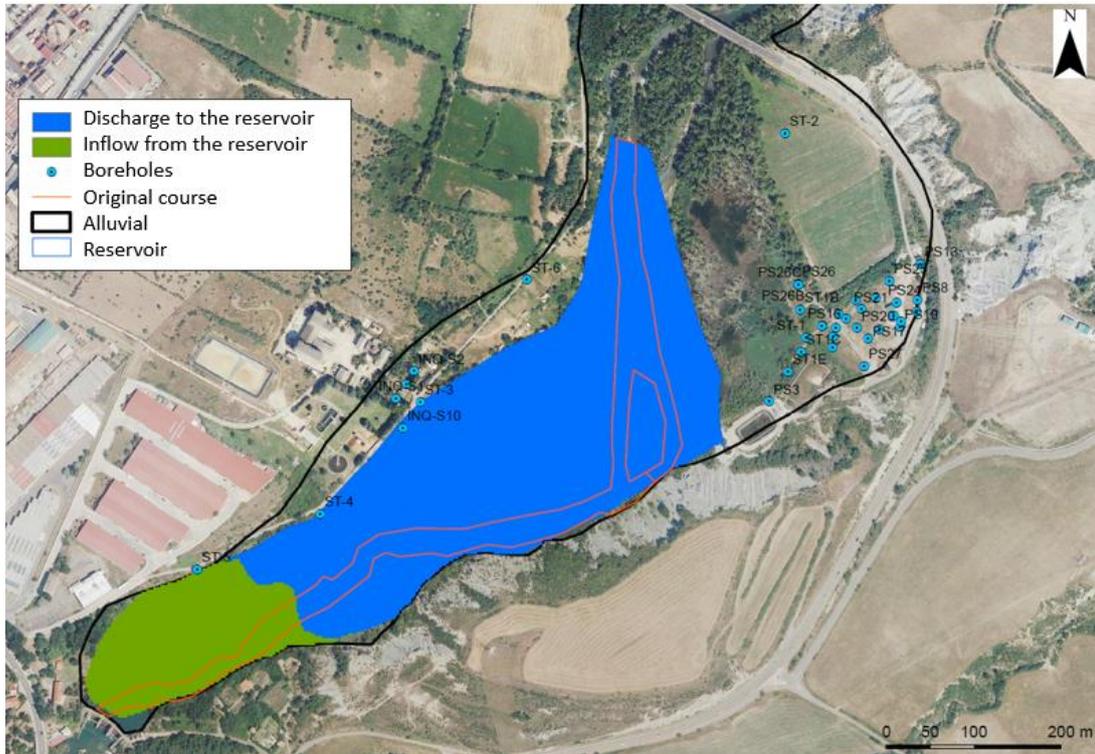
Figure 6.21. Map of the discharge areas from the aquifer to the reservoir and the recharge areas from the reservoir to the aquifer.
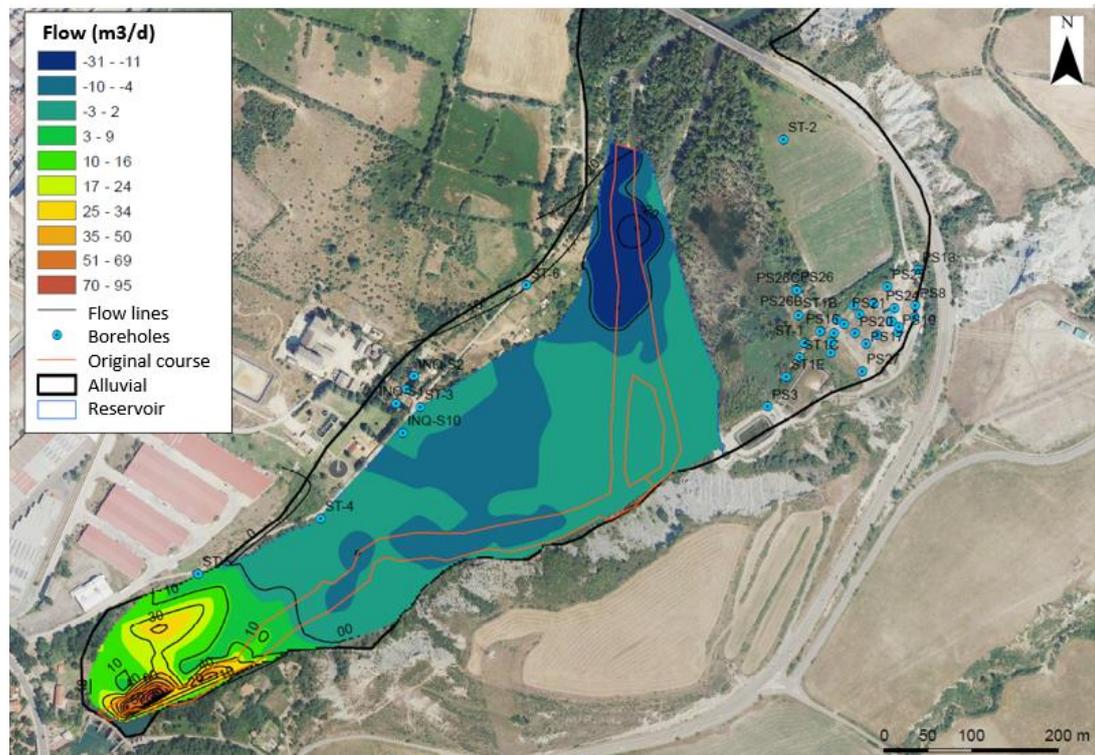
Figure 6.22. Contour plot of inflows (+) and outflows (-) from the aquifer into the reservoir.

6.5 Conclusions

A 2D steady-state groundwater flow horizontal model through the gravels of the Gállego river alluvial aquifer from the mouth of the Aurín river to the Sabiñánigo dam has been presented. The model has been formulated to: 1) Quantify the tidal effect of the daily fluctuations of the Sabiñánigo reservoir level on the aquifer hydraulic heads; 2) Estimate the hydraulic conductivity of the sediments at the bottom of the reservoir; and 3) Estimate the hydraulic conductivity of the gravels.

Groundwater inflows include: 1) Areal recharge from rainfall infiltration; 2) Lateral inflows along the East and West boundaries of the alluvial aquifer and 3) Inflow from the reservoir at the downstream part of the aquifer near the Sabiñánigo dam. Groundwater discharges to the Sabiñánigo reservoir, the Gállego river upstream the reservoir, and the Gállego river underneath the Sabiñánigo dam. Groundwater discharges have been simulated with Cauchy conditions in with leakage coefficients estimated during the model calibration.

Model parameters have been calibrated by using measured hydraulic head data at 40 observation boreholes. The hydraulic conductivity of the gravels on the right bank near the INQUINOSA factory is equal to 1.7 m/d. This value is significantly smaller than the conductivity in the rest of the alluvial aquifer which is equal to 400 m/d. The calibrated values of the vertical hydraulic conductivities of the alluvial silts and of the silting sediments are equal to 0.1 m/d and 0.4 m/d, respectively. The absolute values of the hydraulic head residuals are smaller than 1 m.

The results of the model sensitivity runs show that: 1) The hydraulic heads in the gravels are not significantly sensitive to changes in the hydraulic conductivity of the gravels and to the increase of the vertical hydraulic conductivity of the silting sediments, K_s, for $K_s > 0.2$ m/d; 2) The hydraulic heads in the gravels, on the other hand, are very sensitive to the increase of K_s, the changes in the water level of the reservoir and the water level of the Gállego river upstream the reservoir; 3) The groundwater discharge flow from the gravels into the reservoir is very sensitive to changes of the vertical hydraulic conductivity of the alluvial silts and changes in K_s.

Model results confirm that groundwater discharges into the reservoir at the tail of the reservoir (far from the Sabiñánigo dam). Near the dam, however, there is a downwards vertical water flow from the reservoir into the gravels which later flows underneath the dam through the underlying sandstones of the dam foundation.

7. 2D TRANSIENT-STATE HORIZONTAL GROUNDWATER FLOW MODEL THROUGH THE GRAVELS OF THE ALLUVIAL OF THE GÁLLEGO RIVER

7.1 Introduction

This chapter presents a 2D transient-state horizontal groundwater flow model through the gravels of the Gállego river alluvial aquifer from the mouth of the Aurín river to the Sabiñánigo dam which is based on the stead-state model presented in Chapter 6. Numerical simulations have been performed for two-time horizons. A multiannual time horizon was performed for the period February 26th 2014 to August 29th 2019. The second simulation period is 4 months long (122 days) and extends from June 1st to September 30th 2017. The chapter starts with a description of the numerical model. Then, model results are presented. The chapter ends with the main conclusions.

7.2 Available data

A multiannual time horizon was performed for the period February 26th 2014 to August 29th 2019. The second simulation period is 4 months long (122 days) and extends from June 1st to September 30th 2017. This simulation period was selected due to the availability of reservoir water level and hydraulic head diver data in the aquifer every half hour. The gaps in reservoir water level data have been filled with data from the same day of the previous weeks. The water level of the reservoir fluctuated from 764.5 m to 765.3 m during the simulation period.

7.3 Numerical model

7.3.1 Initial conditions

The computed steady-state hydraulic heads have been used to define the initial heads for the multiannual transient-state simulation. The heads computed with the multiannual model on July 1st 2016 were used as initial heads for the transient-state quarterly model.

7.3.2 Recharge and boundary conditions

The boundary conditions of the transient-state model are the same as those of the steady-state model. Recharge due to rainwater infiltration in the alluvial has been calculated by using a hydrological water balance model (Samper et al., 2018 a). Figure 7.1 shows the calculated time evolution of the recharge by rainwater infiltration after been normalized for a mean recharge value equal to 1 mm/d. The model domain is divided in the same two recharge zones as those of the steady-state model (Figure 6.5). A recharge time function has been defined for each zone by multiplying the normalized recharge time function by the mean values considered for each recharge zone in the steady-state model (Table 6.3).

The reservoir water level changes with time. Figure 7.2 and Figure 7.3 show the time evolution of the reservoir water level in the multiannual and quarterly transient-state models.
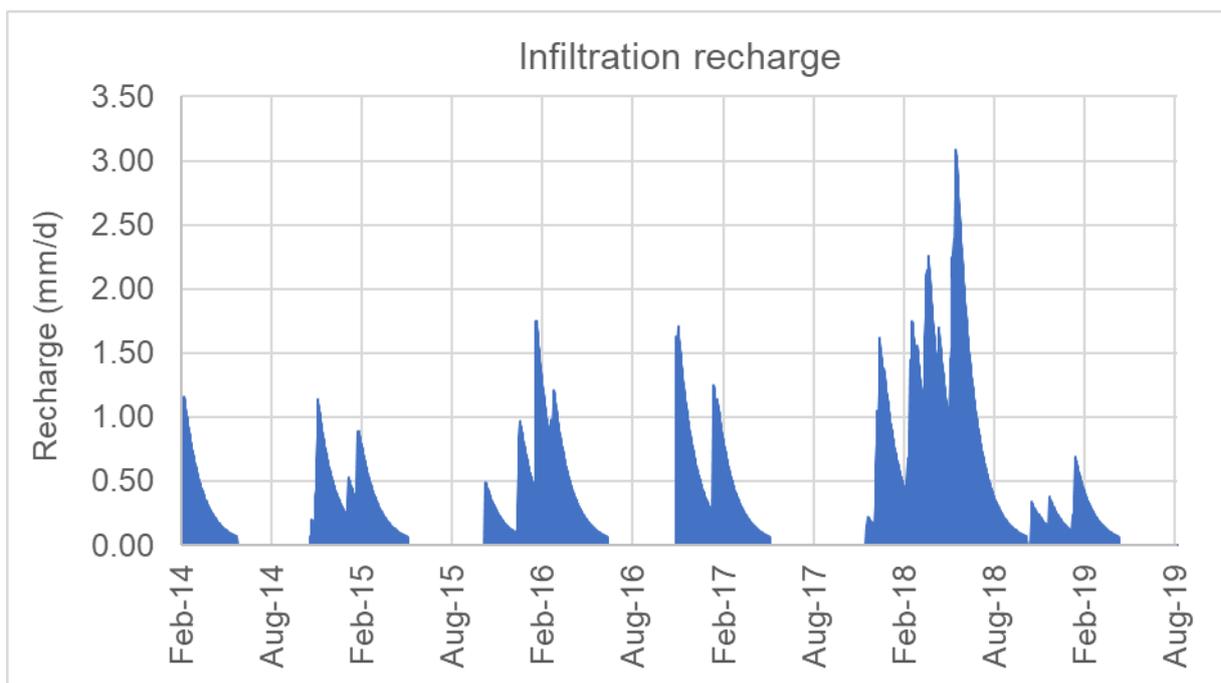
Figure 7.1.   Normalized time function of daily recharge due to rainwater infiltration.
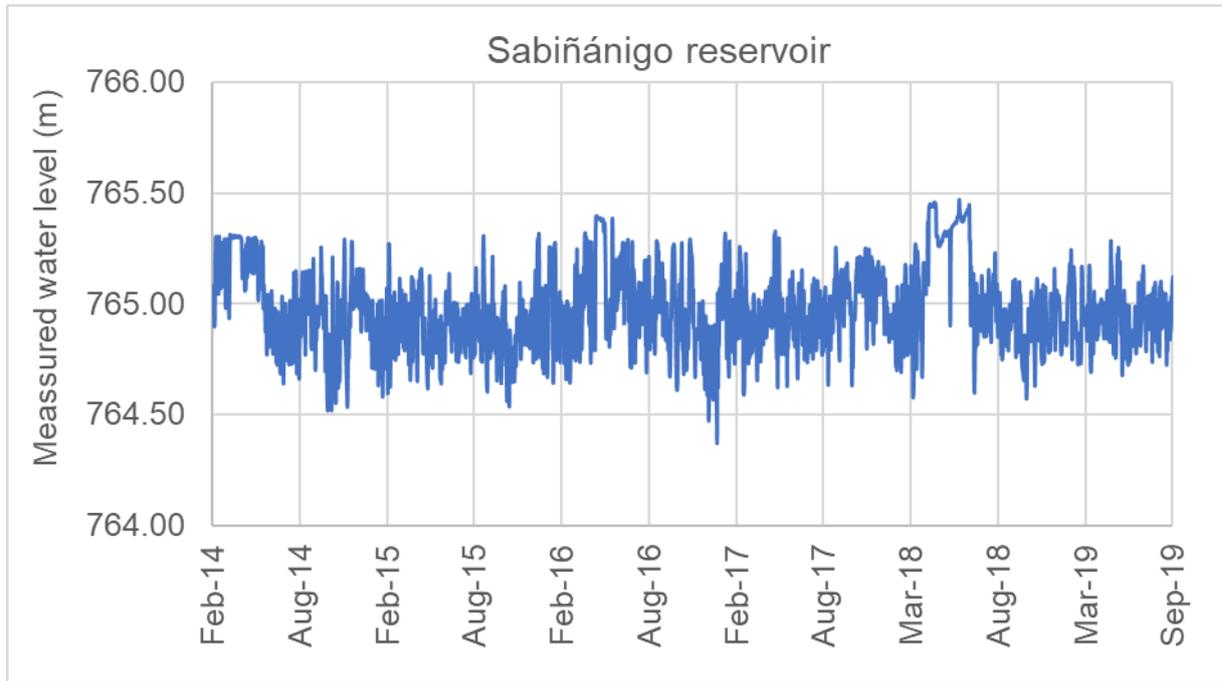
Figure 7.2.   Time evolution of water levels in the Sabiñánigo reservoir from February 26th 2014 to August 29th 2019 in the multiannual transient state model.
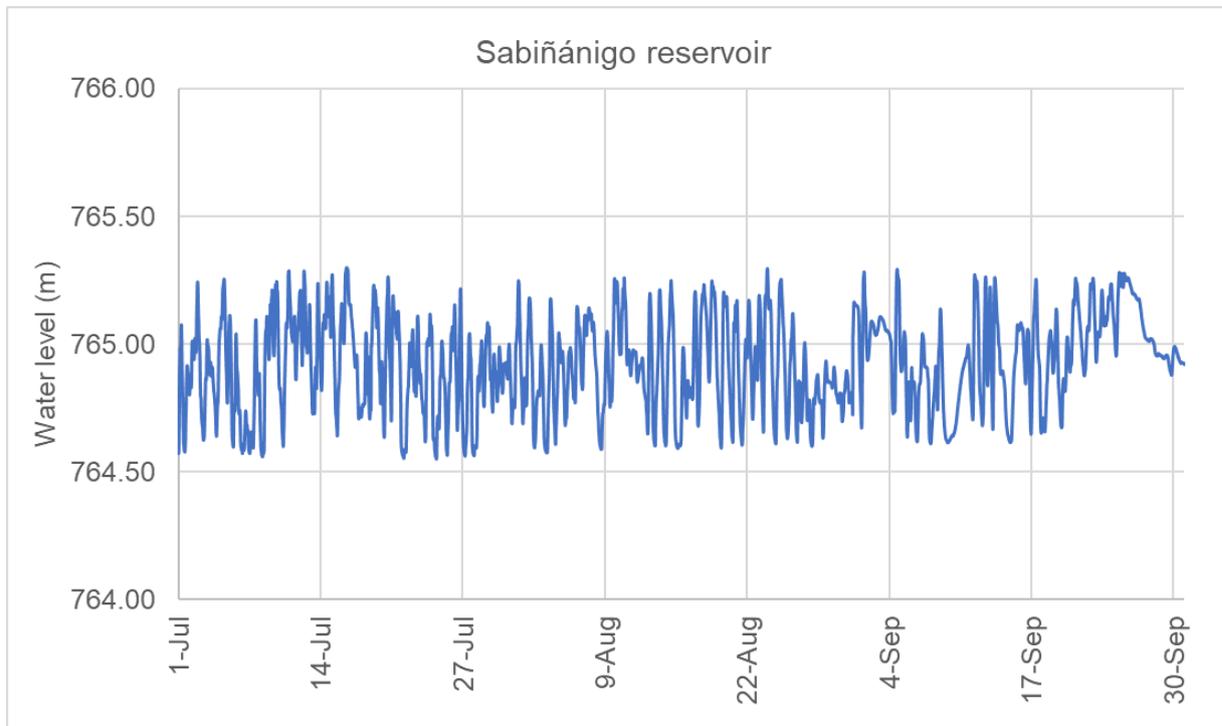
Figure 7.3.   Time evolution of water levels in the Sabiñánigo reservoir from July 1st to September 30th 2017 in the quarterly transient state model.

7.4 Model results

7.4.1 Hydrographs

Figure 7.4 to Figure 7.12 show the measured and calculated hydrographs with the multiannual transient-state model. Model results are shown only for boreholes equipped with divers.
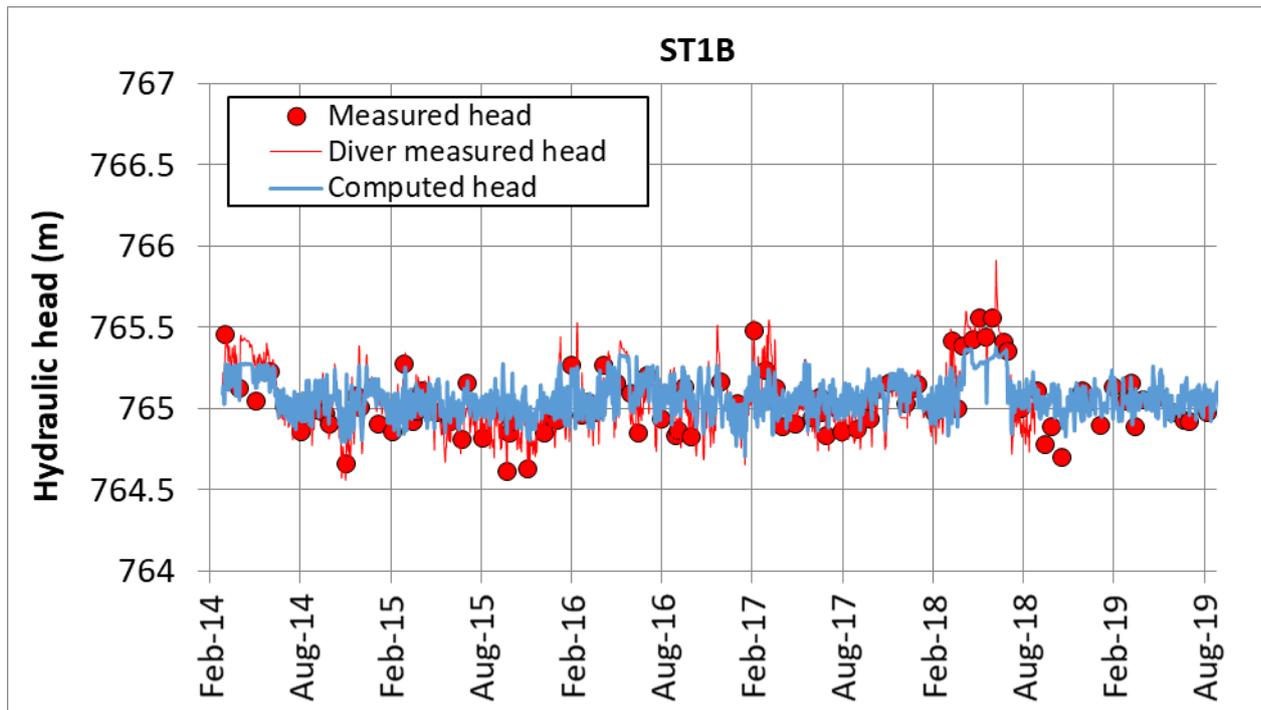
Figure 7.4. Measured hydraulic heads with hydro-level probe (symbols), measured heads with diver (red line) and computed hydraulic heads (blue line) in ST1B borehole.
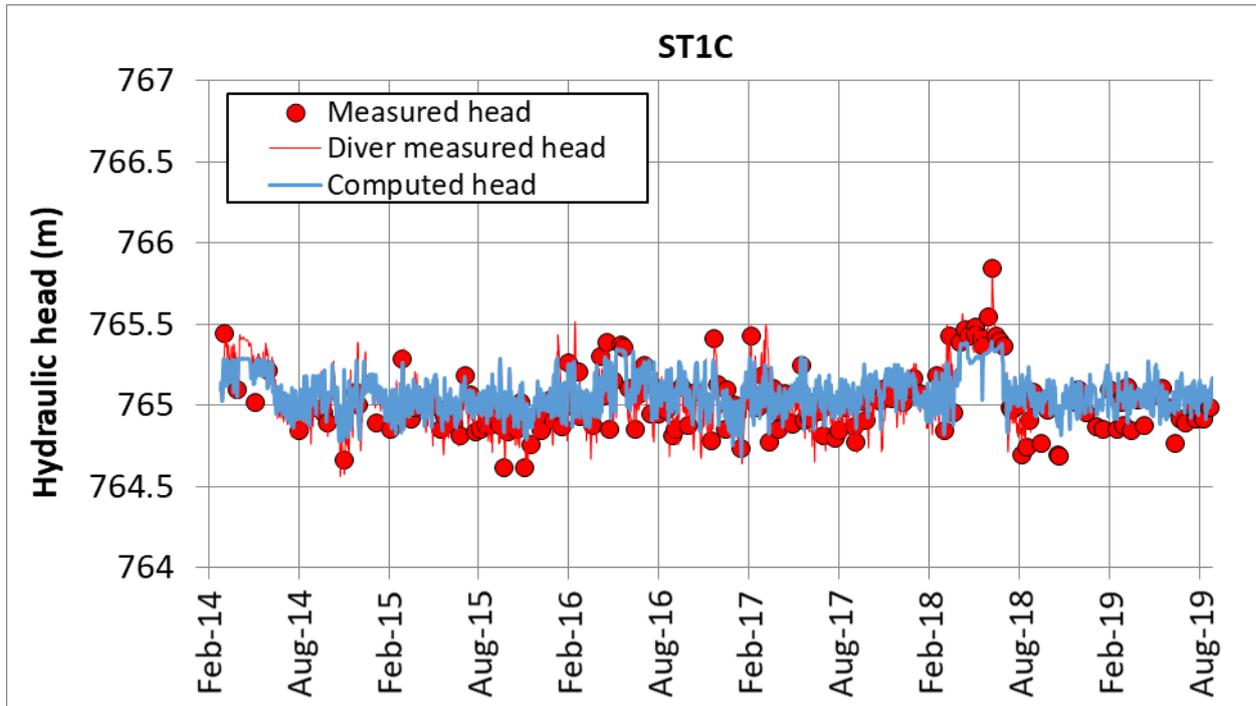
Figure 7.5. Measured hydraulic heads with hydro-level probe (symbols), measured heads with diver (red line) and computed hydraulic heads (blue line) in ST1C borehole.
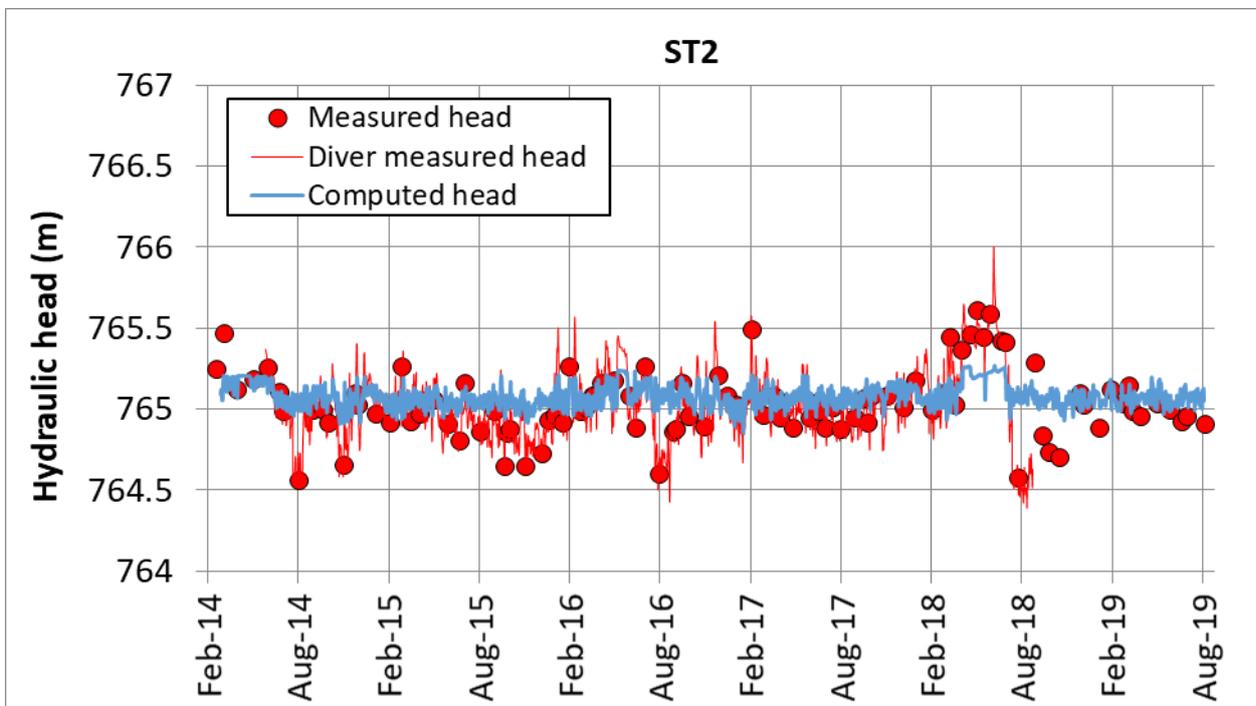
Figure 7.6. Measured hydraulic heads with hydro-level probe (symbols), measured heads with diver (red line) and computed hydraulic heads (blue line) in ST2 borehole.
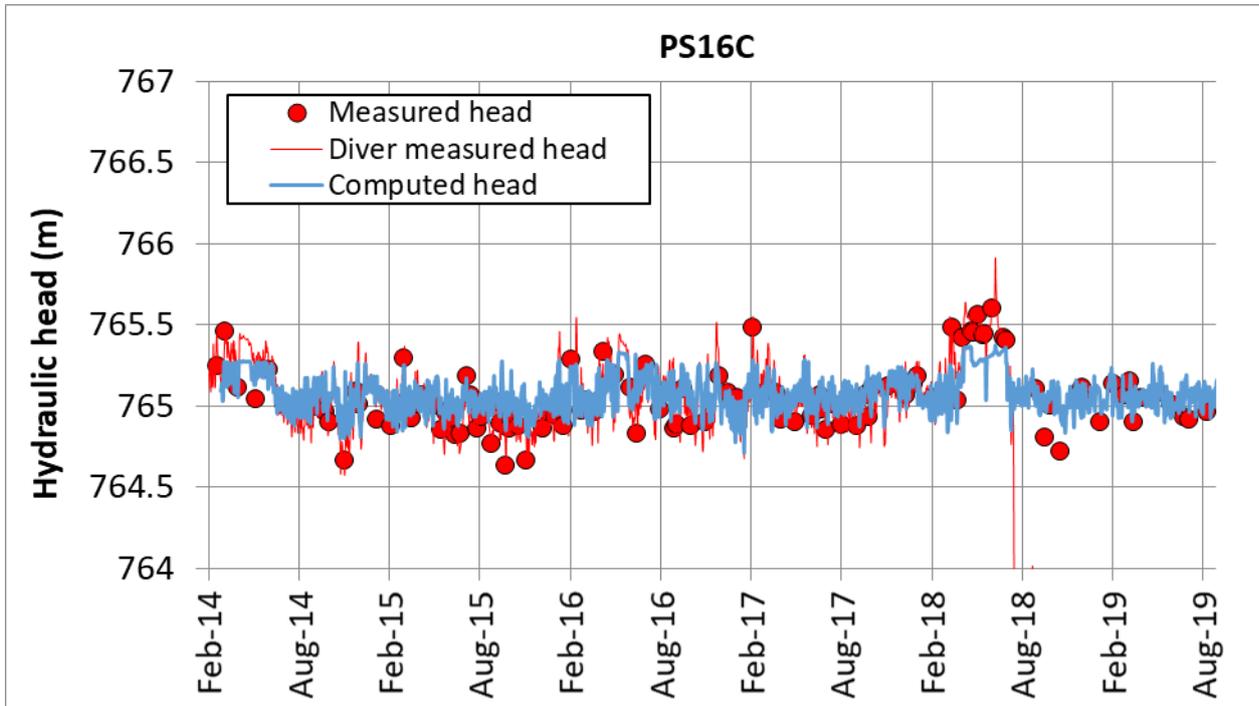
Figure 7.7.   Measured hydraulic heads with hydro-level probe (symbols), measured heads with diver (red line) and computed hydraulic heads (blue line) in PS16C borehole.
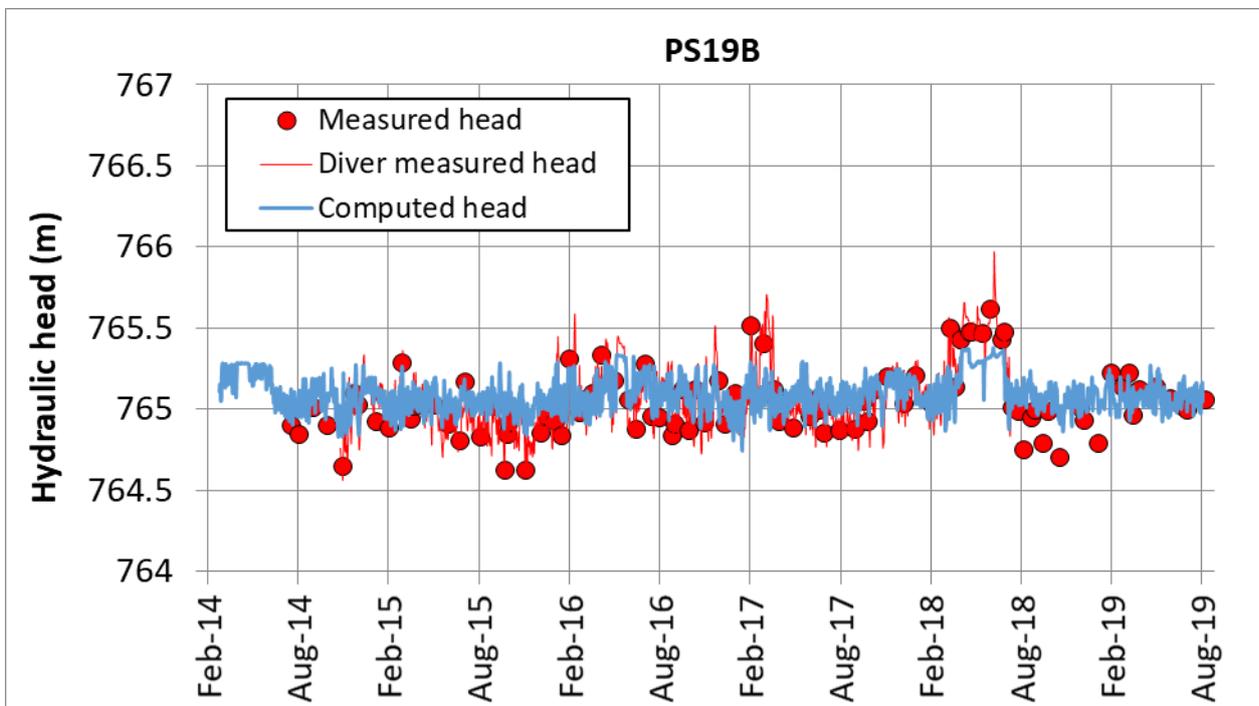
Figure 7.8.   Measured hydraulic heads with hydro-level probe (symbols), measured heads with diver (red line) and computed hydraulic heads (blue line) in PS19B borehole.
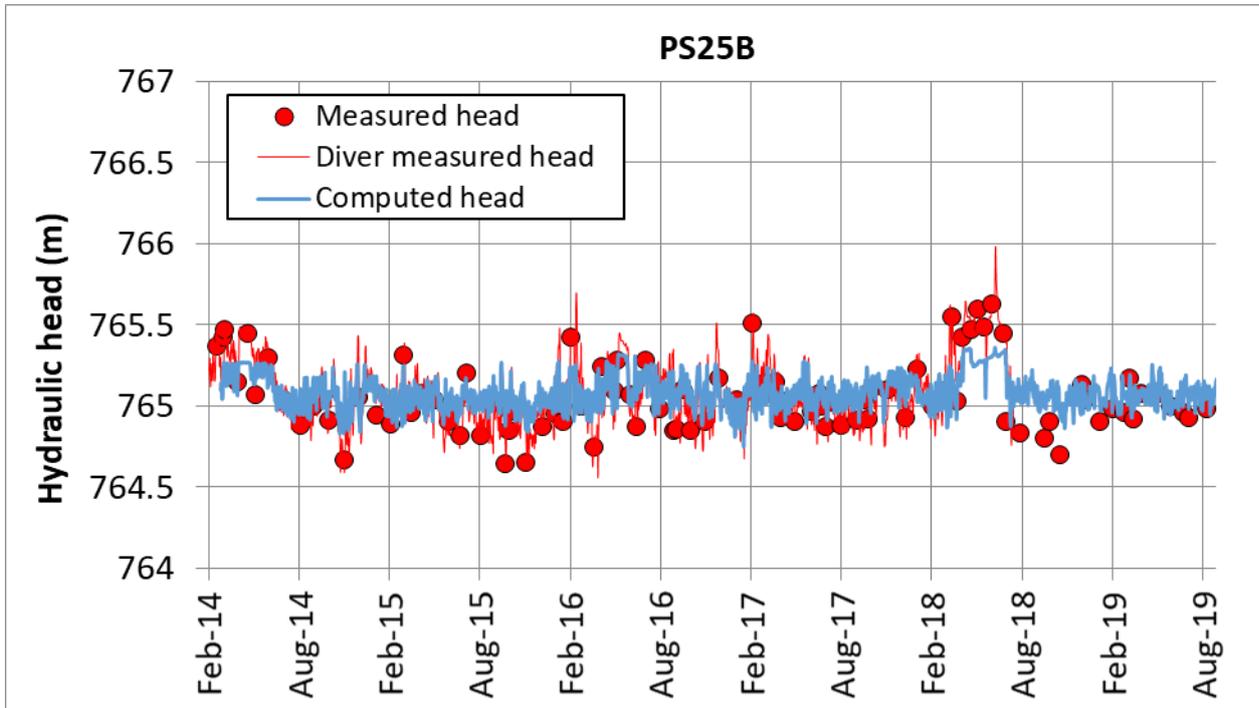
Figure 7.9.   Measured hydraulic heads with hydro-level probe (symbols), measured heads with diver (red line) and computed hydraulic heads (blue line) in PS25B borehole.
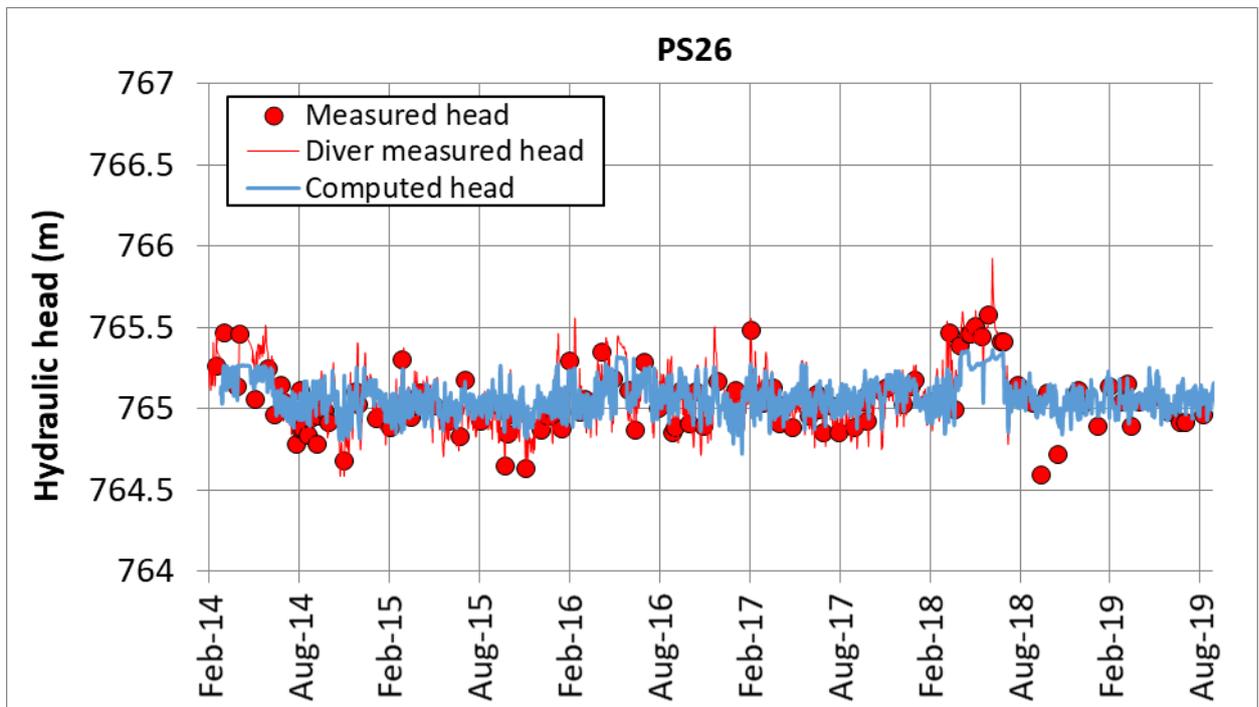
Figure 7.10.   Measured hydraulic heads with hydro-level probe (symbols), measured heads with diver (red line) and computed hydraulic heads (blue line) in PS26 borehole.
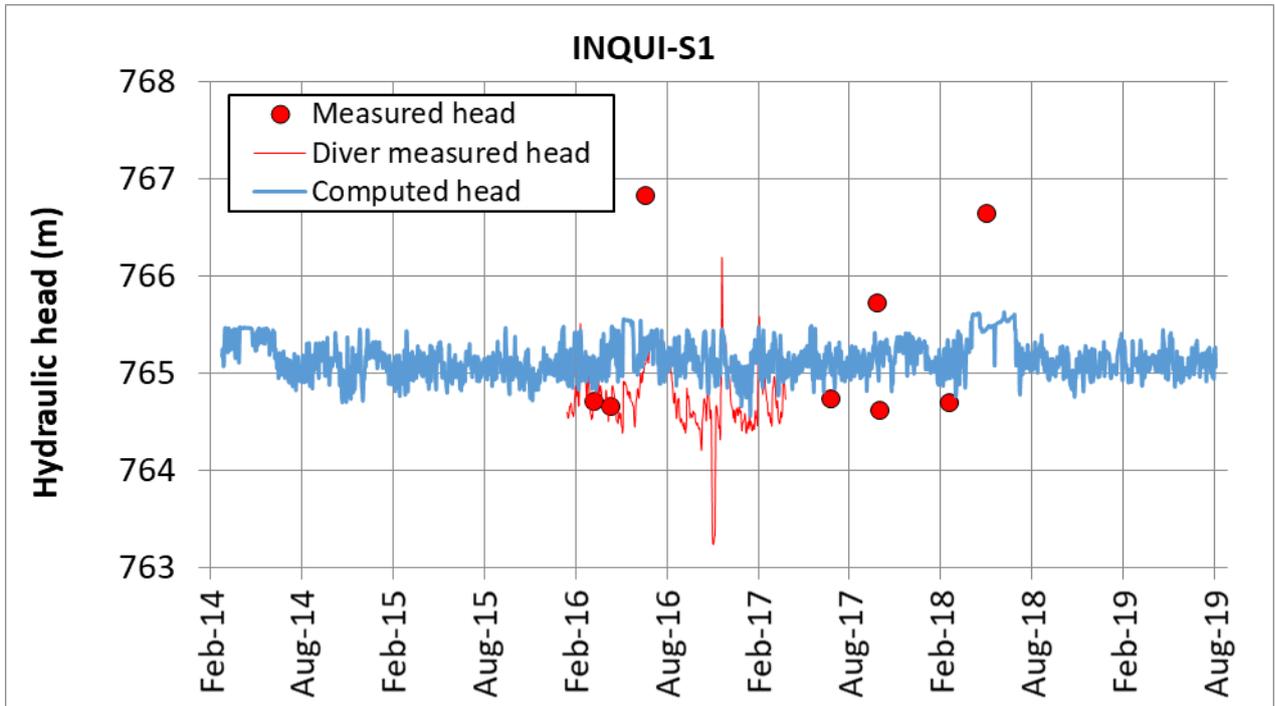
Figure 7.11. Measured hydraulic heads with hydro-level probe (symbols), measured heads with diver (red line) and computed hydraulic heads (blue line) in INQUI-S1 borehole.
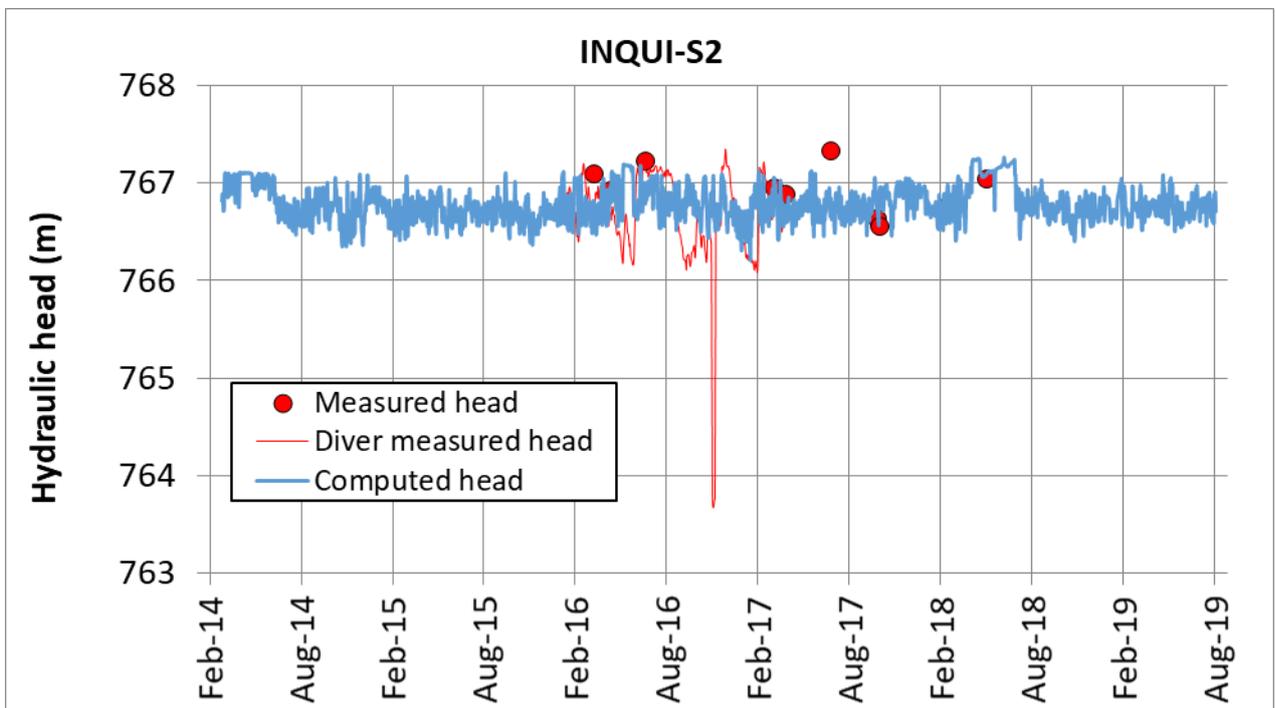
Figure 7.12. Measured hydraulic heads with hydro-level probe (symbols), measured heads with diver (red line) and computed hydraulic heads (blue line) in INQUI-S2 borehole.

The calculated hydraulic heads generally reproduce the measured hydraulic heads. The hydraulic heads measured with hydro-level probe in the INQUI-S1 borehole show fluctuations larger than those of the calculated hydraulic heads (Figure 7.11). It can be concluded that the oscillations of the reservoir water level affect the hydrographs of the boreholes drilled in the alluvial aquifer.

Figure 7.13 to Figure 7.21 show the measured and calculated hydrographs with the quarterly transient-state flow model in the boreholes used for model calibration. Similar to the multiannual transient-state model, the computed hydraulic heads in the quarterly model fit the measured hydraulic heads. The computed hydraulic heads in some boreholes such as PS19B, ST2 and INQUI-S2 are slightly larger than the measured hydraulic heads.
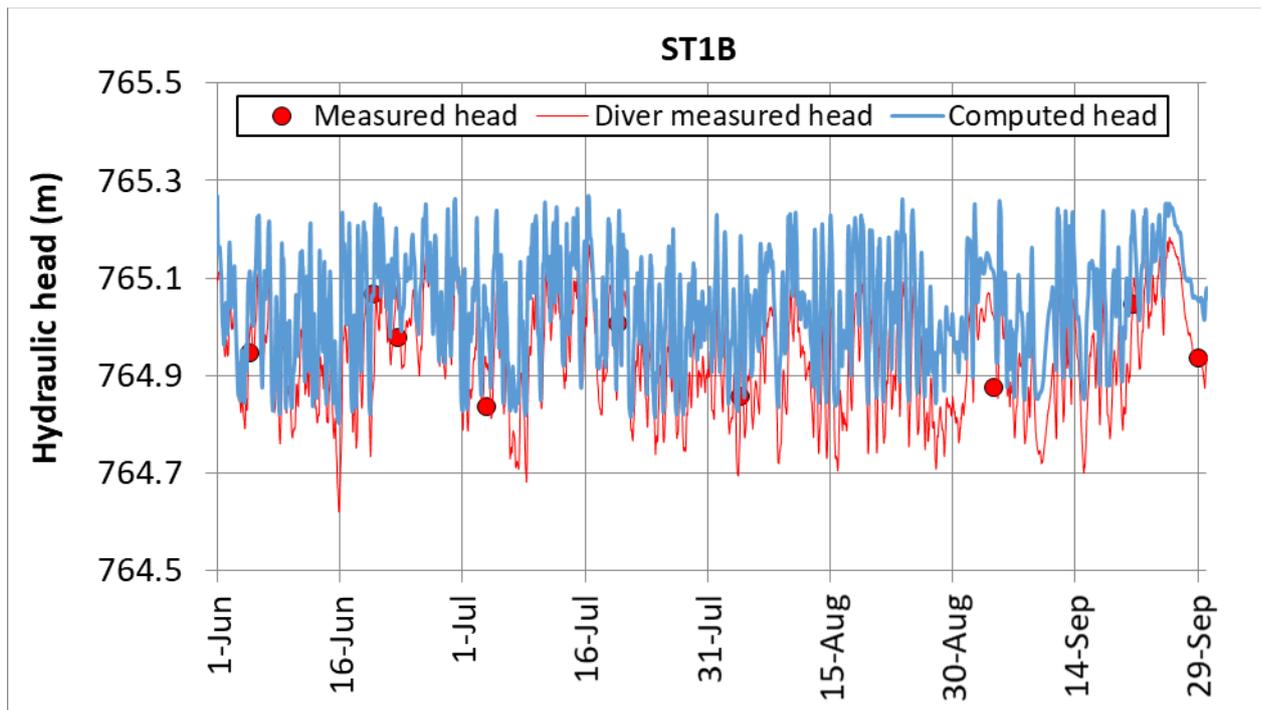
Figure 7.13.   Measured hydraulic heads with hydro-level probe (symbols), measured heads with diver (red line) and computed hydraulic heads (blue line) in ST1B borehole.
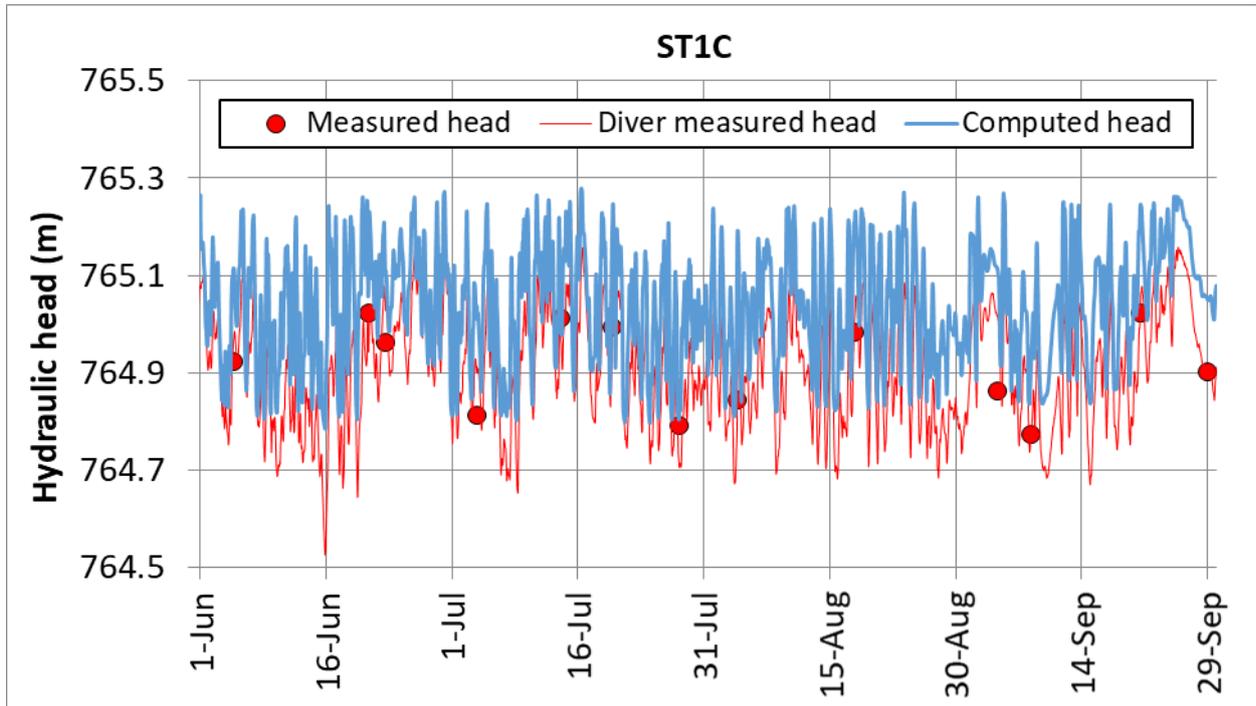
Figure 7.14.   Measured hydraulic heads with hydro-level probe (symbols), measured heads with diver (red line) and computed hydraulic heads (blue line) in ST1C borehole.
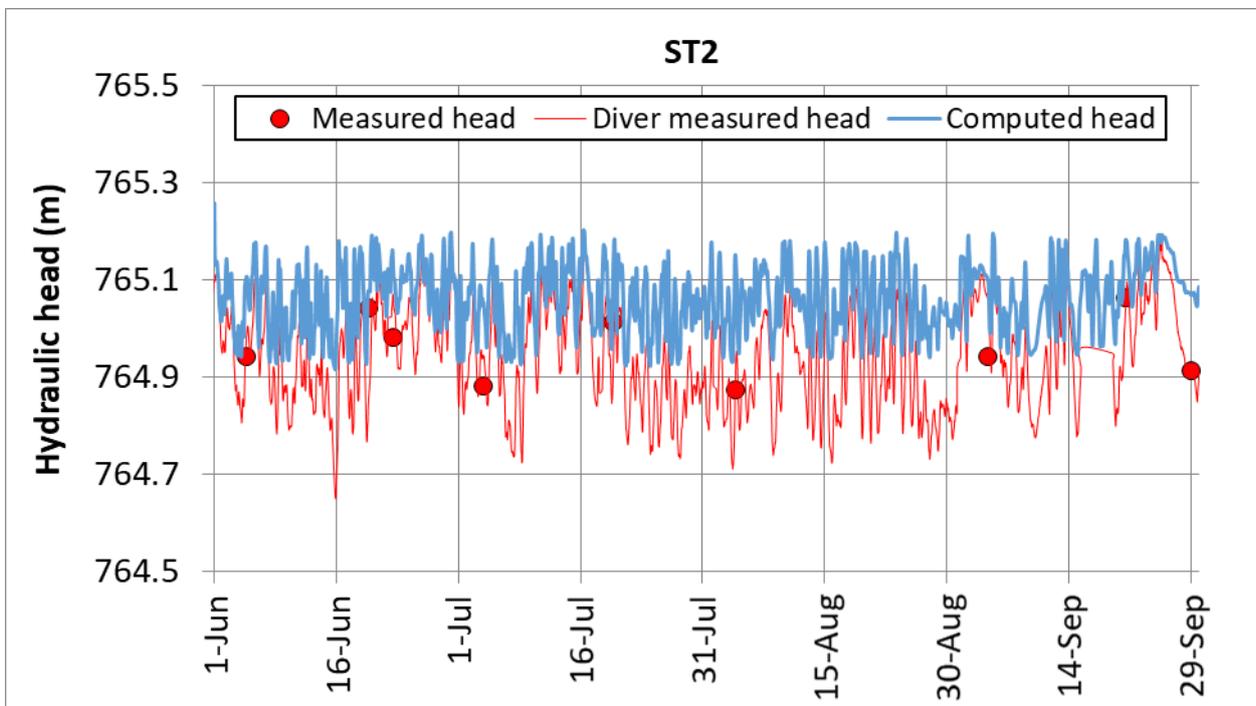
Figure 7.15.   Measured hydraulic heads with hydro-level probe (symbols), measured heads with diver (red line) and computed hydraulic heads (blue line) in ST2 borehole.
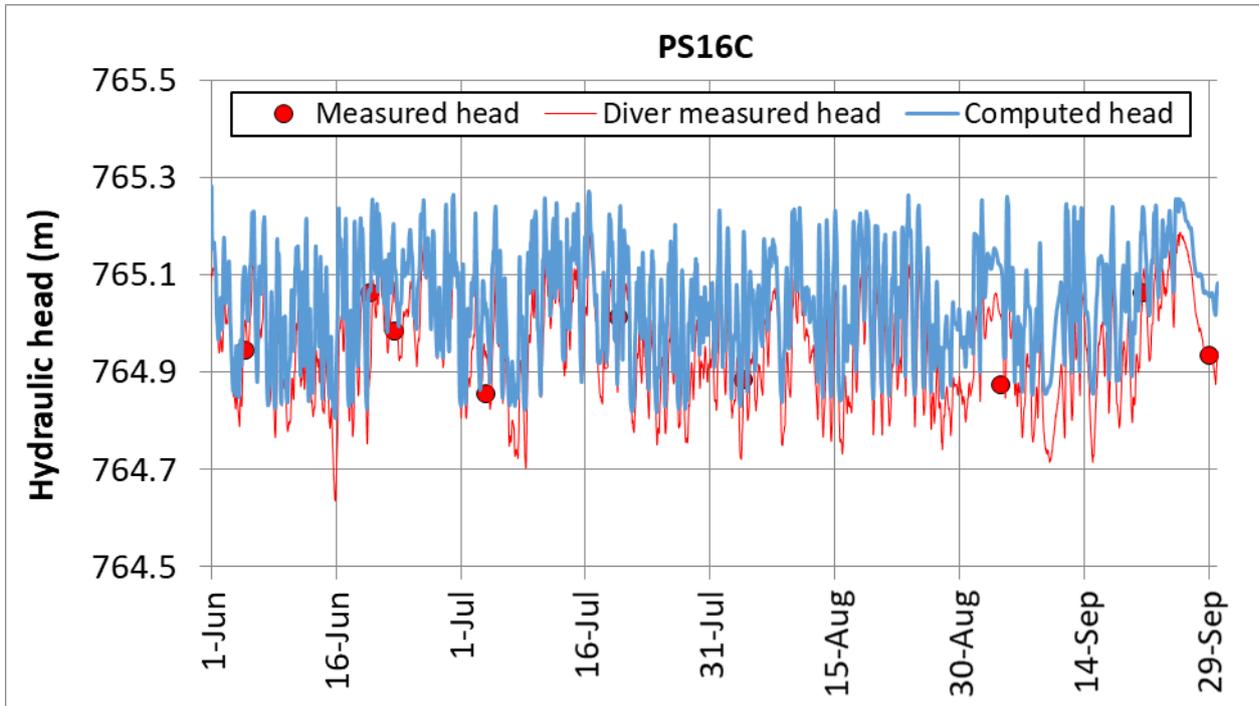
Figure 7.16. Measured hydraulic heads with hydro-level probe (symbols), measured heads with diver (red line) and computed hydraulic heads (blue line) in PS16C borehole.
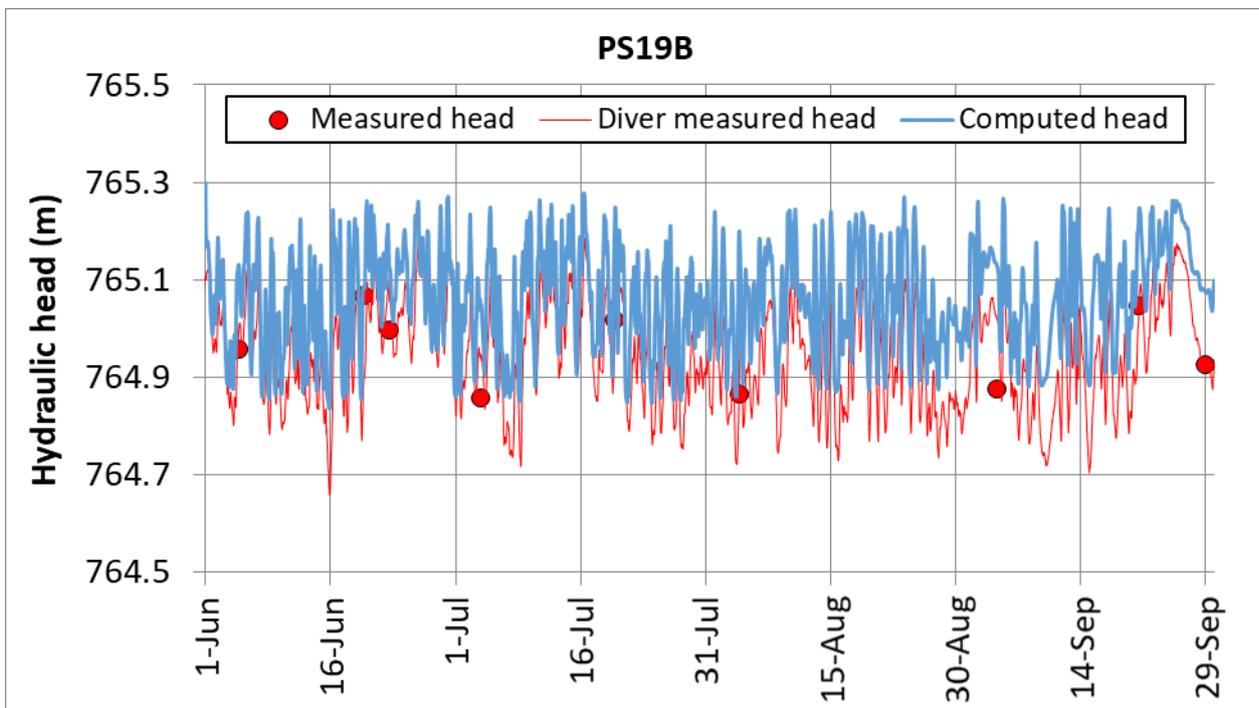
Figure 7.17. Measured hydraulic heads with hydro-level probe (symbols), measured heads with diver (red line) and computed hydraulic heads (blue line) in PS19B borehole.
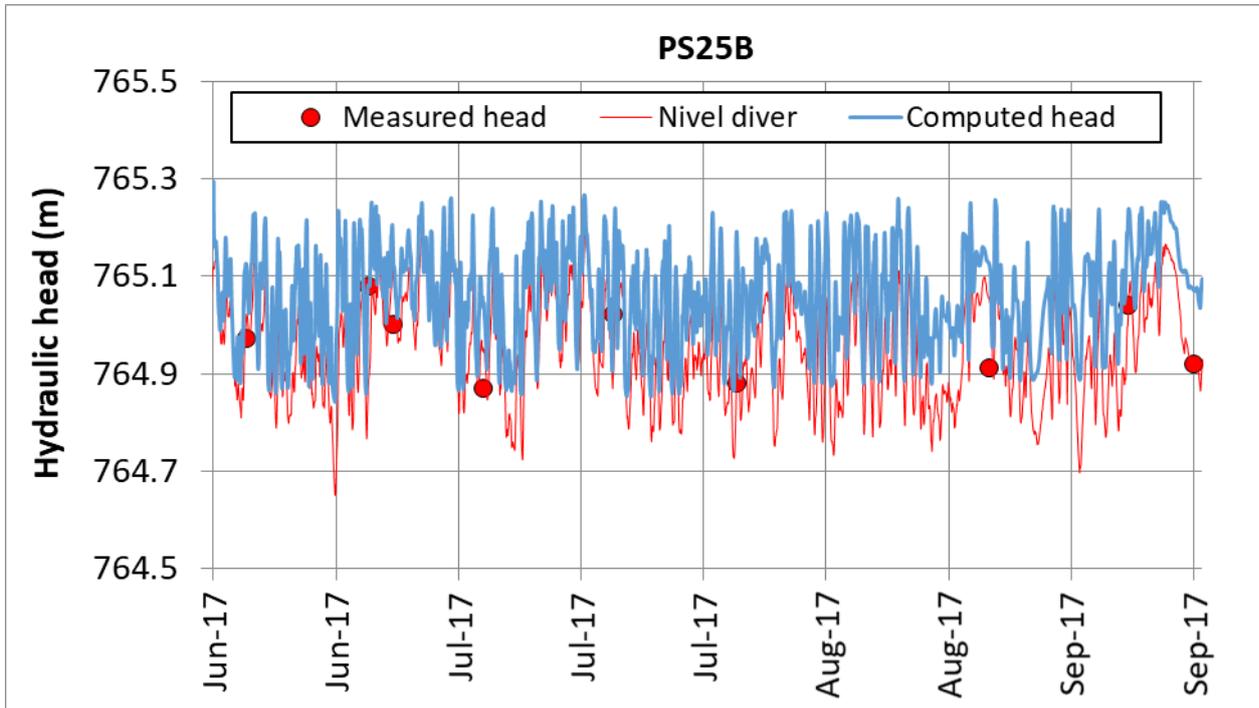
Figure 7.18. Measured hydraulic heads with hydro-level probe (symbols), measured heads with diver (red line) and computed hydraulic heads (blue line) in PS25B borehole.
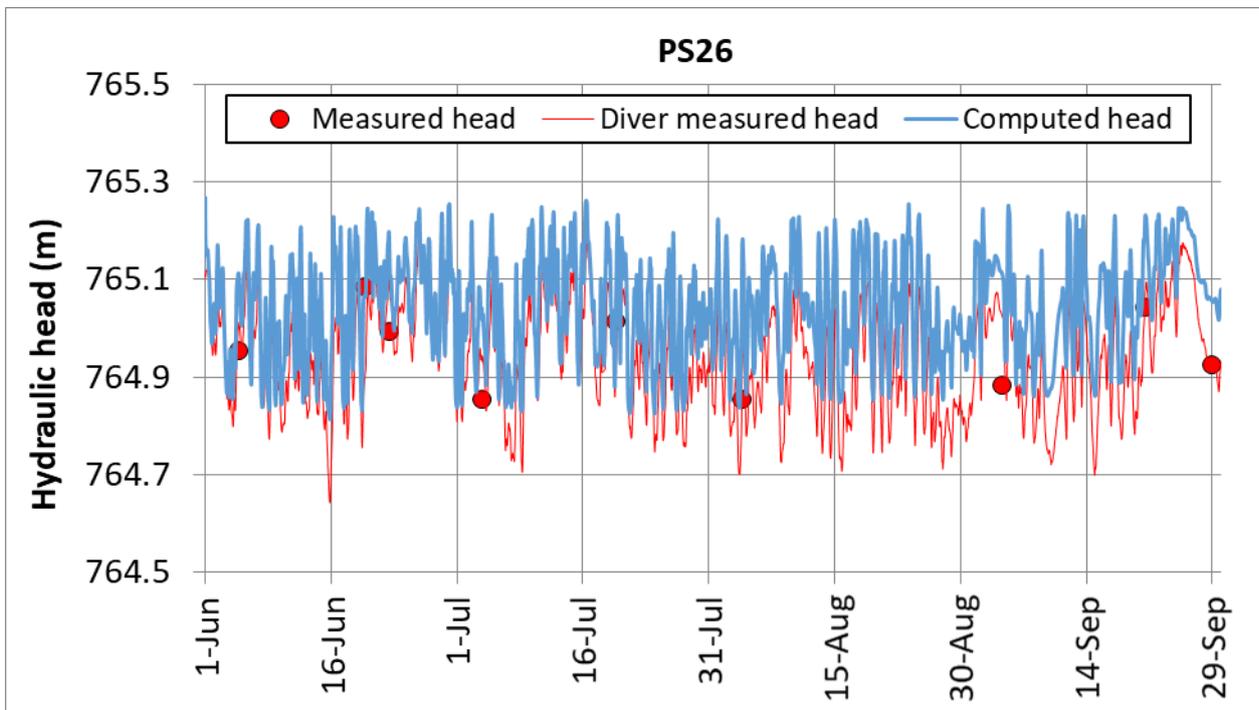
Figure 7.19. Measured hydraulic heads with hydro-level probe (symbols), measured heads with diver (red line) and computed hydraulic heads (blue line) in PS26 borehole.
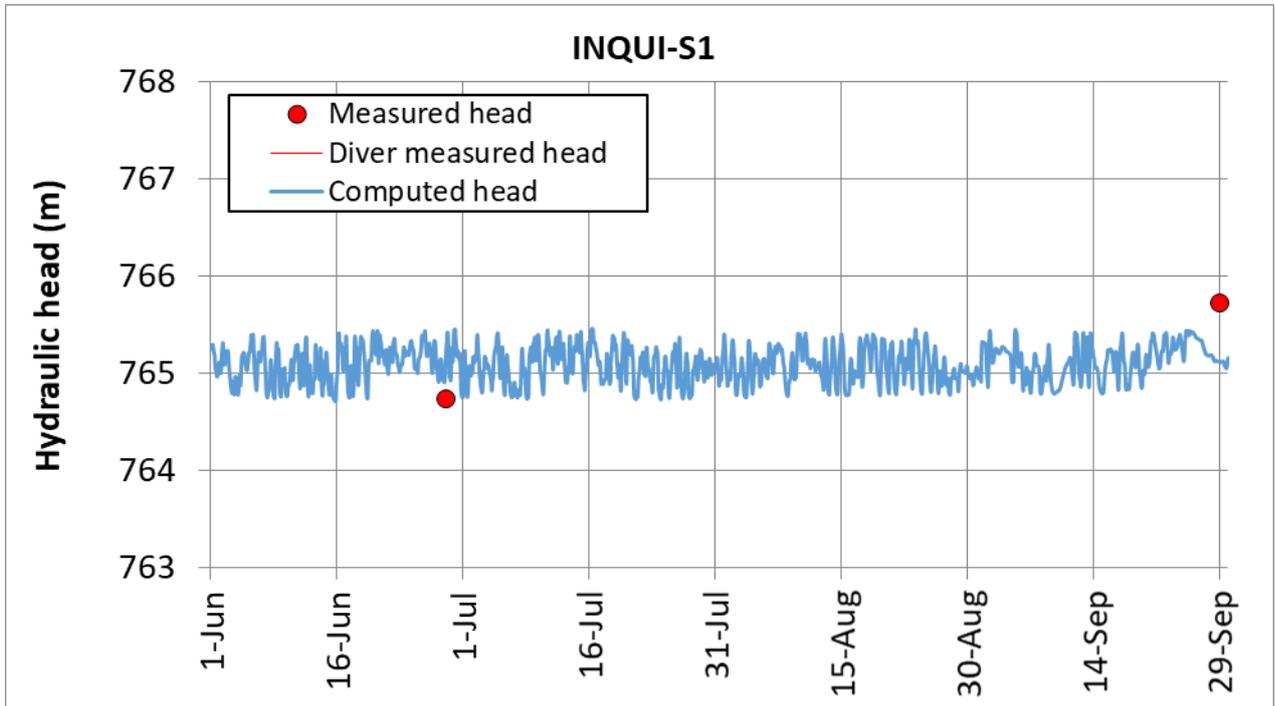
Figure 7.20. Measured hydraulic heads with hydro-level probe (symbols) and computed hydraulic heads (blue line) in INQUI-S1 borehole.
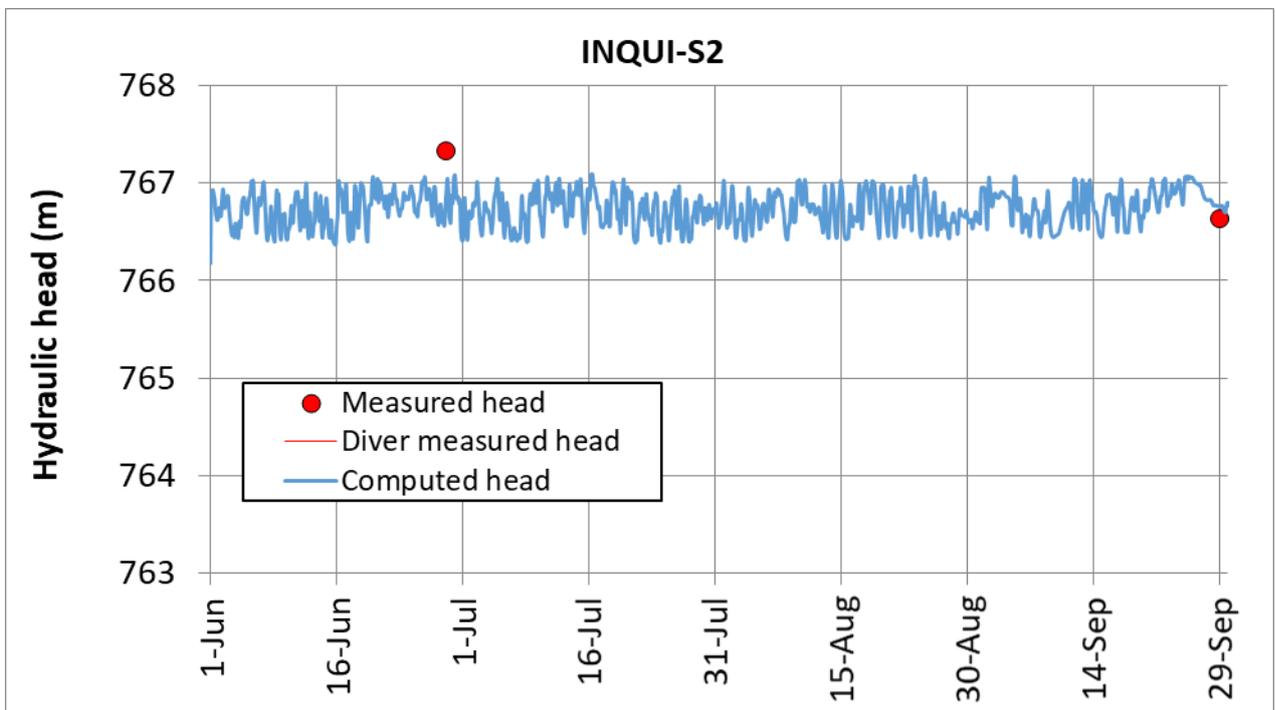
Figure 7.21. Measured hydraulic heads with hydro-level probe (symbols) and computed hydraulic heads (blue line) in INQUI-S2 borehole.

7.4.2   Water balance in the multiannual transient model

The average water inflows of multiannual transient-state model are listed in Table 7.1. They coincide with those of the steady-state model, except for the inflow from the Aurín river. The model outflows are listed in Table 7.2. The inflows are also similar to those computed in the steady-state model. The difference between inflows and outflows is equal to 89.80 m³/day. Therefore, the water balance error is equal to 2.1 %.

Table 7.1.   Average daily inflows (m³/d) of the multiannual transient-state model.

Inflows	m³/day	%
Left margin	278.83	6.62
Right margin	1228.96	29.16
Recharge in confined gravels	100.78	2.39
Recharge in unconfined gravels	67.44	1.60
Aurín riverbed	2537.84	60.23
Total	4213.84	100

Table 7.2.   Average daily outflows (m³/d) of the multiannual transient-state model.

Outflows	m³/d	%
Reservoir	26.75	0.62
Dam	1008.52	23.43
Gállego main river course	3007.17	69.88
Gállego river north branch	83.10	1.93
Gállego river south branch	178.09	4.14
Total	4303.64	100

7.4.3   Maps of the computed hydraulic heads

Figure 7.22 shows the contour map of the computed hydraulic heads with the quarterly transient-state groundwater flow model at 8:30 am July 16th 2017 at using the when the water level of the reservoir reached a maximum value. On the other hand, Figure 7.23 shows the contour map of the computed hydraulic heads at 21:00 June 15th 2017 when the water level of the reservoir reached its minimum. Figure 7.24 and Figure 7.25 show a zoom of the contour maps

at the tale of the Sabiñánigo reservoir when the water level in the reservoir was maximum and minimum, respectively. Groundwater discharges mostly to the Gállego river courses upstream the reservoir when water level in the reservoir is maximum. The discharge to the reservoir is small. On the other hand, groundwater discharges into the reservoir mostly through the silting sediments when the water level in the reservoir is minimum.
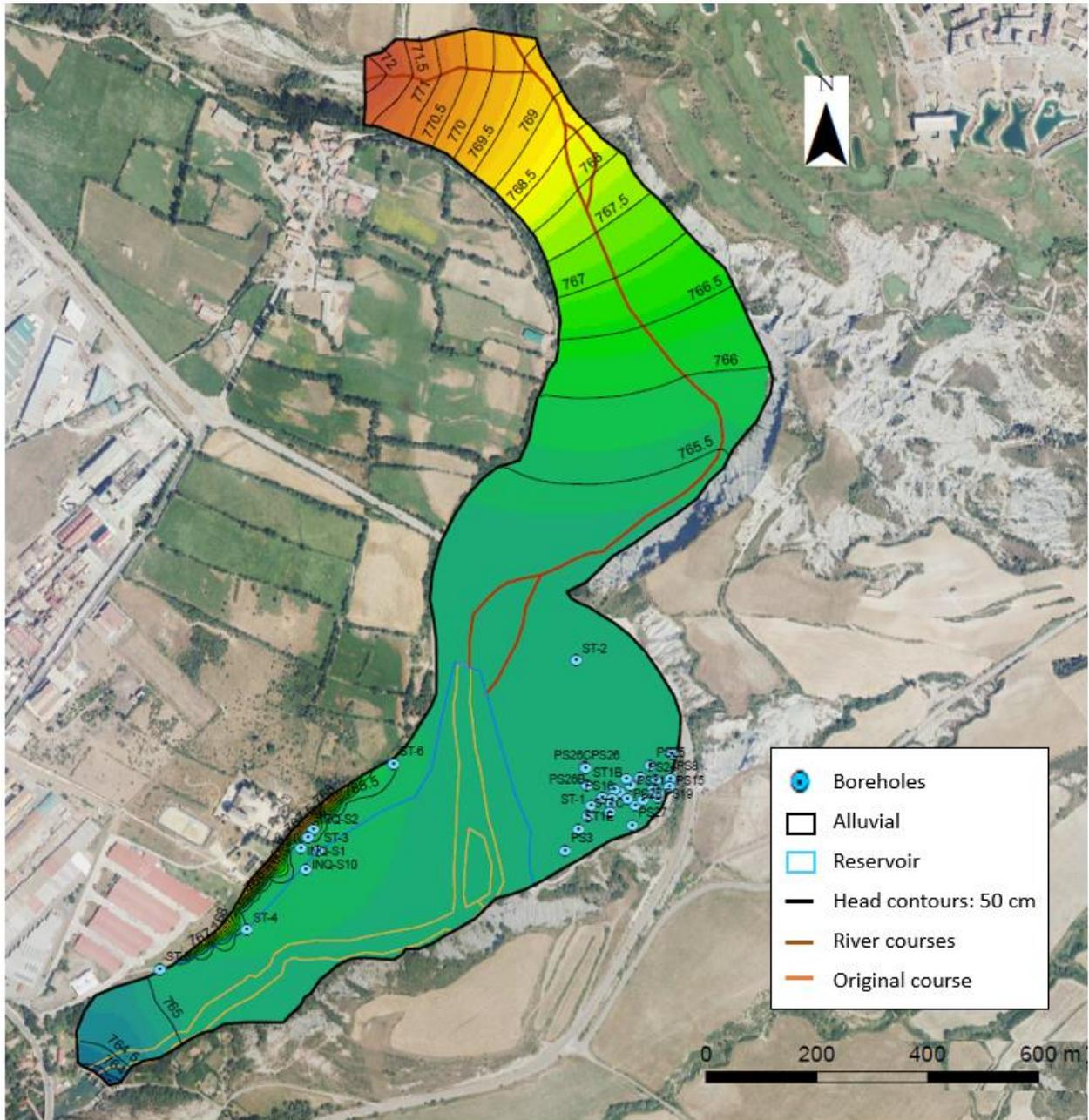
Figure 7.22. Contour map of the computed hydraulic heads with the quarterly transient-state groundwater flow model at 8:30 am on July 16th 2017. This time corresponds to a maximum water level in the reservoir. The hydraulic head contour interval is 0.5 m.
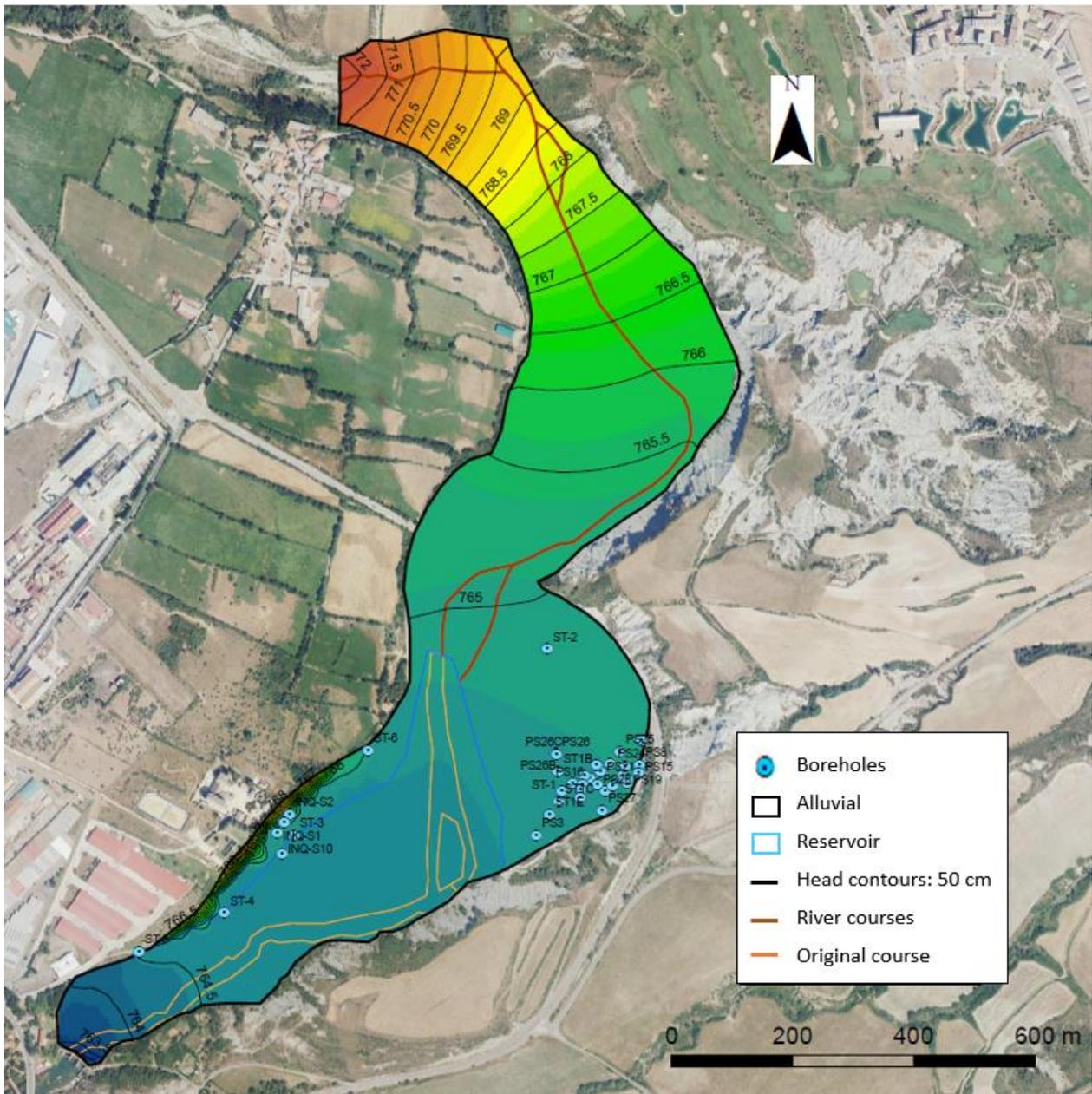
Figure 7.23. Contour map of the computed hydraulic heads with the quarterly transient-state groundwater flow model at 21:00 on June 15th 2017. This time corresponds to a minimum water level in the reservoir. The hydraulic head contour interval is 0.5 m.
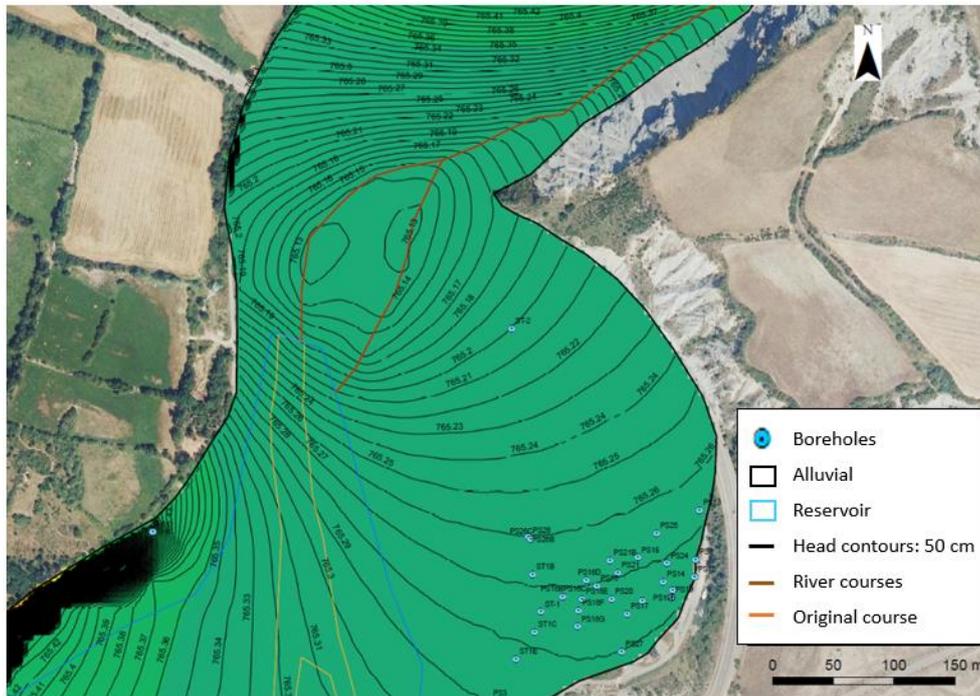
Figure 7.24. Zoom of the contour map of the computed hydraulic heads with the quarterly transient-state groundwater flow model at 8:30 am on July 16th 2017. This time corresponds to a maximum water level in the reservoir. The hydraulic head contour interval is 0.01 m.
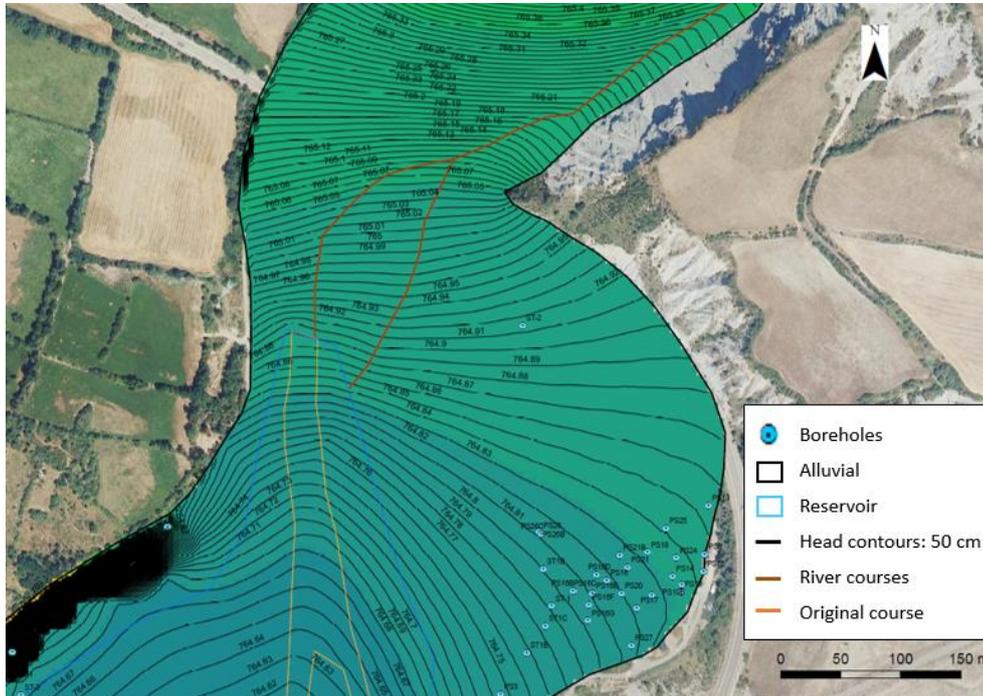
Figure 7.25. Zoom of the contour map of the computed hydraulic heads with the quarterly transient-state groundwater flow model at 21:00 on June 15th 2017. This time corresponds to a minimum water level in the reservoir. The hydraulic head contour interval is 0.01 m.

7.5 Conclusions

A 2D transient-state horizontal groundwater flow model through the gravels of the Gállego river alluvial aquifer from the mouth of the Aurín river to the Sabiñánigo dam has been presented which is based on the stead-state model presented in Chapter 6. Numerical simulations have been performed for two-time horizons. A multiannual time horizon was performed for the period February 26th 2014 to August 29th 2019. The second simulation period extends from June 1st to September 30th 2017.

The computed hydrographs reproduce the measured hydrographs in most of the boreholes. The fit to the measured data in the boreholes located on the right bank near the INQUINOSA factory is slightly worse than in the rest of the aquifer. However, these boreholes are far from the Sardas landfill.

In spite of the uncertainties of the model in areas located far from the Sardas landfill, the selected model domain was needed to account for the effect of the fluctuations in the reservoir levels which affect the hydraulic heads in the aquifer several hundred metres upstream the N-330 bridge. Therefore, the results of the transient state models show that it is necessary to extend the 2D horizontal model domain to the Aurín confluence.

The hydraulic heads in the aquifer vary fluctuate in response to the fluctuations of the water level in the Sabiñánigo reservoir. The hydraulic head contour line of 765 m is near the Sabiñánigo dam when the level of the reservoir is at its minimum value. On the other hand, the hydraulic head contour line of 765 m in the aquifer is near the bridge of the N-330 road, almost 1 km upstream the dam, when the water level in the reservoir is at its maximum.

Groundwater discharges mostly to the Gállego river courses upstream the reservoir when the reservoir water level is maximum. The discharge to the reservoir is small. When the water level in the reservoir is minimum, on the other hand, groundwater discharges into the reservoir mostly through the silting sediments.

8. 2D STEADY-STATE HORIZONTAL GROUNDWATER FLOW AND TRANSIENT HCH TRANSPORT MODEL THROUGH THE GRAVELS OF THE ALLUVIAL OF THE GÁLLEGO RIVER

8.1 Introduction

This chapter presents a 2D steady-state horizontal groundwater flow and transient HCH transport model through the gravels of the alluvial aquifer which aims at quantifying the HCH plumes in the aquifer and the HCH mass flux from the aquifer into the silting deposits. The model assumes that dissolved HCH is in equilibrium with HCH in the solids and the DNAPL. The chapter starts with a description of the available HCH data. Then, the numerical model is presented. The chapter ends with the main conclusions.

8.2 Available dissolved HCH concentration data

Figure 8.1 to Figure 8.23 show the time evolution of the concentrations of dissolved HCH isomers and total dissolved HCH in the alluvial boreholes.

The time evolution of the measured total HCH concentrations from 2015 to 2019 show numerous oscillations. These fluctuations may be caused by factors affecting the water sampling, the chemical analysis, the increase of HCH solubility with temperature, and the presence of DNPAL at the bottom of the boreholes. The detailed analysis of the fluctuations of dissolved HCH data is beyond the scope of this Master Thesis.
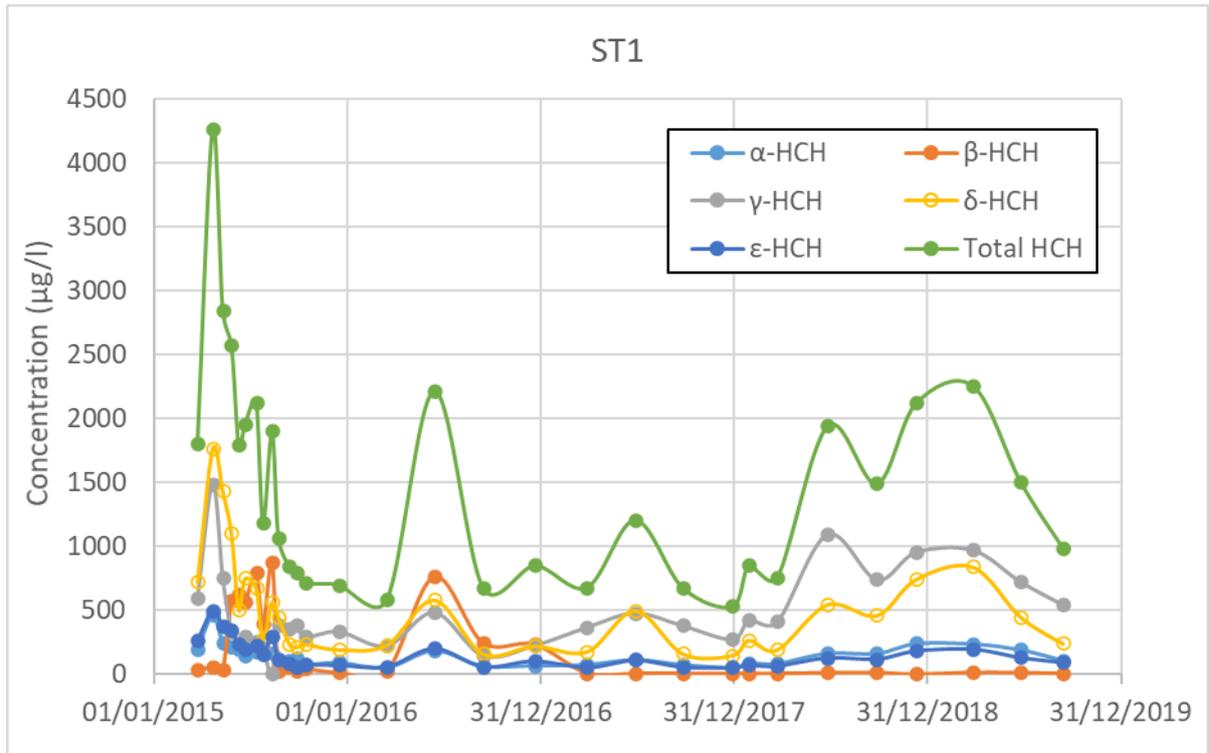
Figure 8.1.   Time evolution of the concentrations of HCH isomers and total dissolved HCH in ST1 borehole.
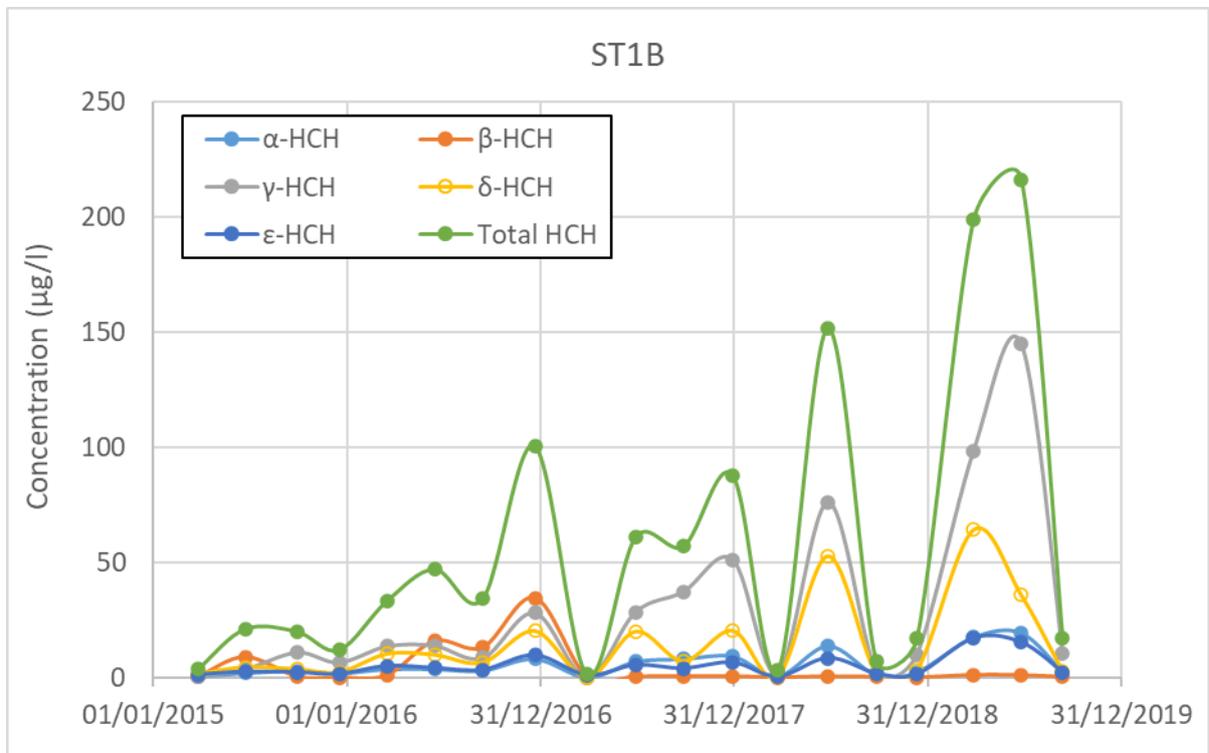
Figure 8.2.   Time evolution of the concentrations of HCH isomers and total dissolved HCH in ST1B borehole.
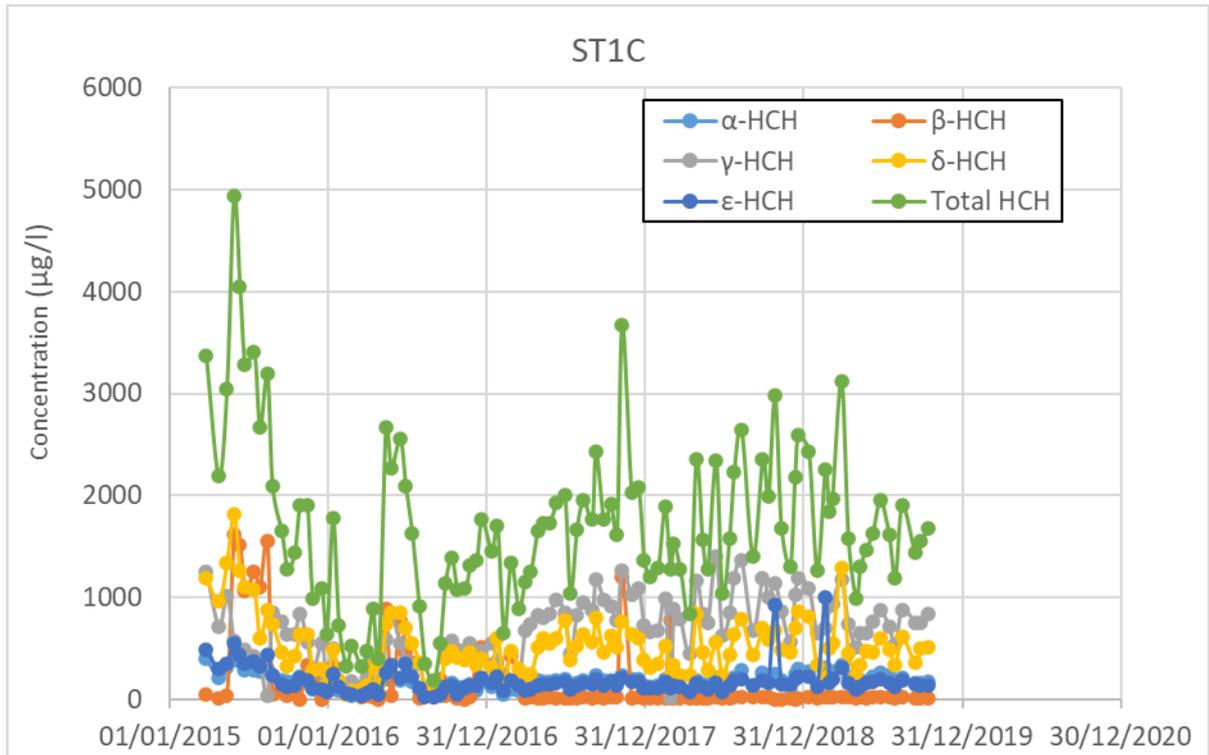
Figure 8.3. Time evolution of the concentrations of HCH isomers and total dissolved HCH in ST1C borehole.
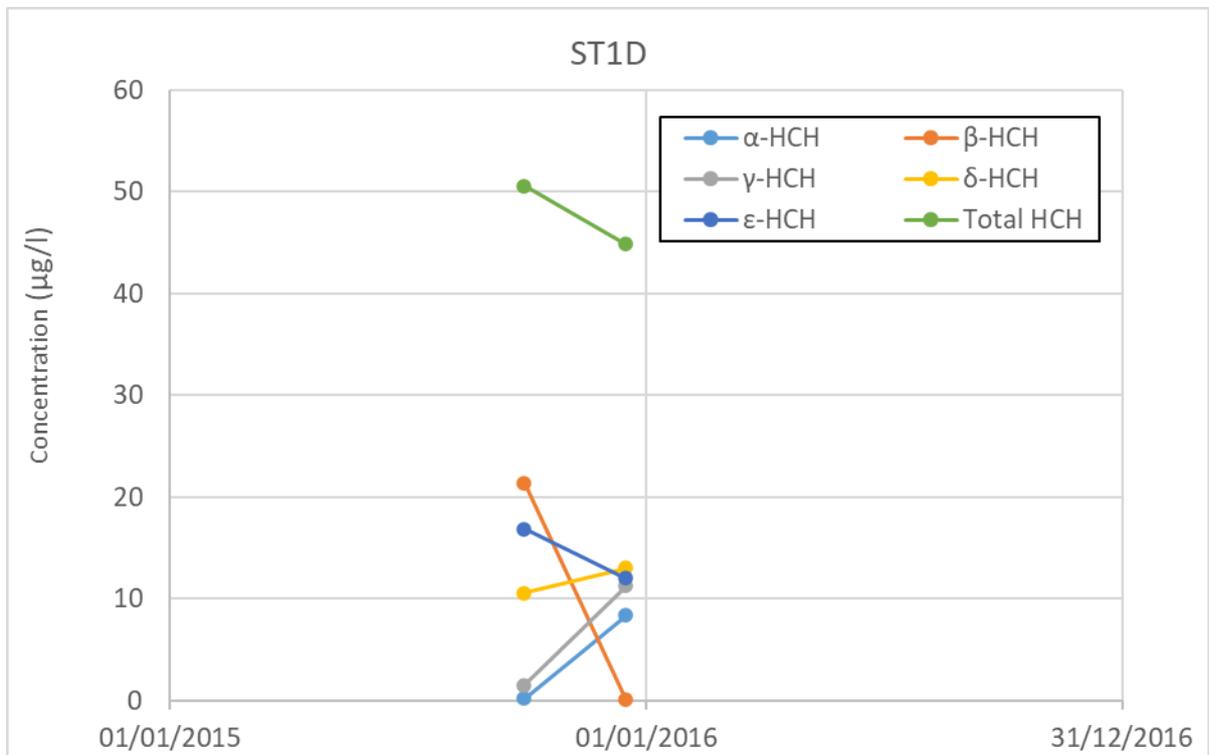
Figure 8.4. Time evolution of the concentrations of HCH isomers and total dissolved HCH in ST1D borehole.
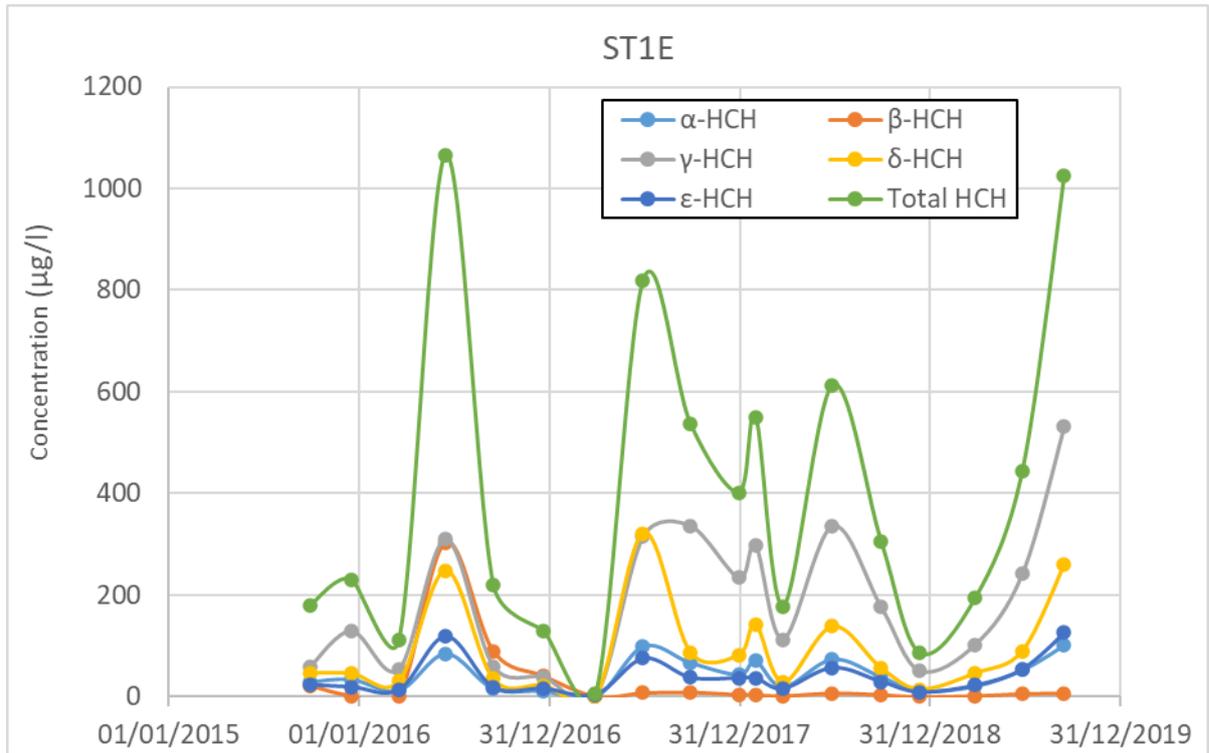
Figure 8.5. Time evolution of the concentrations of HCH isomers and total dissolved HCH in ST1E borehole.
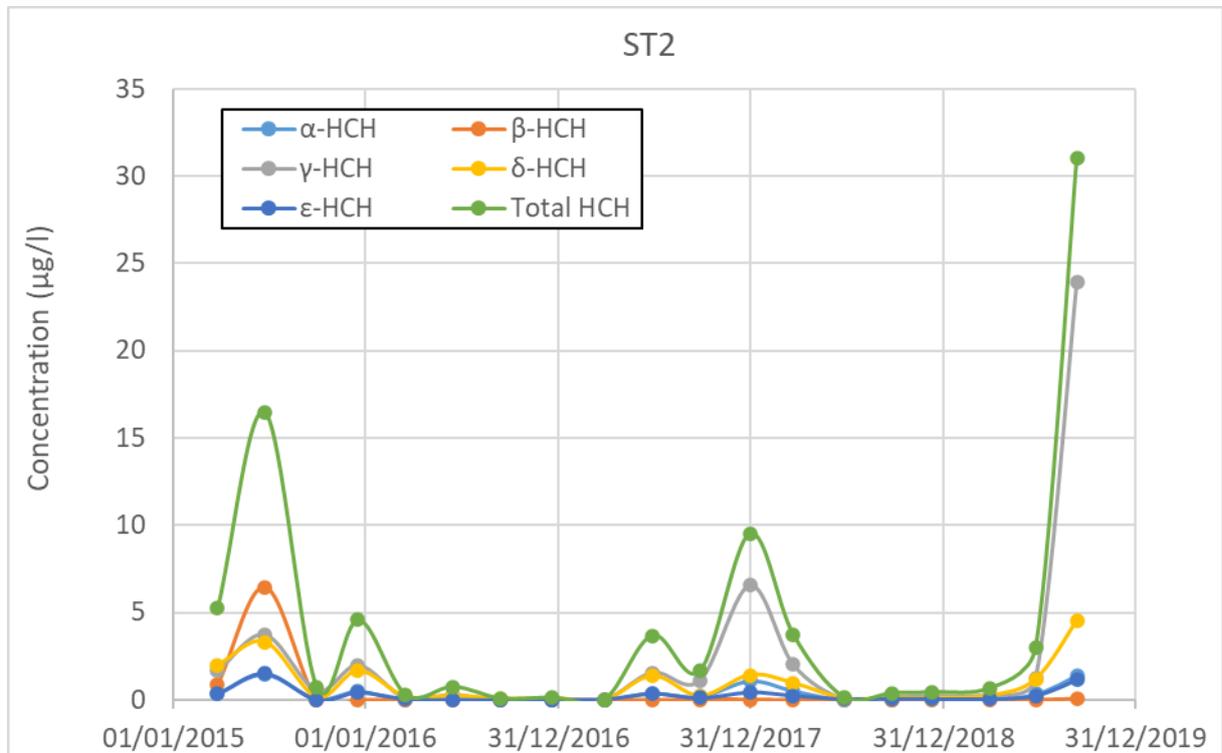
Figure 8.6. Time evolution of the concentrations of HCH isomers and total dissolved HCH in ST2 borehole.
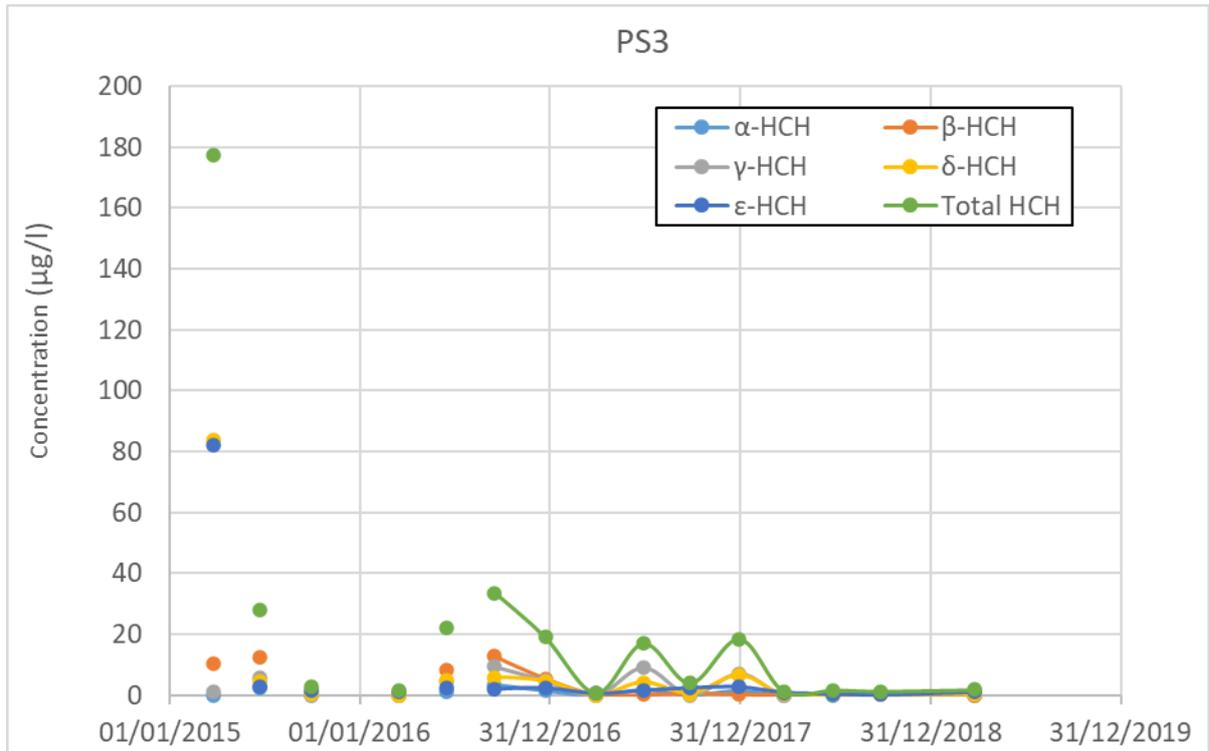
Figure 8.7. Time evolution of the concentrations of HCH isomers and total dissolved HCH in PS3 borehole.
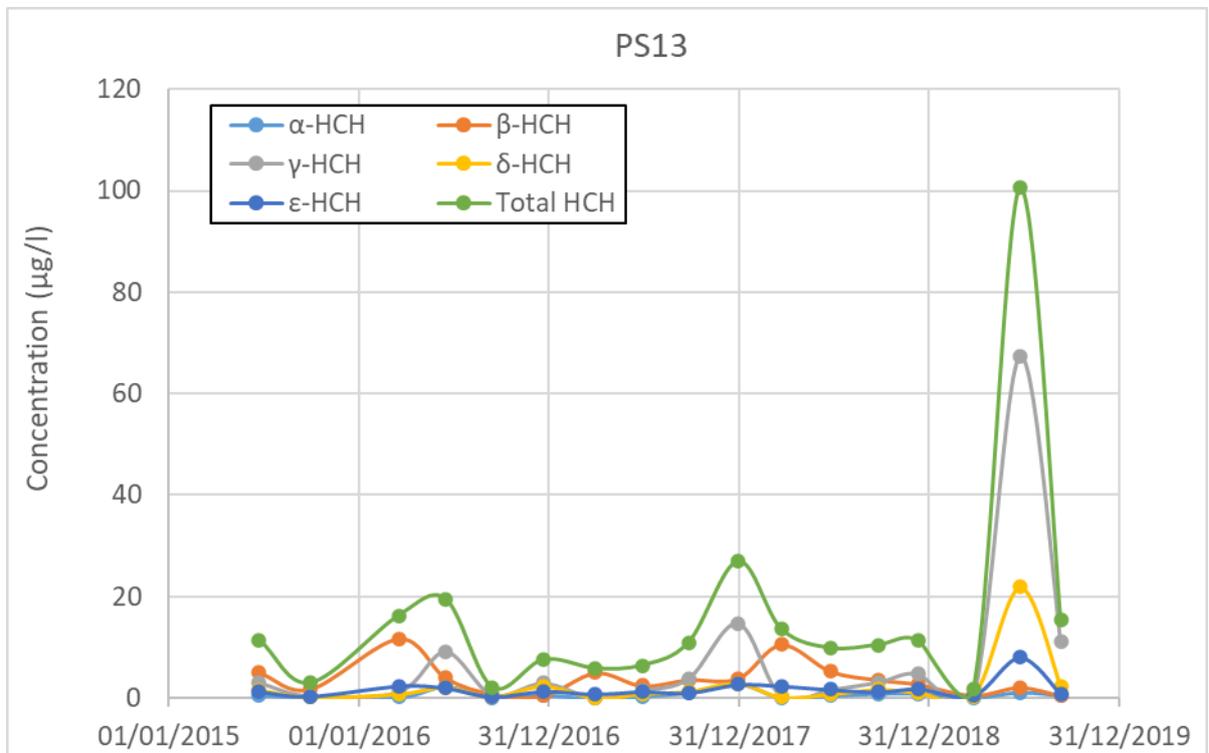
Figure 8.8. Time evolution of the concentrations of HCH isomers and total dissolved HCH in PS13 borehole.
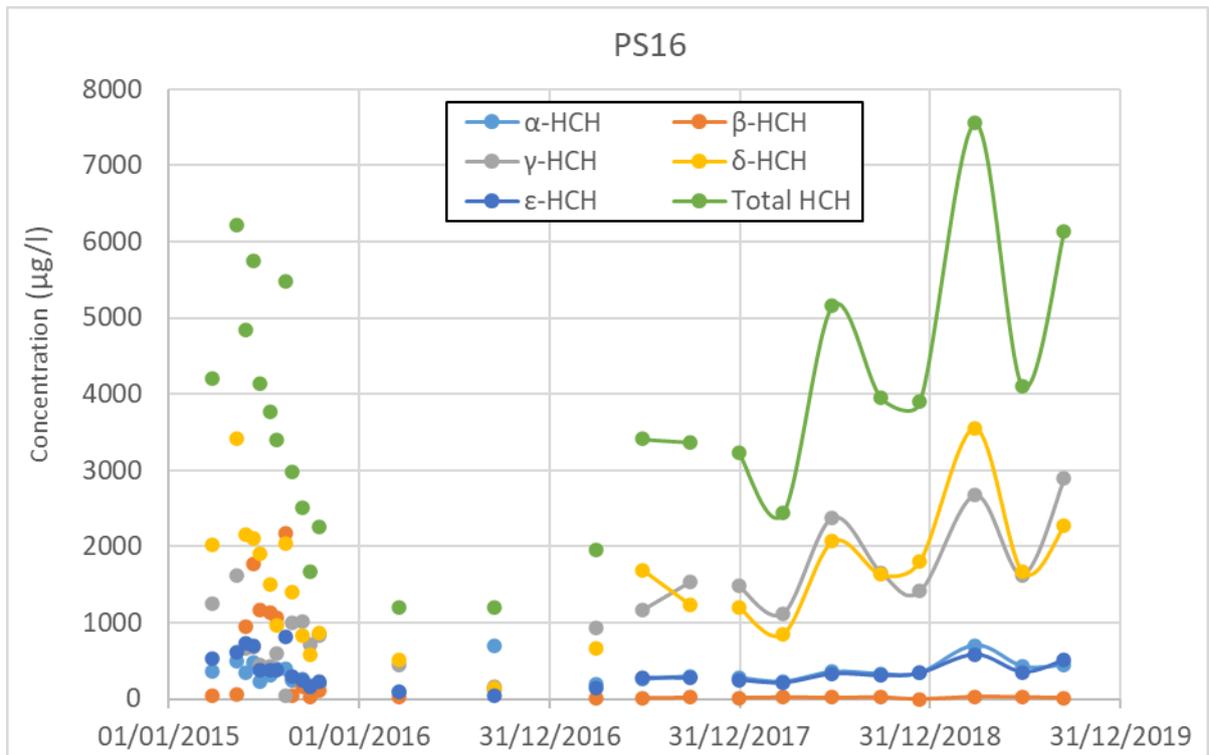
Figure 8.9. Time evolution of the concentrations of HCH isomers and total dissolved HCH in PS16 borehole.
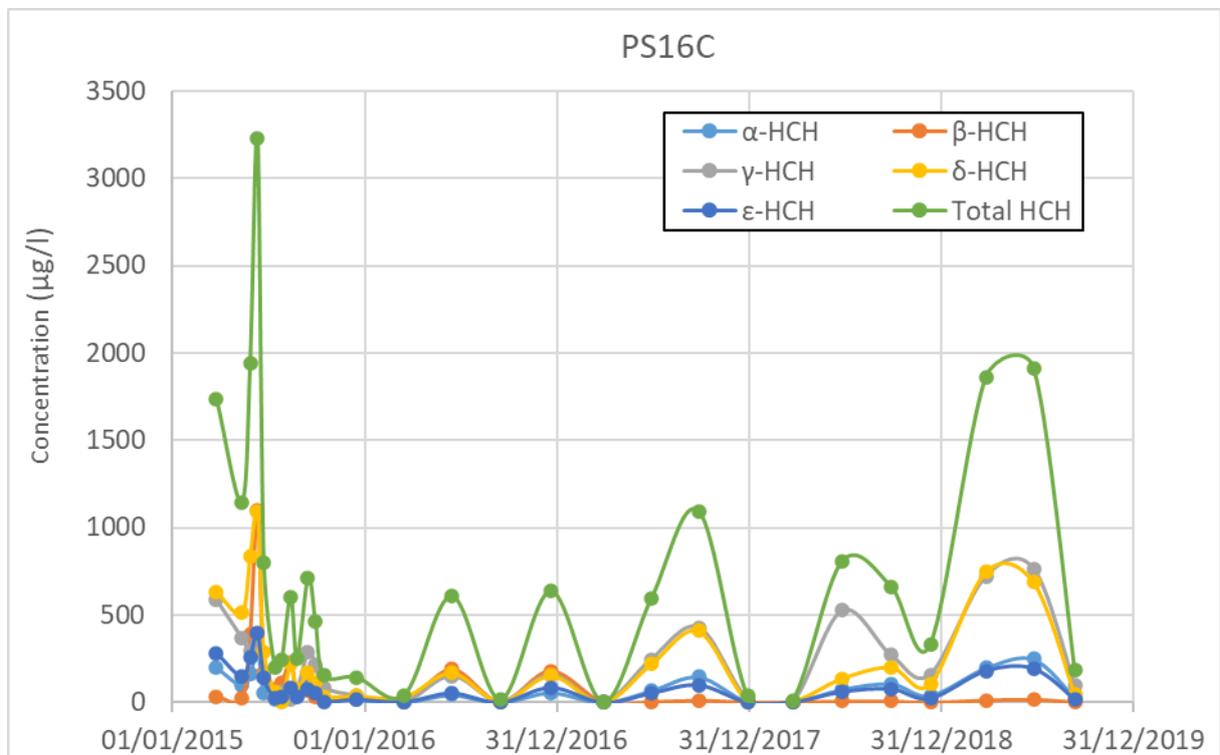
Figure 8.10. Time evolution of the concentrations of HCH isomers and total dissolved HCH in PS16C borehole.
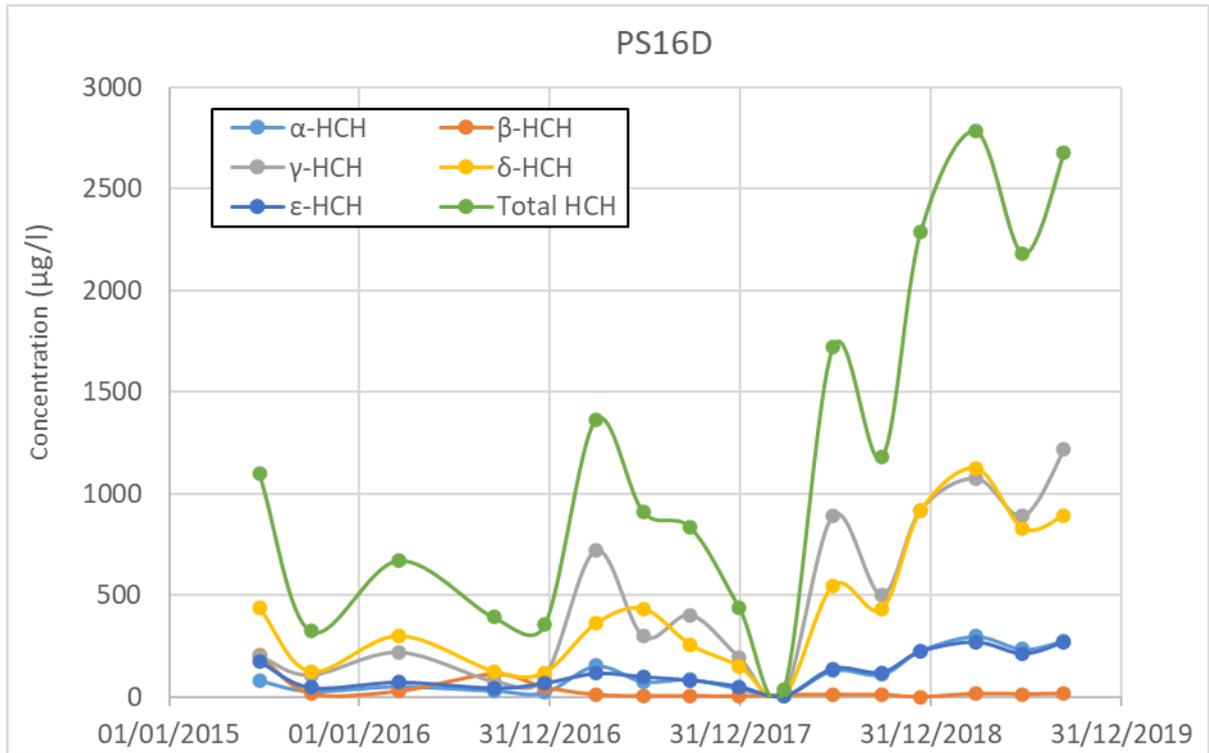
Figure 8.11. Time evolution of the concentrations of HCH isomers and total dissolved HCH in PS16D borehole.
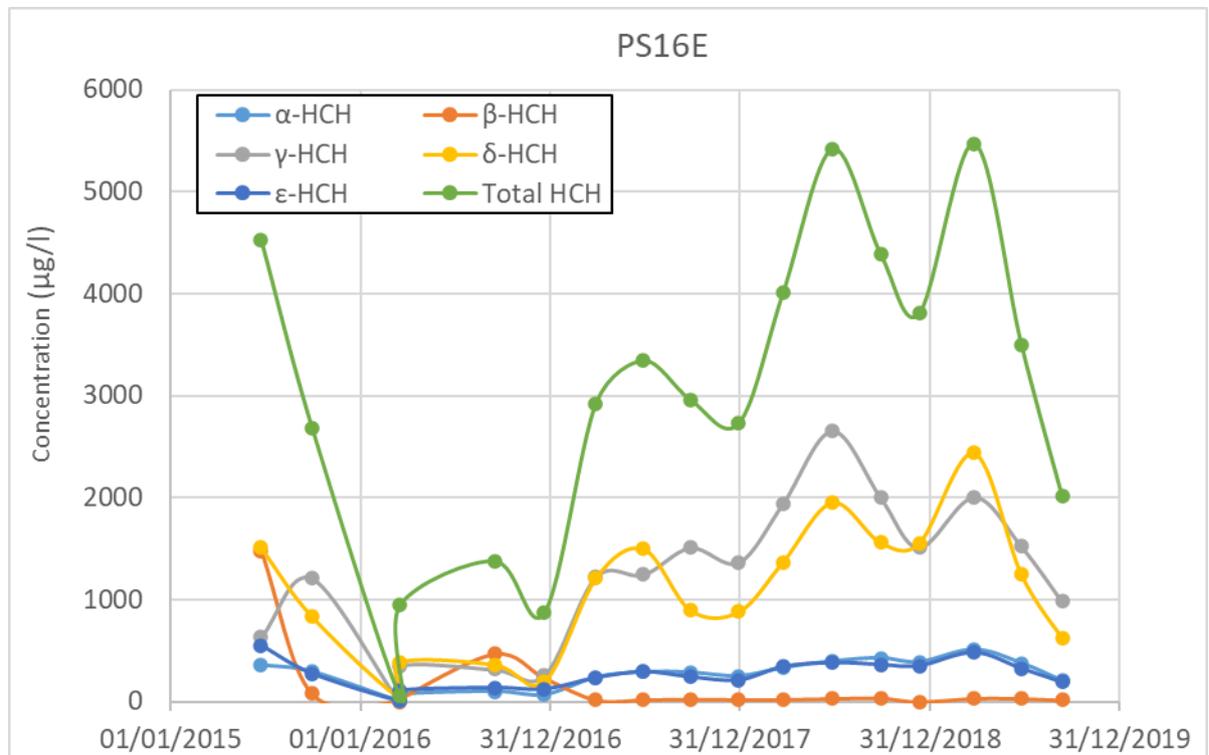
Figure 8.12. Time evolution of the concentrations of HCH isomers and total dissolved HCH in PS16E borehole.
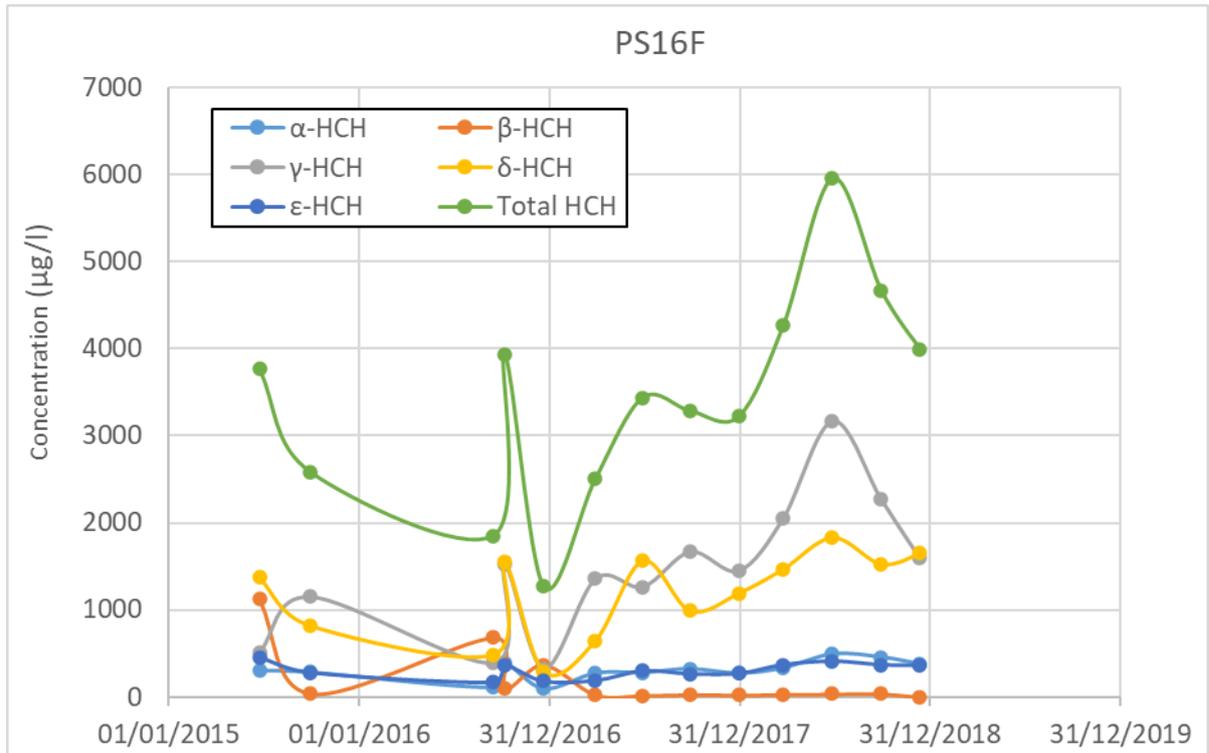
Figure 8.13. Time evolution of the concentrations of HCH isomers and total dissolved HCH in PS16F borehole.
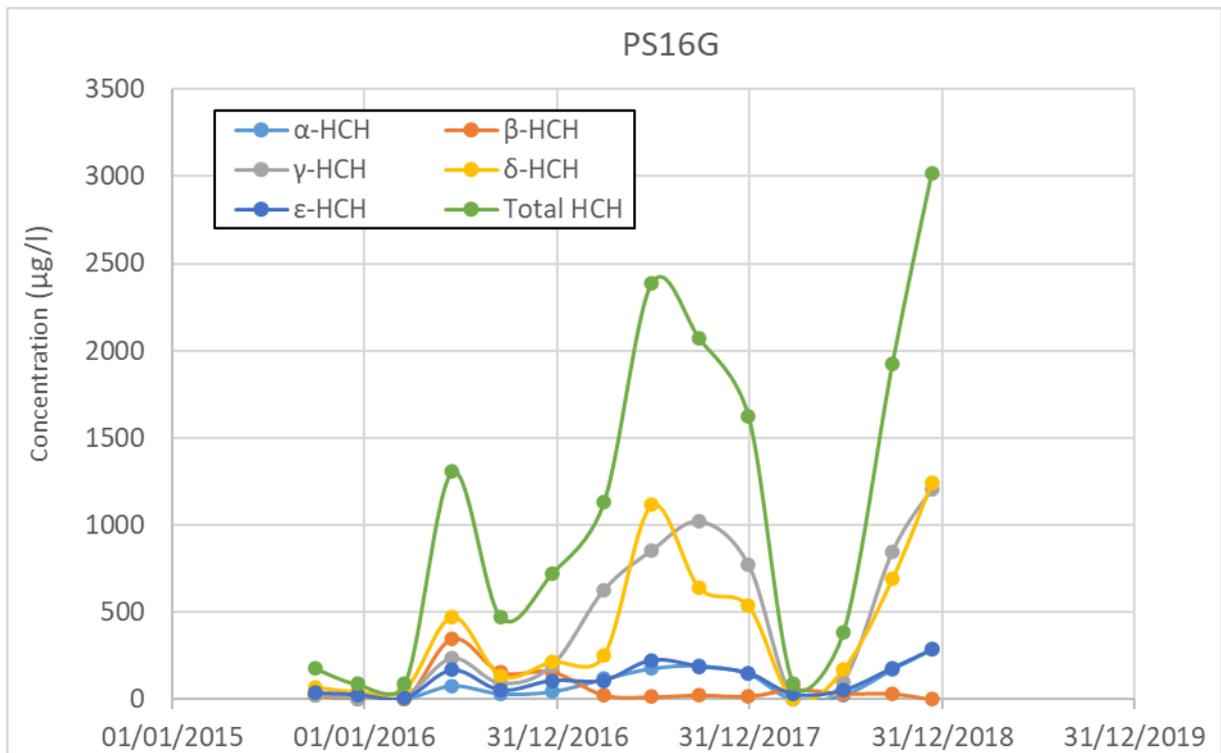
Figure 8.14. Time evolution of the concentrations of HCH isomers and total dissolved HCH in PS16G borehole.
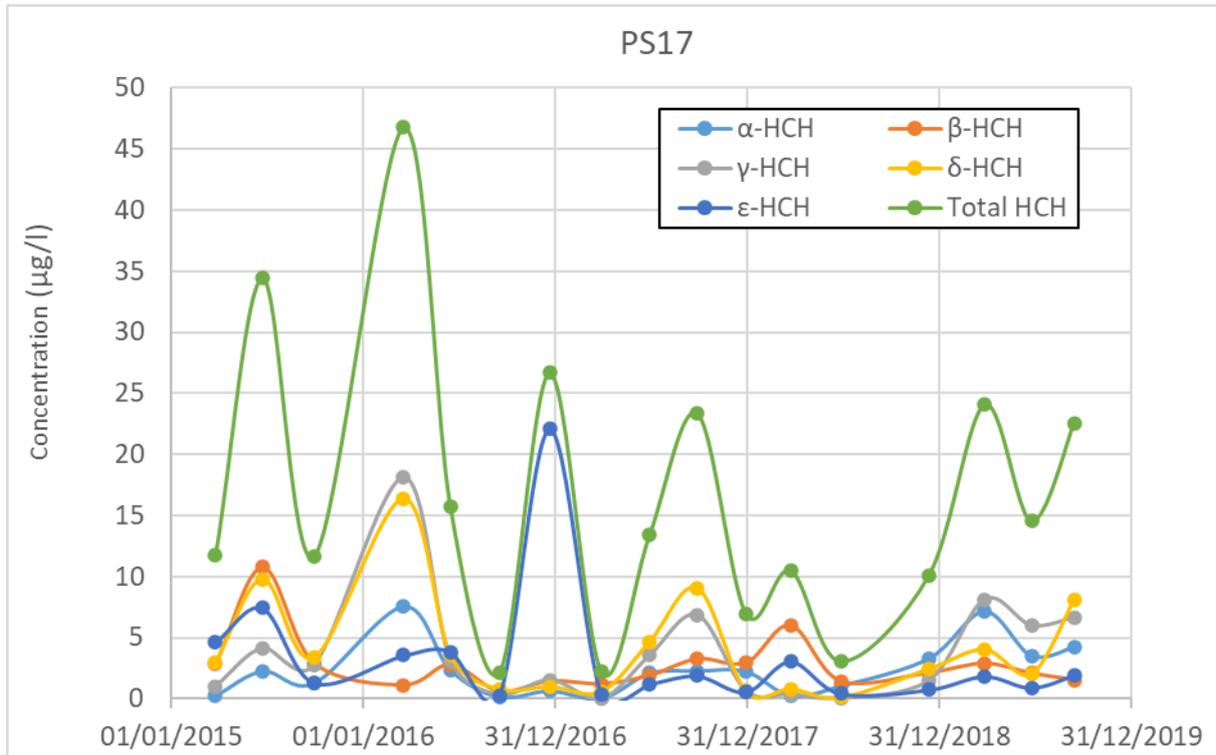
Figure 8.15. Time evolution of the concentrations of HCH isomers and total dissolved HCH in PS17 borehole.
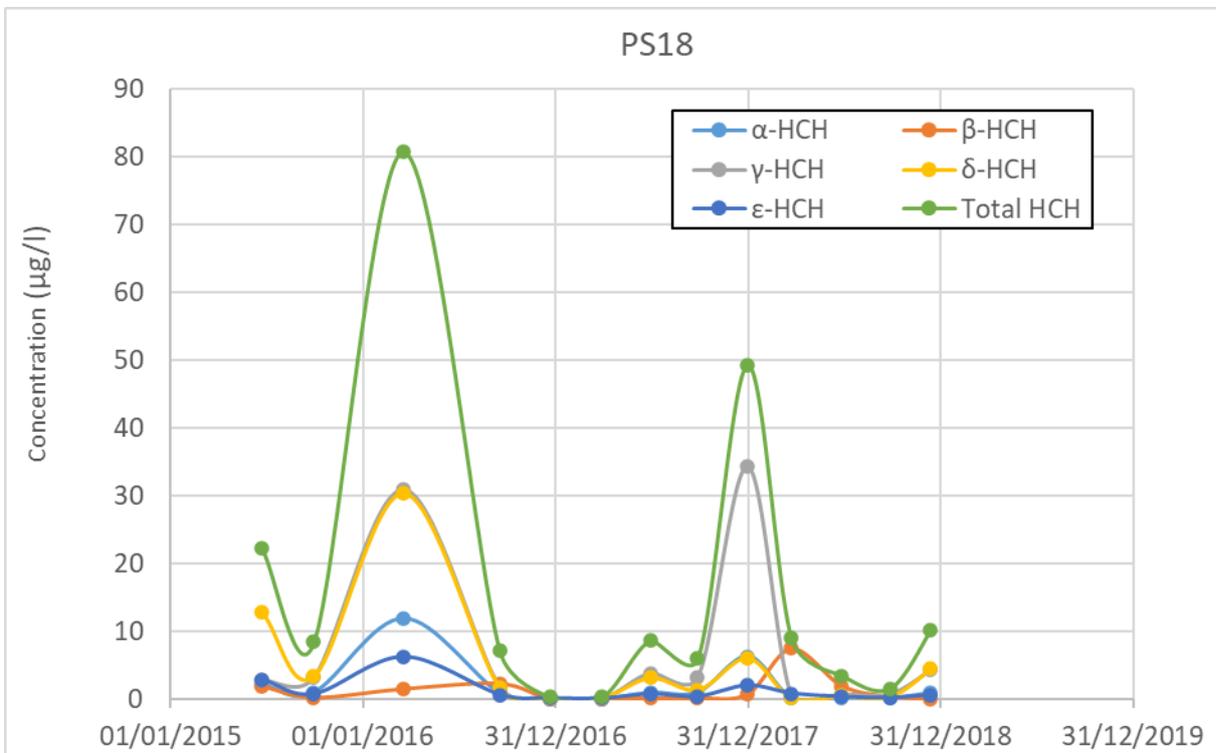
Figure 8.16. Time evolution of the concentrations of HCH isomers and total dissolved HCH in PS18 borehole.
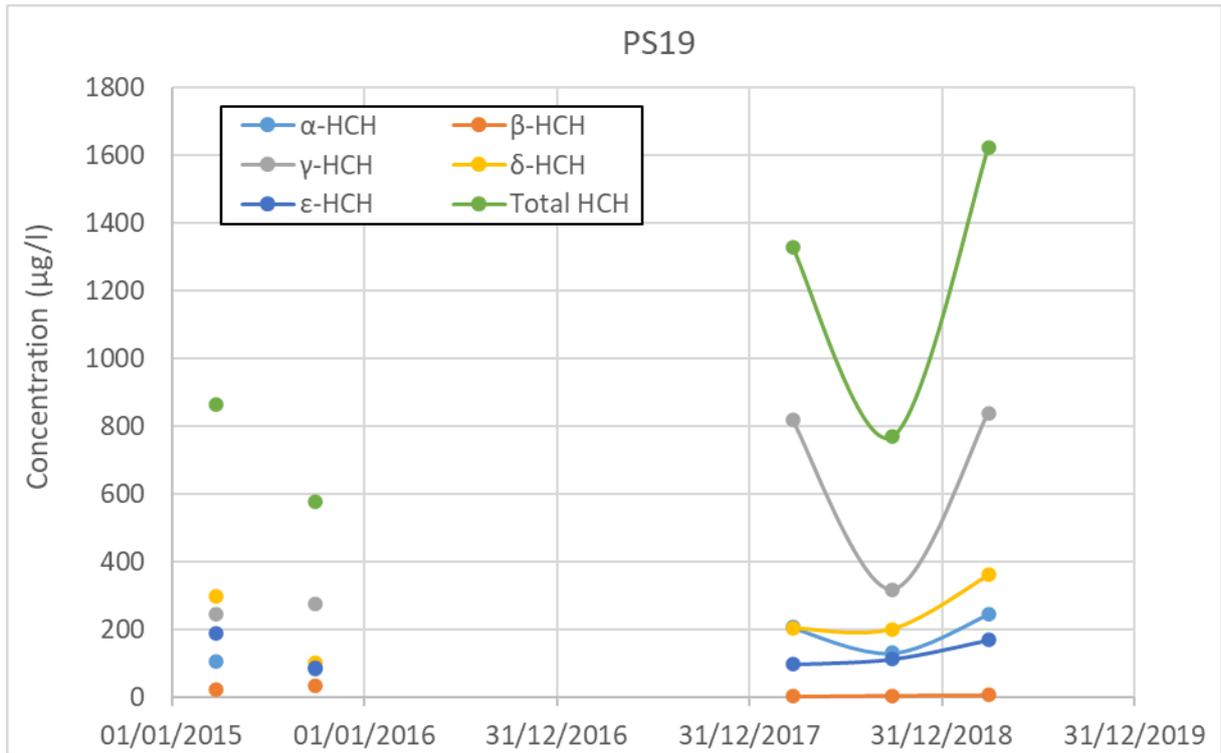
Figure 8.17. Time evolution of the concentrations of HCH isomers and total dissolved HCH in PS19 borehole.
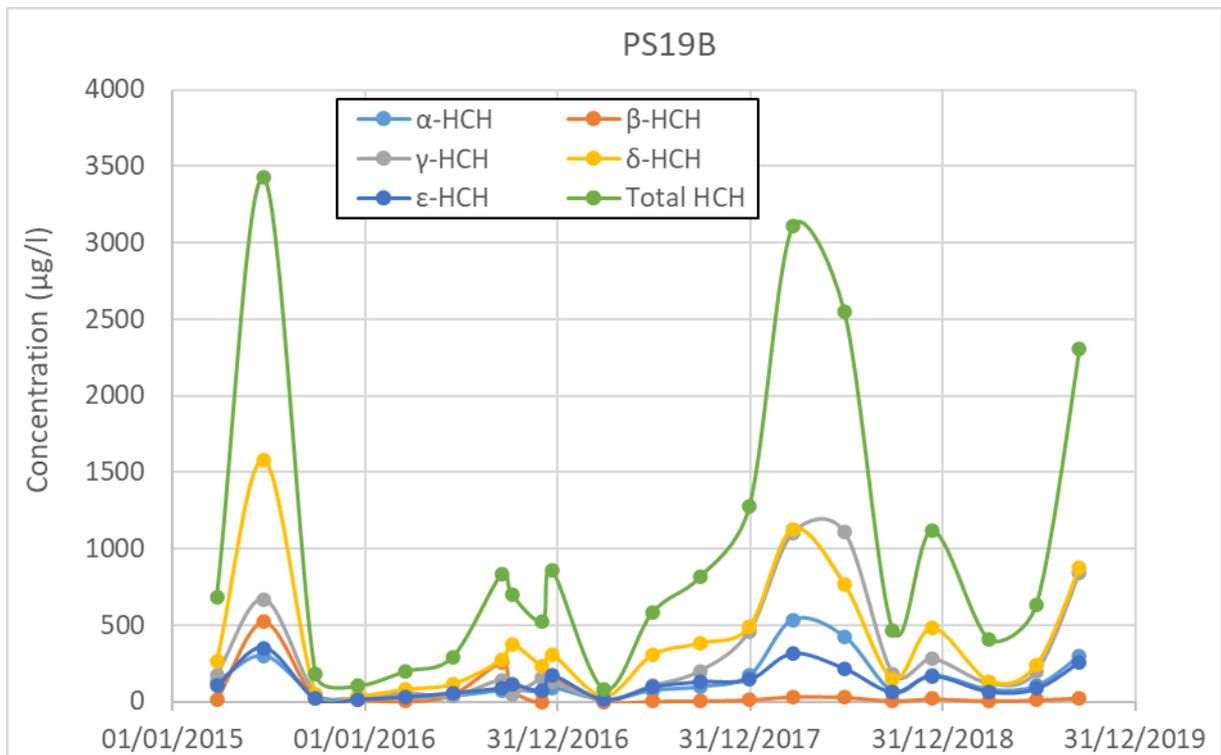
Figure 8.18. Time evolution of the concentrations of HCH isomers and total dissolved HCH in PS19B borehole.
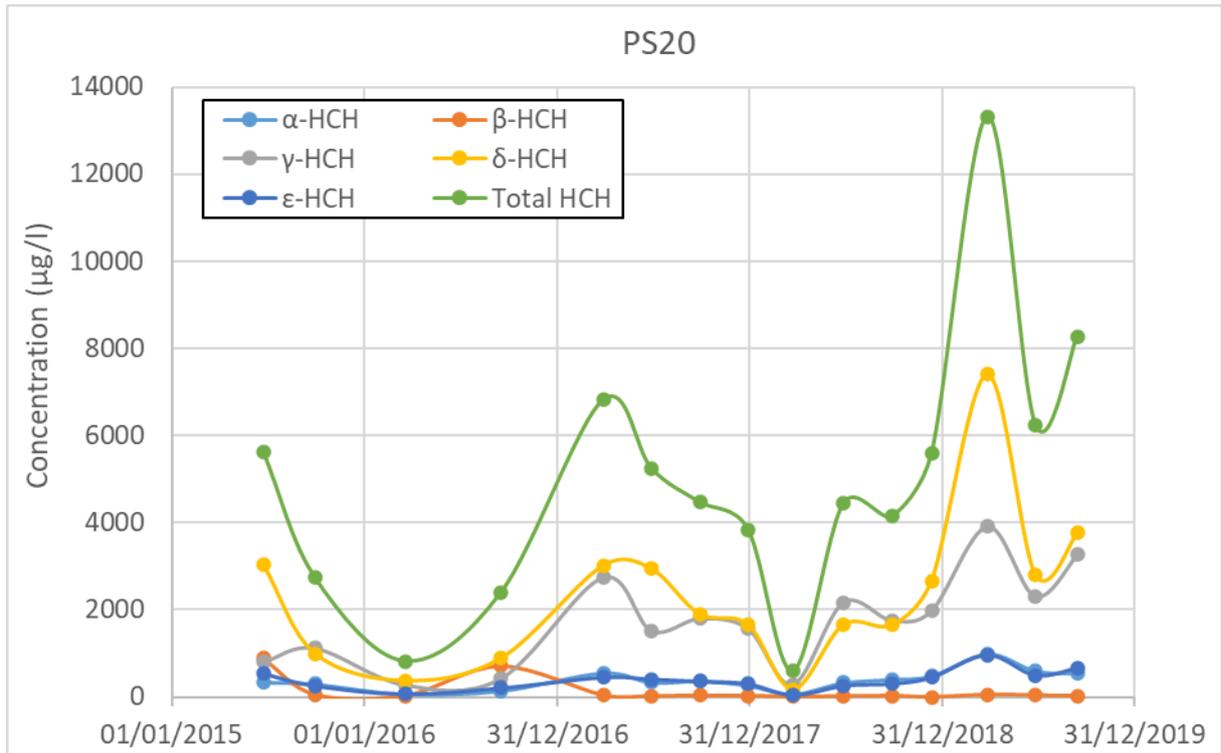
Figure 8.19. Time evolution of the concentrations of HCH isomers and total dissolved HCH in PS20 borehole.
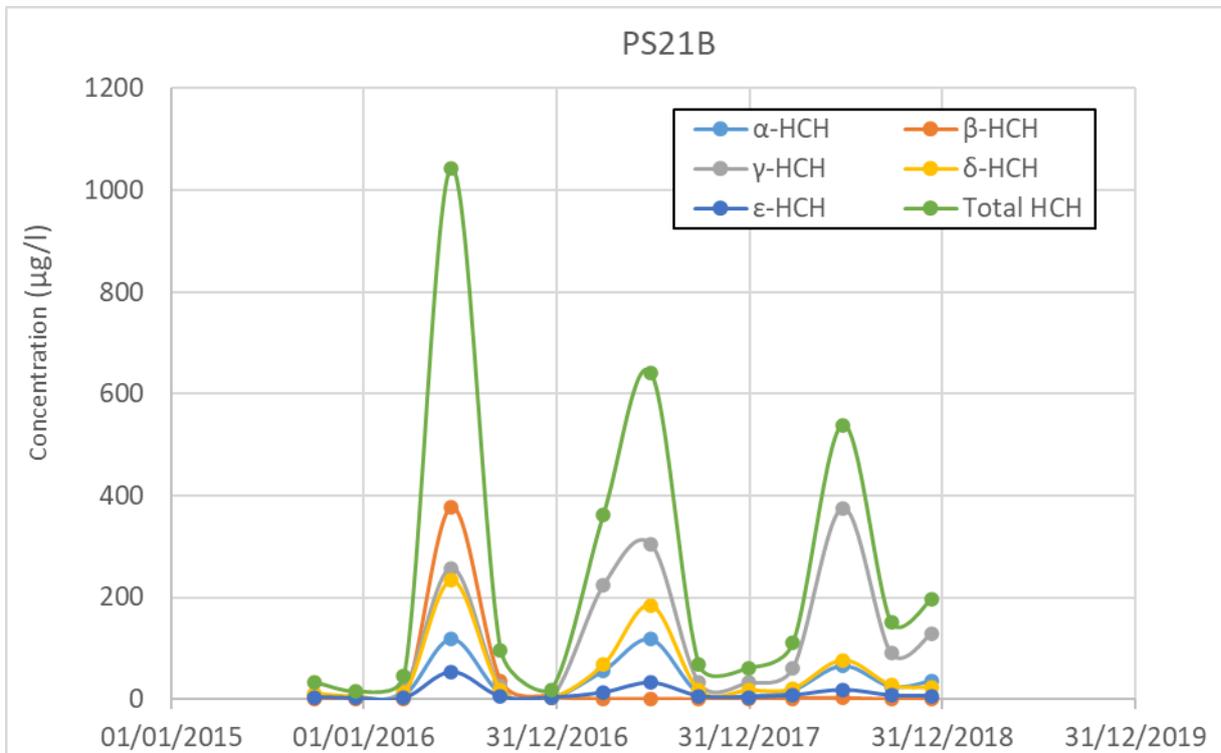
Figure 8.20. Time evolution of the concentrations of HCH isomers and total dissolved HCH in PS21B borehole.
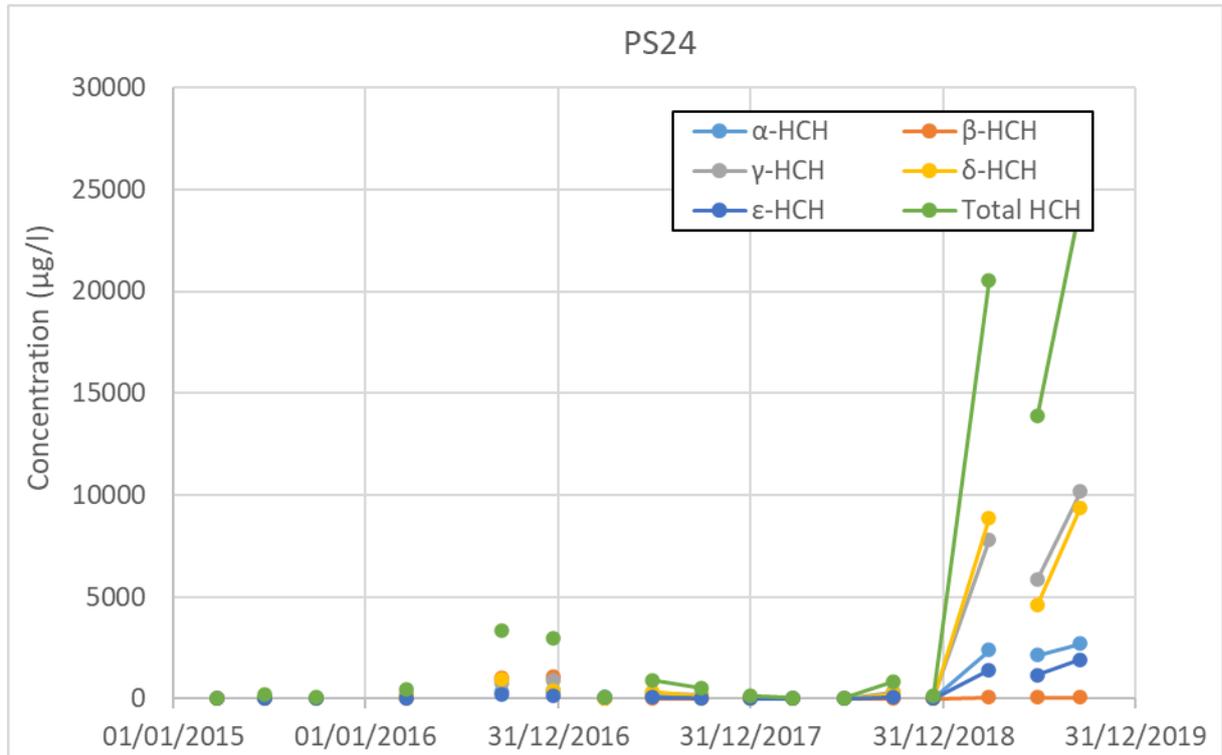
Figure 8.21. Time evolution of the concentrations of HCH isomers and total dissolved HCH in PS24 borehole.
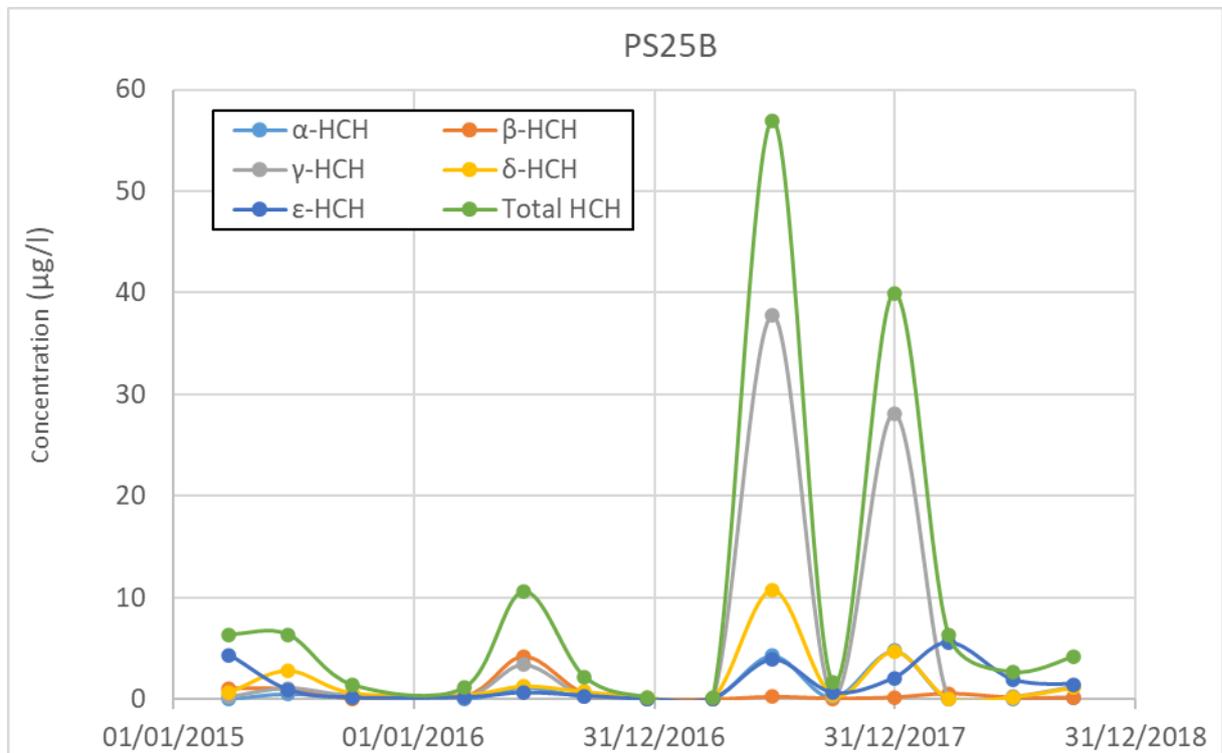
Figure 8.22. Time evolution of the concentrations of HCH isomers and total dissolved HCH in PS25B borehole.
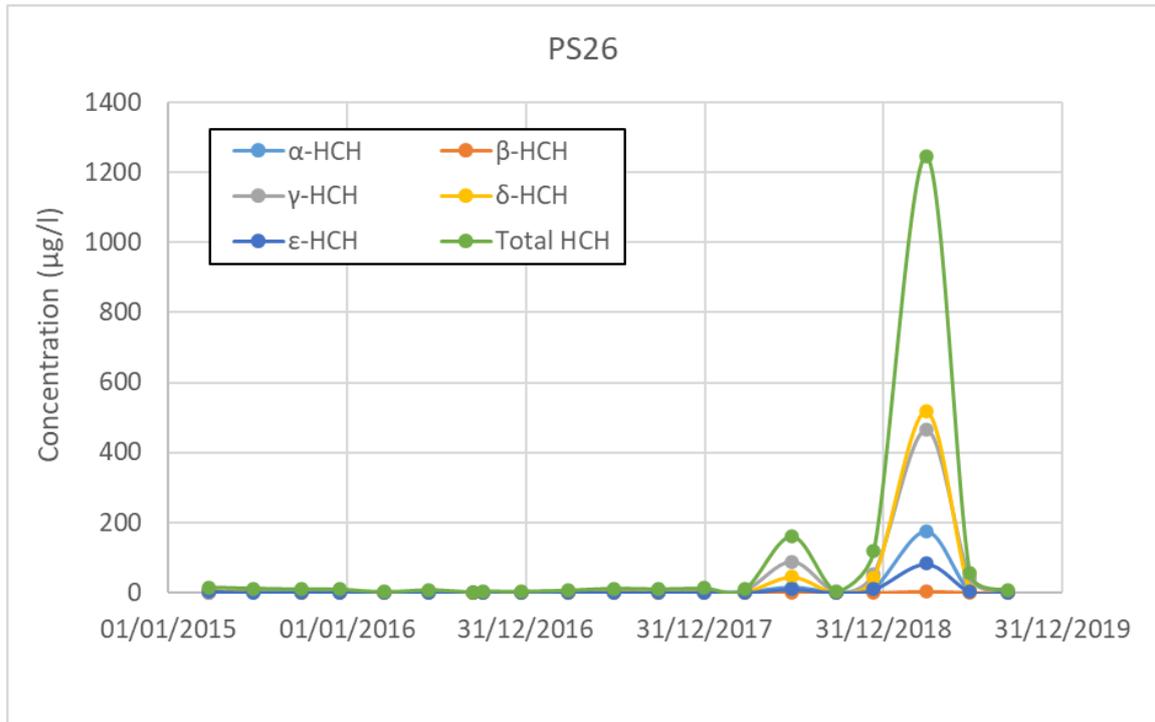
Figure 8.23. Time evolution of the concentrations of HCH isomers and total dissolved HCH in PS26 borehole.

Figure 8.24 shows the plume of the measured total dissolved HCH in September 2018. This plume was prepared by EMGRISA from measured data at selected boreholes.
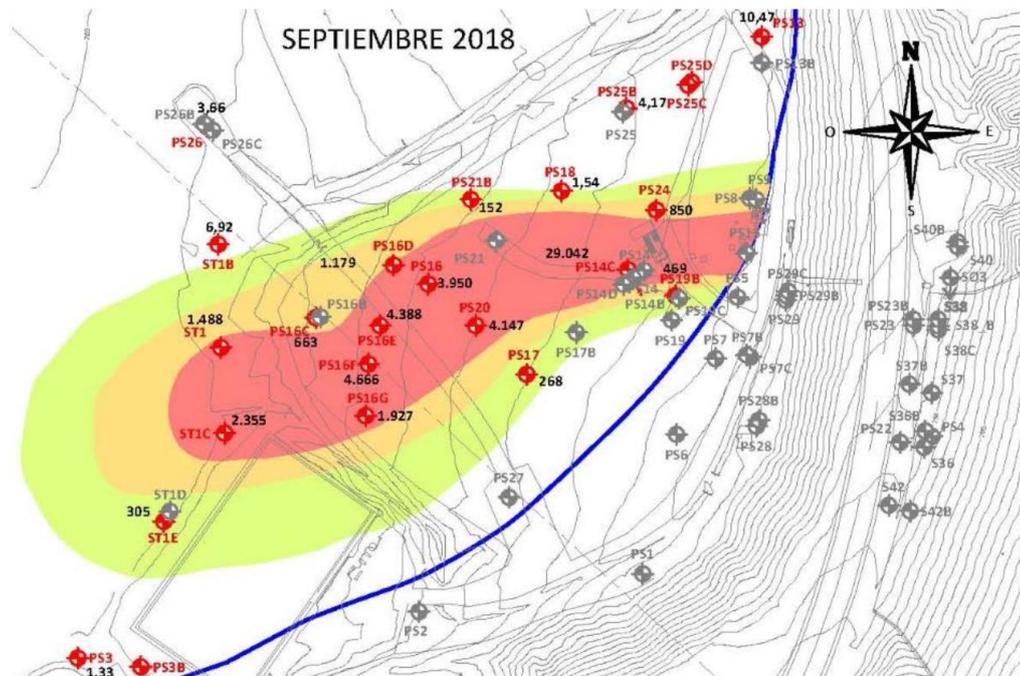
Figure 8.24. Plume of measured total dissolved HCH in September 2018 prepared and provided by EMGRISA.

Concentrations of total dissolved HCH are higher in the areas near the front slurry – wall of the Sardas landfill. The dissolved HCH spreads through the alluvial reaching as far as the PS26 borehole in the north with a concentration of total HCH equal to 3.66 µg/L and to the south with 1.33 µg/L of total HCH in the PS3 borehole. The available data does not cover the area near the reservoir. However, the data from two boreholes located in the reservoir show concentrations of dissolved total HCH ranging from 1 to 17 µg/L (CHE, 2010).

8.3 Steady-state flow and transient HCH transport model

8.3.1 Model parameters

The transport of dissolved HCH has been simulated by assuming steady-state groundwater flow conditions. The steady-state groundwater flow model considers the average water level of the reservoir, the average recharge and the average flows through the boundaries. The steady-state flow model was presented in Chapter 6.

The simulation period of the HCH transport model is 50 years. Time increments are equal to 3.04 days.

The initial concentration of dissolved HCH in the alluvial has been taken equal to 10^{-9} µg/L. The initial HCH concentration in the areas containing DNPAL is equal to 5000 µg/L.

The total porosity of all the material zones is 0.135. The longitudinal and transversal dispersivities are equal to 1 m. The diffusion coefficient in water (D_0) is equal to 10^{-10} m^2/s.

Flow boundary conditions coincide with those considered in the steady-state flow model. The boundary of the model corresponding with the Sardas landfill has been simulated with a fixed concentration boundary condition. The measured HCH plumes provided by EMGRISA (Figure 8.24) have been used to define the portion of boundary through which the dissolved HCH goes into the model and the dissolved HCH concentration of the inflow. The dissolved HCH concentration in the inflow from the landfill is considered constant and equal to 5000 µg/L. All other model inflows are assumed to be free of dissolved HCH. They have been simulated with a fixed constant concentration of dissolved HCH equal to 10^{-9} µg/L.

Table 8.1.   Hydraulic and transport parameters of the material areas for the HCH transport model.

Geological formation	Hydraulic conductivity K_h (m/d)	Total porosity	Longitudinal dispersivity (m)	Transversal d dispersivity (m)
Gravels	$4.00 \cdot 10^{+2}$	0.135	1	1
Gravels under the reservoir	$4.00 \cdot 10^{+2}$	0.135	1	1
Gravels with sand	$4.00 \cdot 10^{+2}$	0.135	1	1
Less permeable material zone in INQUINOSA	$1.70 \cdot 10^{+0}$	0.135	1	1

The distribution coefficient for lindane is calculated with the following expression:

$$K_D = K_{oc} \cdot f_{oc}$$

where K_D is the distribution coefficient (L/kg), K_{oc} is the water-organic carbon distribution coefficient (L/kg) and f_{oc} is the fraction of organic carbon in the soil (dimensionless). Three intervals of K_{oc} values have been selected for lindane from reported measurements of K_{oc} (EPA, 1996) and from values calculated from the K_{oc} ratio and the octanol-water partition coefficient, K_{ow} (Suntio et al., 1988; Prager, 1995; EPA, 1996). These K_{oc} ranges for lindane are shown in Table 8.2.

Table 8.2.   Water-organic carbon distribution coefficient ranges for lindane.

K_{oc} (L/kg)	
Measured (EPA, 1996)	731-3249
Calculated from K_{oc} ratio	864-1224

The range of K_{oc} values for lindane is large due to the different techniques used to measure both K_{oc} and K_{ow}. In addition to the uncertainty associated to K_{oc}, the uncertainty associated to the f_{oc} value must be added. Since no value is available for the Sardas alluvial gravel, a literature search was carried out. The following two ranges were selected: (1) A "wide" range from 0.001 to 0.3, and (2) An "expected" range from 0.002 to 0.03.

Using the largest and smallest K_{oc} ranges and the two f_{oc} ranges to calculate the distribution coefficient gives a wide range of K_D for lindane from 0.73 to 974.7 L/kg:

$$731 < K_{oc} < 3249 \; and \; 0.001 < f_{oc} < 0.3 \rightarrow 0.73 < K_D < 974.7$$

The second range of expected K_D values for lindane is (1.46; 97.47) L/kg based on:

$$731 < K_{oc} < 3249 \; and \; 0.002 < f_{oc} < 0.03 \rightarrow 1.46 < K_D < 97.47$$

The distribution coefficient has been estimated by trial and error by fitting the computed HCH plume to the measured total dissolved HCH plume in September 2018 provided by EMGRISA (Figure 8.29). The best fit has been obtained with a distribution coefficient of 22 L/kg.

8.3.1 Model results for the base run

Figure 8.25 to Figure 8.28 show the computed plumes of total dissolved HCH at different times. Figure 8.30 presents the computed plume of total dissolved HCH at 50 years and the average measured total HCH concentrations in the boreholes downstream the front slurry-wall.
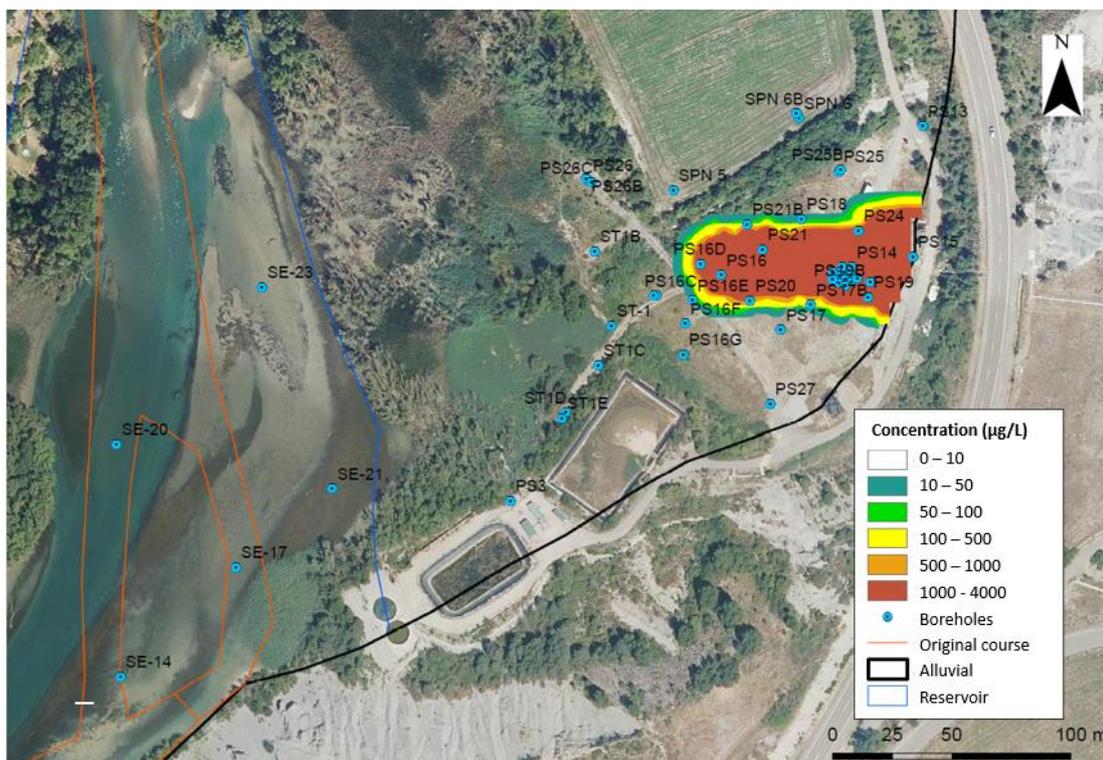
Figure 8.25. Computed plume of total dissolved HCH after a year for a distribution coefficient equal to 22 L/kg.
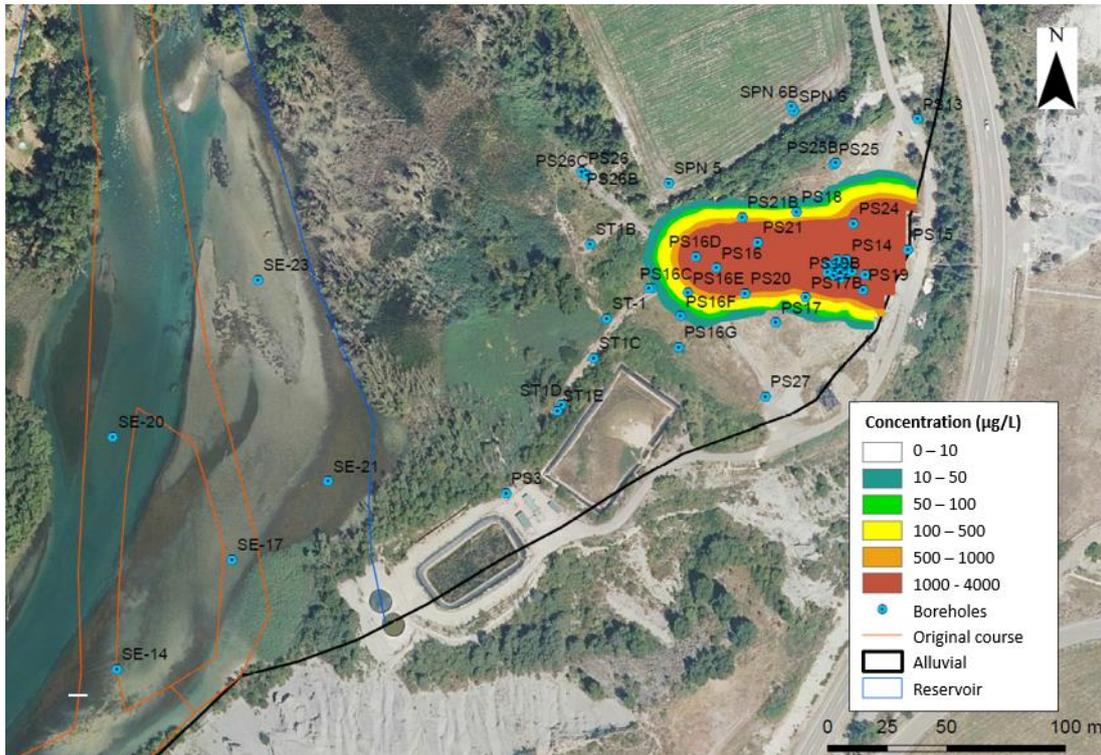
Figure 8.26. Computed plume of total dissolved HCH after 5 years for a distribution coefficient equal to 22 L/kg.
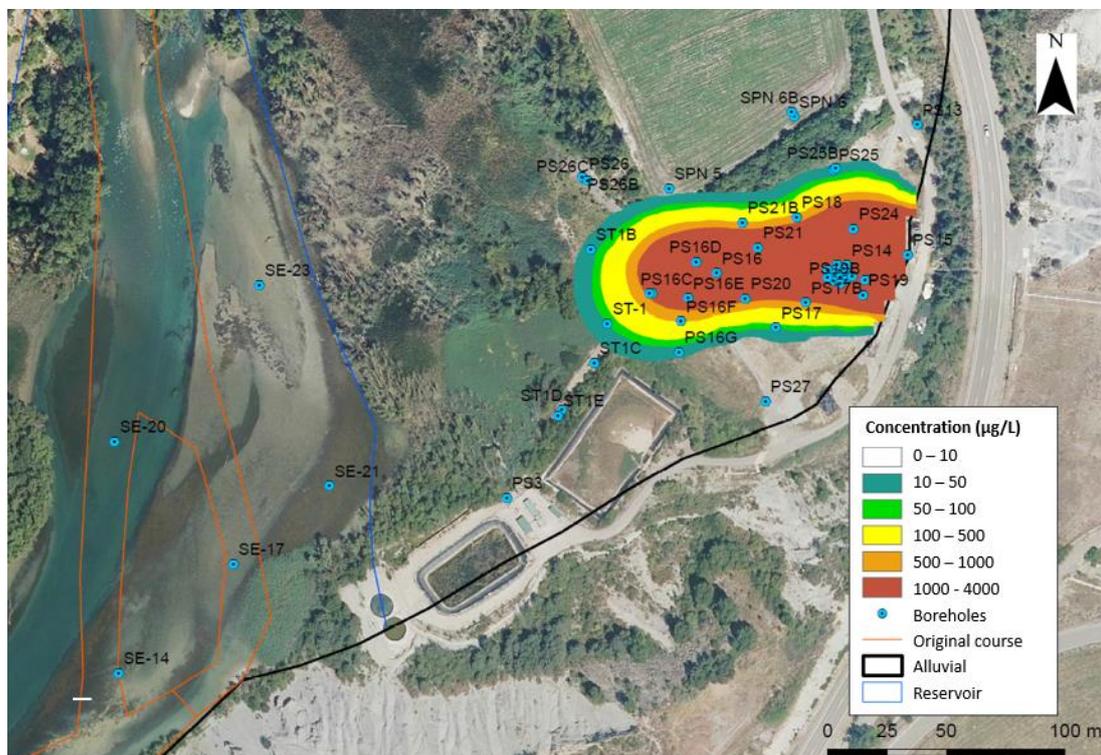
Figure 8.27. Computed plume of total dissolved HCH after 20 years for a distribution coefficient equal to 22 L/kg.
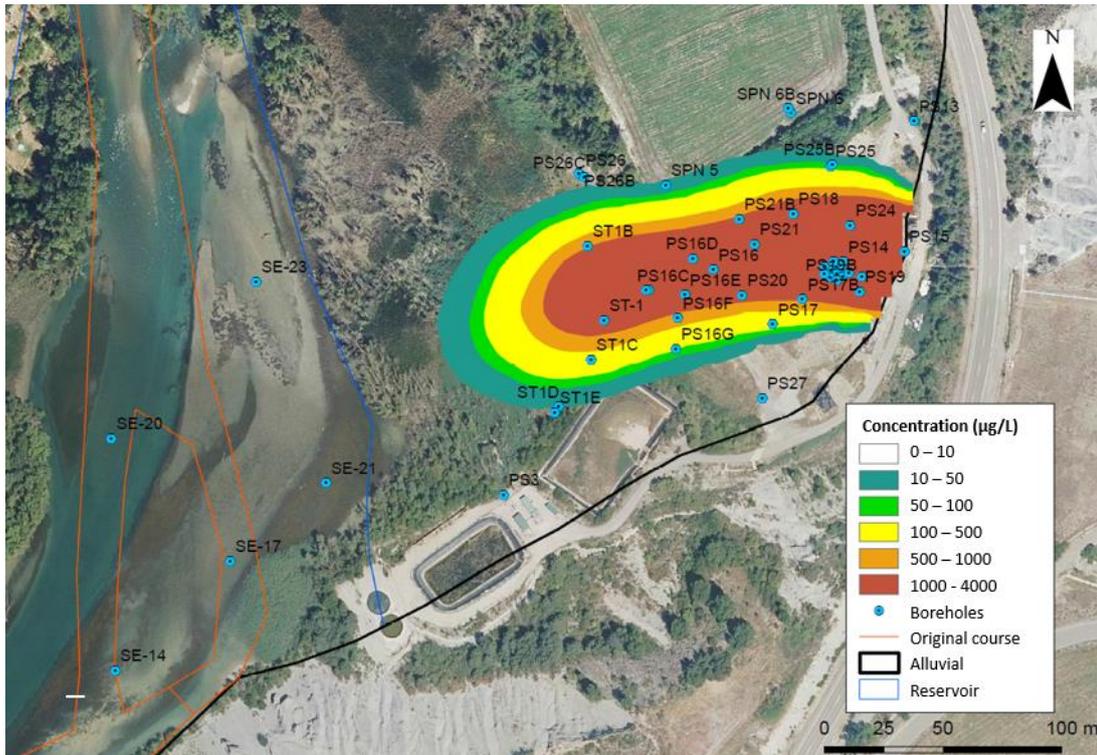
Figure 8.28. Computed plume of total dissolved HCH after 50 years for a distribution coefficient equal to 22 L/kg.
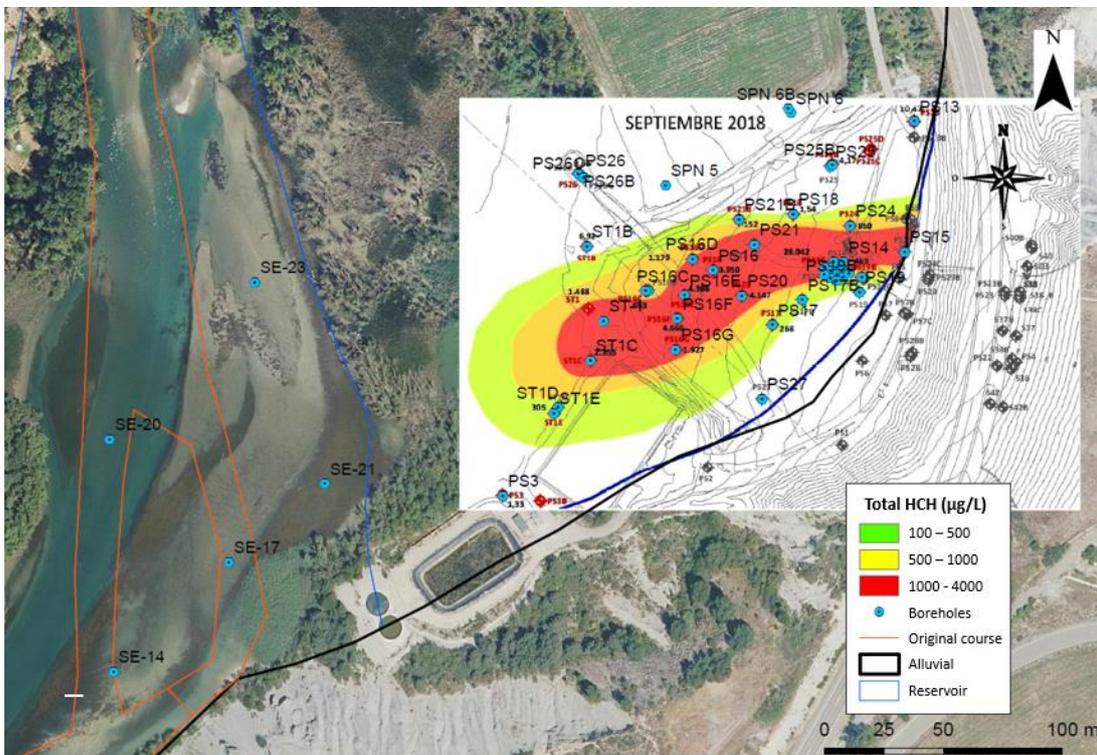
Figure 8.29. Measured plume of total dissolved HCH downstream the Sardas landfill in September 2018 based on measured concentrations in boreholes by EMGRISA.

Figure 8.30. Computed plume of total dissolved HCH at 50 years and average measured total HCH concentrations in the boreholes downstream the front slurry-wall.

The computed plume of total dissolved HCH at 50 years (Figure 8.30) has a similar pattern as that of the measured HCH plume in September 2018 provided by EMGRISA (Figure 8.29). Computed concentrations in a few boreholes are lower than average measured concentrations (ST1B, ST1D, PS17 and PS19). Measured concentrations in the reservoir boreholes show presence of HCH. The calculated plume shows that HCH has not reached to the location of these boreholes. The model should be refined and improved to overcome this discrepancy.

Figure 8.31 to Figure 8.47 show the comparison of the time evolution of measured and computed total dissolved HCH concentration in the boreholes. These graphs show the computed concentrations and the measured concentrations from 2014 to 2019. The start of the simulation period is on 1st January 1985. The computed concentrations at t = 29 years are related to the 2014. The temporal evolution of measured HCH concentrations from 2015 to 2019 shows frequent fluctuations. The calculated concentrations, on the other hand, do not show seasonal fluctuations and vary smoothly. It must be taken into account that the measured concentrations of total dissolved HCH show a very strong temporal variability, alike in PS24 borehole in which it

varies from 20 to 3322 µg/L. There are numerous possible causes for this temporal variability. Their analysis is beyond the scope of this Master's Thesis. However, it will be studied on the future within the framework of the ongoing project.
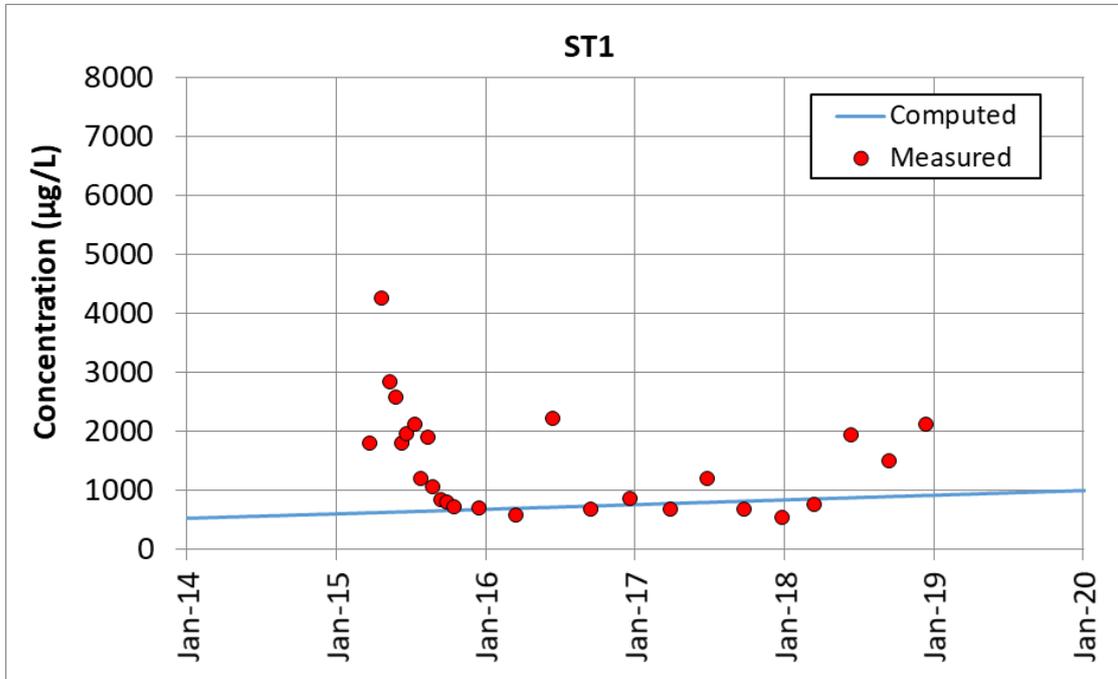
Figure 8.31. Measured HCH concentrations (red dots) and computed HCH concentrations in ST1 borehole using the steady state groundwater flow and transient HCH transport model (blue line).
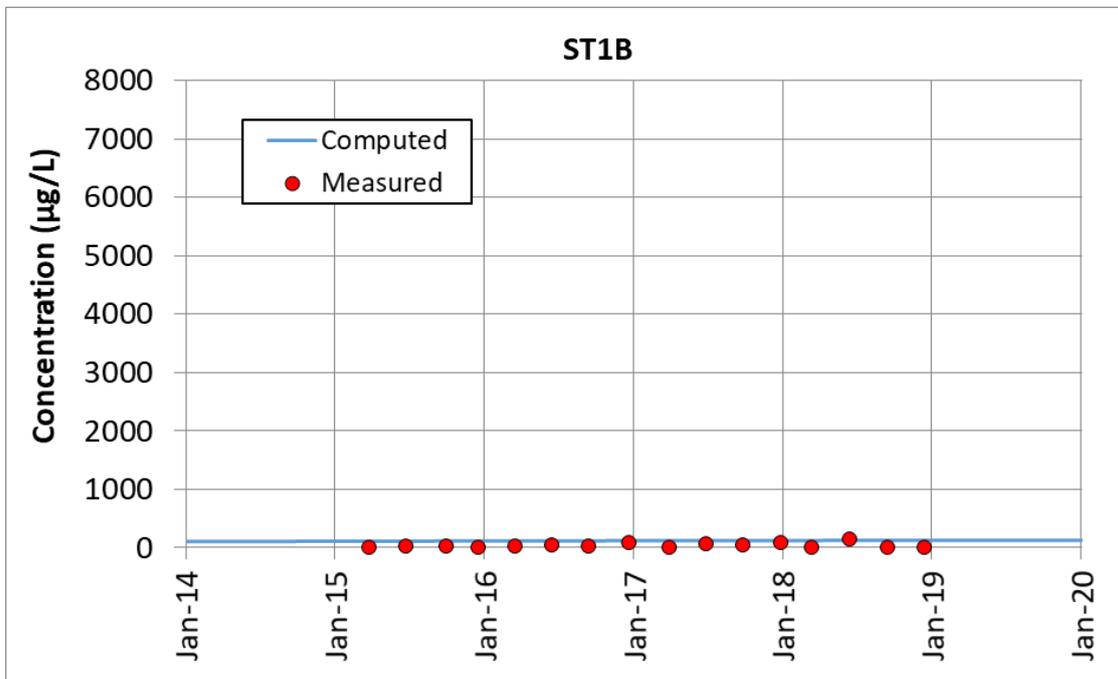
Figure 8.32. Measured HCH concentrations (red dots) and computed HCH concentrations in ST1B borehole using the steady state groundwater flow and transient HCH transport model (blue line).
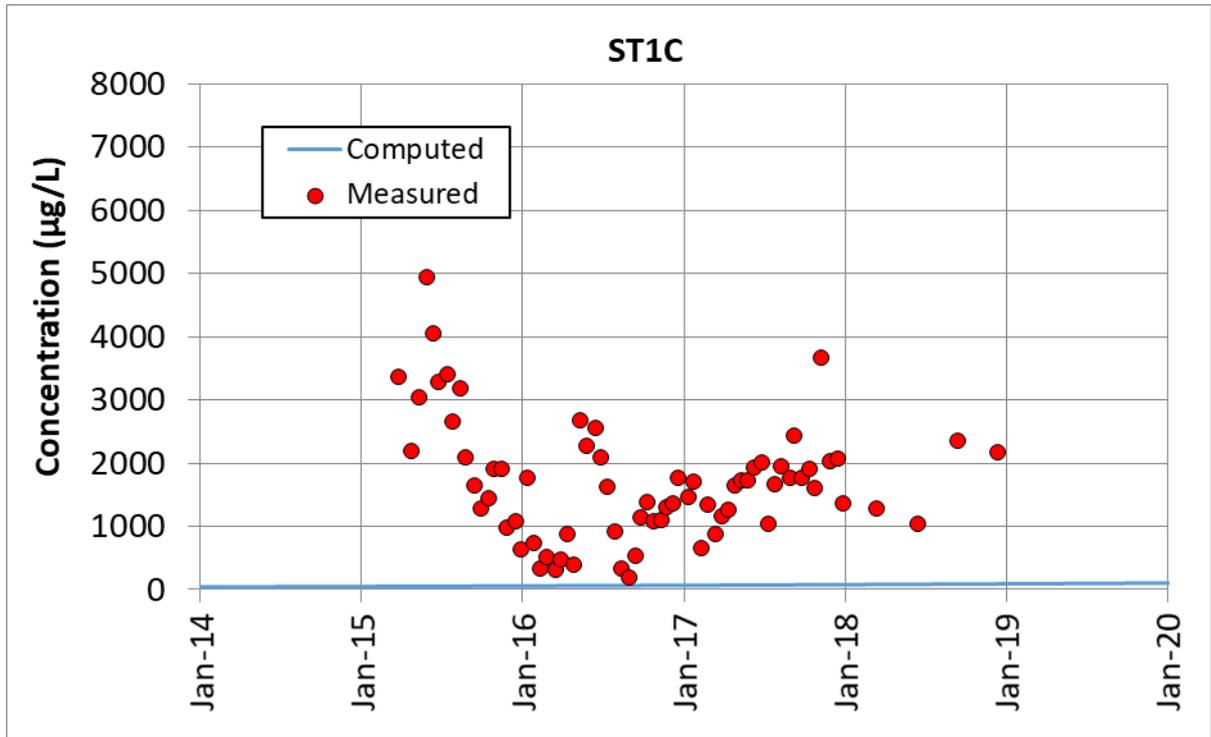
Figure 8.33.   Measured HCH concentrations (red dots) and computed HCH concentrations in ST1C borehole using the steady state groundwater flow and transient HCH transport model (blue line).
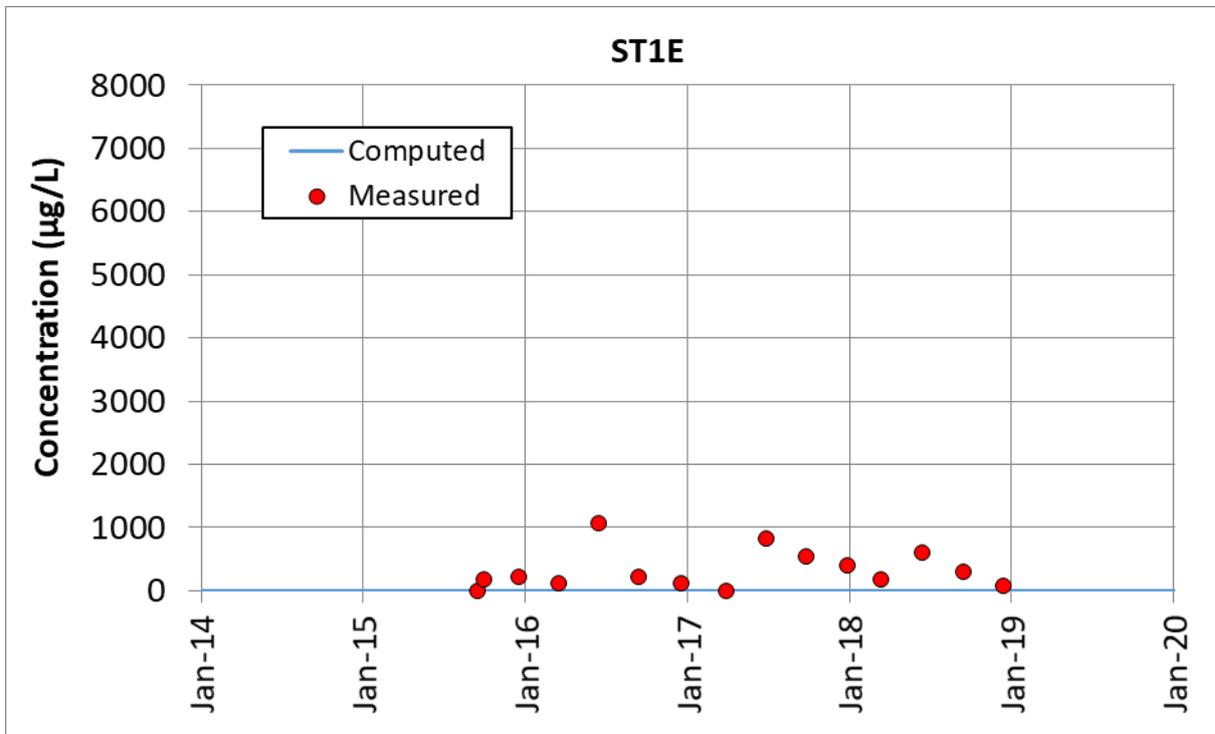
Figure 8.34.   Measured HCH concentrations (red dots) and computed HCH concentrations in ST1E borehole using the steady state groundwater flow and transient HCH transport model (blue line).
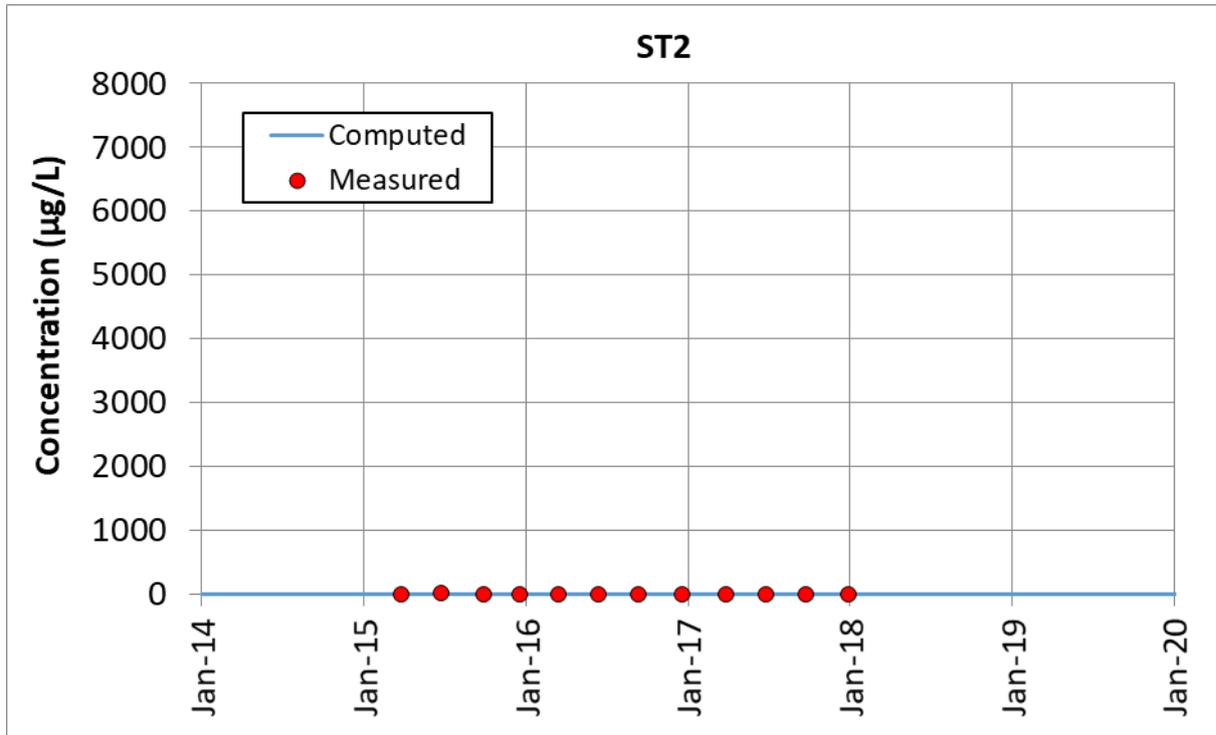
Figure 8.35. Measured HCH concentrations (red dots) and computed HCH concentrations in ST2 borehole using the steady state groundwater flow and transient HCH transport model (blue line).
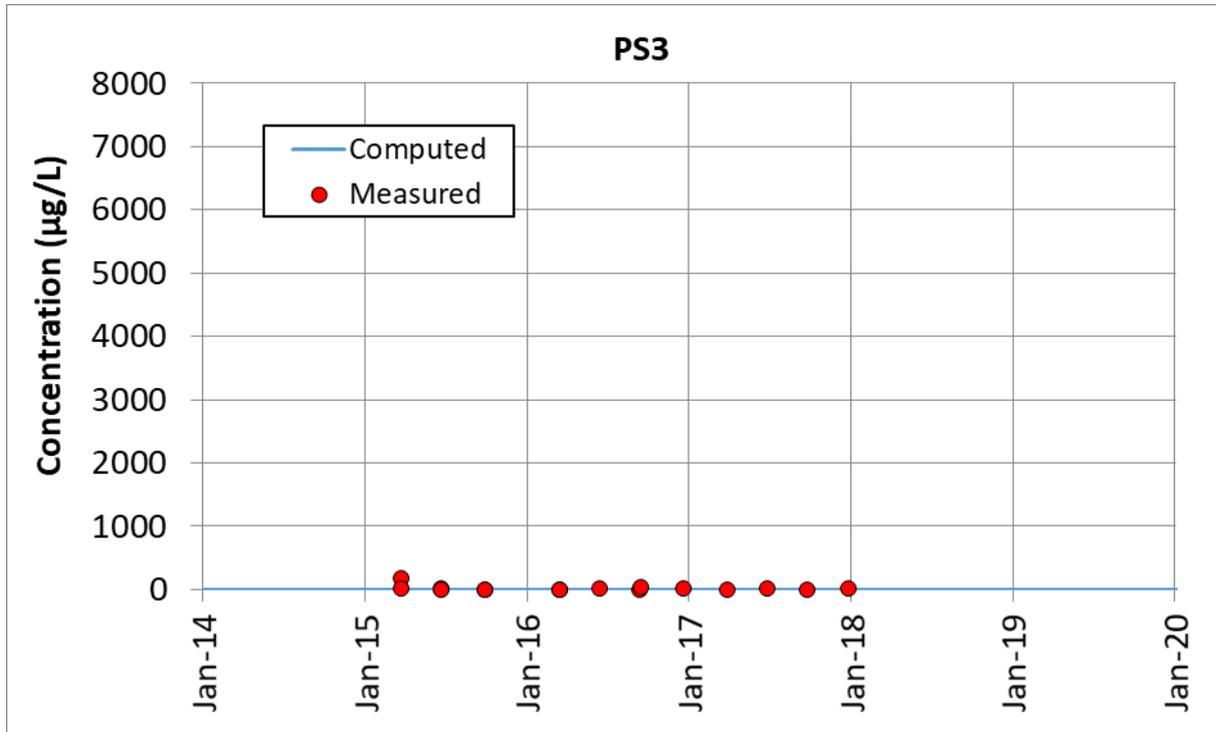
Figure 8.36. Measured HCH concentrations (red dots) and computed HCH concentrations in PS3 borehole using the steady state groundwater flow and transient HCH transport model (blue line).
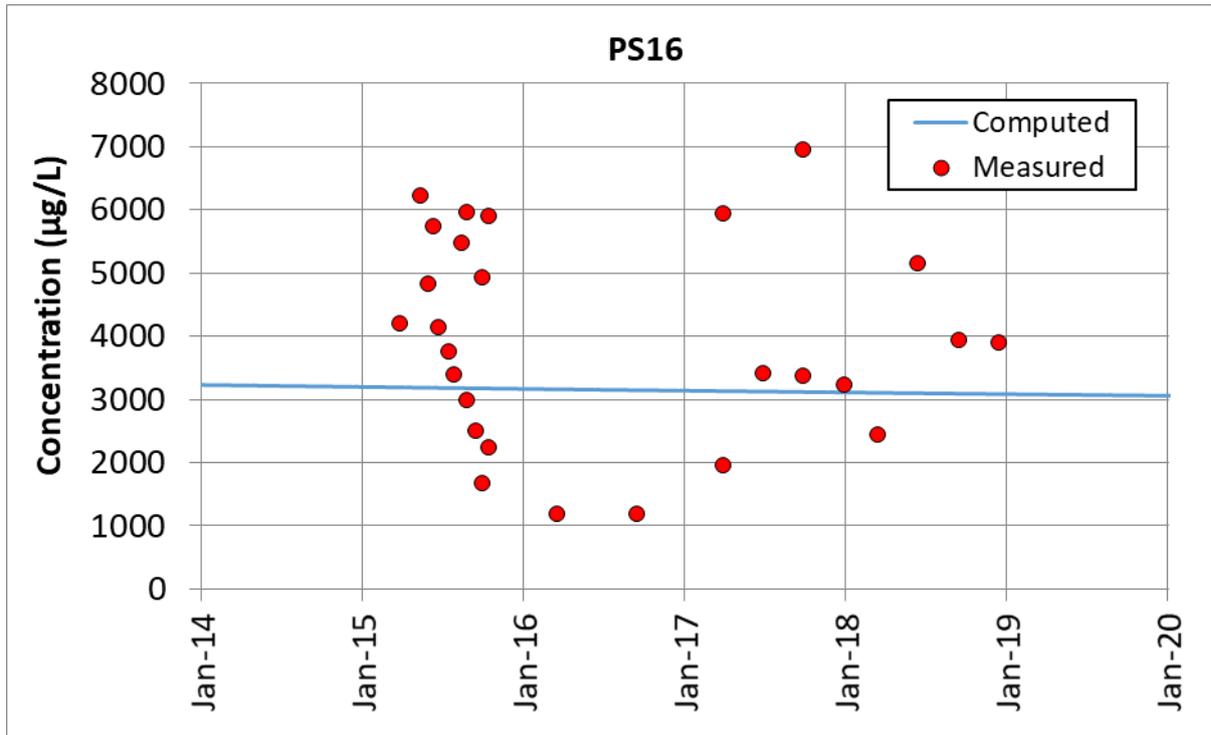
Figure 8.37. Measured HCH concentrations (red dots) and computed HCH concentrations in PS16 borehole using the steady state groundwater flow and transient HCH transport model (blue line).
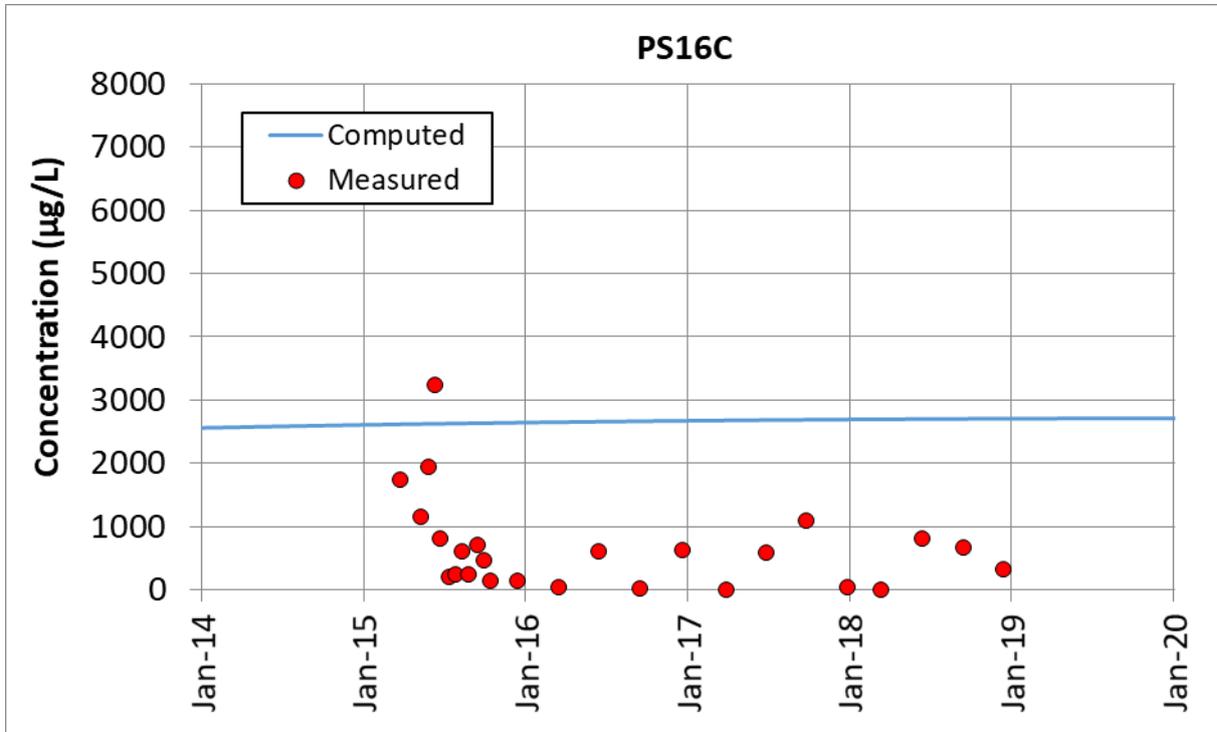
Figure 8.38. Measured HCH concentrations (red dots) and computed HCH concentrations in PS16C borehole using the steady state groundwater flow and transient HCH transport model (blue line).
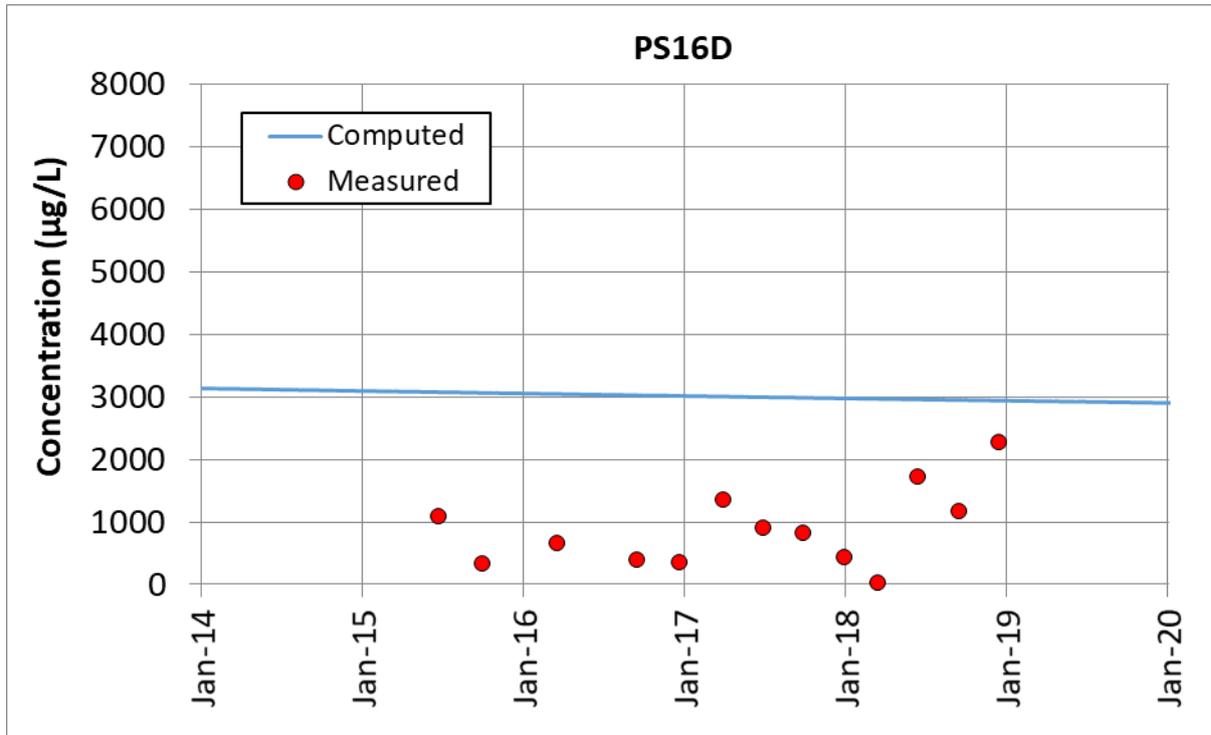
Figure 8.39.   Measured HCH concentrations (red dots) and computed HCH concentrations in PS16D borehole using the steady state groundwater flow and transient HCH transport model (blue line).
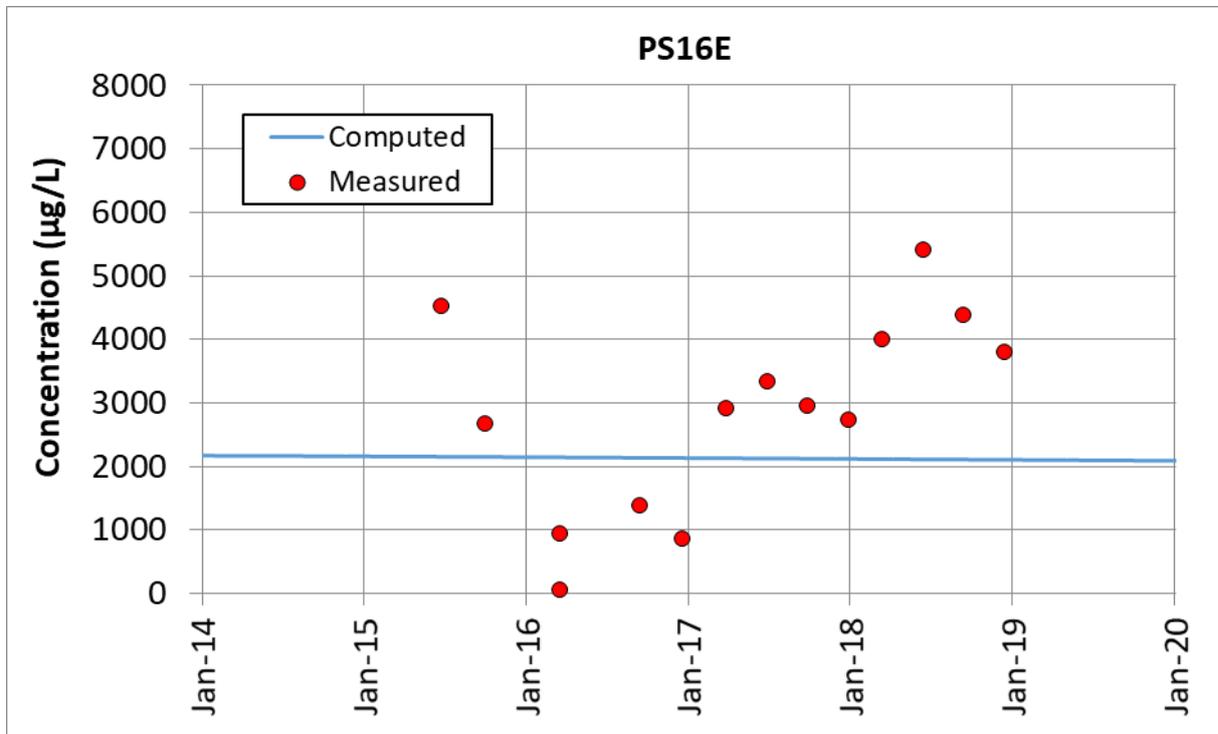
Figure 8.40.   Measured HCH concentrations (red dots) and computed HCH concentrations in PS16E borehole using the steady state groundwater flow and transient HCH transport model (blue line).
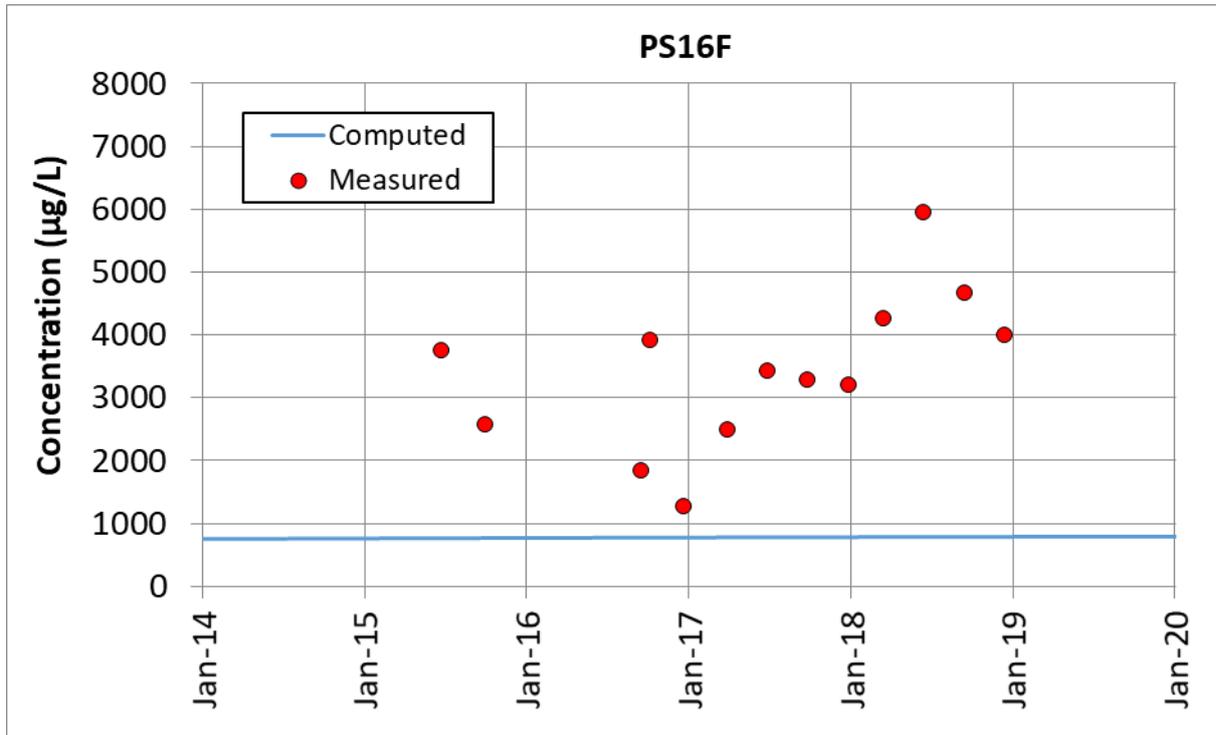
Figure 8.41. Measured HCH concentrations (red dots) and computed HCH concentrations in PS16F borehole using the steady state groundwater flow and transient HCH transport model (blue line).
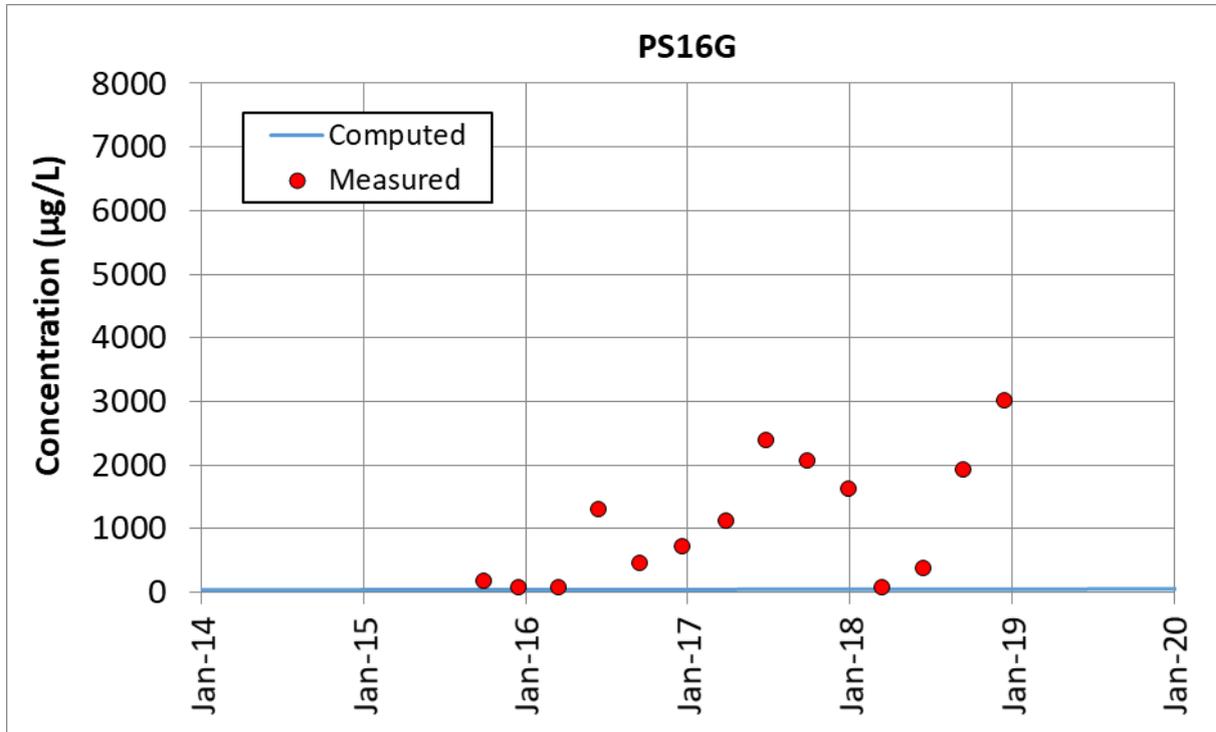
Figure 8.42. Measured HCH concentrations (red dots) and computed HCH concentrations in PS16G borehole using the steady state groundwater flow and transient HCH transport model (blue line).
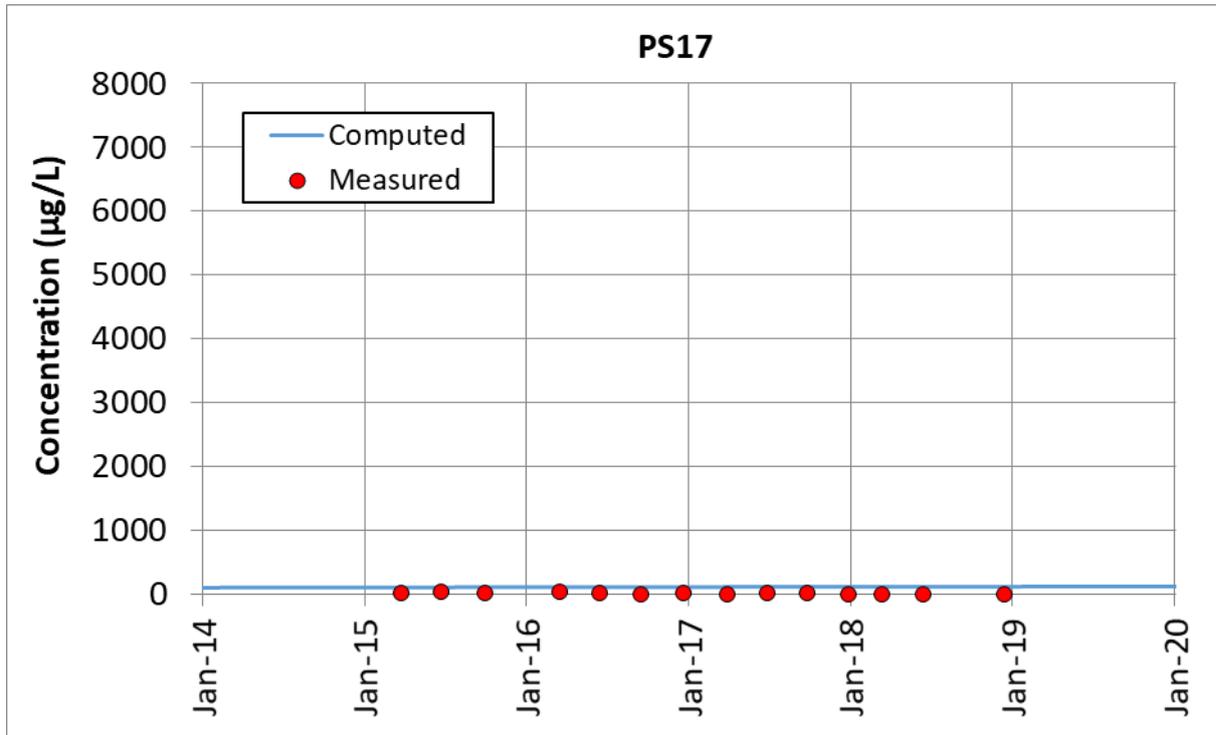
Figure 8.43.   Measured HCH concentrations (red dots) and computed HCH concentrations in PS17 borehole using the steady state groundwater flow and transient HCH transport model (blue line).
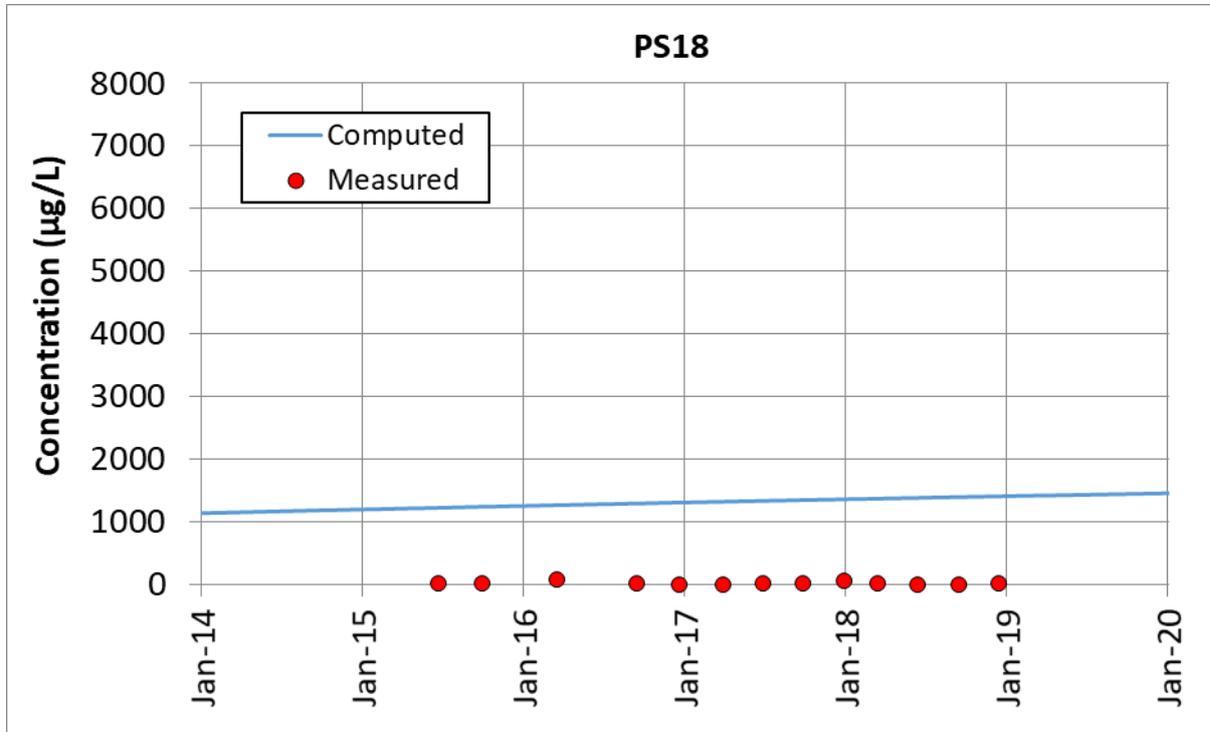
Figure 8.44.   Measured HCH concentrations (red dots) and computed HCH concentrations in PS18 borehole using the steady state groundwater flow and transient HCH transport model (blue line).
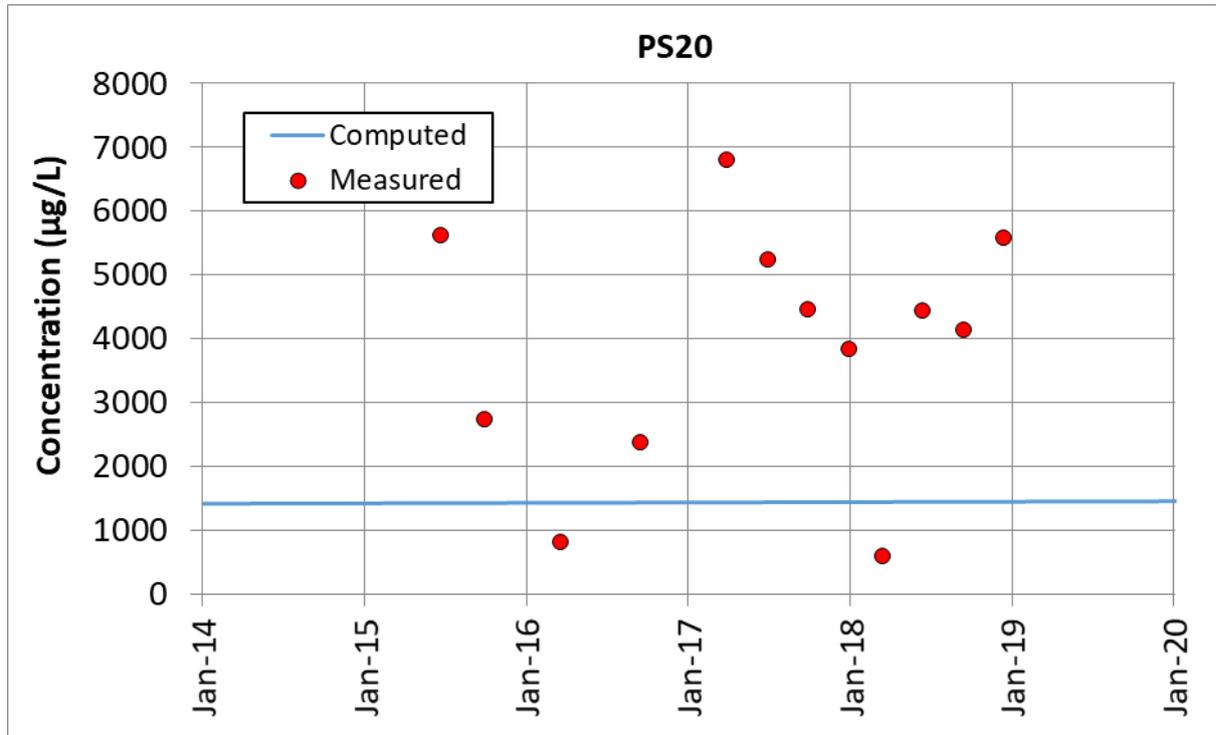
Figure 8.45.   Measured HCH concentrations (red dots) and computed HCH concentrations in PS20 borehole using the steady state groundwater flow and transient HCH transport model (blue line).
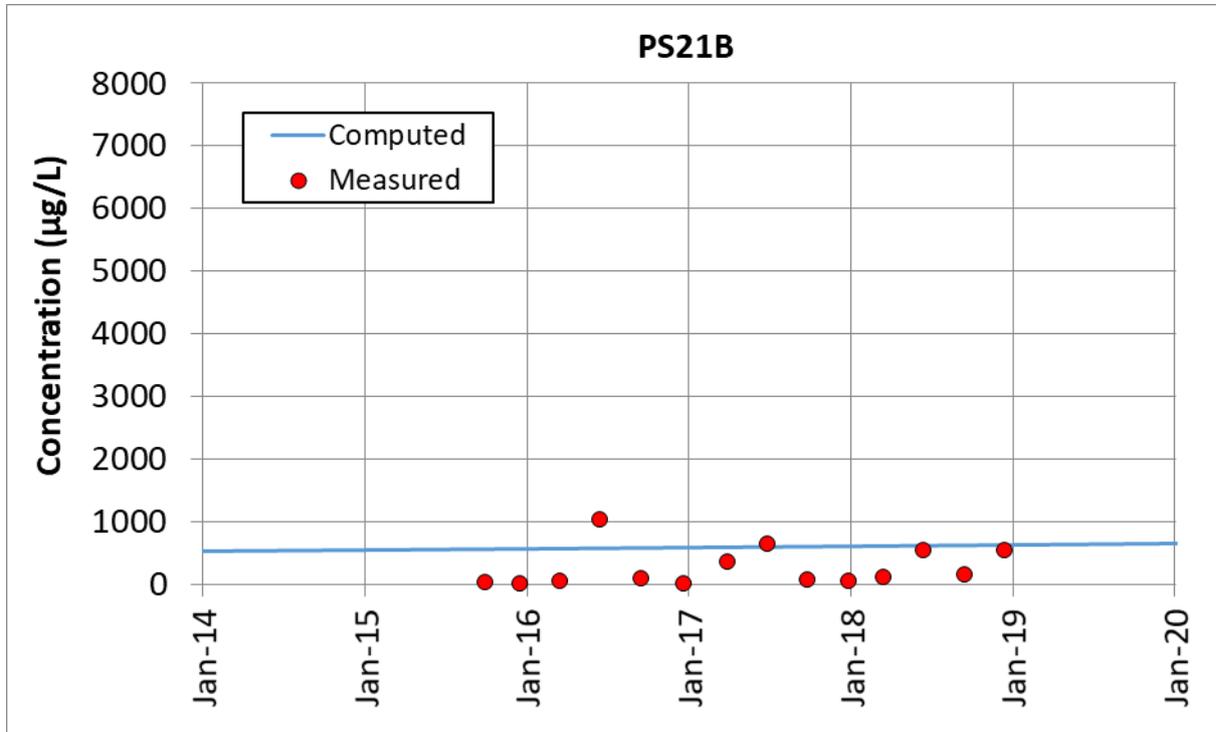
Figure 8.46.   Measured HCH concentrations (red dots) and computed HCH concentrations in PS21B borehole using the steady state groundwater flow and transient HCH transport model (blue line).
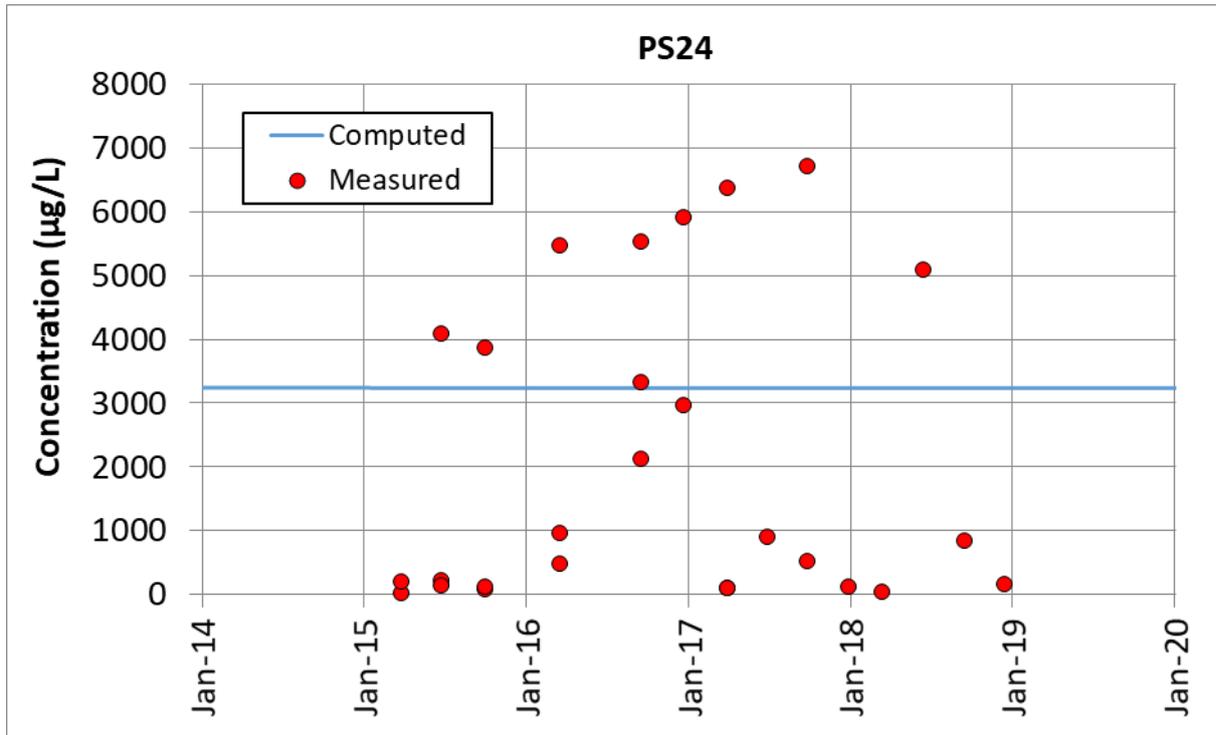
Figure 8.47. Measured HCH concentrations (red dots) and computed HCH concentrations in PS24 borehole using the steady state groundwater flow and transient HCH transport model (blue line).
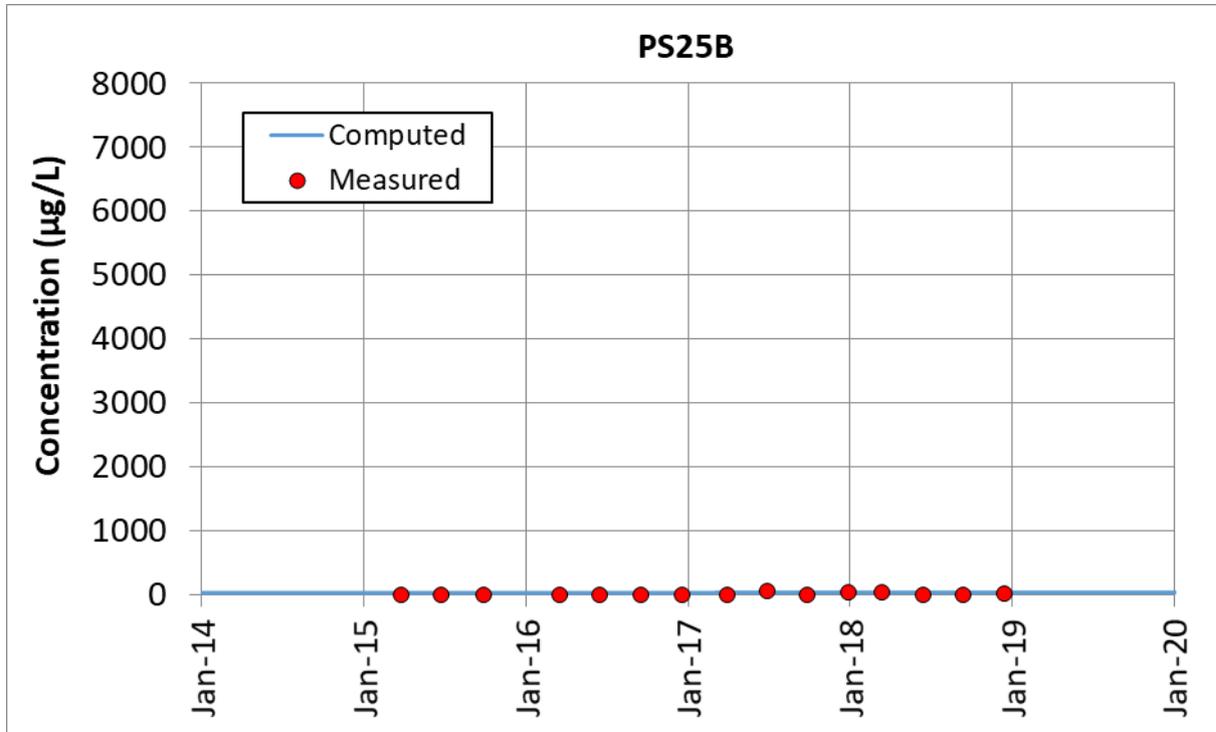
Figure 8.48. Measured HCH concentrations (red dots) and computed HCH concentrations in PS25B borehole using the steady state groundwater flow and transient HCH transport model (blue line).
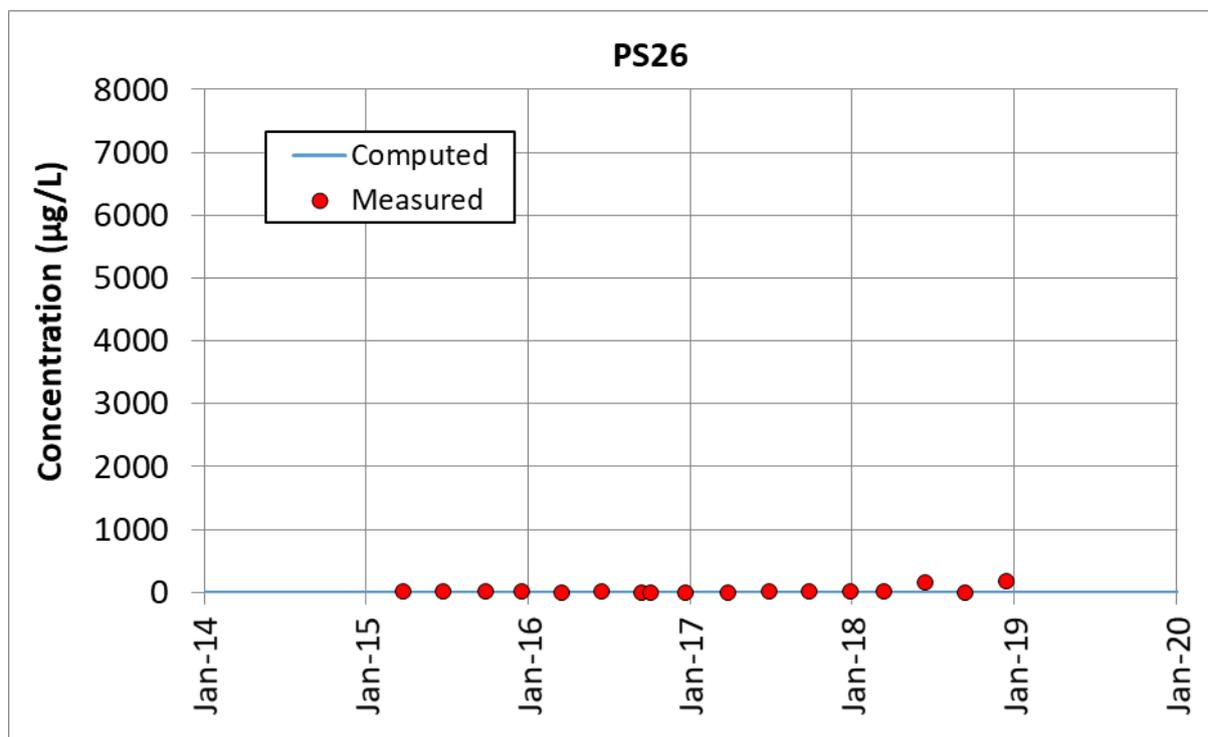
Figure 8.49. Measured HCH concentrations (red dots) and computed HCH concentrations in PS26 borehole using the steady state groundwater flow and transient HCH transport model (blue line).

8.3.2 <u>Sensitivity to the HCH distribution coefficient</u>

Several sensitivity runs have been performed to evaluate the sensitivity of the HCH plumes to the changes in the distribution coefficient of HCH. Figure 8.50 to Figure 8.53 show the computed HCH plumes at 50 years for distribution coefficients equal to 3.6 L/kg, 6 L/kg, 10 L/kg and 15 L/kg.

The lower the distribution coefficient, the larger the HCH plume. For distribution coefficients equal to 3.6, 6 and 10 L/kg the HCH plume reaches the reservoir and the former Gállego riverbed with a concentration of at least 100 µg/L. For K_D equal to 15 L/kg, the concentration of dissolved HCH reaching the reservoir area ranges from 10 µg/L to 50 µg/L. A concentration smaller than 10 µg/L reaches the silting sediments.
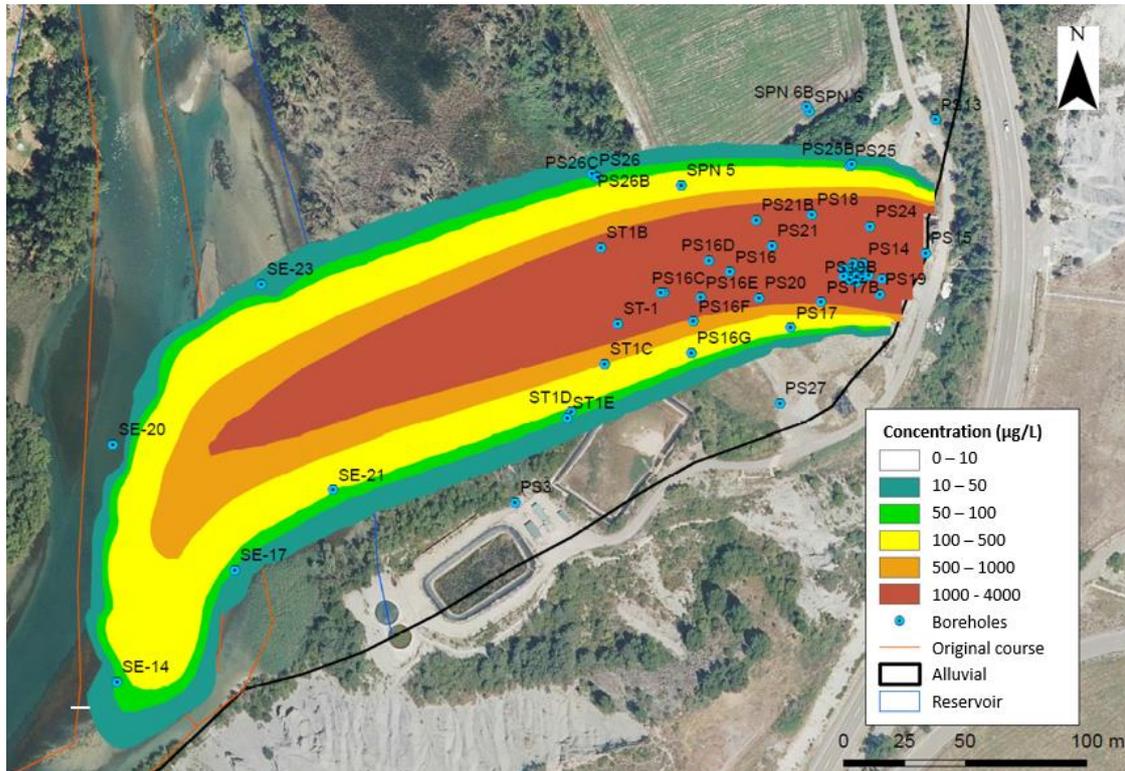
Figure 8.50. Computed plume of total dissolved HCH for a distribution coefficient equal to 3.6 L/kg at t = 50 years.
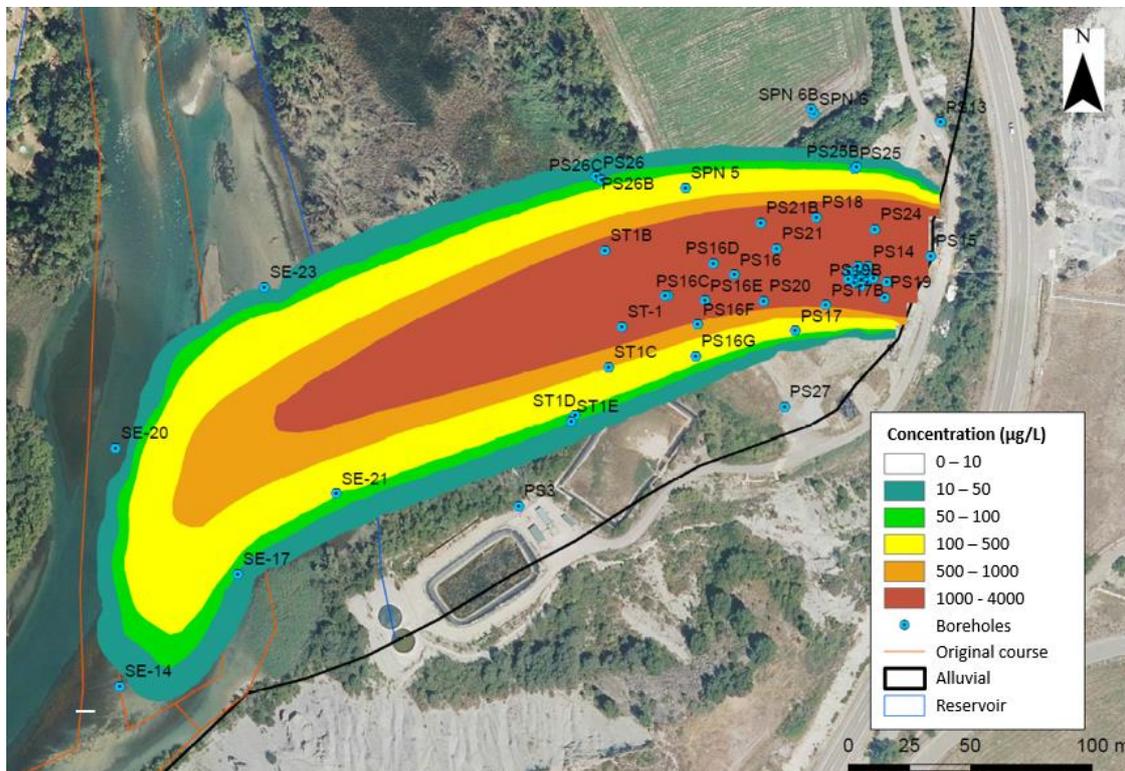
Figure 8.51. Computed plume of total dissolved HCH for a distribution coefficient equal to 6 L/kg at t = 50 years.
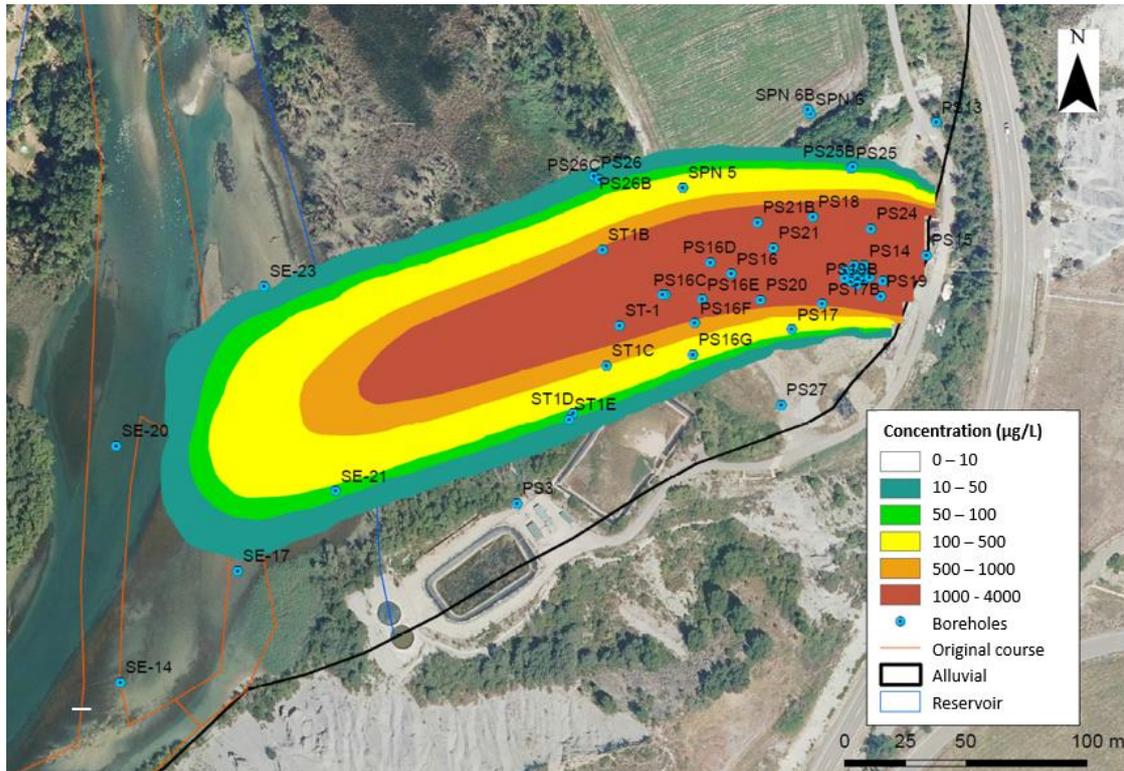
Figure 8.52. Computed plume of total dissolved HCH for a distribution coefficient equal to 10 L/kg at t = 50 years.
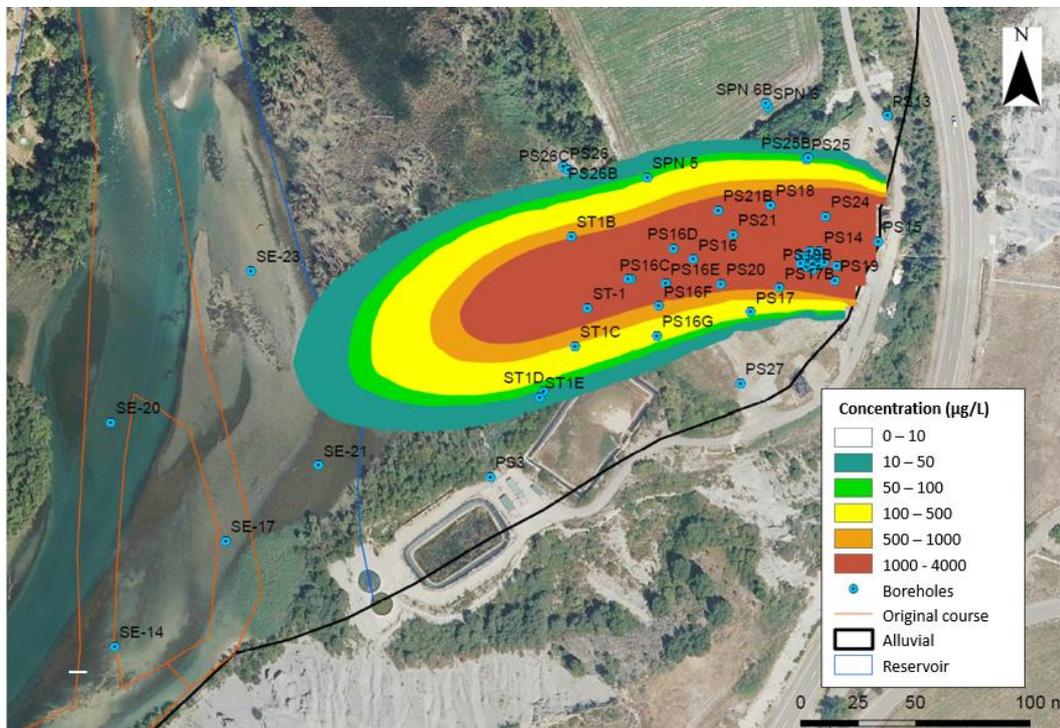
Figure 8.53. Computed plume of total dissolved HCH for a distribution coefficient equal to 15 L/kg at t = 50 years.

From the outflow through the reservoir nodes and the calculated HCH concentration associated to each of those nodes, the mass flow can be obtained as the product of the flow by concentration. The total dissolved HCH mass flow at 50 years arriving to the silting sediments and the silts below the reservoir from the Sardas the landfill has been computed for the base run (K_D = 22 L/Kg) and the sensitivity runs (Table 8.3). The annual mass of dissolved HCH arriving to the reservoir has also been estimated. The lower the distribution coefficient, the greater the mass flow.

Table 8.3. Estimated HCH mass flux and annual HCH mass discharged from the aquifer into the silting deposits at 50 years for distribution coefficients (K_D) equal to 3.6, 6, 10, 15 y 22 L/kg.

K_D (L/kg)	HCH mass flow (g/day)	Annual HCH mass (g)	Annual HCH mass (kg)
3.6	29.52	10 783.07	10.78
6	24.66	9007.36	9.01
10	8.01	2925.93	2.93
15	0.16	57.65	0.06
22	$3.26 \cdot 10^{-4}$	0.12	$1 \cdot 10^{-4}$

8.4 Conclusions

A 2D steady-state horizontal groundwater flow and transient HCH transport model through the gravels of the alluvial aquifer has been presented. The model provided the computed HCH plumes in the aquifer and the HCH mass flux from the aquifer into the silting deposits.

The model assumes that dissolved HCH is in equilibrium with HCH in the solids and the DNAPL. The equilibrium relationship between total dissolved HCH and HCH solid phase concentrations has been simulated with a distribution coefficient, K_D. The distribution coefficient has been calibrated within the range of reported values given the lack of experimental data for the study area. The computed HCH plumes show similarities with those derived from measured total HCH in the alluvial boreholes. The computed plume of total dissolved HCH is very sensitive to changes in the distribution coefficient. The lower the distribution coefficient, the larger the HCH plume. The total mass of dissolved HCH discharged from the gravels into the silting deposits ranges from 0 for the base run to 10 kg/year for K_D = 3.6 L/kg.

The time evolution of the measured HCH concentrations from 2015 to 2019 show numerous oscillations. The computed concentrations of dissolved HCH concentrations, on the other hand, show no time variability. The analysis of these fluctuations poses challenges and difficulties, as many factors can cause these fluctuations. The analysis of the fluctuations of the measured dissolved HCH data is beyond the scope of this Master Thesis.

9. 2D TRANSIENT-STATE HORIZONTAL GROUNDWATER FLOW MODEL FOR THE INTEPRETATION OF A MULTI-OBSERVATION PUMPING TEST IN BOREHOLE PS14B

9.1 Introduction

This chapter presents a 2D transient-state horizontal groundwater flow model through the gravels of the alluvial aquifer for the interpretation of a multi-observation pumping test performed in borehole PS14B on April 26th 2018. The model allows for the estimation of the spatial distribution of the hydraulic conductivity in the gravels and the leakage coefficient and vertical hydraulic conductivity of the silts that confine the gravels. The chapter starts with a description of the pumping test available data. Then, the numerical model is presented. Model calibration and model results are presented next. The chapter ends with the main conclusions.

9.2 Available data from the pumping test

The pumping test took place on April 26th 2018 from 8:05 am to 8:00 pm on the same day. According to EMGRISA (2018), the flow control was carried out with a totalizing flow meter whose values were periodically recorded manually. The pumping rate ranged generally from 85 to 90 m³/day with an average value of 86.88 m³/day (Figure 9.10).

The drawdowns in the pumping well, the PS14B borehole, and in 14 other observation wells were recorded every minute during the 12 hours of pumping and the 6 hours of the recovery phase. The maximum drawdown measured just before pumping shut-off was equal to 0.21 m in the pumping well (Figure 9.16). The drawdowns at the observation points ranged from 0.11 m at the nearest observation points to 0.02 m at the farthest observation points located almost 250 m from the pumping well (Figure 9.12 to Figure 9.25).

9.3 Numerical model

9.3.1 Space and time discretization

The model domain for the model of the pumping test is a sub-domain of the entire alluvial model domain (Figure 9.1). The model domain boundary to the east is the average reservoir coastline. The northwest limit is a branch of the Gállego river at its confluence with the Sabiñánigo reservoir. The limit to the southwest limit is the old course of the Gállego river, which is currently flooded by the reservoir. The model domain occupies an area of 11.23 ha.
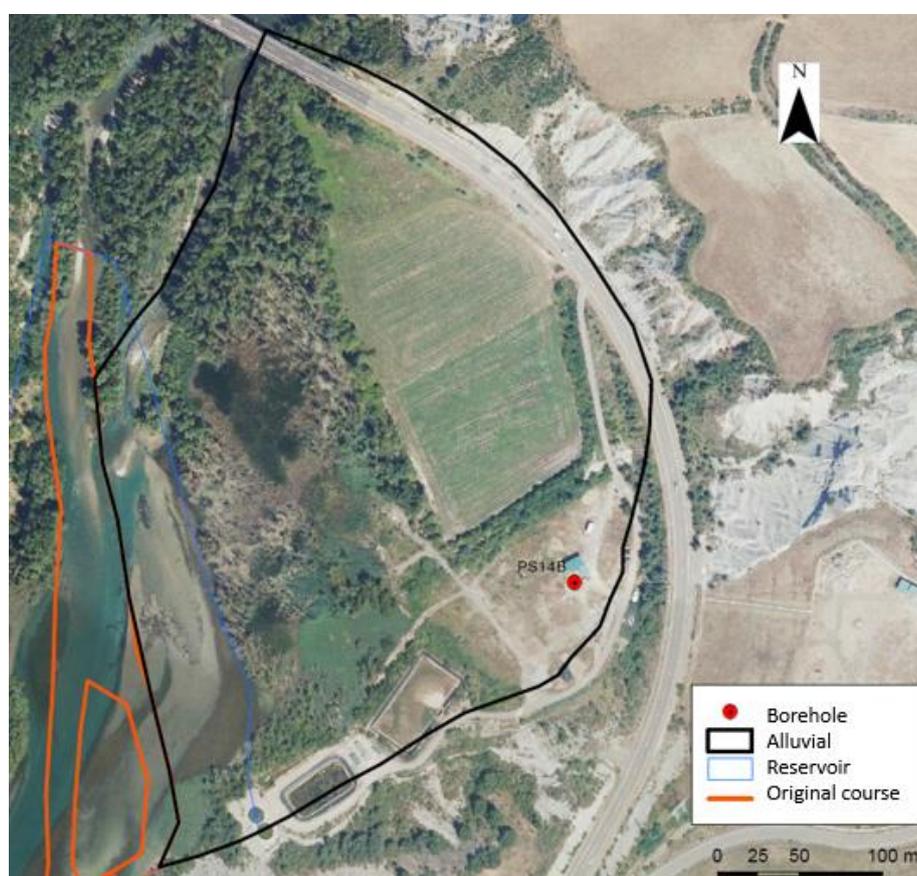
Figure 9.1.   Pumping test model domain on an aerial photograph.

The model domain has been discretized in a triangular finite element mesh with 2738 nodes and 5374 elements. The size of the elements is largest in the areas further away from the PS14B, as the effect of pumping on remote boreholes is small. The mesh has been specially refined around the pumping well (Figure 9.2). Figure 9.3 shows a zoom of the mesh around the pumping well PS14B.
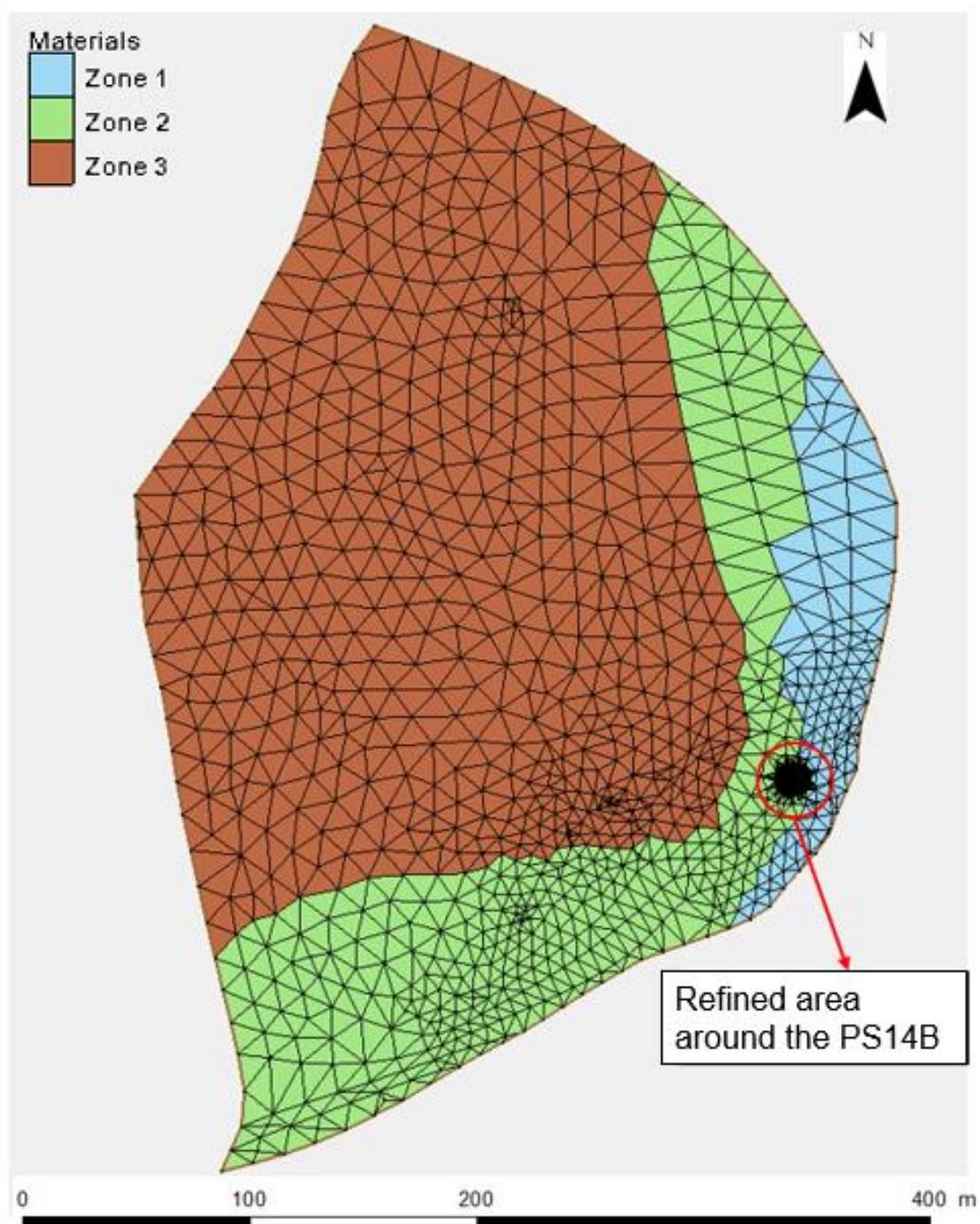
Figure 9.2.   Finite element mesh and material zones of the 2D horizontal groundwater flow model of the pumping test carried out in the PS14B well.
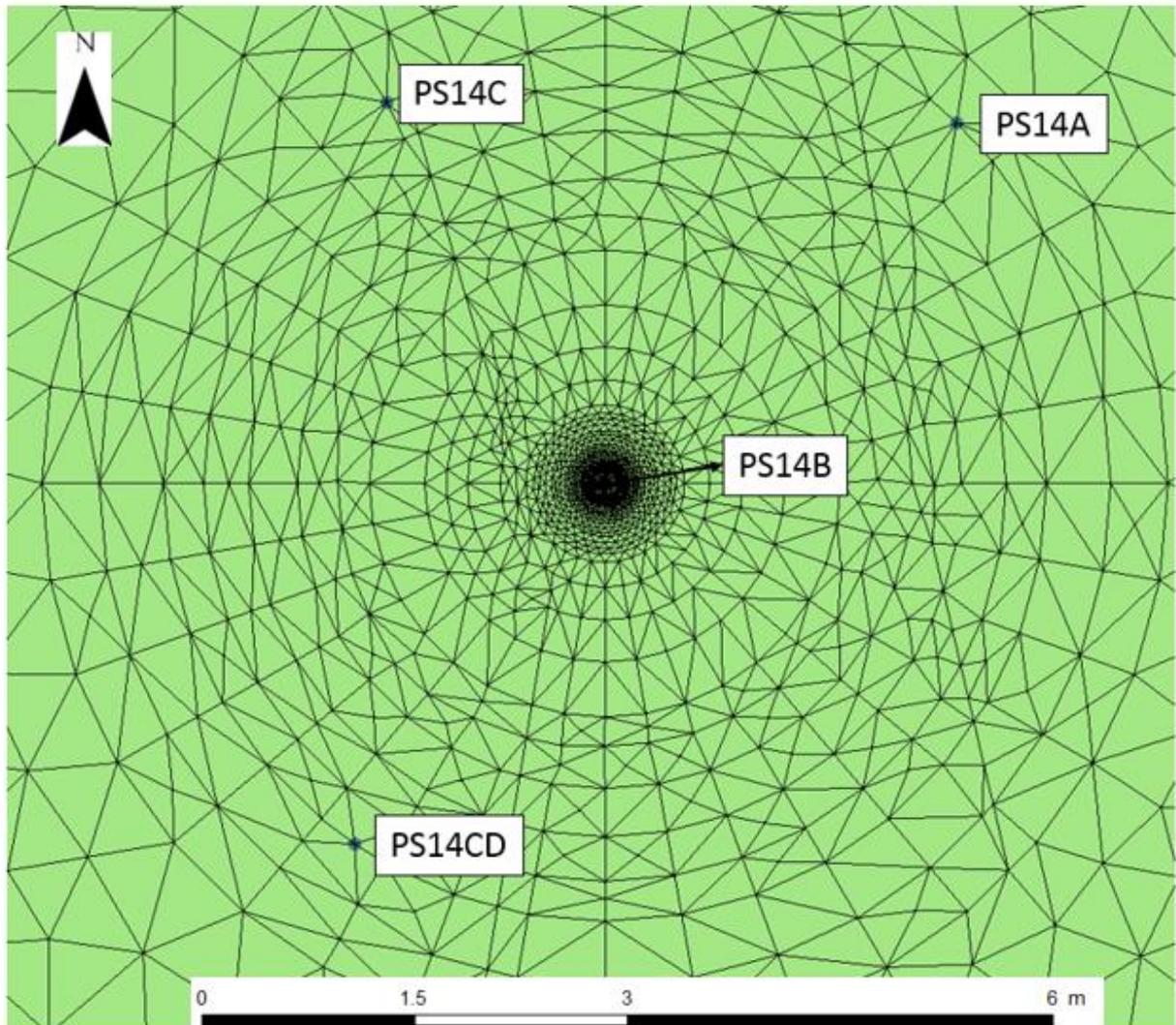
Figure 9.3.   Zoom of the mesh around borehole PS14B (pumping well) showing the location of the nearby observation boreholes.

9.3.2   Model structure

The map of gravel depths in the model is similar to that used in the 2D horizontal groundwater flow model of the entire alluvial (Figure 9.2). For the interpolation of the isopachs, the thickness of the silt and gravel layers measured in the drilled cores of the boreholes PS14B, PS14C and PS14D have been incorporated. The map of the gravel isopachs shows that the gravels are wedged westward near the alluvial boundary. In addition, there is an area of larger gavel thickness in a N - S direction.

Figure 9.3 shows the zoom of the isopachs and gravel thickness zones around the pumping well. Pumping well (PS14B borehole) is located in the area where the gravel thickness ranges from 2.5 m to 3 m. In the PS14 observation boreholes, located around the pumping well, the gravel thickness ranges from 2 m to 2.5 m in the PS14A borehole and from 3m to 3.5 m in the PS14C and PS14D borehole.
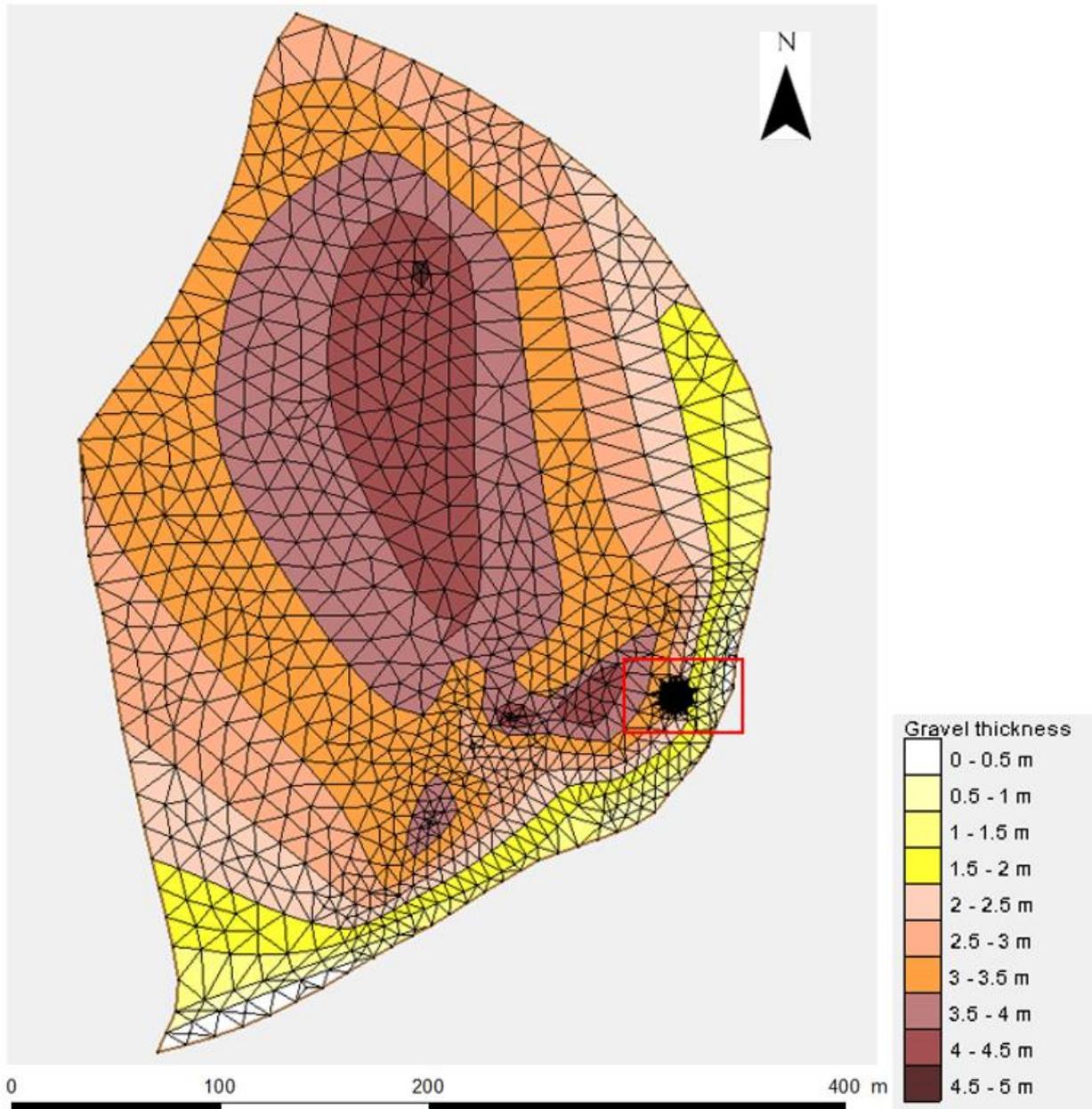
Figure 9.4. Gravel isopachs (m) and areas of different gravel thickness considered in the model of the pumping test. Figure 9.5 presents a zoom of the red square that represents the refined area around the pumping well.
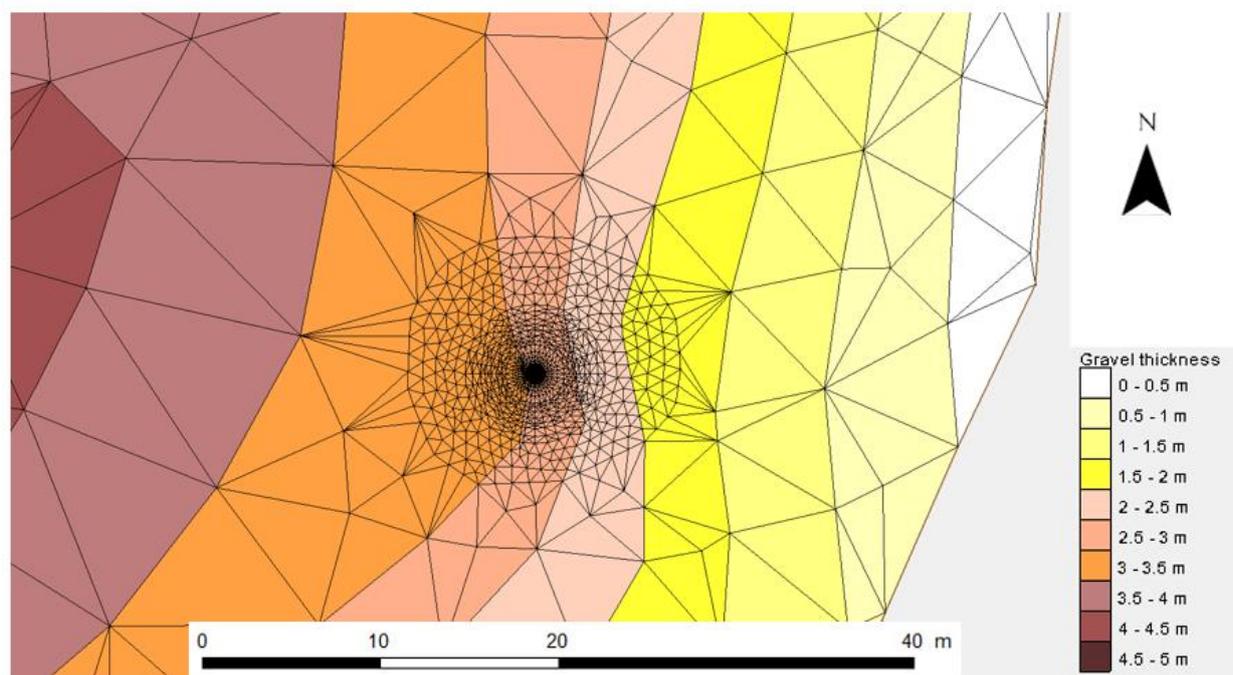
Figure 9.5. Zoom of the map of gravel isopach and the zones of different gravel thicknesses around PS14B borehole (pumping well).

Suso (2018) carried out the separate interpretation of the time evolution of the measured drawdowns in the pumping well and in each the observation boreholes using the Theis method. The estimated values of hydraulic conductivity range from 84 m/d to 430 m/d, while the storage coefficients vary from $5 \cdot 10^{-4}$ to $1.4 \cdot 10^{-3}$. Figure 9.6 shows the values of the hydraulic conductivities, K, and the specific storage coefficients, S_s, estimated by Suso (2018). Estimated K values show the area with the lowest K (around PS26 and PS16 boreholes) and the area with the highest K (around PS19 and PS19B boreholes). Based on that map, 3 material zones have been defined having different K and S_s. Figure 9.7 show the map of material zones considered in the model shown along with the location of the boreholes in where the drawdowns have been monitored.

Figure 9.6. Values of hydraulic conductivity, K, in m/d (upper figure) and specific storage coefficient (m^{-1}) estimated by Suso (2018) from the interpretation of the drawdowns with the Theis method.

The hydraulic conductivity of each material zone has been calibrated by taking as initial value the previous estimate of Suso (2018). The list of material zones and the calibrated values of K and S_s are listed in Table 9.1. Zone 1 is near the boundary and has the highest hydraulic conductivity (600 m/d). The storage coefficient ranges from 10^{-4} m^{-1} in zone 3 to $3 \cdot 10^{-3}$ m^{-1} in zone 2.
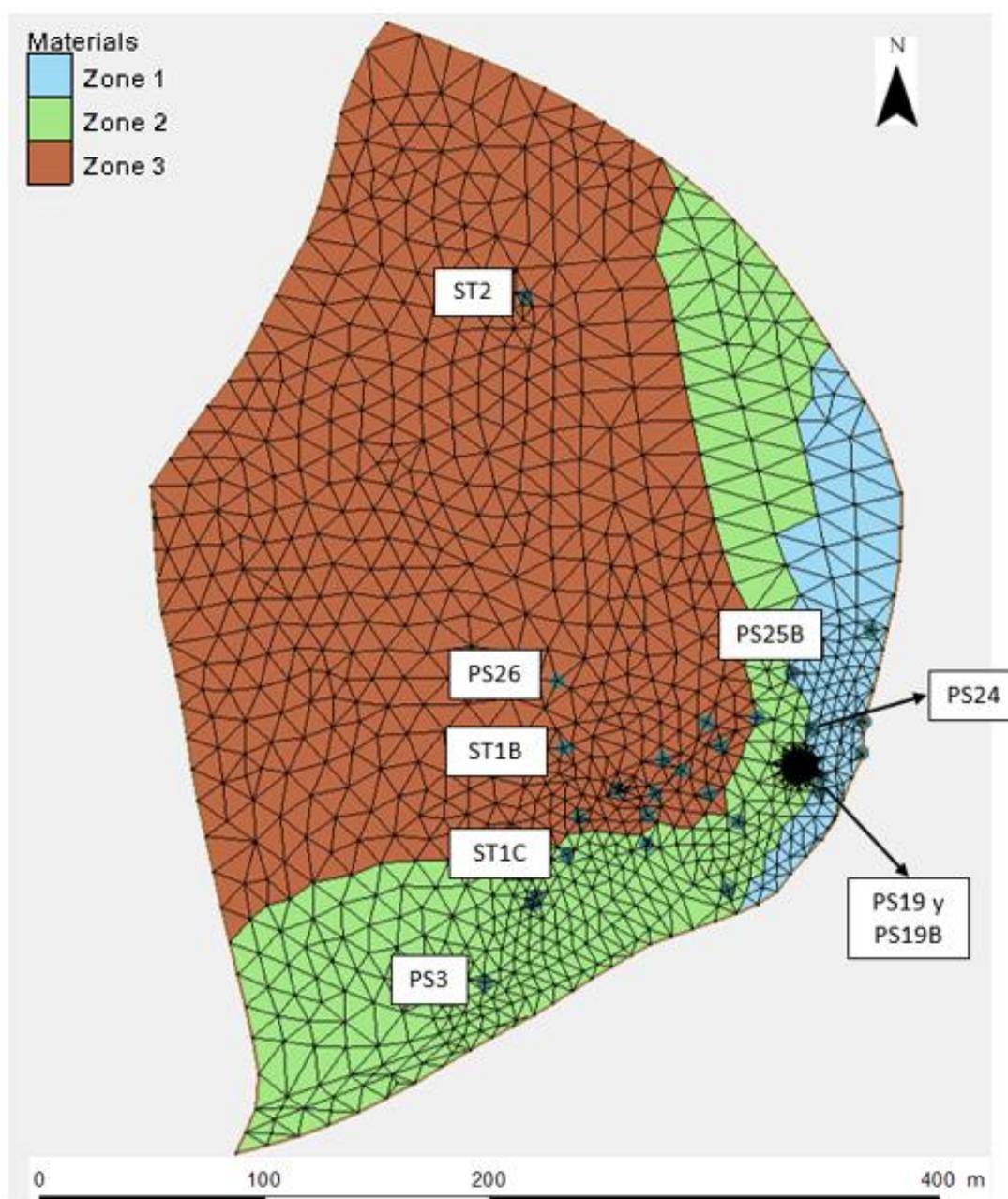
Figure 9.7. Finite element mesh of the 2D model of the pumping test, material zones and location of the observation points in the pumping test.

Table 9.1.   Calibrated hydraulic conductivity, K_h, and S_S in the material zones.

Material zone	Colour	K_h (m/d)	S_S (m^{-1})
Zone 1. Near the landfill		$6 \cdot 10^{+2}$	$2 \cdot 10^{-4}$
Zone 2. Intermediate zone		$3 \cdot 10^{+2}$	$3 \cdot 10^{-3}$
Zone 3. Near the reservoir		$3 \cdot 10^{+2}$	$1 \cdot 10^{-4}$

9.3.3   Initial and boundary conditions

The model has been used to calculate the drawdowns produced by the pumping test in the observation boreholes. Since the flow equation is linear, the flow equation can be formulated in terms of drawdowns, s, instead of hydraulic heads. The initial drawdown is zero everywhere. Model calibration has been performed in terms of drawdowns, s, by comparing the computed to the measured drawdowns in the boreholes.

Figure 9.8 shows the finite element mesh, the material zones and the boundaries of the pumping test model. The boundaries 1, 2 and 3 are simulated with a Neuman type boundary condition as impervious boundaries.
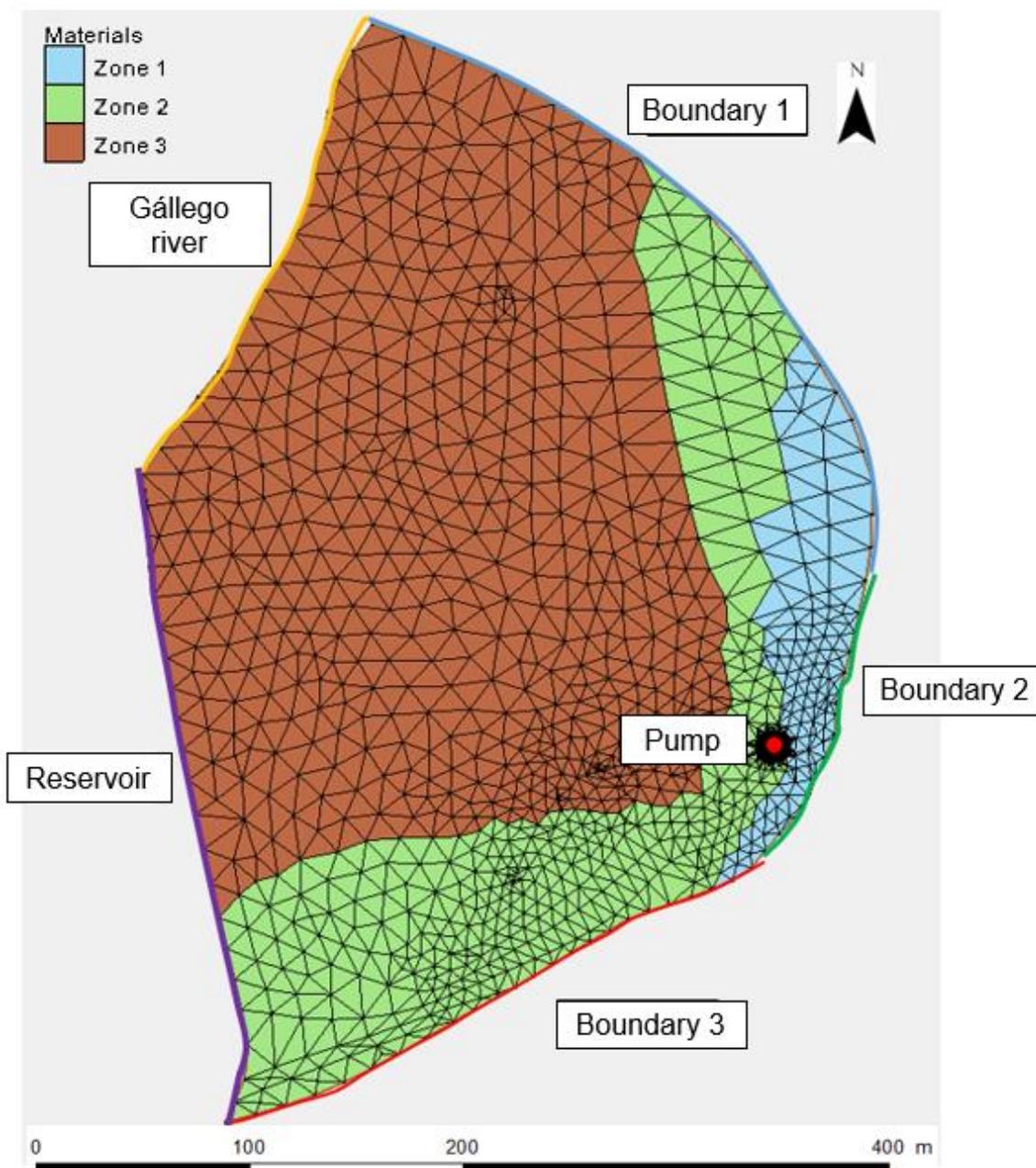
Figure 9.8.   Finite element mesh, material zones and boundaries of the pumping test model.

The reservoir is simulated with a Dirichlet boundary condition in which the time evolution of the drawdown is prescribed. Figure 9.9 shows the time evolution of the drawdown of the reservoir water level during the simulation time period.
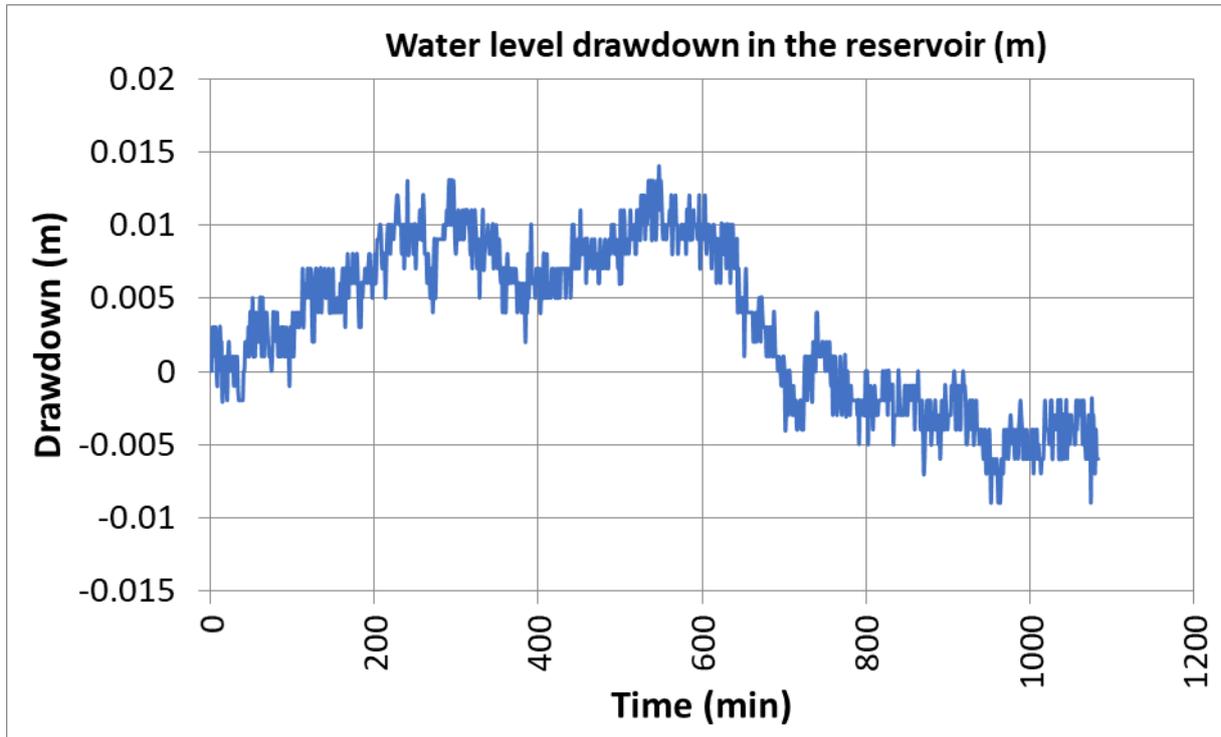
Figure 9.9.   Time evolution of the prescribed drawdown in the reservoir. Drawdowns are positive when the reservoir level decrease and negative when the level increases.

The boundary along the Gállego river has been simulated with a Cauchy-type boundary condition which a fixed drawdown equal to zero and a leakage coefficient equal to that of the model of the entire alluvial aquifer (α = 200 m^2/d).

The pumping rate has been simulated with a Neumann boundary condition in which the pumping rate function (Figure 9.10), provided by EMGRISA, has been considered in the model.
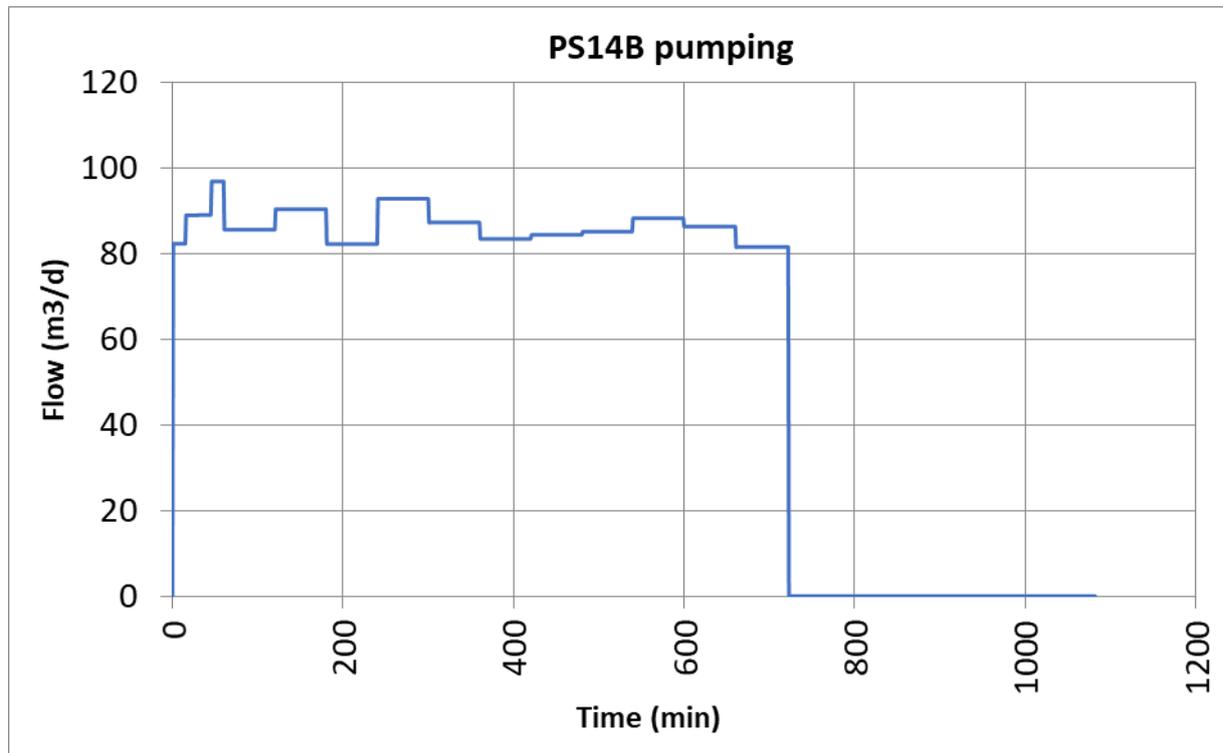
Figure 9.10.   Time evolution of the pumping rate during the pumping test provided by EMGRISA.

A preliminary model of the pumping test was performed with the mesh, material zones, parameters and initial and boundary conditions of the entire alluvial groundwater flow model. The results of this preliminary model indicated that a leakage from the silts would is required to reproduce the measured drawdowns. This leakage has been considered in the model by means of a Cauchy-type boundary condition in all the nodes where the gravels are confined by the silts (Figure 9.11). The fixed drawdown is equal to 0. The nodal leakage coefficient, α, has been derived from the nodal volume of the aquifer, V_n, the vertical hydraulic conductivity of the silt layer (K_l), the thickness of the silts (e) and the thickness of the gravels (b) at the node location. The following expression has been used for the calculation of the leakage coefficient:

$$\alpha_{calibrated} = \frac{K_l \cdot V_n}{e \cdot b}$$

where K_l is equal to 0.02 m/d. The thickness of the silts, e, has been calibrated within the expected range from 3.4 m to 11.6 m. The calibrated value of e is equal to 8 m. The thickness of the gravels at a given node, b, is calculated as the average of the thickness of the elements which have a vertex on that node.
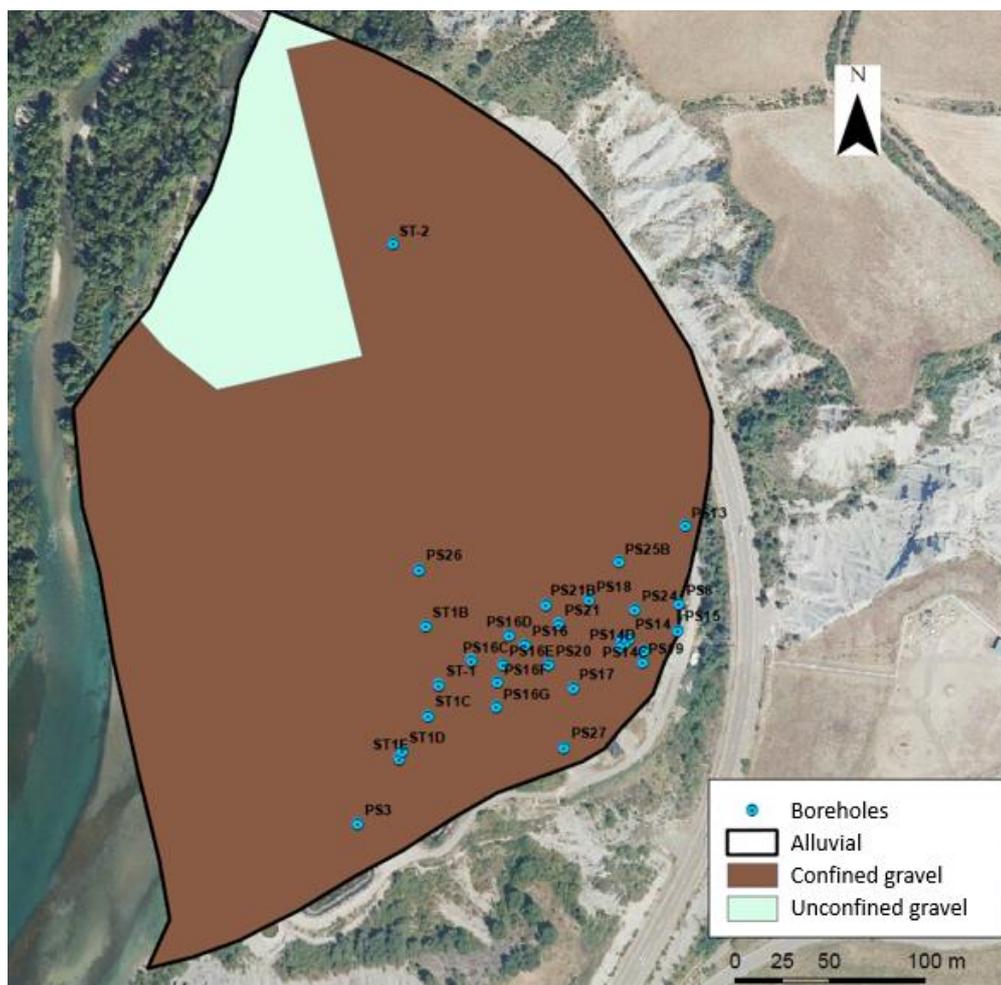
Figure 9.11. Map of confined (brown) and unconfined (green) gravel areas. An inflow from the silts to the gravels has been considered in the model by using a Cauchy boundary condition.

9.4 Model results

9.4.1 Results of the base run

Figure 9.12 to Figure 9.25 present the time evolution of the measured and calculated drawdowns with the calibrated model in the selected boreholes.

The calibration of the hydraulic conductivities and specific storage coefficients has been performed automatically by solving the inverse problem with INVERSE-CORE (Dai and Samper, 2004). The estimation of the leakage coefficient through the silts has been made by trial and error.
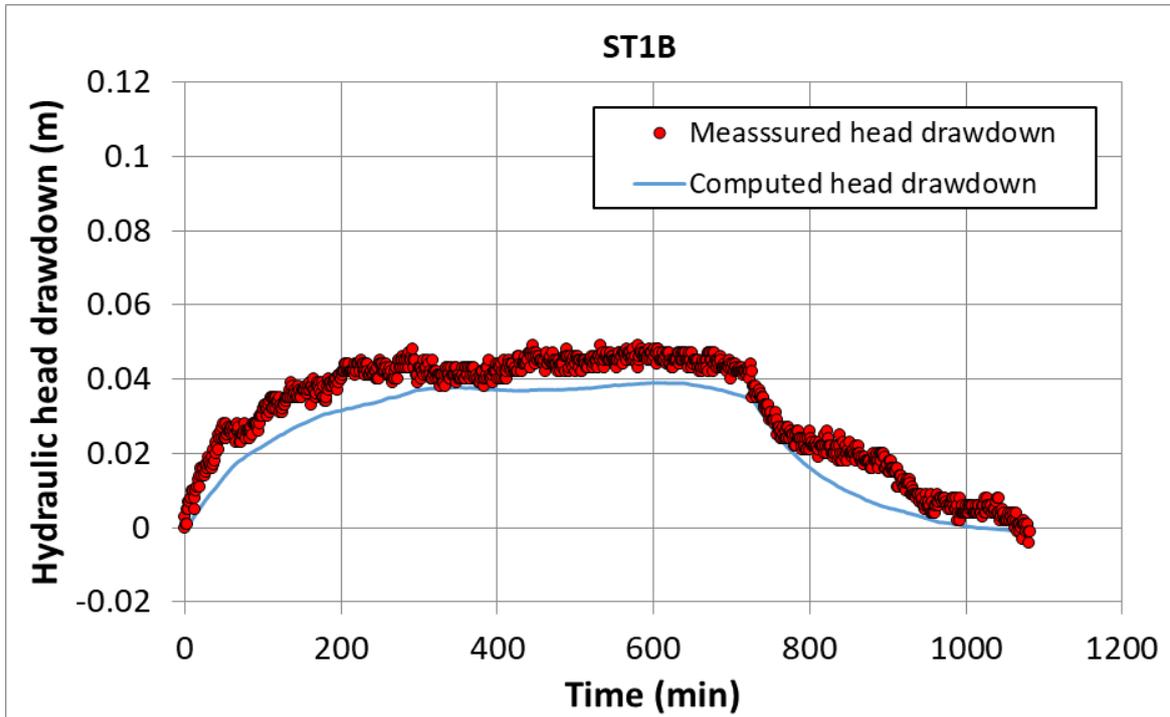
Figure 9.12. Drawdowns measured with diver (red points) in borehole ST1B and computed with the calibrated 2D transient-state horizontal groundwater flow model through the gravels of the alluvial aquifer for the interpretation of the pumping test performed in borehole PS14B on April 26th 2018 (blue line).
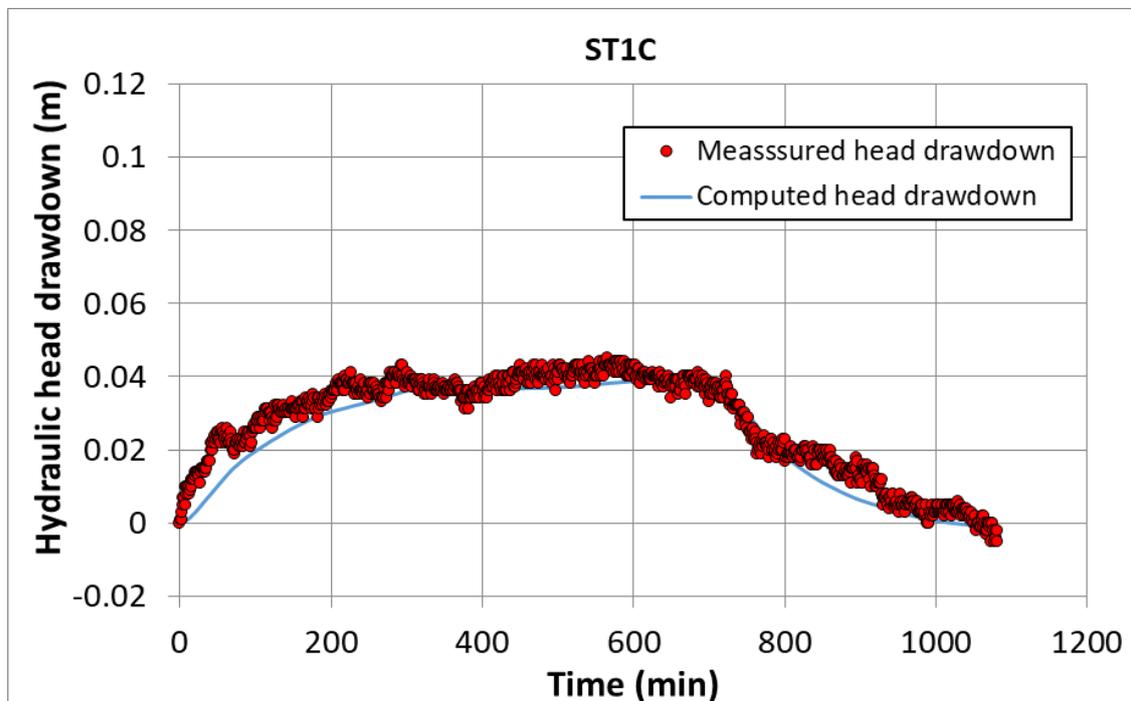
Figure 9.13. Drawdowns measured with diver (red points) in borehole ST1C and computed with the calibrated 2D transient-state horizontal groundwater flow model through the gravels of the alluvial aquifer for the interpretation of the pumping test performed in borehole PS14B on April 26th 2018 (blue line).
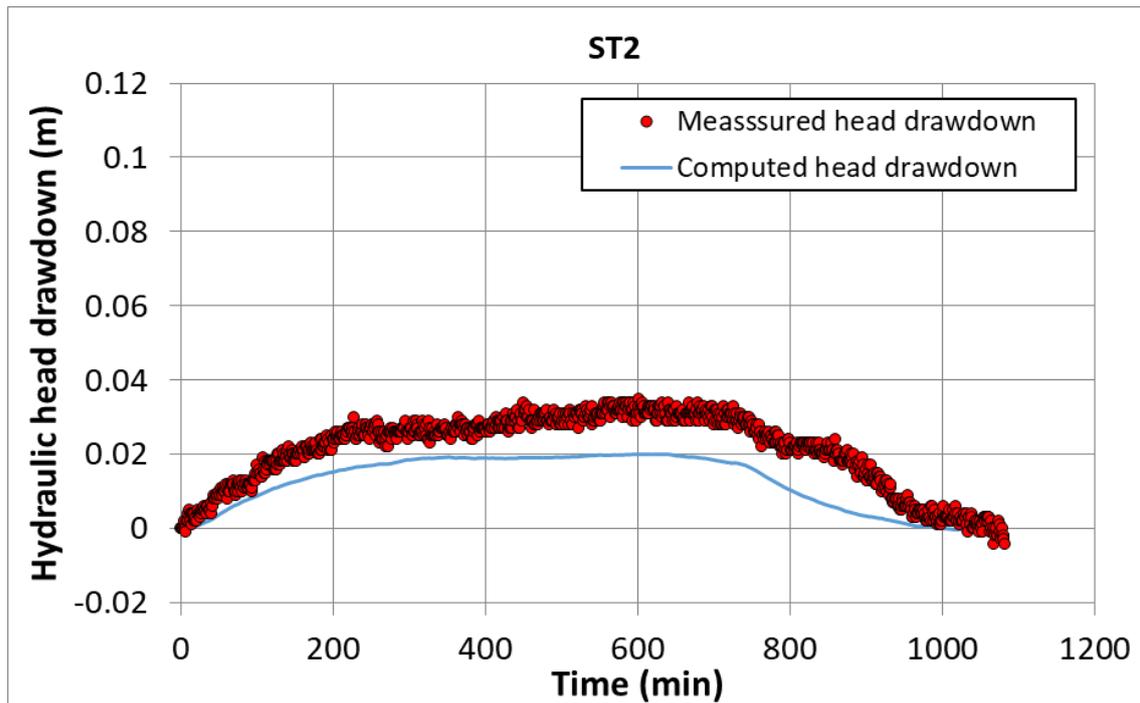
Figure 9.14. Drawdowns measured with diver (red points) in borehole ST2 and computed with the calibrated 2D transient-state horizontal groundwater flow model through the gravels of the alluvial aquifer for the interpretation of the pumping test performed in borehole PS14B on April 26th 2018 (blue line).
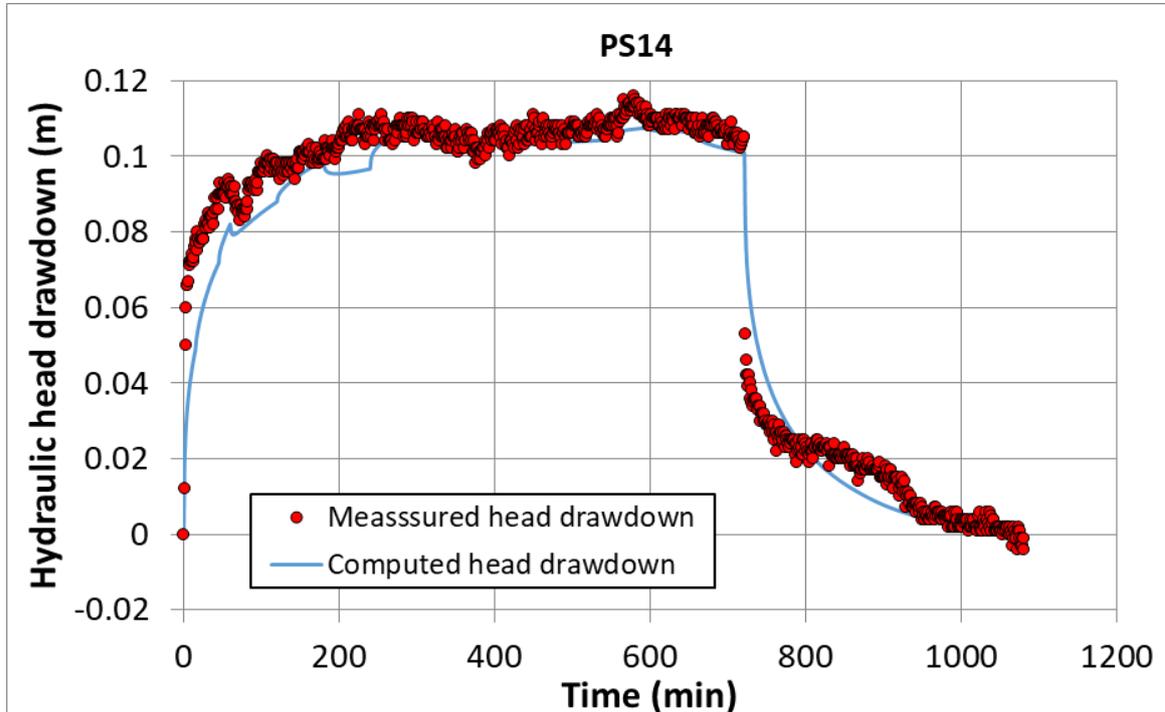
Figure 9.15. Drawdowns measured with diver (red points) in borehole PS14 and computed with the calibrated 2D transient-state horizontal groundwater flow model through the gravels of the alluvial aquifer for the interpretation of the pumping test performed in borehole PS14B on April 26th 2018 (blue line).
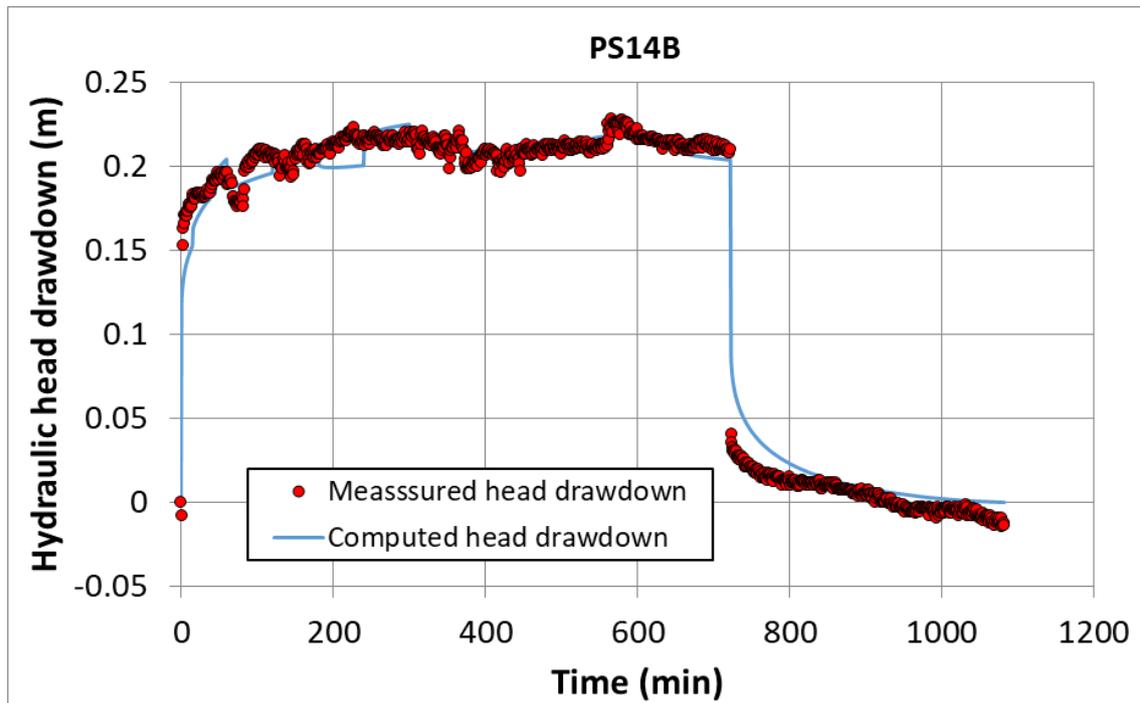
Figure 9.16. Drawdowns measured with diver (red points) in the pumping well (borehole ST14B) and computed with the calibrated 2D transient-state horizontal groundwater flow model through the gravels of the alluvial aquifer for the interpretation of the pumping test performed in borehole PS14B on April 26th 2018 (blue line).
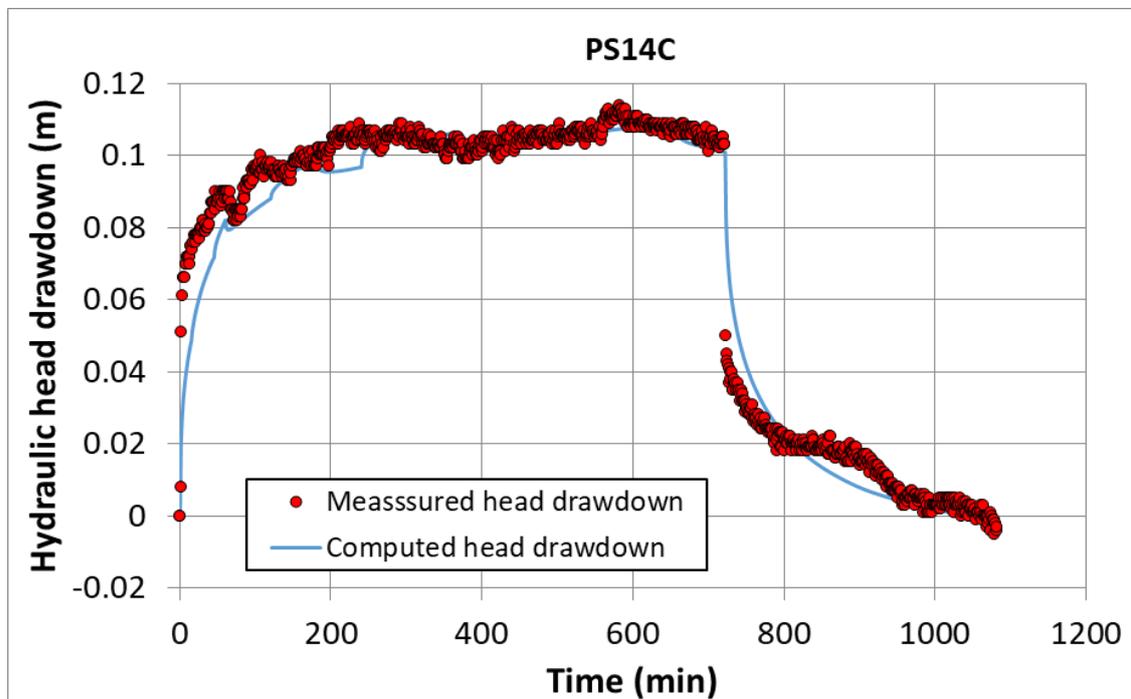
Figure 9.17. Drawdowns measured with diver (red points) in borehole PS14C and computed with the calibrated 2D transient-state horizontal groundwater flow model through the gravels of the alluvial aquifer for the interpretation of the pumping test performed in borehole PS14B on April 26th 2018 (blue line).
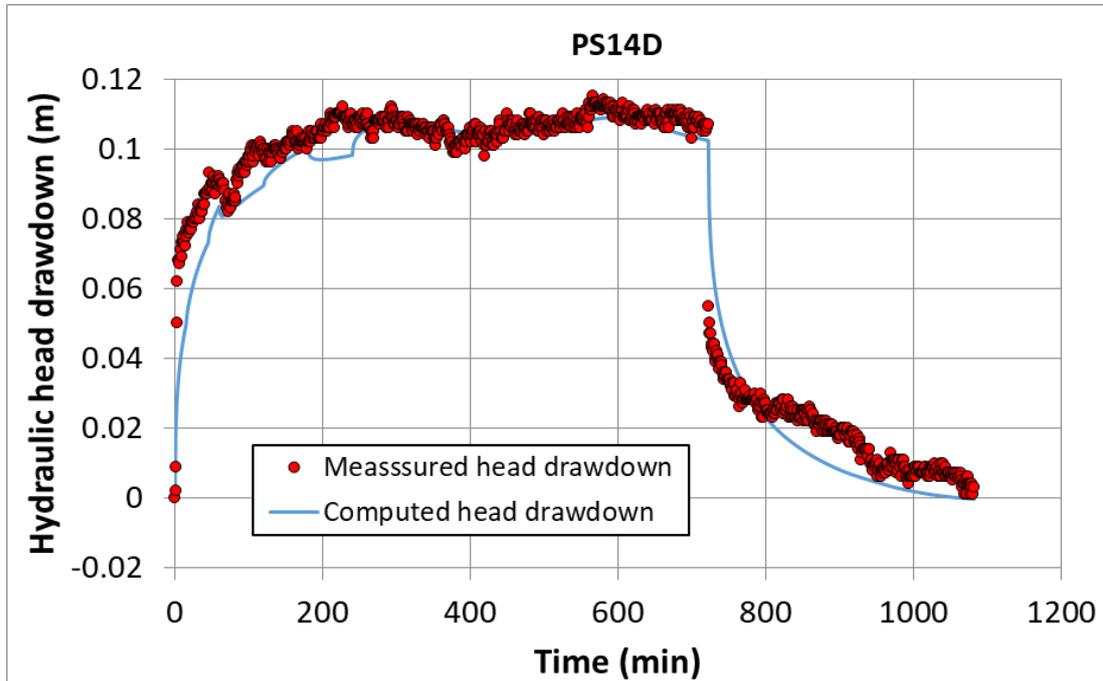
Figure 9.18. Drawdowns measured with diver (red points) in borehole PS14D and computed with the calibrated 2D transient-state horizontal groundwater flow model through the gravels of the alluvial aquifer for the interpretation of the pumping test performed in borehole PS14B on April 26th 2018 (blue line).
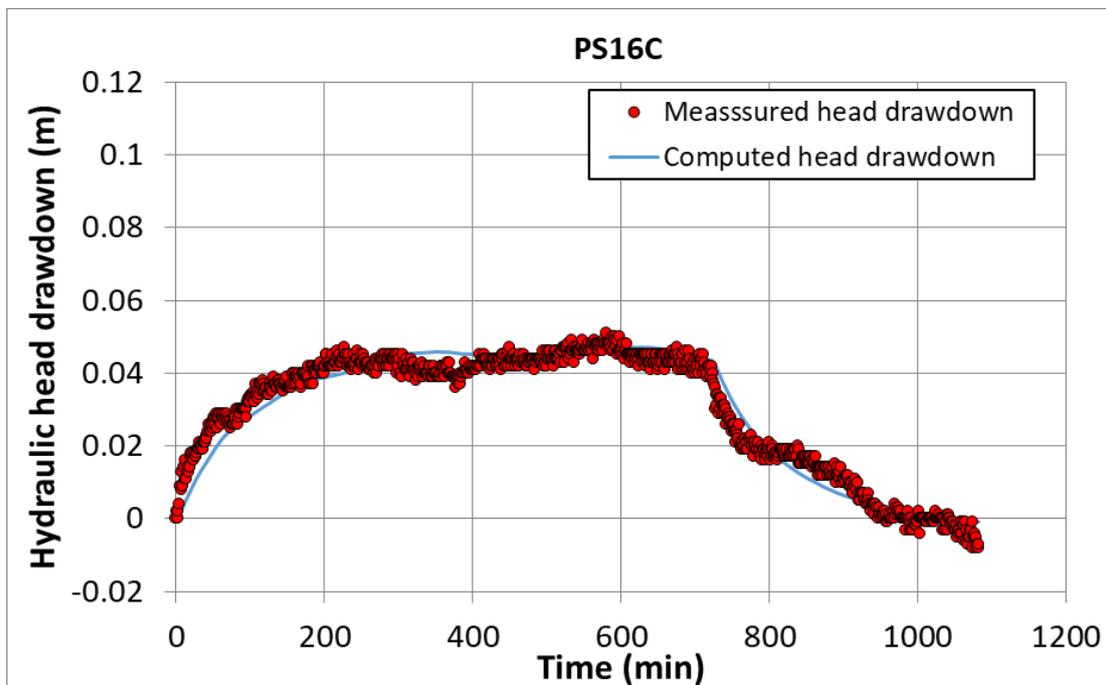
Figure 9.19. Drawdowns measured with diver (red points) in borehole PS16C and computed with the calibrated 2D transient-state horizontal groundwater flow model through the gravels of the alluvial aquifer for the interpretation of the pumping test performed in borehole PS14B on April 26th 2018 (blue line).
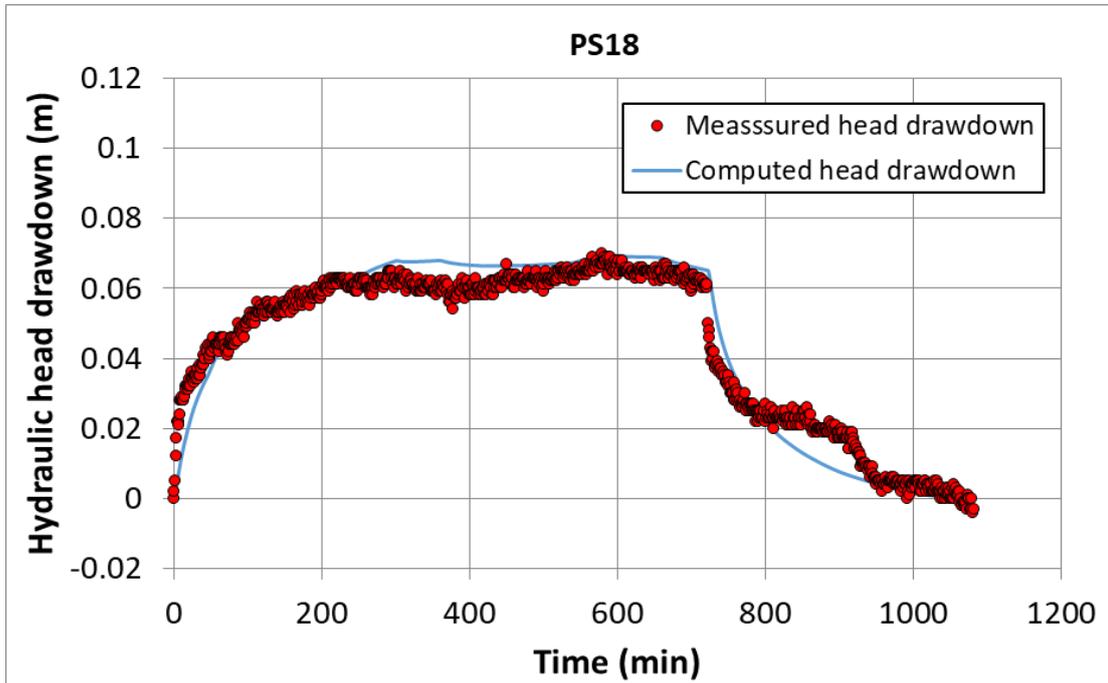
Figure 9.20. Drawdowns measured with diver (red points) in borehole PS18 and computed with the calibrated 2D transient-state horizontal groundwater flow model through the gravels of the alluvial aquifer for the interpretation of the pumping test performed in borehole PS14B on April 26th 2018 (blue line).
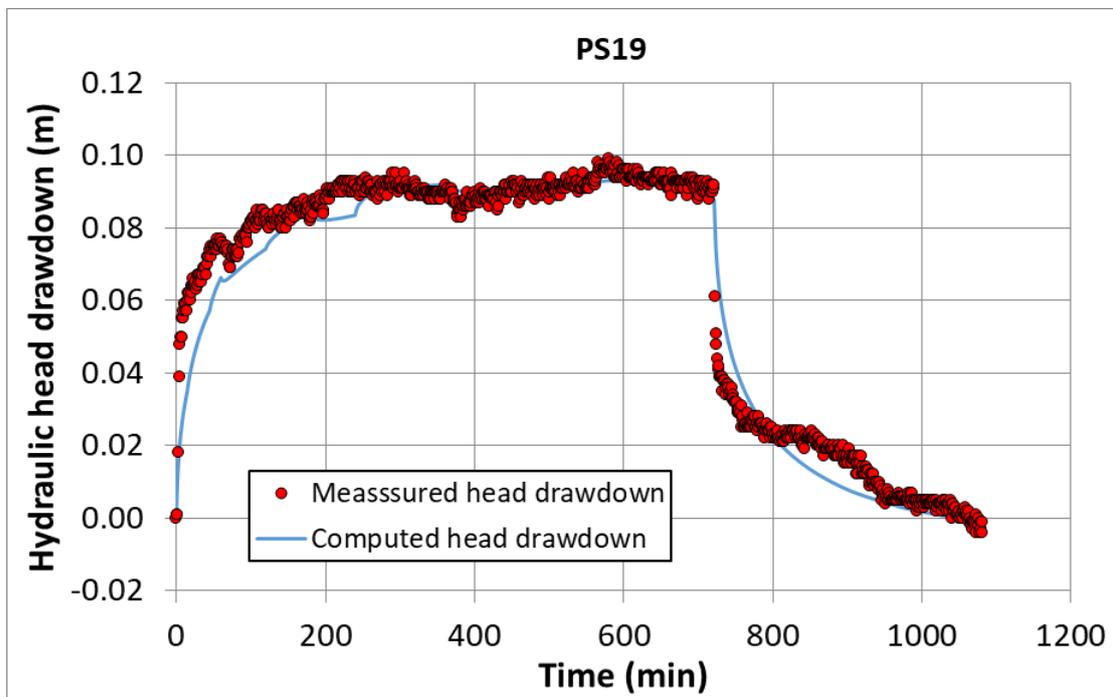
Figure 9.21. Drawdowns measured with diver (red points) in borehole PS19 and computed with the calibrated 2D transient-state horizontal groundwater flow model through the gravels of the alluvial aquifer for the interpretation of the pumping test performed in borehole PS14B on April 26th 2018 (blue line).
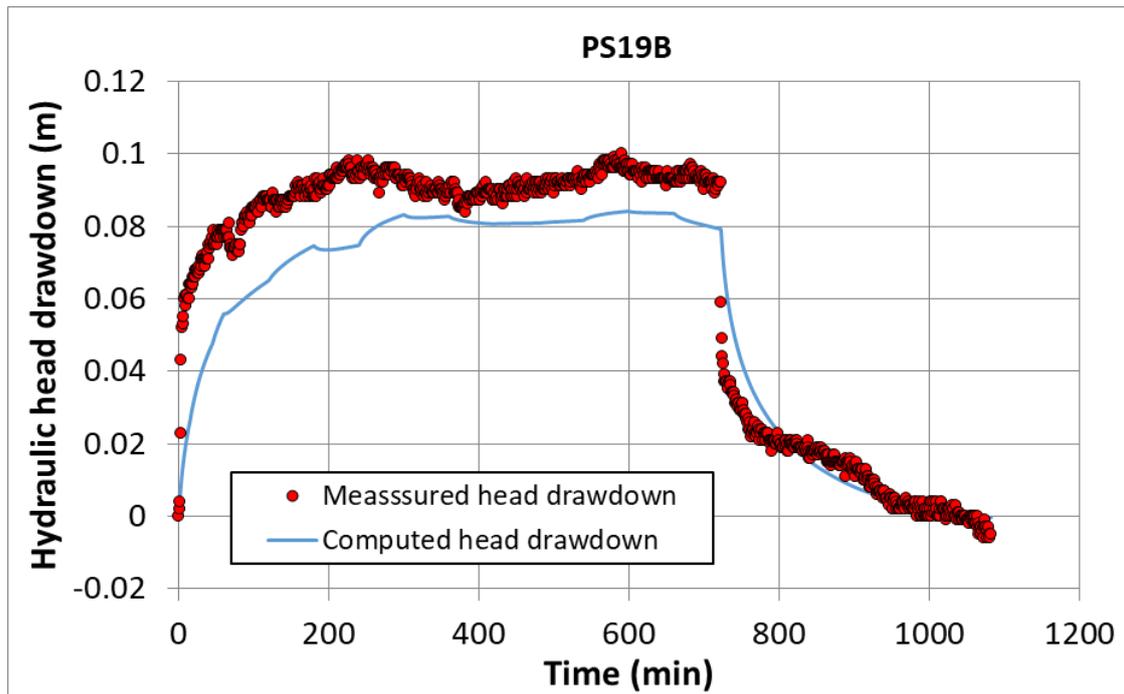
Figure 9.22.   Drawdowns measured with diver (red points) in borehole PS19B and computed with the calibrated 2D transient-state horizontal groundwater flow model through the gravels of the alluvial aquifer for the interpretation of the pumping test performed in borehole PS14B on April 26th 2018 (blue line).
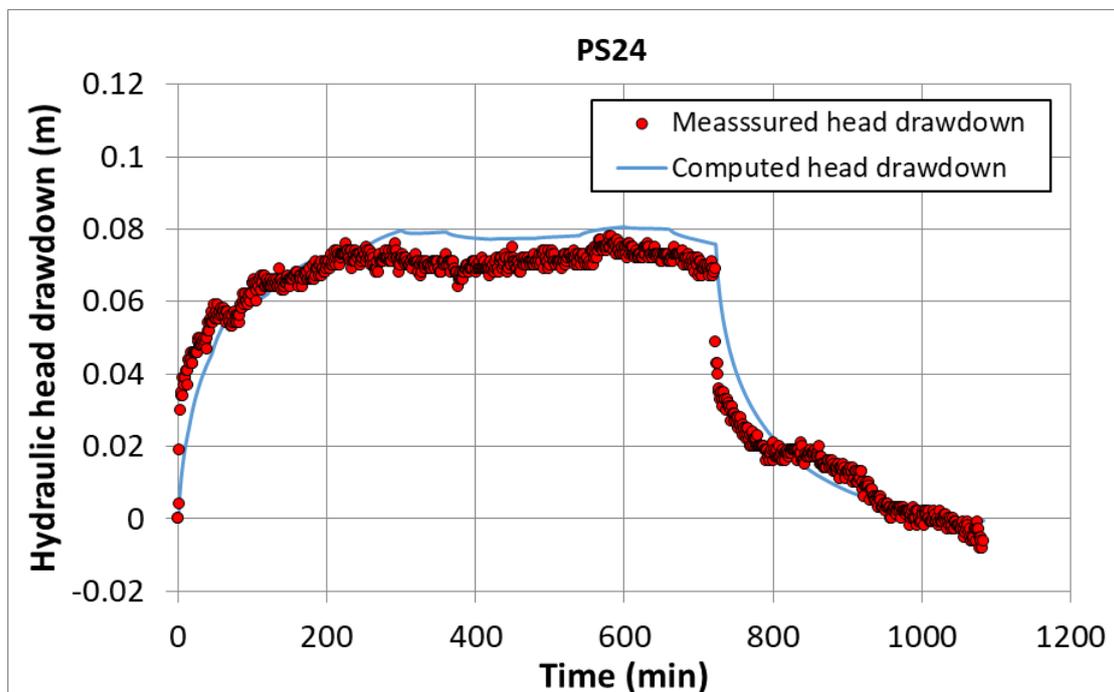
Figure 9.23.   Drawdowns measured with diver (red points) in borehole PS24 and computed with the calibrated 2D transient-state horizontal groundwater flow model through the gravels of the alluvial aquifer for the interpretation of the pumping test performed in borehole PS14B on April 26th 2018 (blue line).
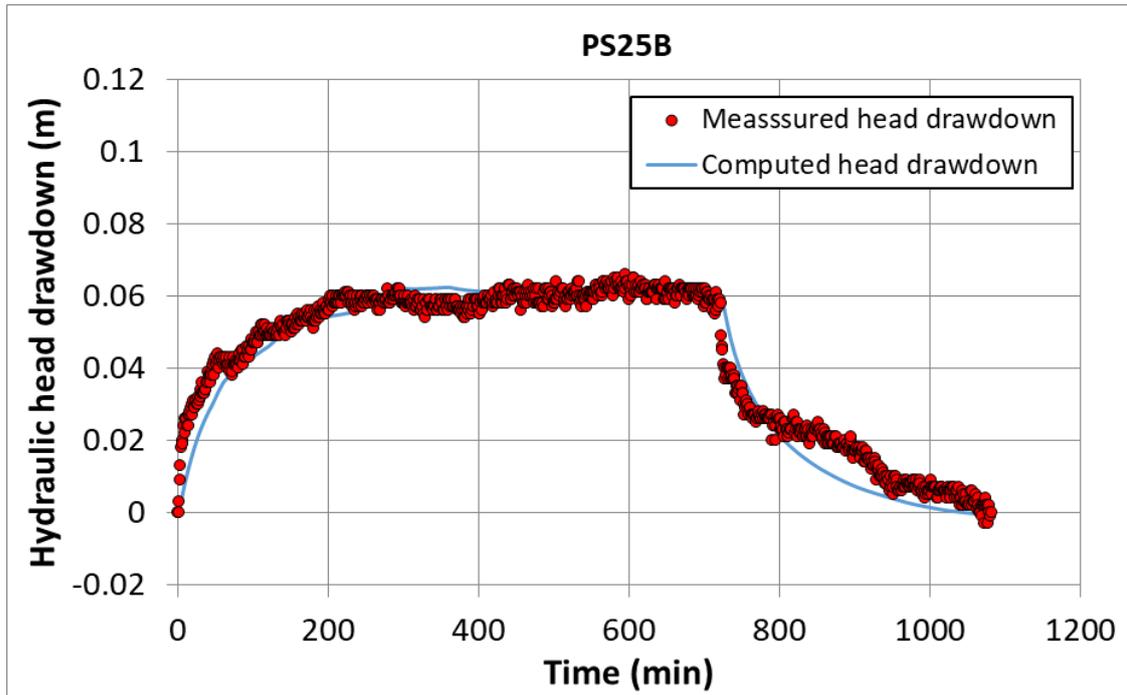
Figure 9.24.   Drawdowns measured with diver (red points) in borehole PS25B and computed with the calibrated 2D transient-state horizontal groundwater flow model through the gravels of the alluvial aquifer for the interpretation of the pumping test performed in borehole PS14B on April 26th 2018 (blue line).
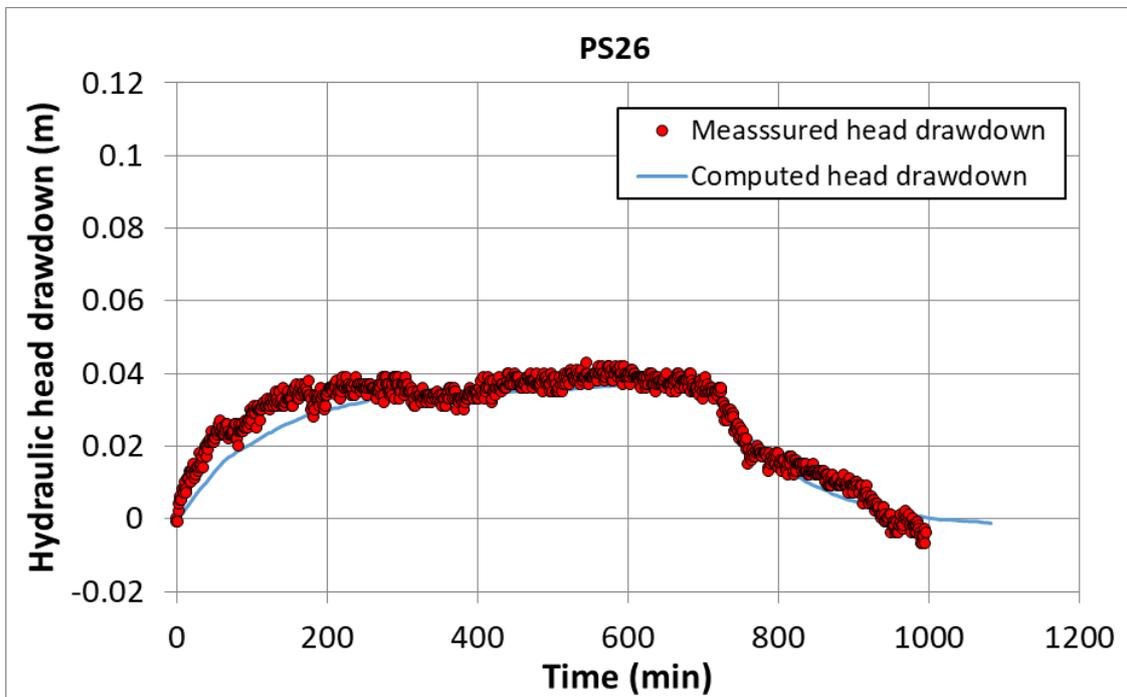
Figure 9.25.   Drawdowns measured with diver (red points) in borehole PS26 and computed with the calibrated 2D transient-state horizontal groundwater flow model through the gravels of the alluvial aquifer for the interpretation of the pumping test performed in borehole PS14B on April 26th 2018 (blue line).

Figure 9.26 to Figure 9.28 show the comparison of the measured and the computed drawdowns in the boreholes for the following three groups which show similar temporal evolution of the drawdowns:

1) Group 1 includes the PS19, PS19B, PS24 and PS25B boreholes located in an intermediate zone to the northwest and southwest of the pumping well.

2) Group 2 includes the three boreholes, ST1B, ST1C and PS16C, nearest the reservoir.

3) Group 3 includes all the boreholes of the PS14 group such as PS14, PS14B, PS14C and PS14D boreholes.
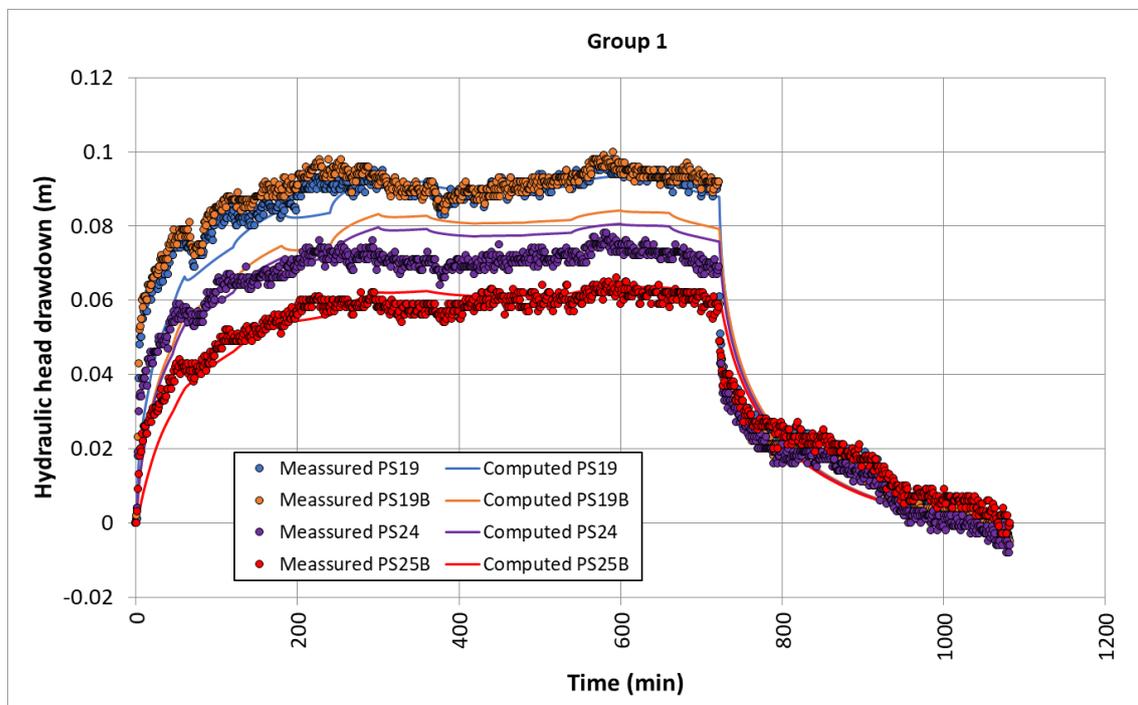
Figure 9.26.   Drawdowns measured with diver (symbols) in boreholes of group 1 (PS19, PS19B, PS24 and PS25B boreholes) and computed with the calibrated 2D transient-state horizontal groundwater flow model through the gravels of the alluvial aquifer for the interpretation of the pumping test performed in borehole PS14B on April 26th 2018 (lines).
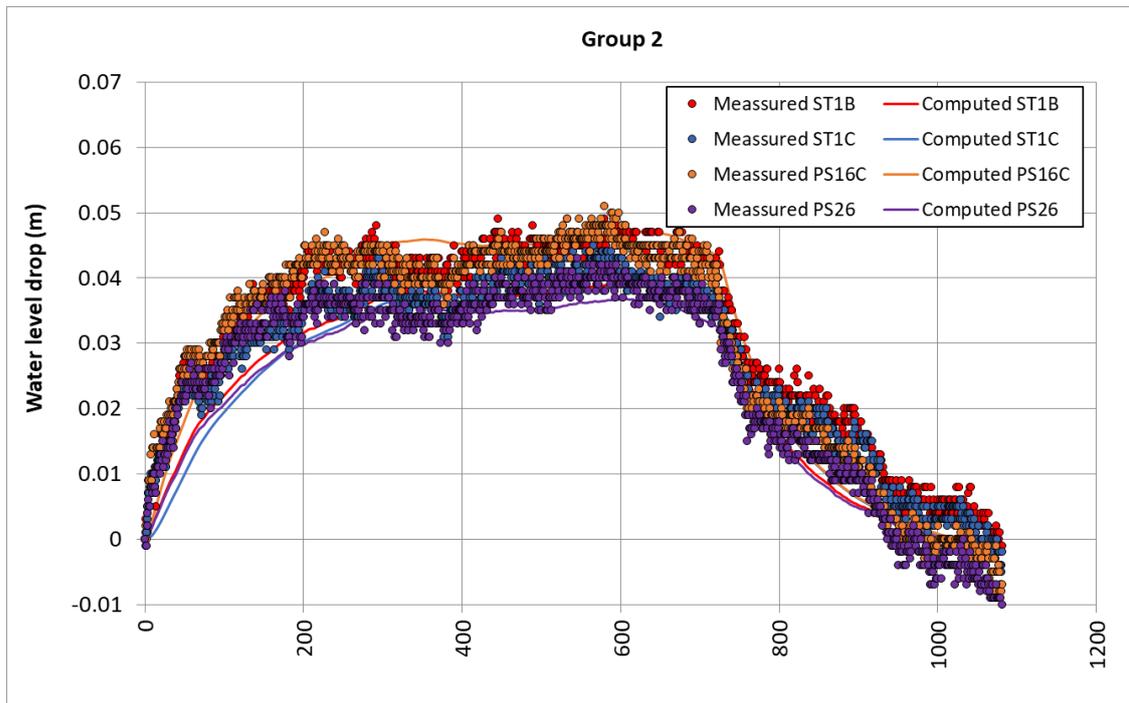
Figure 9.27. Drawdowns measured with diver (symbols) in boreholes of group 2 (ST1B, ST1C, PS16C and PS26 boreholes) and computed with the calibrated 2D transient-state horizontal groundwater flow model through the gravels of the alluvial aquifer for the interpretation of the pumping test performed in borehole PS14B on April 26th 2018 (lines).
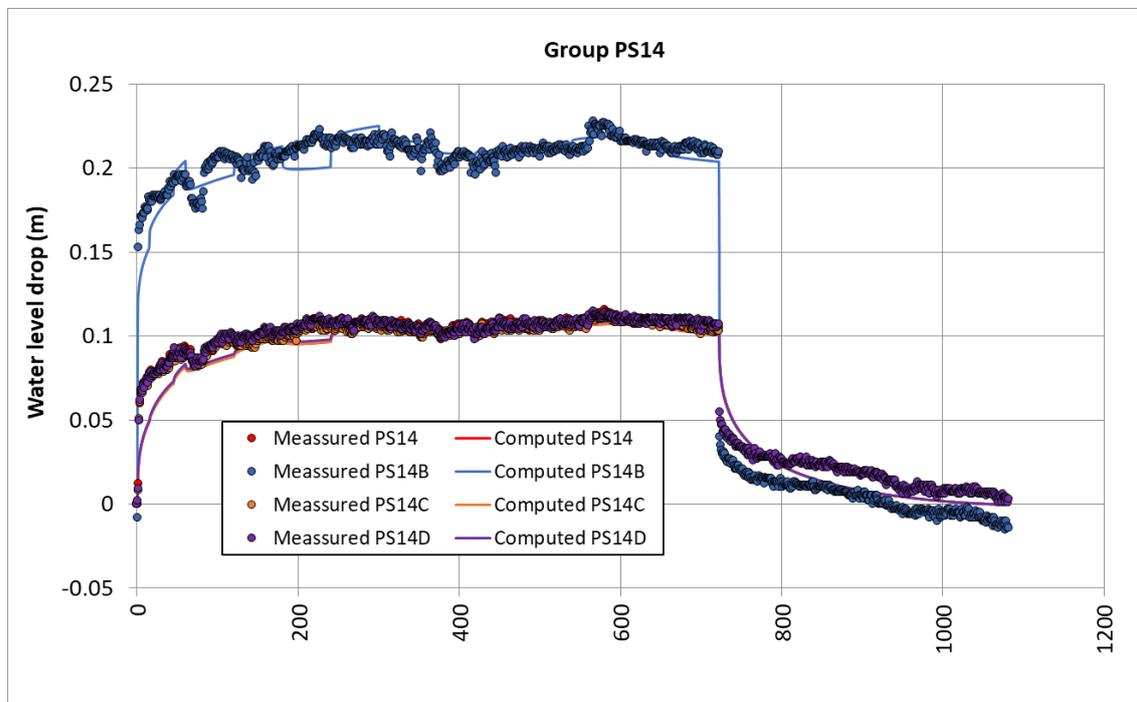
Figure 9.28. Drawdowns measured with diver (symbols) in boreholes of group 3 (PS14, PS41B, PS14C and PS14D boreholes) and computed with the calibrated 2D transient-state horizontal groundwater flow model through the gravels of the alluvial aquifer for the interpretation of the pumping test performed in borehole PS14B on April 26th 2018 (lines).

Table 9.2 summarizes the statistics of the drawdown residuals and the values of the Nash index (Krause *et al.*, 2005) for each borehole. The drawdown residual is defined as the difference between the measured and the calculated drawdowns. The mean absolute residuals range from 1 to 6 mm. The Nash index is almost equal to 1 for most boreholes except for borehole ST2.

Table 9.2. Mean drawdown residual, mean of the absolute values of the residuals, RMSE (root mean square error) ad Nash index (Krause et al., 2005).

Borehole	Mean residual (m)	Mean absolute residual (m)	RMSE	Nash index
ST1B	$6.75 \cdot 10^{-3}$	$6.76 \cdot 10^{-3}$	$7.29 \cdot 10^{-3}$	0.76
ST1C	$3.15 \cdot 10^{-3}$	$3.94 \cdot 10^{-3}$	$5.05 \cdot 10^{-3}$	0.86
ST2	$8.40 \cdot 10^{-3}$	$8.45 \cdot 10^{-3}$	$9.25 \cdot 10^{-3}$	0.17
PS14	$3.46 \cdot 10^{-3}$	$5.29 \cdot 10^{-3}$	$7.49 \cdot 10^{-3}$	0.97
PS14B	$-2.39 \cdot 10^{-3}$	$7.45 \cdot 10^{-3}$	$1.05 \cdot 10^{-2}$	0.99
PS14C	$2.37 \cdot 10^{-3}$	$4.64 \cdot 10^{-3}$	$6.91 \cdot 10^{-3}$	0.97
PS14D	$4.07 \cdot 10^{-3}$	$5.68 \cdot 10^{-3}$	$7.68 \cdot 10^{-3}$	0.97
PS16C	$-1.16 \cdot 10^{-4}$	$3.18 \cdot 10^{-3}$	$3.94 \cdot 10^{-3}$	0.94
PS17	$-1.59 \cdot 10^{-3}$	$4.97 \cdot 10^{-3}$	$6.33 \cdot 10^{-3}$	0.93
PS18	$-7.88 \cdot 10^{-4}$	$4.61 \cdot 10^{-3}$	$5.73 \cdot 10^{-3}$	0.94
PS19	$2.61 \cdot 10^{-3}$	$4.60 \cdot 10^{-3}$	$6.77 \cdot 10^{-3}$	0.96
PS19B	$8.92 \cdot 10^{-3}$	$1.09 \cdot 10^{-2}$	$1.34 \cdot 10^{-2}$	0.87
PS24	$-3.17 \cdot 10^{-3}$	$5.63 \cdot 10^{-3}$	$6.94 \cdot 10^{-3}$	0.94
PS25B	$1.25 \cdot 10^{-3}$	$3.99 \cdot 10^{-3}$	$5.14 \cdot 10^{-3}$	0.94
PS26	$1.88 \cdot 10^{-3}$	$3.57 \cdot 10^{-3}$	$4.32 \cdot 10^{-3}$	0.92

9.4.2   Sensitivity analysis of the computed drawdowns at ST2 borehole

The computed drawdowns at ST2 borehole are smaller than the measured drawdowns (Figure 9.14) and the Nash index is 0.17. This discrepancy could be due to some model simplifications. The numerical model accounts for the time changes of the water level of the reservoir during the pumping test. The base run of the model, however, does not account for the changes in the water level of the Gállego river upstream of the tale of the reservoir. A sensitivity run has been carried out which takes into account the change in the water level of the Gállego river. The results of the sensitivity run improve greatly the fit of the computed drawdowns to the measured drawdowns at borehole ST2 (Figure 9.29). However, the fit of the computed drawdowns at other boreholes.

The model presented here could be improved by accounting for the changes in the water level of the Gállego river upstream of the tale of the reservoir and by recalibrating again all the model parameters.
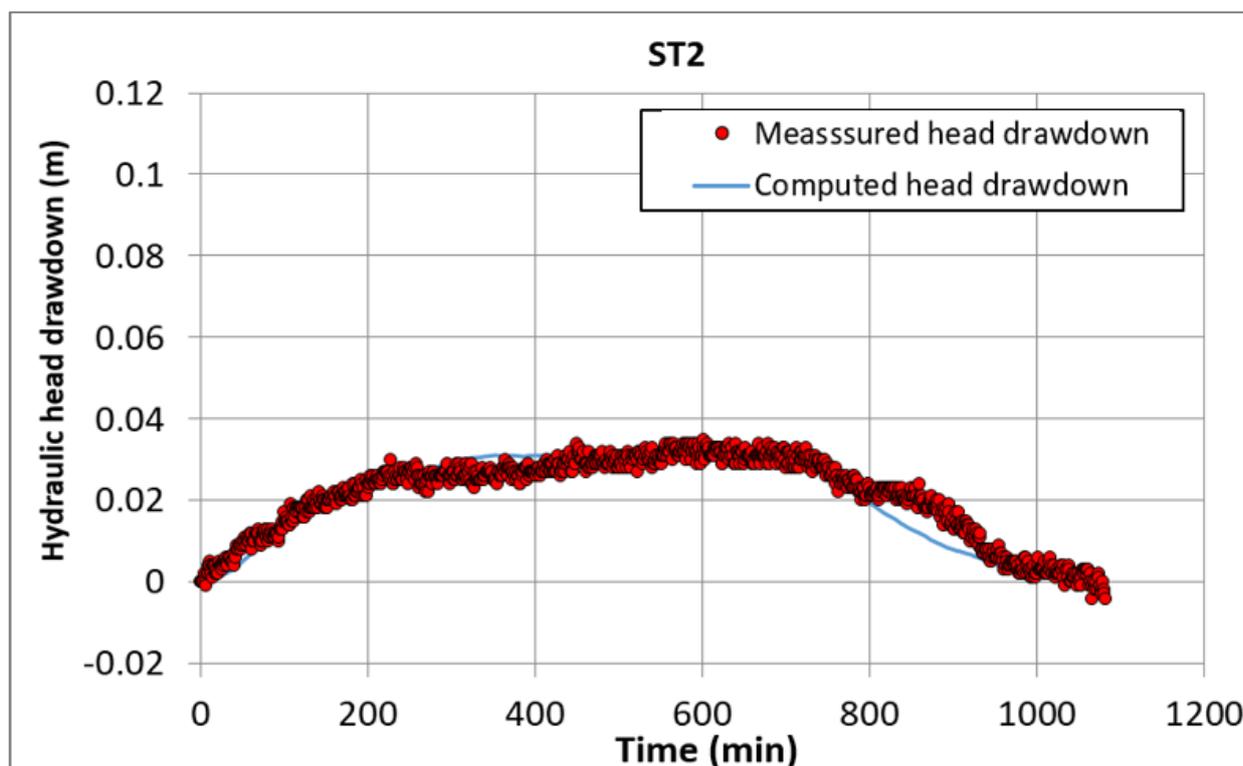
Figure 9.29.   Drawdowns measured with diver (symbols) in ST2 borehole and computed with the sensitivity run of the groundwater flow model of the pumping test performed in borehole PS14B on April 26th 2018 which considers the changes of the water level of the Gállego river upstream the reservoir (line).

9.5 Conclusions

A 2D transient-state horizontal groundwater flow model through the gravels of the alluvial aquifer for the interpretation of a multi-observation pumping test performed in borehole PS14B on April 26th 2018 has been presented. The hydraulic conductivities and storage coefficients have been estimated by solving the inverse problem. The leakage coefficient and the vertical hydraulic conductivity of the silts that confine the gravels have been estimated by trial and error.

The calibrated hydraulic conductivity of gravels for the three material zones range from 300 m/d to 600 m/d, while the calibrated specific storage coefficients range from $1 \cdot 10^{-4}$ m^{-1} to $3 \cdot 10^{-3}$ m^{-1}.

The fit of the computed drawdowns to the measured values is excellent. The main discrepancies (< 0.02 m) occur in borehole ST2, located 245 m from the pumping well. This discrepancy is overcome when the changes in the water level of the Gállego river upstream the reservoir are considered in the model

The transient-state groundwater flow model of the pumping test allowed the estimation of the hydraulic conductivity and the storage coefficient of the gravels and the identification of the relevance of the leakage from the confining silts into the alluvial gravels and the fluctuations of the reservoir water level.

10. 2D TRANSIENT-STATE HORIZONTAL GROUNDWATER FLOW AND SOLUTE TRANSPORT MODEL OF THE INJECTION/EXTRACTION TRACER TEST PERFORMED IN THE PS14B BOREHOLE

10.1 Introduction

This chapter presents a 2D transient-state horizontal groundwater flow and solute transport model of the tracer injection/extraction performed in borehole PS14B from 10:00 June 5th to 17:30 June 6th. The model allows for the estimation of solute transport parameters of the gravels. The chapter starts with a description of the tracer test and the available data. Then, the numerical model is presented. Model results are presented next. The chapter ends with the main conclusions.

10.2 Tracer test and available data

Figure 10.1 shows the location of the PS14 boreholes in the area of the pumping test. The tracer test consisted in the injection in borehole PS14B of a 20 m^3 pool, to which 3.33 kg of BrNa were added. The measured bromide ion, Br$^-$, concentration is equal to 120 mg/kg (Santos et al., 219a,b; Lozano et al. 2020). Tracer concentrations were measured during injection in the observation boreholes PS14A, PS14C and PS14D every 15 to 30 minutes. The extraction started the following day. The tracer concentrations were measured in the observation boreholes and in the pumping borehole PS14B.

Figure 10.2 shows the time evolution of the Br$^-$ concentration measured during the injection phase. Figure 10.3 shows the time evolution of the Br$^-$ concentration measured during the extraction (Santos et al., 219a,b; Lorenzo et al. 2020).
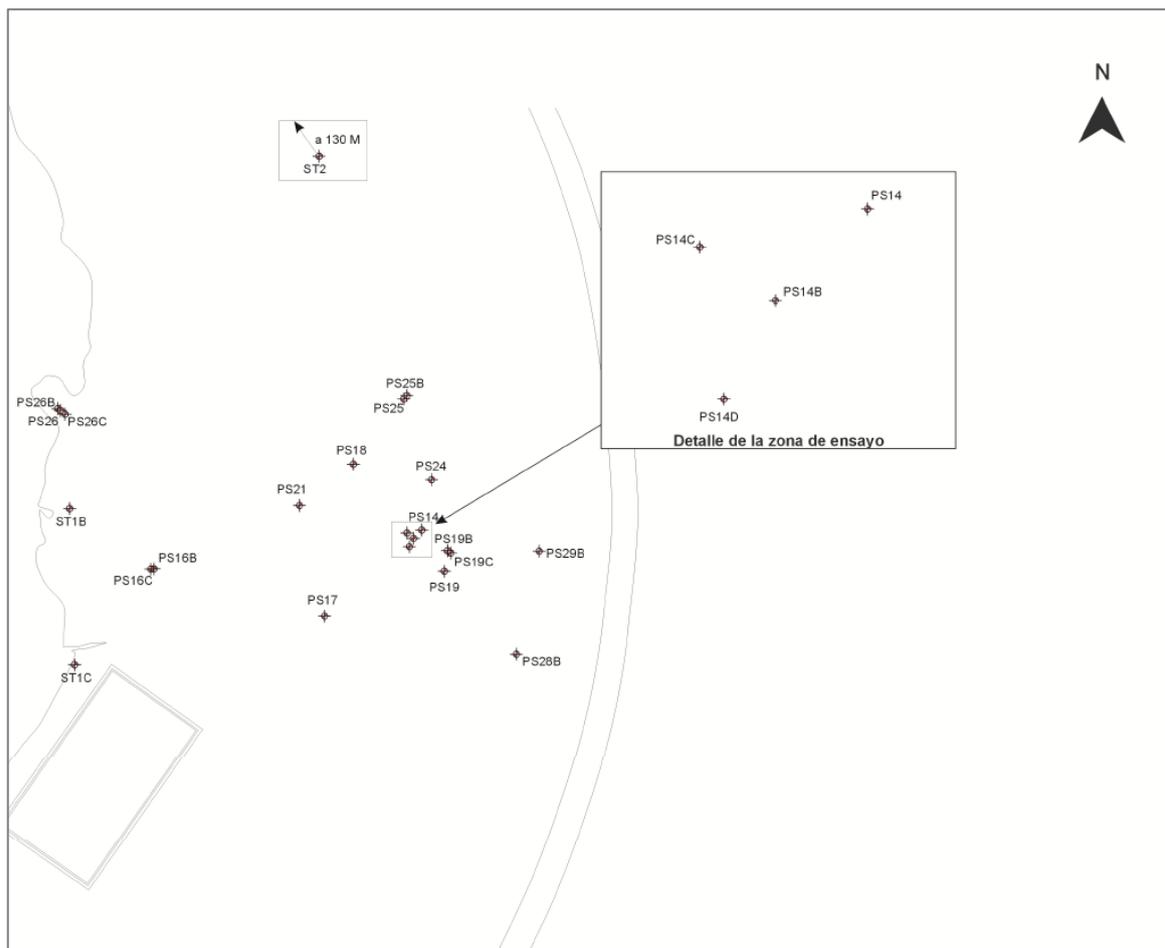
Figure 10.1. Location of the observation and injection boreholes in the tracer test area (EMGRISA 2018).
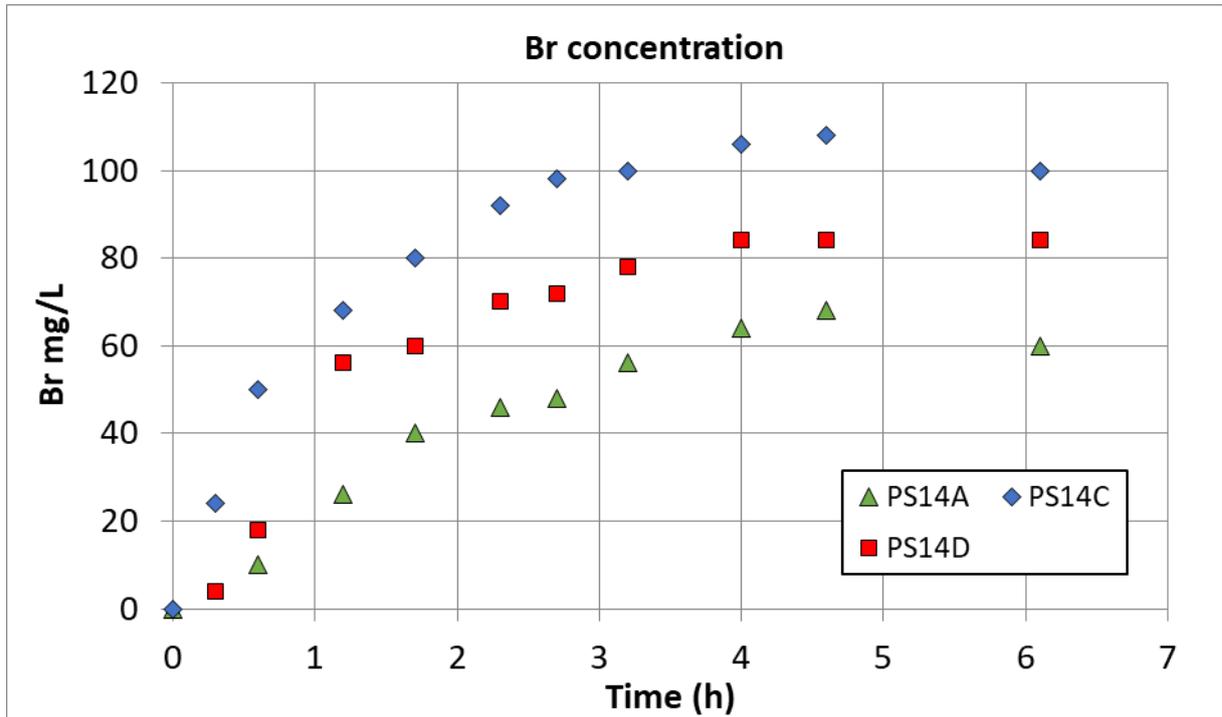
Figure 10.2. Br⁻ concentrations measured in boreholes PS14A, PS14B, PS14C and PS14D during the injection phase (Santos et al., 219a,b; Lozano et al. 2020).
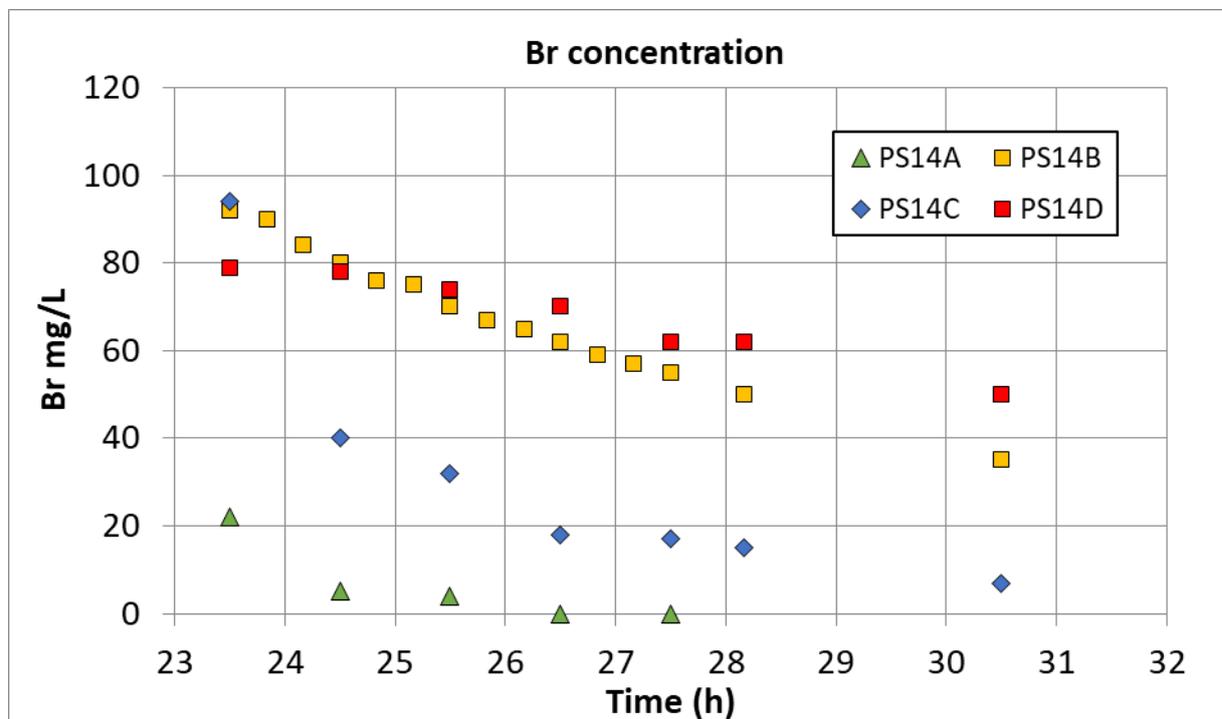
Figure 10.3. Br⁻ concentrations measured in boreholes PS14A, PS14B, PS14C and PS14D during the extraction phase (Santos et al., 219a,b; Lozano et al. 2020).

Water level data of the reservoir are available every 30 minutes. In the absence of data every minute during the test, it has been assumed that head is constant for every half hour. Figure 10.4 shows time evolution of the reservoir water level during the test. In this case, flow injection is considered positive and the extraction negative.

The tracer injection started 10:00 on June 5th and finished at 15:06. According to EMGRISA (2018) the estimated injection flowrate was 3.8 m^3/h. The flow rate has been considered constant in the model. Pumping started at 9:30 on June 6th. The pumping rate was equal to 4.4 m^3/h and remained constant during the extraction (Figure 10.5).

The analysis of Br⁻ concentration data indicates that Br⁻ concentrations during the injection phase are different in observation boreholes PS14A, PS14C and PS14D despite the fact that these boreholes are located at similar distances from the injection well. The highest concentration is reached in well PS14C. Therefore, the measured data indicate the existence of heterogeneities with a marked dispersion and the anisotropy of the hydraulic conductivity with a main direction ranging from NW/SE to WNW/ESE.
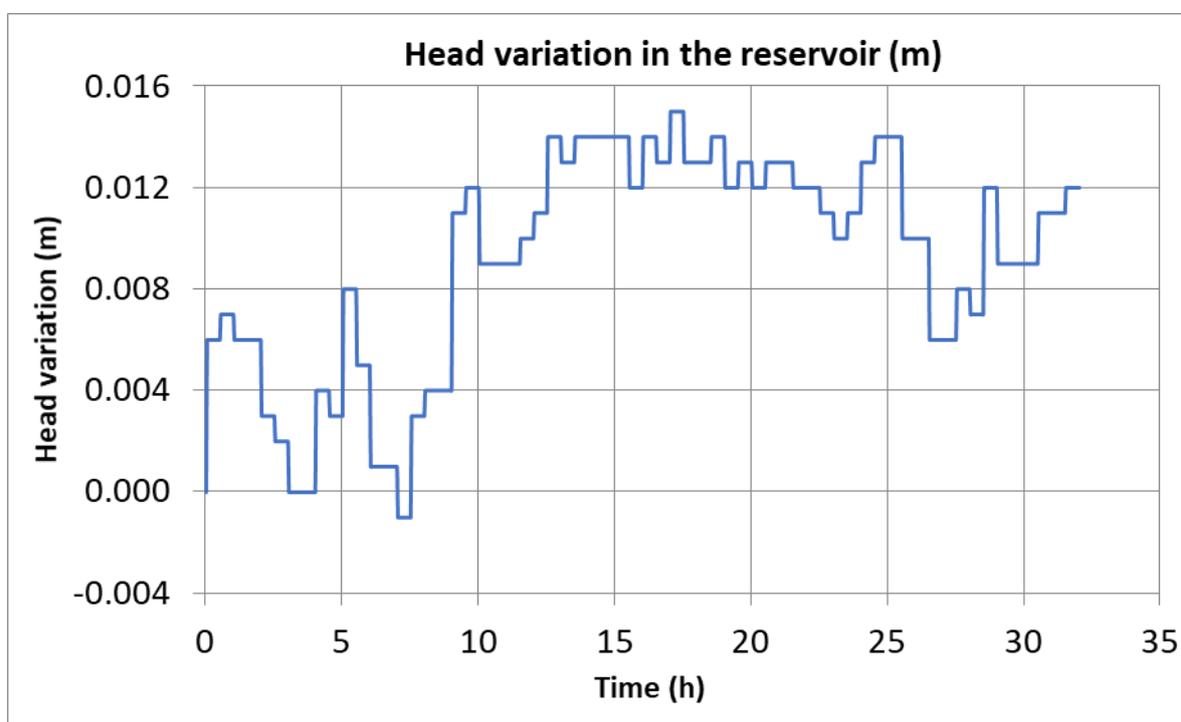
Figure 10.4. Time evolution of the changes in the water level of the Sabiñánigo reservoir compared to the initial water level during the tracer test in the PS14B well. Positive variations correspond to water level increases.
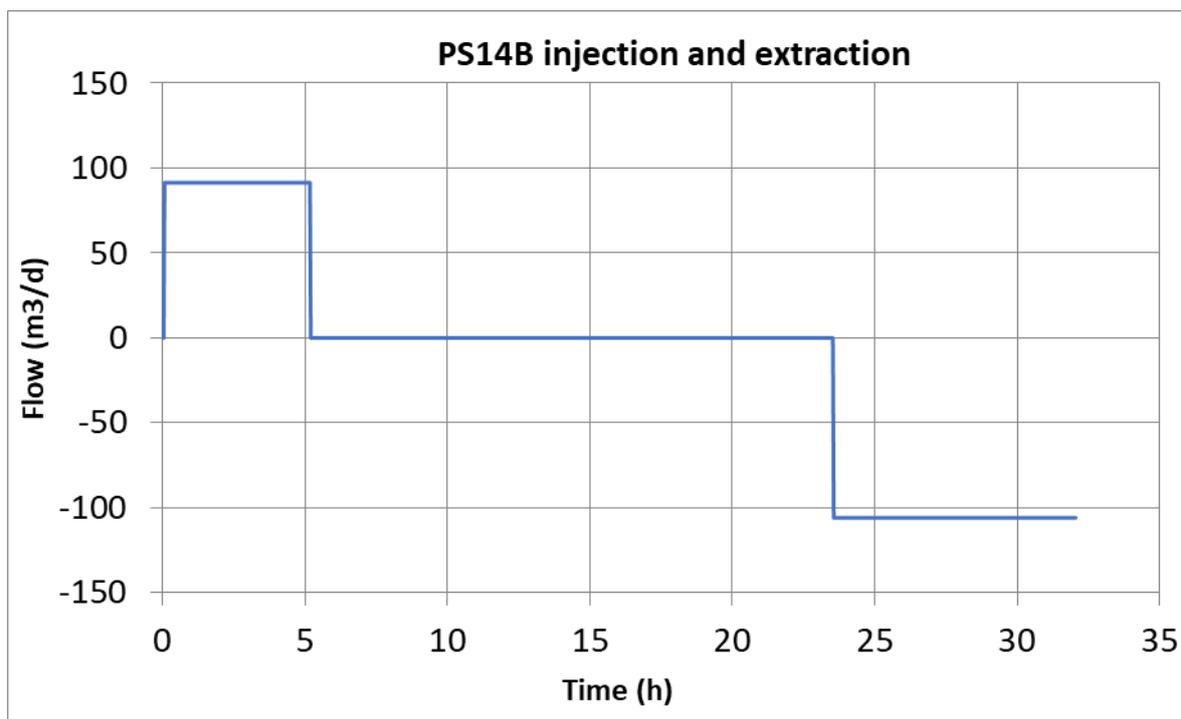
Figure 10.5. Time evolution of injection (positive) and pumping (negative) rate during the tracer test carried out in PS14B well.

10.3 Numerical model

10.3.1 Space and time discretization

The spatial discretization is similar to that of the model of the pumping test presented in Chapter 9.

The simulation runs from 9:58 June 5 to 18:00 June 6, 2018. The time increments are equal to 2 minutes.

10.3.2 Model structure

The model structure is similar to that of the model of the pumping test presented in Chapter 9 (Figure 9.2). The hydraulic conductivities and the specific storage coefficients are listed in Table 9.1. The horizontal anisotropy of the hydraulic conductivity was considered in some sensitivity runs.

The porosity of the gravels is assumed equal to 0.05. The longitudinal and transversal dispersivities are equal to 0.50 m and 0.25 m, respectively. The tracer diffusion coefficient in water is equal to $8.64 \cdot 10^{-5}$ m^2/d.

10.3.3 Initial and boundary conditions

The initial and boundary flow conditions of the tracer test model are similar to those of the model of the pumping test, except for the hydrograph of the water level of the reservoir (Figure 10.4) and the injection/extraction rate in the pumping/injection well PS14B (Figure 10.5).

The injection water has a concentration of Br^- is equal to 120 mg/L. The initial concentration of Br^- is zero.

10.4 Model results

10.4.1 Results of the base run

Figure 10.6 and Figure 10.7 show the measured and calculated Br^- concentrations in the PS14A, PS14B, PS14C and PS14D boreholes. The time evolution of the computed tracer concentrations in the PS14C borehole fits the measured data. The maximum calculated concentration is slightly higher than the measured value. The measured concentrations in the PS14A, PS14D and PS14C boreholes show differences which are not reproduced by the computed concentrations. This discrepancy could be due to the anisotropy of the hydraulic conductivity of the gravels, in a direction which may range from NW/SE to WNW/ESE. The relevance of the anisotropy of the hydraulic conductivity has been analysed in the model sensitivity analysis.
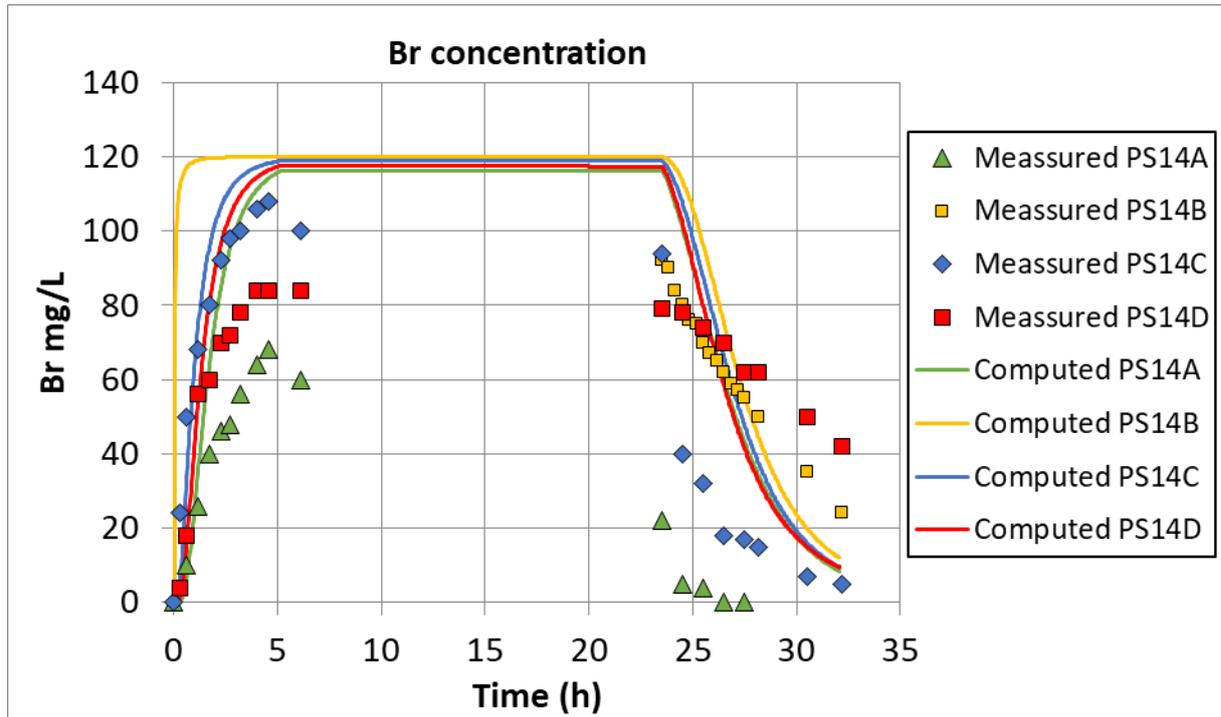
Figure 10.6. Measured (symbols) and computed (lines) Br⁻ concentrations in the observation boreholes (PS14A, PS14B, PS14C and PS14D) during the injection and extraction phases of the tracer test.
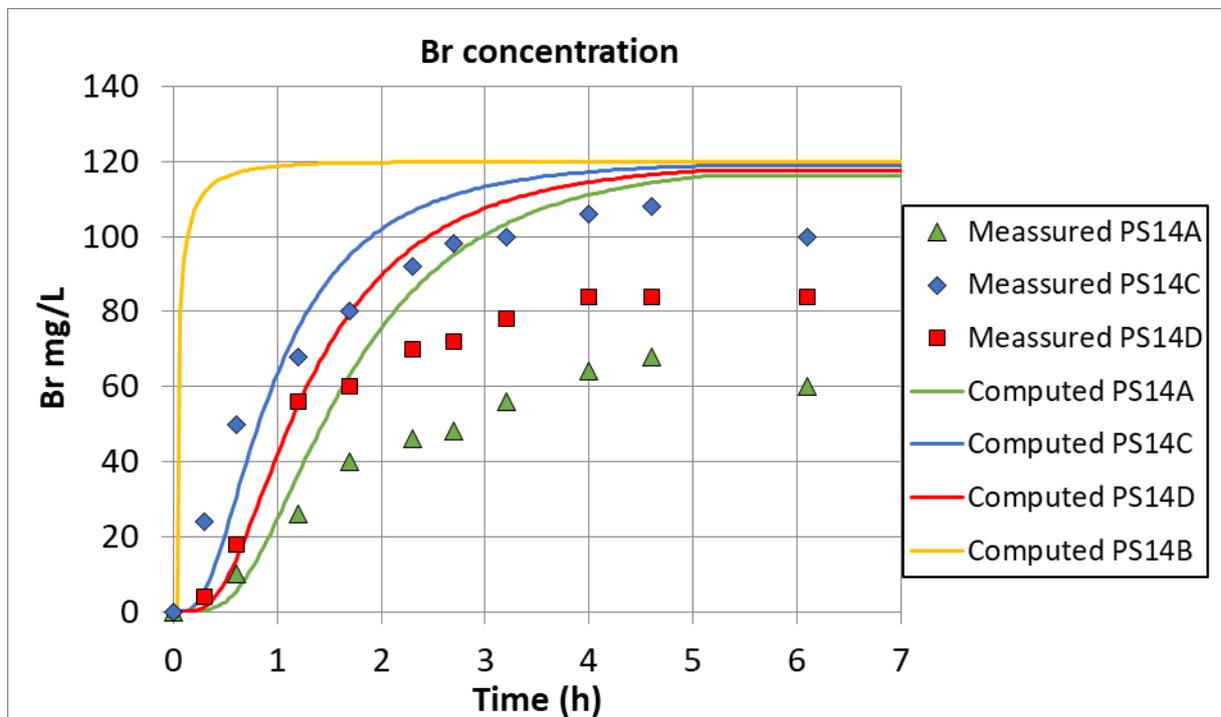
Figure 10.7. Measured (symbols) and computed (lines) Br⁻ concentrations in the observation boreholes (PS14A, PS14B, PS14C and PS14D) during the injection phase of the tracer test.

10.4.2 <u>Sensitivity analysis</u>

Several sensitivity runs have been carried out to analyse the sensitivity of the tracer concentrations to changes in the porosity and the dispersivities. Tracer concentrations are sensitive to an increase of the porosity and to the changes in the longitudinal and transversal dispersivities.

The sensitivity of the tracer concentrations to the anisotropy of the hydraulic conductivity has been evaluated by assuming that the material zone number 2 is anisotropic with a main hydraulic conductivity of 671 m/d along a direction that forms an angle of -22.5° with the W-E direction and a minimum hydraulic conductivity of 134 m/d in the perpendicular direction. Figure 10.8 to Figure 10.11 show the sensitivity of the Br$^-$ concentrations to the anisotropy of the hydraulic conductivity.

The time evolution of the tracer concentration in the PS14C borehole in the sensitivity run is almost similar to that of the base run. The fit during the injection period is good, while the concentration calculated during the extraction decreases slightly slower than the measured concentration. The fit of the computed concentrations in the sensitivity run in the PS14A and PS14D boreholes to the measured concentrations improves compared to that of the base run. However, the maximum concentrations in the sensitivity run are still higher than the measured concentrations.

Figure 10.12 and Figure 10.13 show the contour plots of the computed Br$^-$ concentrations at selected times. The tracer plumes clearly show the effect of the anisotropy of the hydraulic conductivity.
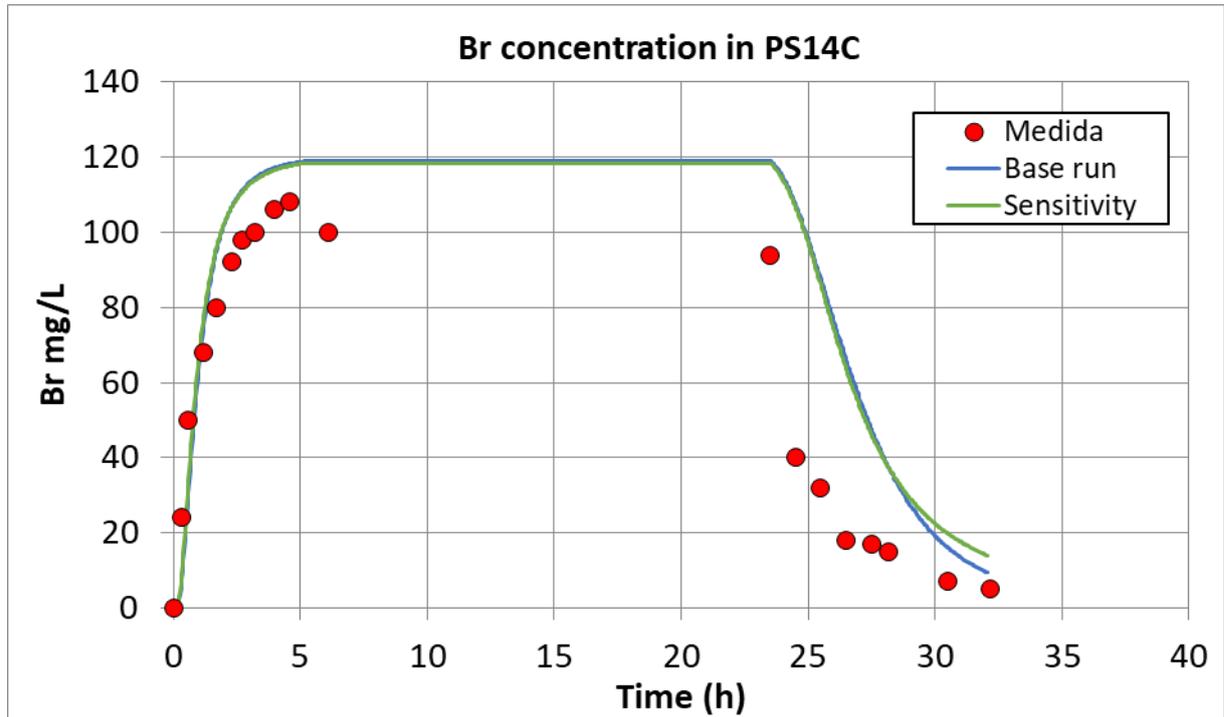
Figure 10.8. Measured (symbols) and calculated Br⁻ concentrations in the base run (blue line) and the sensitivity run (green line) in the PS14C borehole.
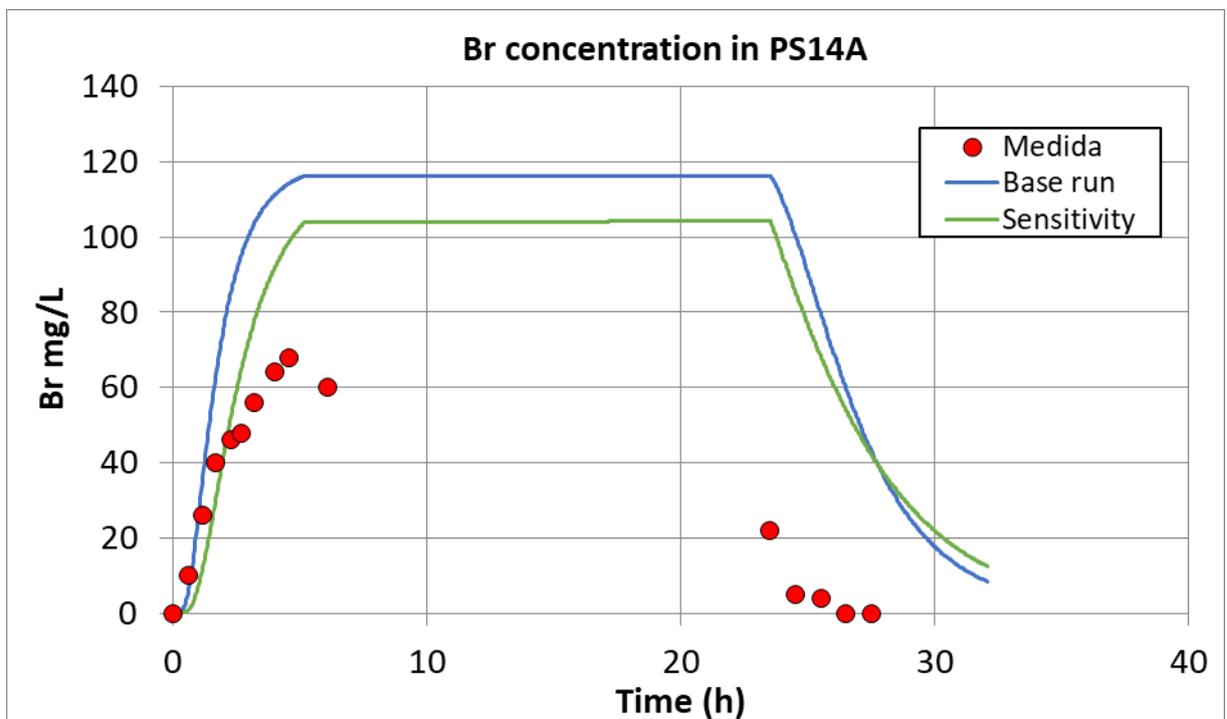
Figure 10.9. Measured (symbols) and calculated Br⁻ concentrations in the base run (blue line) and the sensitivity run (green line) in the PS14A borehole.
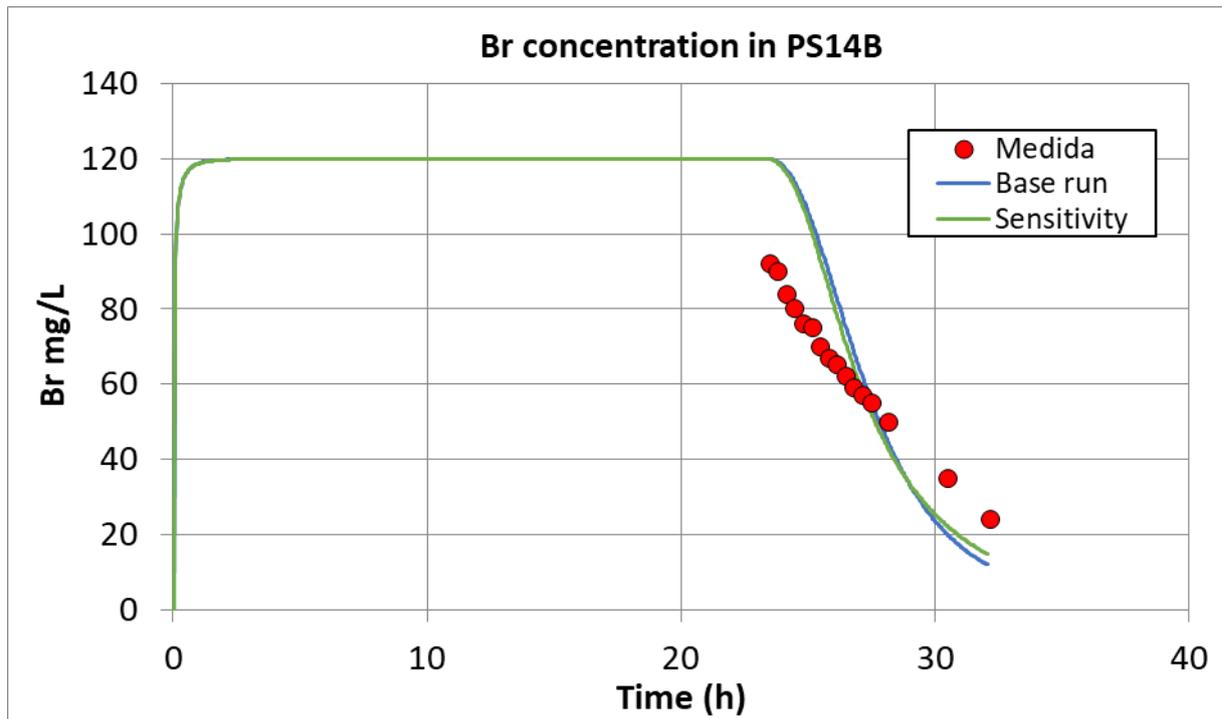
Figure 10.10. Measured (symbols) and calculated Br⁻ concentrations in the base run (blue line) and the sensitivity run (green line) in the PS14B borehole.
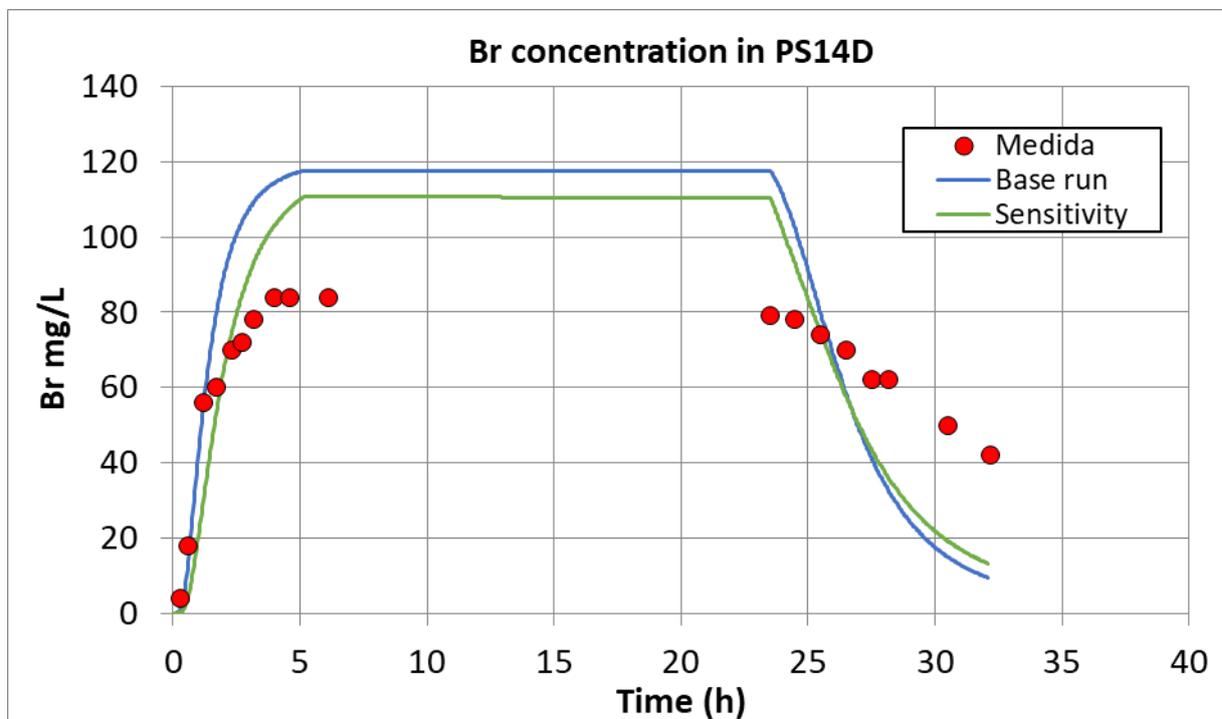
Figure 10.11. Measured (symbols) and calculated Br⁻ concentrations in the base run (blue line) and the sensitivity run (green line) in the PS14D borehole.
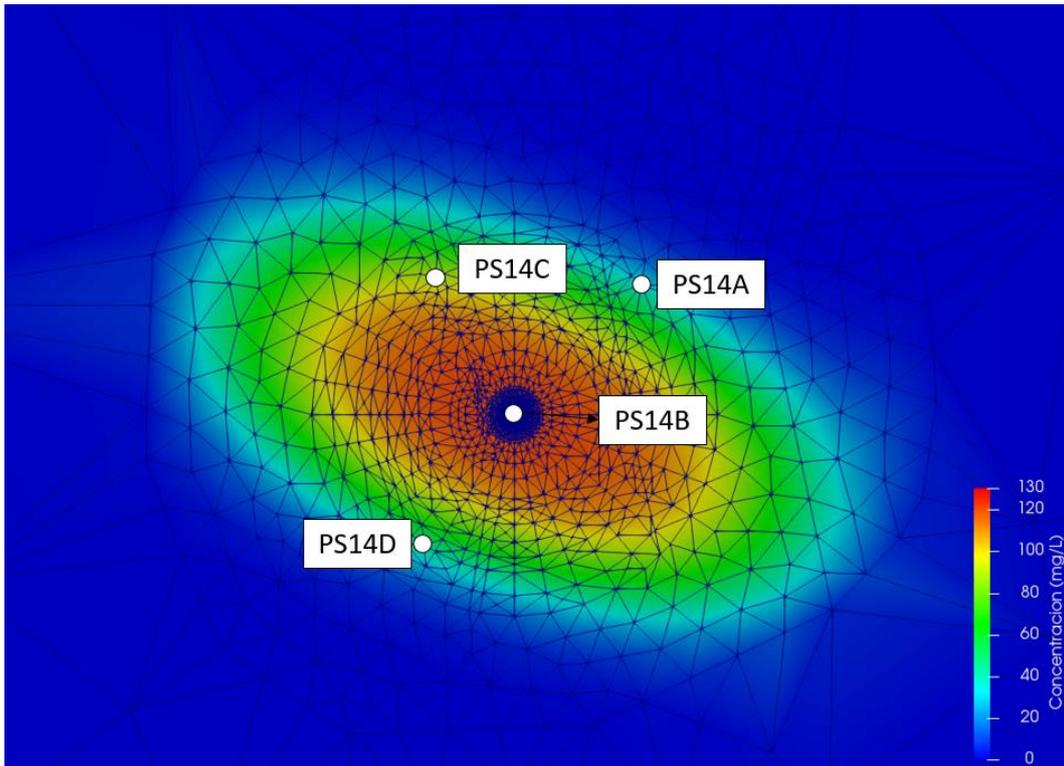
Figure 10.12. Computed Br⁻ plume after 2 hours and 30 minutes of tracer injection which corresponds to the half of the transit time to the borehole PS14A.
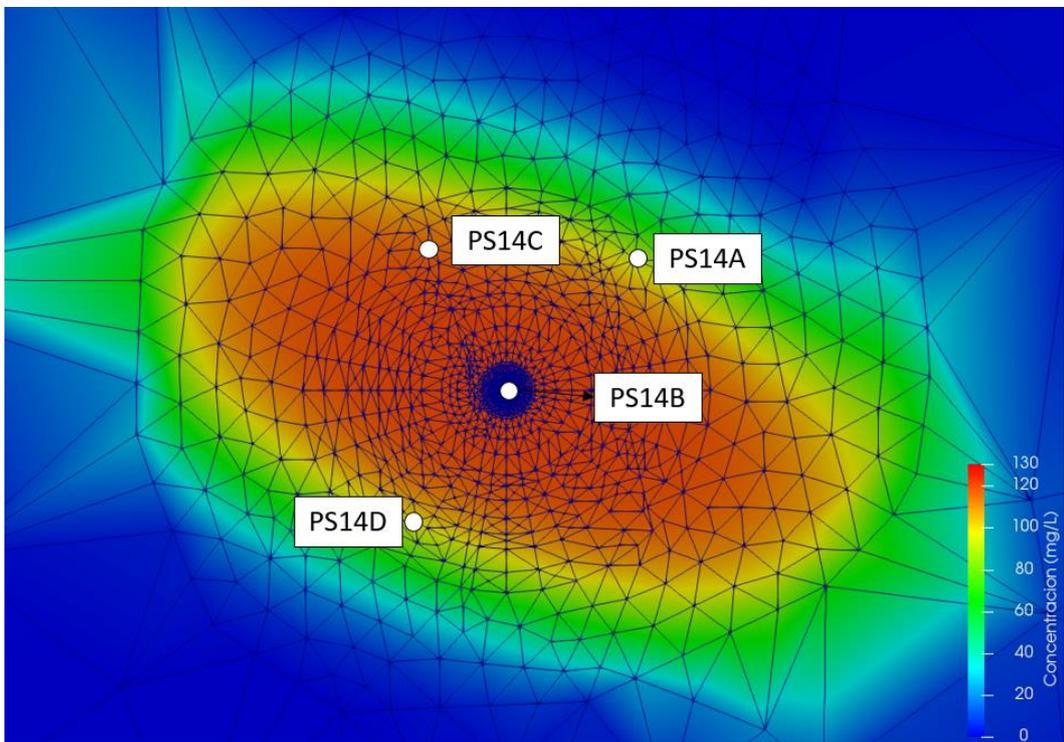
Figure 10.13. Computed Br⁻ plume after 5 hours and 27 minutes of tracer injection which corresponds to the time at which the constant concentration is reached in the PS14A borehole.

10.5 Conclusions

A 2D transient-state horizontal groundwater flow and solute transport model of the tracer injection/extraction performed in borehole PS14B from 10:00 June 5th to 17:30 June 6th has been presented. The model has allowed the estimation of solute transport parameters of the gravels.

Tracer data reveal strong heterogeneities in the gravels which can be modelled by considering the anisotropy of the hydraulic conductivity. The computed tracer concentrations in the PS14A, PS14C and PS14D boreholes are almost identical. The measured Br⁻ concentrations in boreholes PS14A, PS14C and PS14D during injection, however, show significant differences.

A sensitivity run has been performed by considering the anisotropy of the hydraulic conductivity with a main direction forming an angle of -22.5° with the W-E direction. The time evolution of the tracer concentration in the PS14C borehole in the sensitivity run is almost similar to that of the base run. The fit during the injection period is good, while the concentration calculated during the extraction decreases slightly slower than the measured concentration. The fit of the computed concentrations in the PS14A and PS14D boreholes to the measured concentrations in the sensitivity run improves compared to that of the base run. However, the maximum concentrations in the sensitivity run are still higher than the measured concentrations.

11. CONCLUSIONS

In the framework of this Master Thesis the following groundwater flow and pollutant transport have been performed in the site affected by the INQUINOSA factory in Sardas (Huesca):

1) A 2D steady-state groundwater flow along a vertical cross-section in the East-West direction from the headwaters of the Sardas landfill to the Sabiñánigo reservoir, which has been calibrated with piezometric data and used to simulate the average flow conditions and define the initial conditions of a transient state model.

2) A 2D transient-state groundwater flow model along the vertical cross-section in the East-West direction from the headwaters of the Sardas landfill to the Sabiñánigo reservoir, based on the previous steady state model. It has been used to simulate the groundwater flow along several years (multi-annual model) and the tidal effect produced by the changes in the reservoir water level (bimonthly model).

3) A 2D steady-state groundwater flow horizontal model through the gravels of the Gállego river alluvial aquifer from the mouth of the Aurín river to the Sabiñánigo dam. The model has been used to: 1) Quantify the tidal effect of the daily fluctuations of the Sabiñánigo reservoir level on the aquifer hydraulic heads; 2) Estimate the hydraulic conductivity of the sediments at the bottom of the reservoir; and 3) Estimate the hydraulic conductivity of the gravels.

4) A 2D transient-state horizontal groundwater flow model through the gravels of the Gállego river alluvial aquifer from the mouth of the Aurín river to the Sabiñánigo dam. This model is based on the previous stead-state model. Numerical simulations have been performed for a multiannual time horizon for the period February 26th 2014 to August 29th 2019 and for a summer period from June 1st to September 30th 2017.

5) A 2D steady-state horizontal groundwater flow and transient HCH transport model through the gravels of the alluvial aquifer. The model provided the computed HCH plumes in the aquifer and the HCH mass flux from the aquifer into the silting deposits.

6) A 2D transient-state horizontal groundwater flow model through the gravels of the alluvial aquifer for the interpretation of a multi-observation pumping test performed in borehole PS14B on April 26th 2018. The hydraulic conductivities and storage coefficients have been estimated by solving the inverse problem. The leakage coefficient and the vertical hydraulic conductivity of the silts that confine the gravels have been estimated by trial and error.

7) A 2D transient-state horizontal groundwater flow and solute transport model of the tracer injection/extraction performed in borehole PS14B from 10:00 June 5th to 17:30 June 6th. The model has allowed the estimation of solute transport parameters of the gravels.

11.1 Conclusions of the 2D steady-state groundwater flow along a vertical cross-section in the East-West direction

A 2D steady-state groundwater flow along a vertical cross-section in the East-West direction, which runs along the thalveg of the original gully, has been presented. The model has been used to test the conceptual hydrogeological model of the site. The model domain extends from the headwaters of the landfill until the Sabiñánigo reservoir.

The steady-state groundwater flow model has been calibrated with average hydraulic heads measured in boreholes located along the profile. The hydraulic conductivities have been calibrated based on available prior estimates from field tests and previous models. Gradual variations in the hydraulic conductivities have been considered for the shallow altered marls and the alluvial silts.

The model reproduces the average hydraulic heads measured in 19 boreholes. The fit of the numerical model to the measured data is excellent because the average residual is equal to -2.85 cm, the Nash index is equal to 0.9996 and the absolute values of the hydraulic head residuals are smaller than 1 m.

The average water inflow to the Sardas landfill ranges from 20 m^3/d to 30 m^3/d. Most of the inflow comes from the infiltration of the surface runoff of the ravine located in the header of the landfill and the infiltration of surface and subsurface runoff along the perimeter ditches. The landfill outflows take place by pumping wells, underneath and around the front slurry-wall. The

subsurface discharge of the landfill percolates into the Gállego alluvial aquifer. The water inflows into the model domain come from: 1) The runoff of the ravine upstream the landfill near borehole S35E (35%), 2) The recharge along the perimeter ditches (47%) and 3) The recharge from rainfall (18%). Most of the groundwater discharges into the Sabiñánigo reservoir through the layer of silting sediments.

The main conclusions of the 2D steady-state groundwater flow along the vertical cross-section in the East-West direction include:

1) The numerical model confirms the conceptual model proposed by EMGRISA (2014) for the Sardas site.

2) The front slurry-wall acts as a barrier to groundwater flow from the landfill to the floodplain. The numerical model reproduces the piezometric drop measured at both sides of the wall.

3) The hydraulic conductivity of the underlying Larrés marls is very low and hinders groundwater flow except for its shallowest layer, which is more fractured, altered and decompressed (FAD marls).

4) Most of the groundwater flow takes place through the gravels and discharges into the Sabiñánigo reservoir through the layer of silting sediments.

11.2 Conclusions of the 2D transient-state groundwater flow model along the vertical cross-section in the East-West direction

A 2D transient groundwater flow model along a vertical cross-section in the East-West direction, which runs along the thalveg of the original gully, has been presented. The model has been used to test the conceptual hydrogeological model of the site. The model domain extends from the headwaters of the landfill until the Sabiñánigo reservoir. Multiannual and bimonthly numerical simulations have been performed.

The multiannual transient model of groundwater flow confirms the water inflows estimated with the hydrological water balance model. The average inflow ranges from 20 m^3/d to 30 m^3/d. Most of the inflows come from the runoff of the ravine located at the headwaters of the landfill and

the perimeter ditches of the landfill. The outflows of landfill take place underneath the front slurry-wall and by pumping in well S37.

The calculated hydraulic heads reproduce for the most part the measured hydrographs in the alluvial and floodplain silts. Hydraulic head discrepancies are found in wells PS29B and PS29C located near the seepage area. The boundary condition at the seepage should be studied more in depth in future studies.

The model reproduces the hydraulic head hydrographs recorded in the inner landfill boreholes. Groundwater pumping in borehole S37 has been simulated with the simplifying assumption of planar flow. The computed hydraulic heads in the series of S39 boreholes reproduce the measured heads from January 2013 to November 2015. However, the model underestimates the measured hydraulic heads after January 2016.

The water level of the reservoir shows periodic oscillations with an amplitude of 1 m. These oscillations produce a tidal effect on the hydraulic heads in the alluvial aquifer. The bimonthly transient model reproduces the fluctuations of measured hydraulic heads with some smoothing. The discrepancies between measured and computed hydraulic heads may be due to uncertainties in the initial hydraulic heads.

11.3 Conclusions of the 2D steady-state groundwater flow horizontal model through the gravels of the Gállego river alluvial aquifer

A 2D steady-state groundwater flow horizontal model through the gravels of the Gállego river alluvial aquifer from the mouth of the Aurín river to the Sabiñánigo dam has been presented. The model has been formulated to: 1) Quantify the tidal effect of the daily fluctuations of the Sabiñánigo reservoir level on the aquifer hydraulic heads; 2) Estimate the hydraulic conductivity of the sediments at the bottom of the reservoir; and 3) Estimate the hydraulic conductivity of the gravels.

Groundwater inflows include: 1) Areal recharge from rainfall infiltration; 2) Lateral inflows along the East and West boundaries of the alluvial aquifer and 3) Inflow from the reservoir at the downstream part of the aquifer near the Sabiñánigo dam. Groundwater discharges to the Sabiñánigo reservoir, the Gállego river upstream the reservoir, and the Gállego river underneath

the Sabiñánigo dam. Groundwater discharges have been simulated with Cauchy conditions in with leakage coefficients estimated during the model calibration.

Model parameters have been calibrated by using measured hydraulic head data at 40 observation boreholes. The hydraulic conductivity of the gravels on the right bank near the INQUINOSA factory is equal to 1.7 m/d. This value is significantly smaller than the conductivity in the rest of the alluvial aquifer which is equal to 400 m/d. The calibrated values of the vertical hydraulic conductivities of the alluvial silts and of the silting sediments are equal to 0.1 m/d and 0.4 m/d, respectively. The absolute values of the hydraulic head residuals are smaller than 1 m.

The results of the model sensitivity runs show that: 1) The hydraulic heads in the gravels are not significantly sensitive to changes in the hydraulic conductivity of the gravels and to the increase of the vertical hydraulic conductivity of the silting sediments, K_s, for $K_s > 0.2$ m/d; 2) The hydraulic heads in the gravels, on the other hand, are very sensitive to the increase of K_s, the changes in the water level of the reservoir and the water level of the Gállego river upstream the reservoir; 3) The groundwater discharge flow from the gravels into the reservoir is very sensitive to changes of the vertical hydraulic conductivity of the alluvial silts and changes in K_s.

Model results confirm that groundwater discharges into the reservoir at the tail of the reservoir (far from the Sabiñánigo dam). Near the dam, however, there is a downwards vertical water flow from the reservoir into the gravels which later flows underneath the dam through the underlying sandstones of the dam foundation.

11.4 Conclusions of the 2D transient-state horizontal groundwater flow model through the gravels of the Gállego river alluvial aquifer

A 2D transient-state horizontal groundwater flow model through the gravels of the Gállego river alluvial aquifer from the mouth of the Aurín river to the Sabiñánigo dam has been presented which is based on the stead-state model presented in Chapter 6. Numerical simulations have been performed for two-time horizons. A multiannual time horizon was performed for the period February 26th 2014 to August 29th 2019. The second simulation period extends from June 1st to September 30th 2017.

The computed hydrographs reproduce the measured hydrographs in most of the boreholes. The fit to the measured data in the boreholes located on the right bank near the

INQUINOSA factory is slightly worse than in the rest of the aquifer. However, these boreholes are far from the Sardas landfill.

In spite of the uncertainties of the model in areas located far from the Sardas landfill, the selected model domain was needed to account for the effect of the fluctuations in the reservoir levels which affect the hydraulic heads in the aquifer several hundred metres upstream the N-330 bridge. Therefore, the results of the transient state models show that it is necessary to extend the 2D horizontal model domain to the Aurín confluence.

The hydraulic heads in the aquifer vary fluctuate in response to the fluctuations of the water level in the Sabiñánigo reservoir. The hydraulic head contour line of 765 m is near the Sabiñánigo dam when the level of the reservoir is at its minimum value. On the other hand, the hydraulic head contour line of 765 m in the aquifer is near the bridge of the N-330 road, almost 1 km upstream the dam, when the water level in the reservoir is at its maximum.

Groundwater discharges mostly to the Gállego river courses upstream the reservoir when the reservoir water level is maximum. The discharge to the reservoir is small. When the water level in the reservoir is minimum, on the other hand, groundwater discharges into the reservoir mostly through the silting sediments.

11.5 Conclusions of the 2D steady-state horizontal groundwater flow and transient HCH transport model through the gravels of the alluvial aquifer

A 2D steady-state horizontal groundwater flow and transient HCH transport model through the gravels of the alluvial aquifer has been presented. The model provided the computed HCH plumes in the aquifer and the HCH mass flux from the aquifer into the silting deposits.

The model assumes that dissolved HCH is in equilibrium with HCH in the solids and the DNAPL. The equilibrium relationship between total dissolved HCH and HCH solid phase concentrations has been simulated with a distribution coefficient, K_D. The distribution coefficient has been calibrated within the range of reported values given the lack of experimental data for the study area. The computed HCH plumes show similarities with those derived from measured total HCH in the alluvial boreholes. The computed plume of total dissolved HCH is very sensitive to changes in the distribution coefficient. The lower the distribution coefficient, the larger the HCH

plume. The total mass of dissolved HCH discharged from the gravels into the silting deposits ranges from 0 for the base run to 10 kg/year for $K_D = 3.6$ L/kg.

The time evolution of the measured HCH concentrations from 2015 to 2019 show numerous oscillations. The computed concentrations of dissolved HCH concentrations, on the other hand, show no time variability. The analysis of these fluctuations poses challenges and difficulties, as many factors can cause these fluctuations. The analysis of the fluctuations of the measured dissolved HCH data is beyond the scope of this Master Thesis.

11.6 Conclusions of the D transient-state horizontal groundwater flow model through the gravels of the alluvial aquifer for the interpretation of a multi-observation pumping test performed in borehole PS14B

A 2D transient-state horizontal groundwater flow model through the gravels of the alluvial aquifer for the interpretation of a multi-observation pumping test performed in borehole PS14B on April 26th 2018 has been presented. The hydraulic conductivities and storage coefficients have been estimated by solving the inverse problem. The leakage coefficient and the vertical hydraulic conductivity of the silts that confine the gravels have been estimated by trial and error.

The calibrated hydraulic conductivity of gravels for the three material zones range from 300 m/d to 600 m/d, while the calibrated specific storage coefficients range from $1 \cdot 10^{-4}$ m^{-1} to $3 \cdot 10^{-3}$ m^{-1}.

The fit of the computed drawdowns to the measured values is excellent. The main discrepancies (< 0.02 m) occur in borehole ST2, located 245 m from the pumping well. This discrepancy is overcome when the changes in the water level of the Gállego river upstream the reservoir are considered in the model

The transient-state groundwater flow model of the pumping test allowed the estimation of the hydraulic conductivity and the storage coefficient of the gravels and the identification of the relevance of the leakage from the confining silts into the alluvial gravels and the fluctuations of the reservoir water level.

11.7 Conclusions of the D transient-state horizontal groundwater flow and solute transport model of the tracer injection/extraction performed in borehole PS14B

A 2D transient-state horizontal groundwater flow and solute transport model of the tracer injection/extraction performed in borehole PS14B from 10:00 June 5th to 17:30 June 6th has been presented. The model has allowed the estimation of solute transport parameters of the gravels.

Tracer data reveal strong heterogeneities in the gravels which can be modelled by considering the anisotropy of the hydraulic conductivity. The computed tracer concentrations in the PS14A, PS14C and PS14D boreholes are almost identical. The measured Br$^-$ concentrations in boreholes PS14A, PS14C and PS14D during injection, however, show significant differences.

A sensitivity run has been performed by considering the anisotropy of the hydraulic conductivity with a main direction forming an angle of -22.5° with the W-E direction. The time evolution of the tracer concentration in the PS14C borehole in the sensitivity run is almost similar to that of the base run. The fit during the injection period is good, while the concentration calculated during the extraction decreases slightly slower than the measured concentration. The fit of the computed concentrations in the PS14A and PS14D boreholes to the measured concentrations in the sensitivity run improves compared to that of the base run. However, the maximum concentrations in the sensitivity run are still higher than the measured concentrations.

12. REFERENCES

CHE (2010). Análisis ambiental de los sedimentos y del entorno del embalse de Sabiñánigo (Huesca) y evaluación de riesgos. Informe técnico de la Confederación Hidrográfica del Ebro (Ministerio de Medio Ambiente, Medio Rural y Marino). Septiembre de 2010.

Dai Z, Samper J (2006). Inverse modelling of water flow and multicomponent reactive transport in coastal aquifer systems. J Hydrol, 327(3-4), 447-461.

EMGRISA (2011). Ejecución de sondeos para el control de la extensión de la pluma de HCH en el pie del vertedero de Sardas (Sabiñánigo, Huesca). Informe de trabajos realizados. Mayo de 2011.

EMGRISA (2013). Servicio de seguimiento hidrogeológico de Sardas, Sabiñánigo (HUESCA) 2012-2013. Informe final de ejecución de sondeos y trabajos complementarios.

EMGRISA (2014). Servicio de seguimiento hidrogeológico de Sardas, Sabiñánigo (HUESCA) 2013-2014. Informe de elaboración de modelo de simulación de flujo de la parcela al pie de vertedero y zonas aledañas. PD 513004-134.

EMGRISA (2015). Servicio de seguimiento hidrogeológico de Sardas, Sabiñánigo (Huesca). Memoria anual 2015. PD 513007-222.

EMGRISA (2016). Servicio de seguimiento hidrogeológico de Sardas, Sabiñánigo (Huesca) - 2015 exp.: 1407-4422-2015/01. Memoria anual 2015.

EMGRISA (2017). Servicio de seguimiento hidrogeológico de Sardas, Sabiñánigo (Huesca) - 2015, prórroga 2016 y emergencia oct-dic 2016. Expedientes 1407-4422-2015/01 y 1404-4422-2016/12. Memoria anual 2016.

EMGRISA 2018. Servicio de seguimiento Hidrogeológico de Sardas, Sabiñánigo (Huesca) 2017-2018. Expediente: 1470-4422-2016/02. Memoria anual 2018. Febrero de 2019

EPA (1996). Soil Screening Guidance: User's Guide. EPA/540/R-96/018, April 1996.

Fernández J, Arjol M, Cacho C (2013) POP-contaminated sites from HCH production in Sabiñánigo, Spain. DOI 10.1007/s11356-012-1433-8.

Guadaño J (2018). Estudio hidrogeológico del acuífero aluvial del río Gállego en Sabiñánigo (Huesca). Trabajo práctico realizado en el marco de la 16ª edición del Curso Internacional de Hidrología Subterránea de la Universidad Politécnica de Cataluña. Junio de 2018.

Harbaugh, A.W., Langevin, C.D., Hughes, J.D., Niswonger, R.N., and Konikow, L. F., 2017, MODFLOW-2005 version 1.12.00, the U.S. Geological Survey modular groundwater model: U.S. Geological Survey Software Release, 03 February 2017, http://dx.doi.org/10.5066/F7RF5S7G

Krause, P., D. P. Boyle, D.F. Base, 2005. Comparison of different efficiency criteria for hydrological model assessment. ADGEO (5), pp.89–97.

Lorenzo D, Santos A, Dominguez C.M, Guadano J, Gomez J, Fernandez J, 2020, "Transport model of fluids injected in a landfill polluted with lindane wastes", The 30th European Symposium on Computer Aided Process Engineering, May 24-27, 2020 - Milano, Italia

NOTIO (2017). Ensayos de bombeo dentro de las labores de investigación complementaria del emplazamiento de la antigua fábrica de Inquinosa afectada por contaminación de HCH. CD: SARGA-NOTIO-17-NT-01

Prager J. C. 1995. Environmental Contaminant Reference Databook. Volume 1. Van Nostrand Reinhold. New York.

Samper J, Yang C, Montenegro L (2003). CORE2D Version 4: A code for non-isothermal water flow and reactive solute transport. User's Manual. Universidade de A Coruña.

Samper J, Pisani B, Lu C, Bonilla M, Galíndez JM (2009). Evaluación del impacto de las obras del eje atlántico de alta velocidad en el tramo Meirama-Bregua sobre las captaciones de agua y propuestas de alternativas. Informe final del proyecto. Universidade da Coruña, A Coruña, España. 137 pp.

Samper J, Yang C, Zheng L, Montenegro L, Xu T, Dai Z, Zhang G, Lu C y Moreira S (2011). CORE2D V4: A code for water flow, heat and solute transport, geochemical reactions, and microbial processes, Chapter 7 of the Electronic book Groundwater Reactive Transport Models, F Zhang, G-T Yeh, C Parker & X Shi (Ed), Bentham Science Publishers, pp 161-186, ISBN 978-1-60805-029-1.

Samper J, B Pisani, A Naves, B Sobral (2018a). Hidrogeología y modelos de balance hidrológico, y modelos de flujo subterráneo y transporte de contaminantes en los emplazamientos

afectados por Inquinosa, Actividad 1: Modelo de balance hidrometeorológico de la cuenca del vertedero de Sardas. Informe Final, ETS Ingenieros de Caminos, Coruña, UDC, febrero 2019.

Samper J, B Sobral, A Naves, B Pisani (2018c). Hidrogeología y modelos de balance hidrológico, y modelos de flujo subterráneo y transporte de contaminantes en los emplazamientos afectados por Inquinosa, Actividad 3: Modelos numéricos de flujo y transporte de contaminantes en el emplazamiento de Sardas. Informe de Progreso de la Actividad 3, ETS Ingenieros de Caminos, Coruña, UDC, junio 2018

Santos A, C M. Domínguez, D Lorenzo, R García-Cervilla, M A. Lominchar, J, J Gómez, J Guadaño, (2019a), Soil flushing pilot test in a landfill polluted with liquid organic wastes from lindane production, Heliyon, Volume 5, Issue 11, 2019,

Santos A, A Romero, C M. Domínguez, M A. Lominchar, D Lorenzo, R García-Cervilla, (2019b) Anexo 3.1 Ensayos Previos para la Remediación in situ por SEAR y/o S-ISCO del Aluvial de SARDAS. Informe Elaborado por INPROQUIMA (UCM), Departamento de Ingeniería Química y de Materiales. Universidad Complutense de Madrid, 20 Enero 2019. http://www.stoplindano.es/app/uploads/2019/03/Memoria_Sardas_2018.pdf.

Schonard M (2016) Directorate General for Internal Policies Policy Department C: Citizens' Rights and Constitutional Affairs. Lindane (persistant organic pollutant) in the EU.

Suntio LR, Shiu WY, Mackay D, Seiber JN, Glotfelty D (1988) Critical review of Henry's law constants for pesticides. Rev Environ Contam Toxicol 103: 1–59.

Suso J., 2018. Interpretación del ensayo de bombeo realizado en el sondeo PS14B de la red de control de las aguas subterráneas del vertedero de Sardas (Sabiñánigo, Huesca). Informe para EMGRISA. Código: EMG-18-NT-01.

Vijgen J, Abhilash, P.C., Fan Li Y, Lal R, Forter M, Torres J, Singh N, Yunus M, Tian C, Schäffer A, Weber, R (2011). Hexachlorocyclohexane (HCH) as new Stockholm Convention POPs—a global perspective on the management of lindane and its waste isomers. Springer – Verlag 2010.

Vijgen J, Borst B, Weber R, Stobiecki T, Forter M (2019). HCH and lindane contaminated sites: European and global need for a permanent solution for a long-time neglected issue. Enviromental pollution

13. ACKNOWLEDGMENTS